A. A.

2014/2015

UNIVERSITÀ di CATANIA

Dipartimento di Fisica e Astronomia

Dottorato di Ricerca in

Scienza e Tecnologia dei Materiali

XXVII CICLO

ANTONELLA GENTILE

Structural and optical properties of complex-morphology materials based on metal nanostructures

Tesi di Dottorato

Tutor: Prof.ssa M. G. Grimaldi

Supervisor: Dott. F. Ruffino

Coordinatore: Prof.ssa M. G. Grimaldi

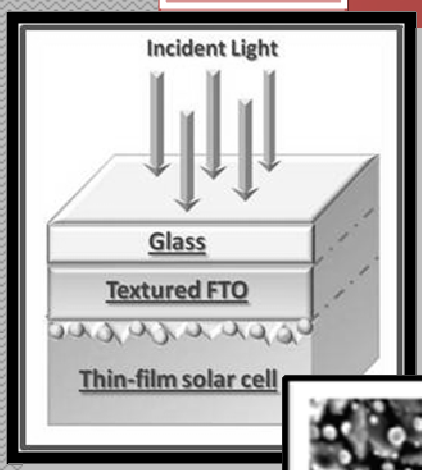

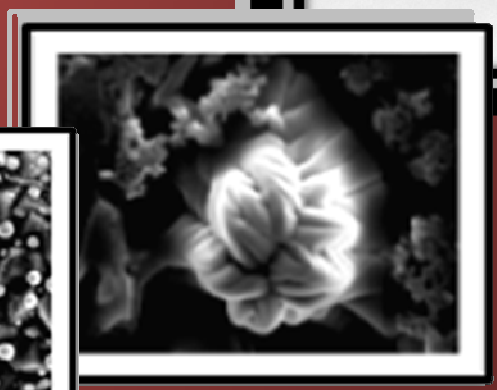

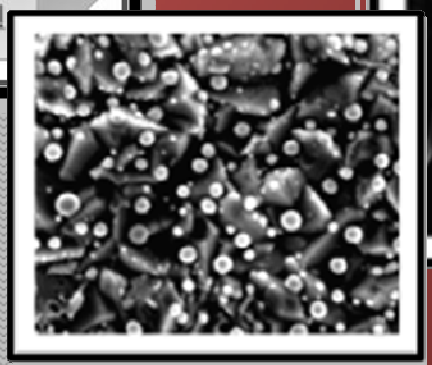

Rare sono le persone che usano la mente.
Poche coloro che usano il cuore e
uniche coloro che usano entrambi.

[Rita Levi Montalcini]

UNIVERSITÀ DEGLI STUDI DI CATANIA

Dottorato di Ricerca in Scienza e Tecnologia dei Materiali
XXVII Ciclo

ANTONELLA GENTILE

Structural and optical properties of complex-morphology materials based on metal nanostructures

Tutor: Prof.ssa M. G. Grimaldi

Supervisor: Dott. F. Ruffino

Coordinatrice: Prof.ssa M. G. Grimaldi

Tesi per il conseguimento del titolo

A.A. 2014/2015

LIST OF ABBREVIATIONS

Abs: Absorption

AFM: Atomic Force Microscopy

BF: Bright Field

CCA: Cluster-Cluster Aggregation

DDA: Discrete Dipole Approximation

DLA: Diffusion Limited Aggregation

EDX: Energy Dispersive X-Ray

EELS: Electron Energy-Loss Spectroscopy

EFTM: Energy Filtered Transmission Electron Microscopy

EF: Enhancement Factor

EM: Electromagnetic

FA: Filled area

FF: Fill Factor

FIB: Focused Ion Beam

FL: Fermi-Level

FDTD: Finite Difference Time Domain

FTIR: Fourier Transform Infrared

FTO: Fluorine Tin Oxide

HPR: Hole Plasmon Resonances

Is: Islands

LTM: Light Trapping Multilayer

MB: Methylene Blue

MIGS's: Metal-Induced Gap States

MOM: Metal-Oxide-Metal

MNPs: Metal Nanoparticles

MS: Metal/Semiconductor

NDs: Nanodendrites

NP: Nanoporous

NPs : Nanoparticles

NSOM: Near Scanning Optical Microscopy

NSs: Nanostructures

NWs: Nanowires

PV: Photovoltaic

RBS: Rutherford Back Scattering Spectroscopy

R&G: Recombination and Generation

RRS: Resonant Raman Spectra

SBH: Schottky Barrier Height

S/C: Semiconductor Contacts

SEM: Scanning Electron Microscopy

SLS: Solid Liquid Solid

SOI: Silicon On insulator

SOS: Silicon On Oxide

SPPs: Surface Plasmon Polaritons

SPRs: Surface Plasmon Resonances

SERS: Surface Enhancement Raman Scattering

t_ FTO: Textured Fluorine Tin Oxide

TEM: Transmission Electron Microscopy

VLS: Vapor Liquid Solid

Contents

Introduction: general overview and outline

For their peculiar properties, metal nanostructures have been extensively used in applications such as catalysis, electronics, photography and information storage, among others. New applications for metals in areas such as photonics, sensing, imaging and medicine have also being developed. Significantly, most of these applications require the use of metals in the form of nanostructures with specific controlled properties. The properties of nano-scale metals are determined by a set of physical parameters, which include the size, shape, composition and structure. In recent years, many research fields have focused on the synthesis of nano-scale size metallic materials with complex shape and composition in order to optimize the optical and electrical response of devices containing metallic nanostructures. This thesis work is in line with this field of scientific literature.

We begin with an overwiev of the basic concepts on the correlation between structural and optical parameters of nano-scale metallic materials with complex shape and composition, and the possible solutions offered by nanotechnology in a large range of applications (catalysis, electronics, photonics, sensing). The aim is to assess the state of the art and, then, show the innovative contributions that can be proposed in this research field.

Then, we report on innovative, versatile and low-cost synthesis techniques, suitable to provide a good control on the size, surface density, composition and geometry of the metallic nanostructures. The main purpose of this study is the fabrication of functional nanoscale-size materials, whose properties can be tailored (in a wide range) simply by controlling the structural characteristics. The modulation of the structural parameters is required to tune the plasmonic properties of the nanostructures for applications such as biosensors, opto-electronics or photovoltaic devices and SERS-active substrates.

The structural characterization of the nano-scale materials is employed in order to define how the synthesis parameters affect the structural characteristics of the resulting metallic nanostructures. Besides, macroscopic measurements are used to probe their electrical and optical properties. Phenomenological growth models are drafted to explain the processes involved in the growth and evolution of such composite systems. After the synthesis and characterization of the metallic nanostructures, we study the effects of the incorporation of the complex morphologies on the optical and electrical responses of each specific device.

The structure of the present work is as follows:

- *Chapter 1 "Complex-morphology materials based on metal nanostructures"*: in this Chapter, we explain the motivations to synthesize metal nanostructures with complex geometry and composition. The need to create morphology alternatives to isotropic shapes, such as spherical geometry, comes from the strong correlation between the structural characteristics and the response of the Localized Surface Plasmon Resonances (LSPR) of the nano-structured metallic materials. The flexibility and scope of the change are highly sensitive to the specific structural parameter. For this reason, we report some experimental studies that demonstrate that the shape and structure of an Au or Ag nanocrystal play the most important

role in determining the number, position and intensity of LSPR modes. Such works show that the LSPR of a single metallic nanoparticle can be shifted in frequency via alterations in particle shape and size. Besides, in nanoparticle ensembles, additional shifts are expected to occur due to the electromagnetic interactions between the localized modes related to neighboring metal nanoparticles. Both experimental and computational studies highlight that two regimes have to be distinguished, depending on the magnitude of the interparticle distance. For closely spaced particles, near-field interactions dominate, and the particle array can be described as an array of point dipoles interacting via their near field. Therefore, interparticle junctions serve as hot-spots for field enhancement, which will be further discussed in Chapter 2 in a context of Surface Enhanced Raman Scattering (SERS). Therefore, the interparticle coupling will lead to shifts in the spectral position of the plasmon resonance compared to the case of an isolated particle. On the contrary, for larger particle separations, far-field dipolar coupling dominates. Far-field coupling field has pronounced influences on the plasmon lineshape, both in terms of resonance frequency, as well as spectral width. Taking into account these properties of plasmonic nanostructures, we report the more common synthesis methods and experimental results related to metal nanostructures with complex shape and composition Taking into account these properties of plasmonic nanostructures, we report the more common synthesis methods and experimental results related to metal nanostructures with complex shape and composition (e.g. metallic dendritic nanostructures, SiO_2 nanowires-Au nanoparticles pea-podded) for advanced applications in the field of electronics, opto-electronics, sensing, bio-sensing and for magnetic devices.

In the Appendix to this Chapter, we report the correlation between structural and optical parameters related to other complex morphologies metal based materials (e.g. gold nanoring and ring dimmers, gold nanorice, nanoporous gold films, nanoporous Au NWs, etc.)

- *Chapter 2 "Structural and optical properties of branched metallic nanostructures for SERS applications"*: this Chapter reports the motivations that lead to synthesize branched metallic nanostructures and the state of the art.

Metallic nanodendrites, defined as large fractal aggregates, with hyperbranched architectures have attracted much attention due to their importance in understanding the fractal growth phenomena (to be distinguished from non-fractal structures such as compact or periodic geometries), and their potential applications in functional devices, plasmonics, biosensing and catalysis. To explain the synthesis techniques and growth kinetics, we report many experimental works. In these works, the controlled growth of Au dendritic structures is obtained using chemical synthesis methods. The analyses of the experimental results suggest that the growth conditions strongly affect the morphology of the resulting complex nanostructures. Indeed, the interaction between chemical solutions and growing metal crystals results in a delicate balance between the diffusion and reaction rate under non-equilibrium conditions, favoring the formation of planar dendrites with a symmetric single-crystalline structure. The well-known growth mechanisms

under non-equilibrium conditions are explained on the basis of the Diffusion Limited Aggregation (DLA) model and Cluster–Cluster Aggregation (CCA) model. In a DLA regime, the growth takes place by bonding of individual atoms to the growing surface after the reduction of the metal ions. Whereas, according to the CCA model, the individual metal clusters aggregate to form a branched morphology. Besides, to understand the processes involved in the transiction from faceting to branching, we report the physics of a snow crystal. When the crystal growth is dominated by attachment kinetics, the resulting crystals are faceted. Instead, when the particle diffusion dominates the crystal growth dynamics, branching occurs. If the crystal morphology exhibits numerous branches and side-branches, then the growth is dendritic, which literally means "tree-like". Dendritic crystal growth is one example of the more general phenomenon of pattern formation in non-equilibrium growing systems.

In comparison with the methods reported in the literature, we also suggest a simple and versatile physical procedure for obtaining Au dendrites (Au Ds), reminiscent of fractal structures, on sample surfaces. In particular, we observe a peculiar structural evolution of the Au film (20 nm thick film) on Si substrate from a continuous coating to Au Ds as a consequence of thermal treatment at 1373 K (1100 °C), in the presence of fast heating and cooling stages (1373 K/min.). Our structural characterizations of Au dendrites suggest that these structures are formed by Si atoms originating from the substrate and are covered by crystalline Au nanostructures. In order to understand the formation mechanism of the dendritic structures, the role of the substrate (using three different substrates: c-Si, poly-Si and SOS) and the temperature (the samples have been processed at three different temperatures, T_1 = 1073 K, T_2 = 1273 K and T_3 = 1373 K) in the growth process are investigated.

Besides, we draft the phenomenological model for the growth of the dendritic structures by considering the kinetic processes that occur at the Au-Si interface in a far-from-equilibrium condition.

Finally, we report the results of the optical measurements that show the efficient behavior of the Au Ds as scattering centers in the infrared region of the spectral range. In addition, SERS measurements, performed by MB or thiophenol as probe molecules, highlight that dendritic nanostructures can be used as SERS-active substrate to obtain amplification factors of electromagnetic field, due to the resonant coupling between the Raman signal and plasmonic oscillations related to sharp metallic tips of the Au dendritic structures. The comparison between SERS spectra related to Au Ds on different substates suggests that to obtain higher EF, the planar size of the Au dendrites, and then, the SERS-active area, must be in μm-scale. Also, the dendrite surface must be uniformly covered by Au, such that most MB molecules are adsorbed to the dendritic structures.

Another important result, from SERS measurements, is the depolarization factor of the silicon signal due to the interaction between laser radiation and dendritic structures. The changes of the characteristic ratio between the polarized components of the Si signal suggest the depolarization effect due to the Au dendritic structures acting as micro-antennas.

- *Chapter 3 "SiO_2 Nanowires-Au Nanoparticles pea-podded composites: synthesis and structural analyses"*: in this Chapter, we explain why the research in biosensing and optoelectronic devices is focused on the study of the structural and optical properties of metallic nanoparticles (MNPs) embedded in the dielectric matrix. Many works in the literature have shown that noble metal nanoparticle-dielectric matrix composite systems have practical applications in ultrafast all-optical switching devices owing to their enhanced third-order nonlinear susceptibility, especially near the surface-plasmon-resonance (SPR) frequency. Therefore, metal-dielectric nanocomposites (see SiO_2 nanowires-Au nanoparticles pea-podded composites) have been applied in optical switching devices for non-linear and fast optical response near the SPR. The experimental results in the literature have suggested that the electronic, optical and magnetic properties of metal NPs embedded in a dielectric matrix depend on the size and shape of NPs, the interparticles distance and the dielectric costant of the surrounding medium. To understand the growth dynamics of these composite systems, we report the most common synthesis approaches, such as the sol-gel process, metal-dielectric co-sputtering deposition, metal-ion implantation into a dielectric matrix and pulsed laser deposition, to prepare metal-dielectric nanocomposites. Taking into account the previous literature, we focus our attention on a simple and versatile method for the direct growth of SiO_2 NWs on Si surface (a method allowing direct applications in Si-based solid state devices). We observe that amorphous SiO_2 NWs can be grown on a crystalline Si substrate by first deposting a thin metal film (Au, for example) on its surface, and then heating the system to elevated temperature (>1273 K), in an inert ambient (e.g. N_2 or Ar), containing trace amounts (3–5 ppm) of oxygen. Typical annealing conditions for the growth of such a structure are 60 minutes at 1373 K (1100 °C). The prevalence of such bead strings in the SiO_2 nanowires depends critically on the growth conditions and may vary between about 1% and 80%, even on a single wafer. In particular, after the growth of SiO_2 nanowires-Au nanoparticles pea-podded composites (from 30 to 150 nm in diameters and until 1mm in length), using TEM analyses, we proceed to the quantification of the SiO_2 NWs diameters (D_{NWs}) and Au NPs diameters (d_{NPs}) embedded in them, in order to establish a specific correlation between D_{NWs} and d_{NPs}. A further correlation is established between the diameter of the Au NPs embedded in a single NW and their center-to-center distance (s_{NPs}). From the experimental correlations of such parameters, information on the characteristics of the mechanisms governing the formation of the SiO_2 NWs-Au NPs pea-podded structures is inferred.

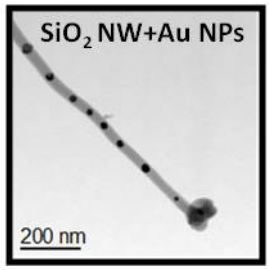

Then, on the basis of the experimental data, we propose a phenomenological model for the formation and time evolution of the SiO_2 NWs/Au NPs pea-podded structures, based on the coexistence of instability and diffusion processes**.**

- *Chapter 4 "Nanoscale structuration and optical properties of thin gold films on textured FTO"*: in this Chapter, we show that thermal treatments of thin Au films, deposited on a glass/textured_FTO (t_FTO) substrate, can induce the growth of Au nanoparticles (NPs), whose

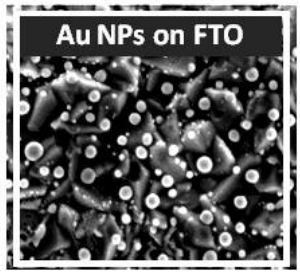

structural characteristics can be modulated by varying the parameters of the heating stages. For standard thermal processes, the temperature and time of the heating process are key parameters to induce the gold film break up and NPs growth. The structural characterizations of the thermal treated samples show that a temperature well below the gold melting point (1064 °C) induces the formation of arrays of Au nanodroplets due to the solid-state dewetting process. In particular, the treatment at high temperature (500 °C-180 min) allows a whole break-up of the Au film into nanoparticles, while it induces structural changes of the substrate, so that the electrical response of the glass/t_FTO/Au NPs multilayer is worsened. Our results imply that the standard thermal process at temperature above 400°C does not allow to obtain a glass/t-FTO/Au NPs multilayer with electrical properties suitable for photovoltaic applications.

We also show that laser irradiation at increasing fluence (0.50-1.0 J/cm^2) of the samples as deposited optimizes the synthesis process of Au NPs, and preserves the structural and electrical properties of the t_FTO/glass substrates. Electrical measurements, indeed, suggest that the laser operating at 532 nm does not produce any thermal damage due to local heating of the t_FTO layer. Structural analyses of the Au coated-substrates indicate that the metallic films are molten and broken up into discrete-nanometer scale islands after laser exposure. At lower energy, the break up into discrete droplets is incomplete. At fluencies higher than the threshold for break up (1.0 J/cm^2), the films are fully dewetted in Au NPs. The comparison between the absorption spectra, related to the substrates covered by 5 nm or 10 nm of Au and submitted to laser treatment at higher energy, indicates an improvement of the absorbed radiation from the sample with larger Au NPs. The simulated trends of the ratio between scattering cross section and absorption cross section in the visible spectral range suggest that the efficiency of absorption dominates over scattering efficiency in the spectral range between 200 and 600 nm for both samples. For wavelength values above 600 nm, instead, the results of the simulation suggest that the glass/t_FTO/Au NPs with larger gold nanoparticles exhibit a reduction of the parasitic absorption and an improvement of the scattering cross section. By varying the NPs radius from about 18 nm to 24 nm, the simulation shows that the scattering remains symmetric in forward and reverse directions. Thus, the experimental results confirm that the surface coverage size distribution of Au NPs is the key parameter to correlate the structural and optical properties of the glass/t_FTO/Au NPs multilayer.

For its peculiar optical and electrical properties, we have introduced the glass/t_FTO/Au NPs multilayer (obtained by nanosecond laser irradiation) with optimized Au NPs coverage size distribution as Light-Trapping-Multilayer (LTM), into thin film solar cells. In order to obtain information about the effects of the introduction of Au NPs at the t_FTO/p-i-n interface of solar devices, the I-V characteristics have been taken into account. The analysis of I-V characteristics under dark conditions indicate a decrease of the Schottky barrier (φ_B) by increasing the Au NPs size. This phenomenon induces an improvement of the saturation current (I_s) of about one order of magnitude ($I_{S\_Au5nm}=2.64\cdot10^{-10}$ A, and $I_{S\_Au10nm}=6.25\cdot10^{-9}$ A). The enhancement of the

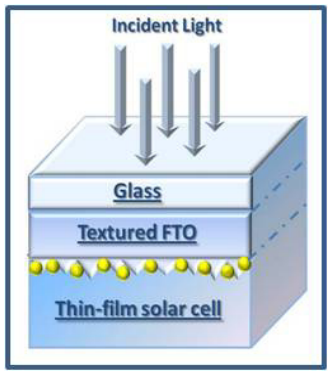

saturation current and the reduction of Schottky barrier height (determined by mechanisms such as the recombination or diffusion currents) induce an open circuit voltage (V_{OC}) reduction, which increases with the improvement of the NPs size. The V_{OC} reduction suggests a higher amount of recombination phenomena in the solar devices with larger Au NPs at the t_FTO/p-i-n interface, with respect to the reference device. We deduce that the improvement of the recombination processes may be due to the presence of metal-induced gap states or defect-realeted states, in agreement with the FL pinning by electronic states at the MS interface. These processes reduce the light trapping and then the short-circuit current (I_{SC}) values. Indeed, the analyses of I-V characteristics under light conditions highlight a decrease of I_{SC} due to the improvement of the parasitic absorption by larger NPs. Thus, we conclude that the incorporation of Au NPs at the FTO/p interface (in the p-i-n structure) induces changes of I_{SC} and V_{OC} that worsen the solar cell parameters, such as the Fill Factor (FF) and yield factor (η), as highlighted by the analyses of I-V characteristics under light condition.

Chapter 1

Complex-morphology materials based on metal nanostructures

1.1 Metal nano-scale size structures with complex shape and composition: synthesis methods, properties and applications

Nano-scale size materials are materials with at least one dimension between 1 and 100 nm [1]. The crystalline nanomaterials are also characterized by a single-domain crystalline lattice, without the complicating presence of grain boundaries [2]. Scientific interest in nanomaterials has been growing steadily due to their unique position as a bridge between atoms and bulk solids, as well as their fascinating properties and potential applications [3]. The ability to generate such nano-scale size materials is central to advances in many areas of modern science and technology. In principle, the electron confinement by a nano-material provides the most powerful means to manipulate the electronic, optical and magnetic properties of a solid material. This notion explains why nanomaterials have been the primary source for discovering and studying quantum size effects, with examples of quantized excitation [4-7], Coulomb blockade [8], metal-insulator transition [9, 10], and superparamagnetism [11]. Metallic materials have been one of the most ancient fields of study. Among all kinds of inorganic solids, metals deserve special attention because they represent more than two thirds of the elements in the periodic table. Most metals crystallize in the same cubic close-packed (*ccp*) structure, a face-centered cubic (*fcc*) lattice that allows for easy characterization. Properties such as strength, toughness, thermal and electrical conductivities, ductility and high melting point make the metals useful for applications ranging from household items to space ship. Traditional applications are mainly based on the bulk metallic properties. New applications exploit the novel properties of metal nanomaterials [12]. Nanomaterials exhibit fascinating size-, shape- and crystal form-dependent properties. Like the bulk metals, nanomaterials of metals are also going to bring profound changes in many spheres of science, technology and industry. Though metal nanoparticles have a long history of preparation and applications, the field has undergone explosive growth in recent years. Metal nanoparticles with excess of morphologies have been prepared, such as polyhedrons, plates, prisms, rods, wires, nanoboxes, nanocages, dumbbells, nanoshuttles, stars, branched rods and wires, dendrites, nanorings, nanotubes, and so on. Such metal nanostructures possess a range of great properties, and many metals have found extensive use in applications that include catalysis [13], electronics [14], photography [15], and information storage [16], among others [17]. New applications for metals in areas such as photonics [8, 19], sensing [20], imaging [21], and medicine [22] are also being developed. Significantly, most of these applications require the use of metals in a finely divided state, preferably in the form of nanocrystals with precisely controlled properties. The properties of a metal nano-crystal are determined by a set of physical parameters that may include its size, shape, composition and structure. In principle, one can tailor and fine-tune the properties of a metal nanocrystal by controlling any one of these parameters, but the flexibility and scope of change are highly sensitive to the specific parameter. For example, in the case of Localized Surface Plasmon Resonance (LSPR) and Surface-Enhanced Raman Scattering (SERS), both computational and experimental studies have demonstrated that the shape and structure of a Au or Ag nanocrystal play the most important role in determining the number, position and

intensity of LSPR modes, as well as the spectral region or polarization dependence for effective molecular detection via SERS [23]. In the case of catalysis, it is well-established that the activity of a metal nanocrystal can be enhanced by reducing its size [24]. The selectivity, however, is most sensitive to the packing of atoms on the surface or the exposed facets of a nanocrystal [25]. For example, Pt can selectively catalyze different types of chemical reactions, with the {100} and {210} facets being most active for reactions involving H_2 and CO, respectively [26]. Of course, the facets exposed on a nanocrystal have a strong correlation with the shape. These and many other examples clearly illustrate the importance of shape control to the efficient utilization of metal nanocrystals. The last decade has evidenced the successful synthesis of metal nanocrystals in a variety of shapes. Examples include: sphere; spheroid; cube; cuboctahedron; octahedron; tetrahedron; right bipyramid; decahedron; icosahedron; thin plate with a triangular, hexagonal, or circular profile; and rod or wire with a circular, square, rectangular, pentagonal, or octagonal cross sections. The emergence of many novel approaches induces to synthesis and synthetic design, control of composition, size, morphology, and assembly structure and impressive advances in the characterization and manipulation techniques of metallic nanoparticles. A number of applications have been realized and multitudes of new applications have been envisaged. Among the many morphologies investigated, the anosotropic metal nanostructures have attracted great attention in the last decade due to their unique properties originated in their shape and their potential impact in new technologies. Examples of anisotropic NPs include rods, bars, triangular plates, disks, hierarchical structures among others (fig. 1.1) [27-34].

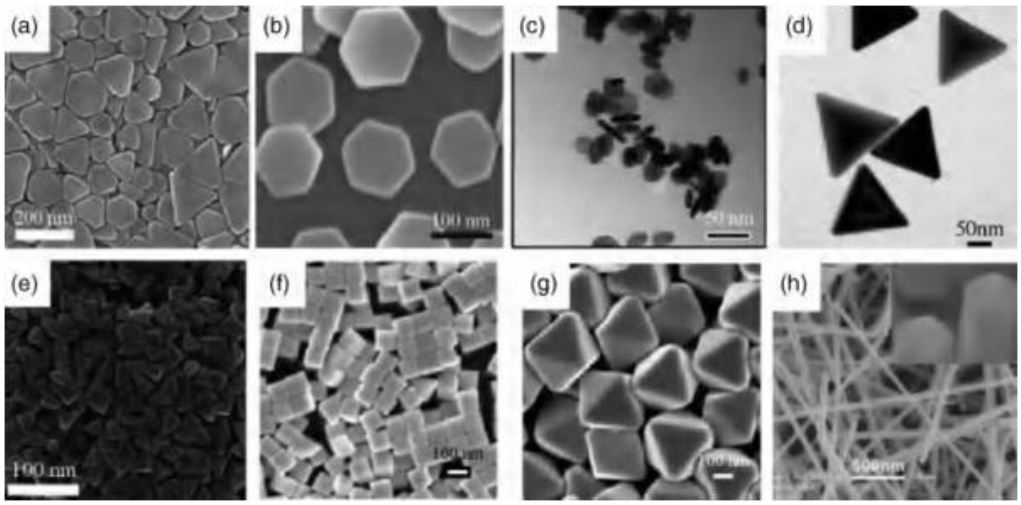

Figure 1.1 - Examples of silver NPs with different shapes obtained by colloidal synthesis. (a) Triangular (and some hexagonal) nanoplates. (b) Hexagonal plates. (c) Disklike plates. (d) Tetrahedral NPs. (e) Bipyramids. (f) Cubic and (g) octahedral NPs [34].

By controlling the shape of the particle, the crystallographic planes that are exposed at the surfaces are tailored and, as a consequence, the atomic arrangement that makes the interface with the medium can be tuned. This has been shown to be critical for most chemical-physical properties, expanding the already broad range of applications of NPs. One of the most appealing examples impacted by the shape-dependent properties of NPs is heterogeneous catalysis [35]. Several catalysts are composed by metal NPs dispersed on high surface area supports. In a heterogeneous catalytic reaction, the binding of the reagent molecules and the formation of the new bonds, which will form the product molecules, depend not only on the available orbitals of the reagents but also on the geometry of the atomic arrangement at metal surface. Hence, controlling the exposed facets of a NP can be a major step toward a deeper understanding of the catalytic reaction and the design of better catalysts.

Metals, such as gold and silver, show a resonance in the ultraviolet-visible region of the spectra known as surface plasmon [36]. This resonance arises from collective oscillations of the conduction electrons of the metal and strongly depends on the size, shape, local environment [37], and assembly of the NPs [38]. When a molecule is attached to the surface of a metal NP, its Raman scattering cross section can be enhanced by several orders of magnitude, from 10^6 up to 10^9 if the incident light is tuned to the surface plasmon resonance of the particle [39]. This effect, known as SERS, results from an intense local amplification of the electric field near a metal surface when surface plasmon resonates in phase with the incident light. Because the electromagnetic near-field intensity is higher at sharp edges and tips, anisotropic NPs exhibit high Raman scattering enhancement factors that have been exploited for the detection of diluted molecules in analytical applications. For example, Mulvihill et al. [40] explored Langmuir-Blodgett monolayers of cubic, cuboctahedral, and octahedral silver NPs to detect trace amounts of arsenic in water. The best results were obtained with octahedral silver NPs, for which a detection level in the ppb range was achieved.

To understand the effects of the complex shape of the metallic nanoparticles on the plasmonic properties, the results of the optical characterizations related to non-regular geometries are reported. For example, dark-field optical microscopy and near-field optical extinction microscopy enable the observation of plasmon resonances of a single particle. In dark-field optical microscopy, only the light scattered by the structure under study is collected in the detection path, while the directly transmitted light is blocked using a darkfield condenser. This enables the study of single particles dilutely dispersed on a substrate. Figure 1.2 (a) shows as an example of the dipolar plasmon lineshapes related to colloidal silver particles of different shapes. In near-field optical spectroscopy, instead, a thin (metalized or uncoated) fiber tip with an aperture on the order of 100 nm is brought into close proximity of the particle using an appropriate feedback scheme. The plasmon resonances can then be mapped out using either illumination through the tip and collection in the far-field, or evanescent illumination from the substrate side and light collection via the tip. Figure 1.2 shows scattered light images (fig. 1.2 (b)) and plasmon lineshapes (solid lines in fig. 1.2 (c)) of a variety of gold nanoparticles [41].

Figure 1.2 highlights that the localized plasmon resonance of a single metallic nanoparticle can be shifted in frequency from the Fröhlich frequency [41] via alterations in particle shape and size. Besides, in particle ensembles, additional shifts are expected to occur due to electromagnetic interactions between the localized modes. For small particles, these interactions are essentially of a dipolar nature, and the particle ensemble can in a first approximation be treated as an ensemble of interacting dipoles. Two regimes have to be distinguished, depending on the magnitude of the interparticle distance (*d*).

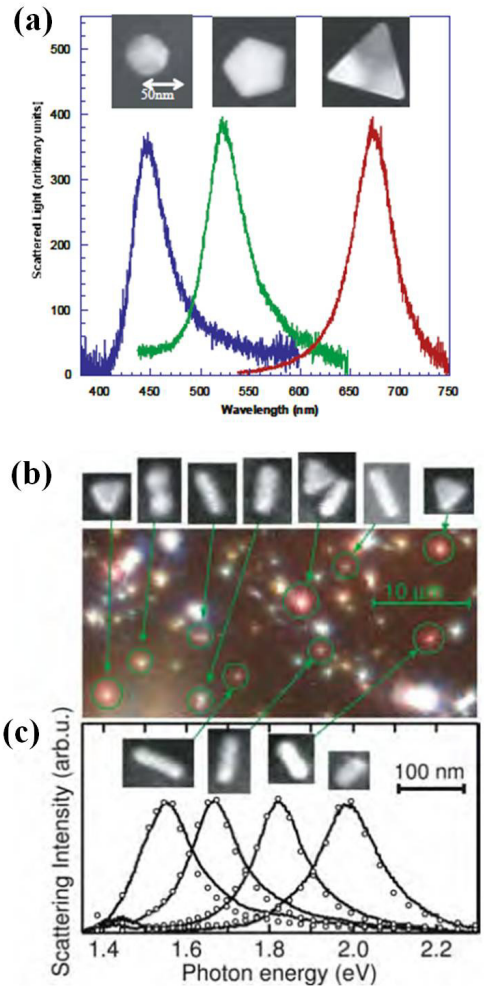

Figure 1.2 - (a) Scattering spectra of single silver nanoparticles of different shapes obtained in dark-field configuration. Optical dark field images together with SEM images of individual gold nanoparticles (b) and corresponding scattering spectra (c) for an incident light polarization along the long particle axis [41]**.**

For closely spaced particles, $d<<\lambda$, near-field interactions with a distance dependence of d^{-3} dominate, and the particle array can be described as an array of point dipoles interacting via their near-field. In this case, strong field localization in nano-sized gaps between adjacent particles has been observed for regular one-dimensional particle chains [42]. The field localization is due to a suppression of scattering into the far-field via excitation of plasmon modes in particles along the chain axis, mediated by near-field coupling. Figure 1.3 illustrates this fact by showing the simulated distribution of the electric field above single gold nanoparticles (fig. 1.3 (a)) and a particle chain (fig. 1.3 (b)). From the images, it can clearly be seen that scattering is drastically suppressed for closely spaced particles, and that the fields are instead highly localized at interstitial sites. Interparticle junctions such as these therefore serve as hot-spots for field enhancement, which will be further discussed in Chapter 2 in a context of SERS. Therefore, the interparticle coupling will lead to shifts in the spectral position of the plasmon resonance compared to the case of an isolated particle.

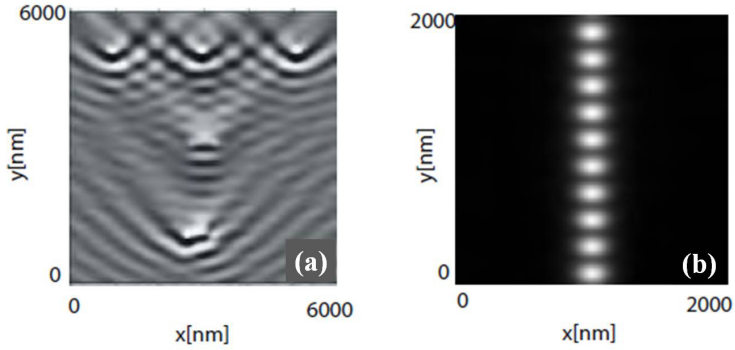

Figure 1.3 - Simulated intensity distribution of the optical near-field above an ensemble of well-separated gold particles (a) and a chain of closelyspaced gold nanoparticles (b). While for separated particles interference effects of the scattered fields are visible, in the particle chain the fields are closely confined in gaps between adjacent particles. Plasmon resonances were excited using prism coupling with the direction of the in-plane moment component as outlined in the pictures [41].

Maier et al. [43], using one-dimensional arrays of 50 nm gold particles with varying interparticle distance, demonstrated experimentally the shifts in resonance energy using far-field extinction spectroscopy Due to the strong scaling of the interaction strength with d^{-3} particle separations in excess of 150 nm are sufficient to recover the behavior of essentially isolated particles.

For larger particle separations, $d>>\lambda$, far-field dipolar coupling with a distance dependence of d^{-1} dominates. For the example of two-dimensional gratings of gold nanoparticles with various lattice constants, fig. 1.4 shows that far-field coupling has pronounced influences on the plasmon lineshape, both in terms of resonance frequency as well as spectral width. We note that interactions between metal nanoparticles can be further enhanced by providing additional

coupling pathways, for example in the form of propagating SPPs for particle arrays fabricated on a conductive substrate [41].

In this subsection, we report the synthesis methods and experimental results of the characterizations related to metal nanostructures with complex shape and composition for advanced applications in the field of electronic, opto-electronic, sensing, bio-sensing and magnetic devices.

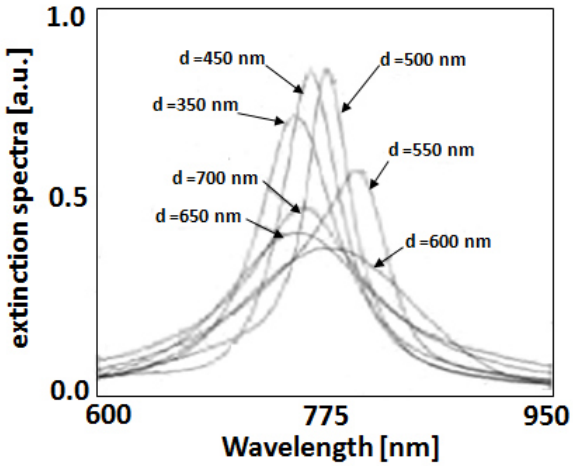

Figure 1.4 - Extinction spectra for square two-dimensional gratings of gold nanoparticles (height 14 nm, diameter 150 nm) with grating constant *d* situated on a glass substrate [41].

1. <u>Metallic nanodendrites</u>: the field enhancement surrounding nanoscale metallic particles offers an efficient tool to manipulate the light-matter interactions at optical frequencies [44, 45]. For spectroscopic applications, the field confinement near these structures reduces the mismatch between the wavelength of incident light and the size of molecules under study. In the SERS, this propertie can boost the Raman cross section of molecules by many orders of magnitude. SERS offers a very sensitive tool for biological and chemical sensing [46], enabling vibrational spectra to be obtained even from single molecules [47]. The signal enhancement in SERS mostly comes from the excitation of localized surface plasmon resonances (LSPRs) and the "lightning-rod" effect [48]. The latter is particularly pronounced for sharp tips and nanoparticle dimers with small inter-gap size. The optimum substrate for SERS should have the highest average field enhancement possible, be highly tunable, and offer a broad resonance bandwidth, although satisfying all these criteria is very challenging. One of the candidates for a highly tunable substrate is the non-isotropic geometry, such as the dendritic nanostructures. Metallic nanodendrites, defined as large fractal aggregates, with hyperbranched architectures (see fig. 1.5) have attracted much attention due to their importance in understanding the fractal growth

phenomena (to be distinguished from non-fractal structures such as compact or periodic geometries), and their potential applications in functional devices, plasmonics, biosensing and catalysis.

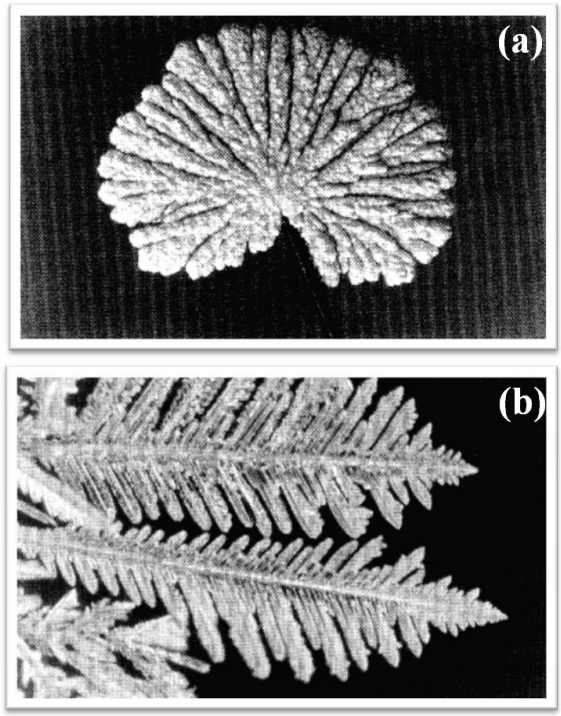

Figure 1.5 - Dendritic structures obtained by electrochemical deposition of copper. (a) from 0.5M $CuSO_4$/0.5M H_2SO_4 at 350 mV (frame width = 2.5 mm); and (b) from 0.5M CuClq/0.5M H_2SO_4 at 500 mV (frame width = 0.6 mm) [49].

Fractal nanostructures can be formed by metals (Au [50, 51], Pt [53, 54], Pd [55, 56], Rh [57, 58], Ni [59], Ru [60, 61], metal oxides [62–65], and semiconductors [66–72]. Because of their higher structural complexity, compared to nanospheres, nanowires and nanodiscs, these branched nanostructures are expected to have a wide range of technological applications [68, 73]. For example, they have interesting catalytic [60, 61], magnetic [57, 59, 72], optical [50, 68, 72], and electronic [68, 69] properties, and semiconductor heterostructures have potential uses in solar cells [69]. Branched nanostructures have also been suggested as interconnections in the bottom-up self assembly of future nanocircuits and nanodevices. Therefore, it is important the mechanism by which these structures are formed [52, 70, 72], which is a crucial step toward realizing synthetic control over their structural and functional properties. Synthetic control over the size and shape of these nanostructures is achieved using

different chemical approaches. The controlled synthesis of these metal complex morphologies allows the modulation of the optical properties for each specific application.

Au and Ag nanoparticles show a characteristic absorption in the visible region of the electromagnetic spectrum due to the surface plasmon resonance. The position and width of the surface plasmon resonance band are considerably influenced by the size and shape of the nanocrystals. The wavelength dependence of the extinction coefficient is fairly well described by Mie theory [43] for metal particles with sizes much smaller than the wavelength of light [63]. According to Mie theory, the extinction coefficient is given by [74]

$$k = \frac{18\pi N V \varepsilon_m^{3/2}}{\lambda} \frac{\varepsilon_2}{[\varepsilon_1 + 2\varepsilon_m]^2 + \varepsilon_2^2} \tag{1.1}$$

where λ is the wavelength of incident light, and ε_1 and ε_2 are the real and imaginary parts of the complex dielectric function of the metal, and ε_m is the dielectric constant of the surrounding medium assumed to be an invariant with respect to the frequency of the light. The overall dielectric constant is given by

$$\varepsilon = \varepsilon_1 + i\varepsilon_2 \tag{1.2}$$

One can readily see that the dependence of the extinction coefficient on wavelength is Lorentzian. Besides, it is known that anisotropic metallic nanoparticles normally exhibit two principal SPR absorption peaks, characteristic of the short (transverse band) and long (longitudinal band) axes.

To obtain more information about the changes in the optical response that occurs from a regular to a complex morphology of metallic nanostructures, we report the results of some experimental works. T. Huang et al. [74] show the UV-vis absorption spectrum of the as-prepared Au nanodendrites suspended in water (see inset in fig. 1.6). The spectrum displays a gradual increase in absorption from ~500 nm to the near-IR region without indication of leveling off, which could be attributed to the longitudinal plasmon band, indicating a remarkable overlapping between the transverse band and the longitudinal band. It is well-known that the position and intensity of the longitudinal band depend largely on the size, aspect ratio and mutual coupling of Au nanocrystals. The authors suggest that the observed overlapping between the transverse band and the longitudinal band for the obtained Au nanodendrites could be attributed to the polydispersity in the length and diameter of the trunks and branches, which may lead to a variety of sizes and aspect ratios. The multiple coupling between neighboring trunks and side branches may also result in a longitudinal plasmon band with the position lying in a wide range of wavelengths. So, the observed absorption spectrum may represent a contour combining the size, aspect ratio and coupling factors of the hierarchical dendritic structures.

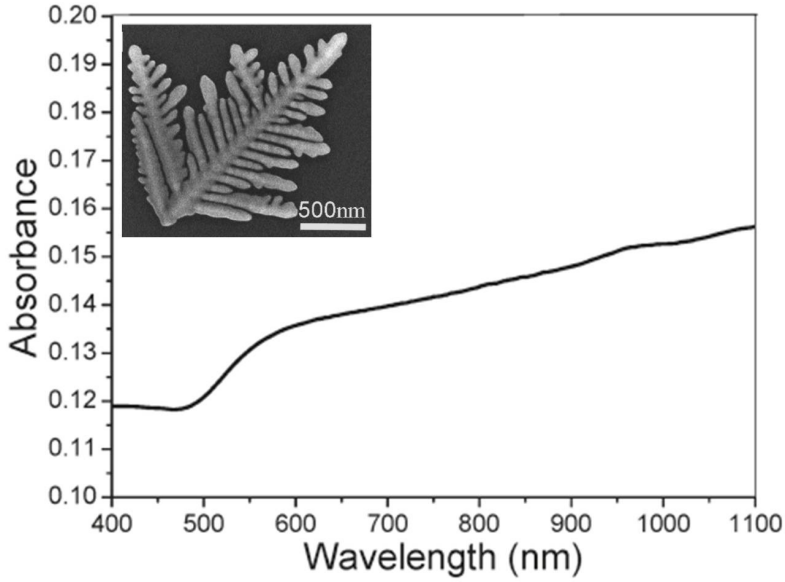

Figure 1.6 - UV-vis absorption spectrum of Au nanodendrites. The inset shows the Au nanodendrites grown in mixed DTAB/β-CDsolution. [DTAB]=5.0 mM; [β-CD]/[DTAB]=0.5 [74].

S. Kaniyankandy et al. [75], instead, report the optical properties of silver nanodendrites, synthesized by electrodeposition using $AgNO_3$ as the source in ammoniacal solution. They reports that SEM patterns of the samples show that as consequence of the addition to the starting solution of a small amount of Ammonia, the deposits (Ag B) show a dramatic change in morphology from irregularly shaped to long strands or rods. Furthermore increase of NH_3 (Ag D) is not greatly affect the morphology. The structutal characterizations, shown in this work, indicate that the average value of thickness of the central stem of a dendrite is ~50 nm. Along the central stem (with an average length of ~5 μm), branching is visible for every ~50 nm, and in some cases it is also hyperbranched. The branches of the dendrites are predominantly planar and hyperbranched. To illustrate the changes of the optical properties due to the different morphology of the resulting nanostructures, the authors compare the results of the simulation with the results of the optical measurements (fig. 1.7). The simulation of the UV–vis spectra related to the metal colloids is shown in the inset of fig. 1.7. The authors highlight that the spectra show the Lorentzian nature of the band, and that the decrease in the size of nanoparticles leads to a decrease in the peak height and an increase in the peak width. The experimental UV–vis spectra (fig. 1.7) clearly give a single broad peak with maxima at λ = 380 nm. This indicates that the particles are predominantly spherical and do not have shape anisotropy. Besides, the peak is highly asymmetric and has a large tail towards the lower energy region, i.e. towards red. The peak extends to the entire visible region of the electromagnetic spectrum. This is contrary to the expected Lorentzian line shape. S. Kaniyankandy et al. explain

that this result is due to the fact that, according to Mie theory, metal nanoparticles are assumed to be non-interacting spheres. However, in their work the metal nanoparticles are assembled in the form of a supramolecular dendritic structure. Therefore, a considerable amount of interaction is expected among the nanoparticles. Hence, the contribution from higher order multipoles and the distribution of depolarization factors have to be taken into consideration while simulating the absorption spectra. The distribution of depolarization factors in interacting metal spheres gives rise to a shape asymmetry for the SPR band. This has been previously observed by several authors [76]. The peak position at 380 nm is indicative of the particle sizes in the range 20–30 nm. Besides, with increase in the NH_3 (hyperbranched nanostructures) content, the peak position shows only a extremely small shift towards the blue region, indicating a small decrease in the particle size, while the peak width increases with increasing ammonia content in the electrolyte. To explain these effects, the authors consider the size effects of metal nanoparticles. Depending on the size, there exist two regimes in the influence of particle size on the UV–vis spectrum [77].

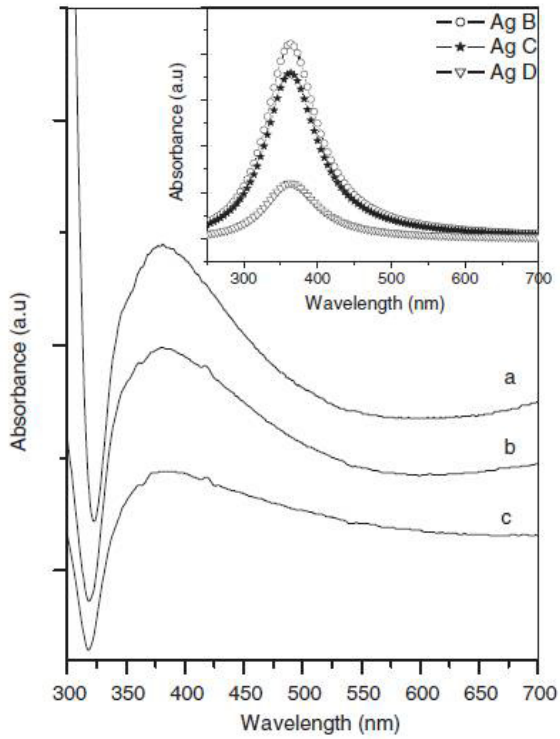

Figure 1.7 - UV–vis absorption spectra of the samples: (a) Ag B, 0.3M aqueous NH_3 solution; (b) Ag C, 0.6 M aqueous NH_3 solution and (c) Ag D, 1.2 M aqueous NH_3 solution. The inset reports the simulated absorption spectrum from Mie theory for the samples [75].

The size regime is defined by the electron mean free path of the metal. For the bulk silver, the electron mean free path is ~52 nm. For particles smaller than the mean free path of the electrons, the influence of the grain boundary scattering cannot be ruled out, and must be taken into consideration. In the scenario when silver particle size is >52 nm, the peak position shows a red shift with increasing size, and the peak width increases with respect to the size (this is defined as an extrinsic size effect). For particle sizes lower than 52 nm, the peak position shows a very little change towards blue, and the peak width increases with decreasing size. S. Kaniyankandy et al. [75] indicate that this is the intrinsic size effect. In this case, the size of all samples are in the range where the intrinsic size effect is operational. Therefore, the observation of the increase in the peak width with decreasing particle size can be explained on the basis of the intrinsic size effect. It is interesting to note that the SPR band spreads throughout the entire visible region of the electromagnetic spectrum. This observation is suggestive of aggregated silver nanoparticles, as well as in the present case where the aggregates form an ordered supramolecular structure. This hints at the applicability of these structures in SERS studies, because of an enhancement based on an electromagnetic mechanism, in which the high overlap of incident and scattered light with a metal SPR absorption band is important. The greater the overlap, the higher the enhancement. In the present case, since the SPR band extends throughout the entire visible region, the light of any wavelength in the visible region will be enhanced, thereby giving more flexibility with respect to the application in SERS. Furthermore, the highly branched dendritic structure has a higher surface area, which enables an increase in the sensitivity of SERS [78].

To highlight the good response of the metallic nanodendrites as SERS-active substrates, we report the results of Teng Qiu et al. [79]. They use SERS, which operates with enhanced Raman signals excited by surface plasmons, to investigate C_{60} nanoclusters. SERS is supposed to consist of a five-step process: (1) An ingoing photon interacts with the substrate exciting a Plasmon; (2) The plasmon polarizes a molecule bound to the surface, creating a large effective dipole moment; (3) If the molecule now changes the vibrational state, then its molecular polarization alters; (4) The change in molecular polarization couples back into an emitted Plasmon; (5) Finally, the plasmon couples into an outgoing Raman scattered photon. When the C_{60} nanoclusters are adsorbed on silver nano-dendrites, the symmetry of the C_{60} molecule is reduced, resulting in the splitting of the Raman bands from the degenerate modes of C_{60}. As a result, the number of the vibration modes is greatly increased in the SERS spectrum (fig. 1.8). Besides, the authors couple C_{60} nanoclusters on the silicon wafer, using a 1mM C_{60} solution for comparison. No visible C_{60} Raman bands (see bottom of fig. 1.8) are observed. The results suggest that such strong enhancement for the dendritic pattern should be attributed to the fact that the nano-dendrites are assembled on the Si substrate with a very high density and with many horns and, thus, C_{60} nanoclusters in abundant hot spots between closely spaced dendrite arms lead to intense SERS enhancement.

Anisotropic nano-objects such as nanorods and nanowires have been shown to possess interesting size- and shape-dependent properties, thus motivating interest in the controlled assembly of them into functional architectures for SERS. Nikoobakht and El-Sayed discovered

that SERS intensities are far higher for molecules on aggregated gold nanorod deposits compared with monomeric nanorods, an observation attributed to an enhanced EM field in the inter-nanorod region. In a comprehensive study of Teng Qiu et al., highly ordered and regular silver nanowires with tunable inter-nanowire gap size have been fabricated for placing analyte molecules in hot spots between closely spaced nanowires, leading to tunable SERS enhancement. The studies indicate that the precise control of gaps between nanorods or nanowires on a SERS active substrate is likely to be critical for the fabrication of substrates with uniformly high EFs, and for understanding collective surface plasmons. This is the critical reason many works carried out theoretical examinations of the local EM properties by the simulation method to assess the EM near-field distributions for a dendrite-like model pattern with different inter-arm gap dimensions.

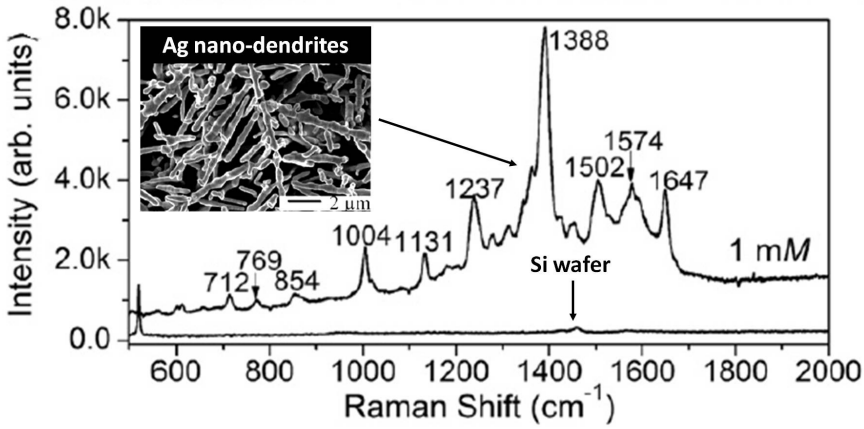

Figure 1.8 - SERS spectrum of C60 nanoclusters coupled silver dendrites from solution of 1mM C60 in toluene. The Raman spectrum at the bottom corresponds to the sample of C60 nanoclusters coupled Si wafer from 1mM C60 toluene solution [79].

2. <u>SiO_2 Nanowires-Au Nanoparticles pea-podded:</u> noble-metal nanoparticles encapsulated in a dielectric matrix have attracted sustained interest over several centuries owing to their unusual optical and electrical properties. Metal-dielectric nanocomposites show non-linear and fast optical response near the SPR frequency due to their enhanced third-order optical susceptibilities [80]. Thus, they have been applied in optical switching devices [81, 82]. Several approaches, such as the sol-gel process, metal-dielectric co-sputtering deposition, metal-ion implantation into a dielectric matrix and pulsed laser deposition have been used to prepare metal-dielectric nanocomposites [83, 86]. In addition to the mentioned metal-dielectric nanocomposites that are mainly prepared in thin film or bulk forms, the one-dimensional noble-metal nanoparticle chain has become an intensive research focus because of its potential applications for nanoscale integrated optics below the diffraction limit of light. It has been suggested theoretically and experimentally that the electromagnetic energy can be transported below the diffraction limit by a coupled-plasmon mode in the linear chains of noble-metal

nanoparticles. The successful synthesis of a one-dimensional hybrid nanosystem known as a "peapod", offers a promising opportunity to realize a wide variety of functionalities. The best-known example among them is the all-carbon hybrid peapod structure, consisting of fullerene molecules encapsulated in single-walled carbon nanotubes, which has been demonstrated to show several unusual physical properties.

In the paper of M.S. Hu et al. [80], it is reported the approach for fabricating a self-organized metal nanoparticle chain encapsulated in a dielectric nanowire with SPR-induced conductivity therein. Cathodoluminescence measurements on the gold nanopeapodded silica nanowires are carried out using a Gatan with an acceleration voltage of 8 keV. Figure 1.9 shows typical cathodoluminescence spectra of gold nanopeapodded silica nanowires at five different temperatures.

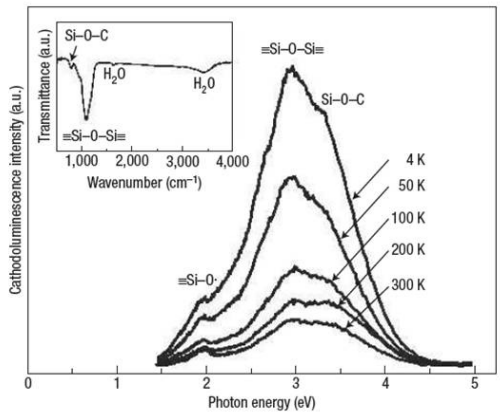

Figure 1.9 - Temperature-dependent cathodoluminescence spectra of gold nanopeapodded silica nanowires. The inset shows the corresponding FTIR spectrum [80]

The authors highlight that the spectra are composed of three characteristic peaks at 1.9, 3.0, and 3.3 eV. The 1.9 eV band can be ascribed to the non-bridging oxygen hole centres or oxygen dangling bonds (≡Si–O) [87]. The 3.0 eV band corresponds to the two fold coordinated Si lone pair centres originating from the formation of strain bonds (≡Si–O–Si≡), when mechanical stress is applied to the silica glass [88, 89]. The 3.3 eV band may be correlated with the formation of the Si–O–C owing to the reaction between ≡Si–O defects and carbon atoms during nanowire growth, which has been reported in carbon-doped silica [90, 91]. As no carbon-containing gas reactants are intentionally introduced during nanowire growth, the authors suppose that the incorporated carbon might originate from the sputtering process of gold thin films under ambient air or the residual contaminant in their reaction chamber. Analyses of bonding configurations from Fourier transform infrared (FTIR) data also confirm the existence of Si–O–C and ≡Si–O–Si≡ (fig. 1.11, inset) .

Ultraviolet-visible absorption measurements are performed on a set of the composite nanowires grown on quartz substrate with different gold filling in the silica nanowires. The room-temperature ultraviolet-visible absorption spectra for plain silica nanowires (dotted line), gold-peapodded silica nanowires (solid line) and gold-filled silica nanowires, wherein the gold segments show an aspect ratio of 3-5 (dashed line), are shown in fig. 1.10

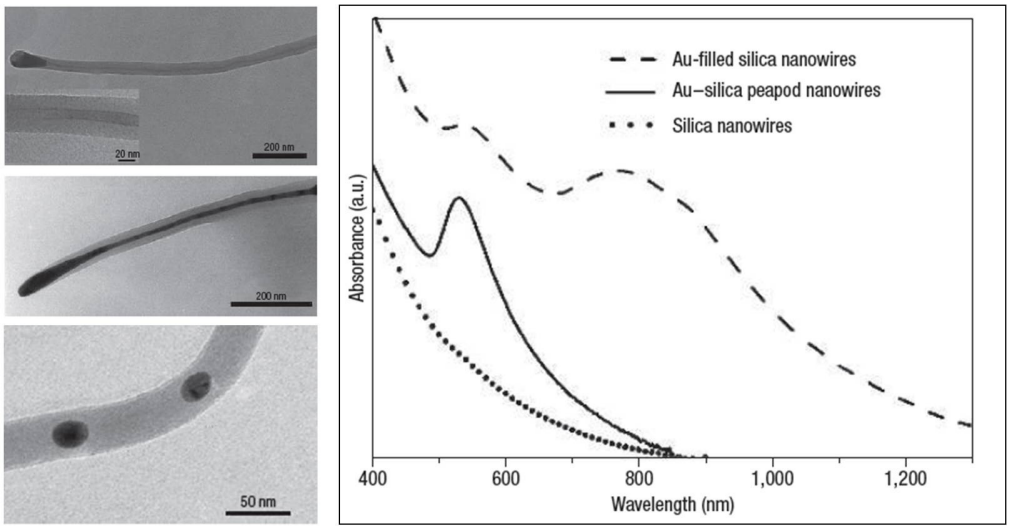

Figure 1.10 - Optical absorption spectra for plain silica nanowires (dotted line), gold peapodded silica nanowires (solid line) and gold-filled silica nanowires wherein the aspect ratio of the gold segment is about 3-5 (dashed line) [80].

The gold-filled and gold-peapodded silica nanowires reveal a pronounced SPR absorption band at 532 nm, whereas the plain silica nanowires do not show any SPR absorption. The SPR band at 532 nm is attributed to the transverse plasmon mode, and the longer wavelength band is associated with the longitudinal plasmon mode [92], which was observed for composite nanowires containing gold segments of high aspect ratio (see the dashed line in fig. 1.10 (b)). The absence of the longitudinal mode in the gold-peapodded nanowires (see the solid line in fig. 1.10 (b)) may be ascribed to the small aspect ratio (<1.2) of the gold nanoparticles. The observed background in the composite nanowires originates from an interband transition of valence electrons to the Fermi surface.
Photoresponse measurements based on the nanowire ensemble devices are conducted under alternate light illumination of different wavelengths and under dark conditions.

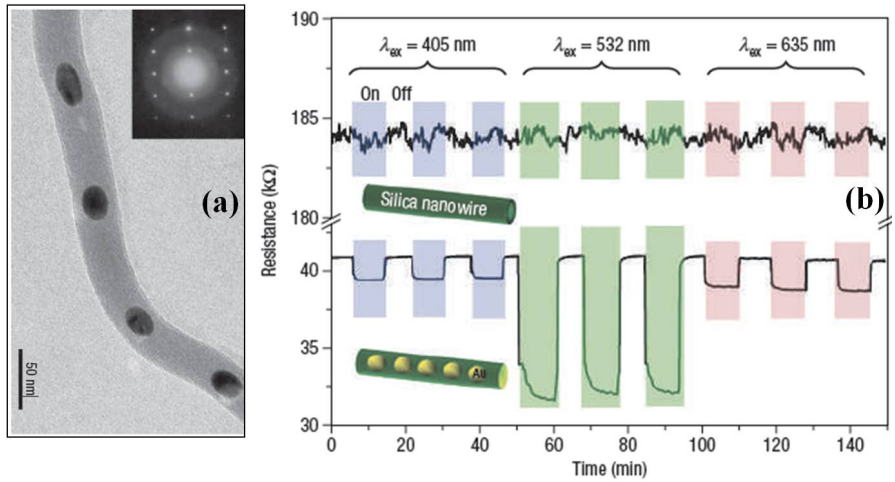

Figure 1.11 – (a) TEM images showing the structure of metal nanoparticles encapsulated silicon dioxide nanowire. The inset in in fig. (a) shows an electron-diffraction pattern recorded along the [120] zone axis. (b) Photoresponse measurements. The room-temperature resistance response as a function of time to light illumination for plain silica nanowires (upper part) and gold nanopeapodded silica nanowires (lower part). Shaded (pink, excitation wavelength lex =635 nm; green, lex =532 nm; purple, lex =405 nm) and unshaded regions mark the light-on and light-off periods [80].

The resistance of the hybrid peapod nanowire device shows nearly a five times smaller value than its counterpart without gold nanoparticles. More interestingly, the hybrid peapod nanowire device presents a wavelength-dependent photoresponse in resistance. The photoresponse behaviour at a SPR wavelength of 532 nm shows a larger difference in resistance between the illumination on and off conditions (fig. 1.11). The resistance change is nearly five times that observed using 632 and 405 nm light. Furthermore, an excitation-intensity-dependent resistance is measured using 532 nm light at various pumping powers. M.S. Hu et al. believe that the enhanced photosensitive behaviour observed from the hybrid nanowire device can be attributed to the SPR, as the hybrid nanowires have a pronounced SPR absorption at 532 nm. The enhancement of photoresponse behaviour arising from the excitation of the surface plasmon has been reported for metal-oxide-metal (MOM) tunnelling junctions, which is attributed to the generation of hot electrons owing to the decay of surface plasmon polaritons. The generated hot electrons drift or diffuse to the oxide barrier, and tunnel to the counter electrode. In the case of their study, one-dimensional gold nanopeapodded silica nanowire can be regarded as an MOM tunnelling junction in series. The generation of hot electrons and electron tunnelling through the oxide nanowires may contribute to the enhanced photoresponse behaviour in our hybrid nanowire. The authors suggest that this simple one-step approach could be extended to the preparation of other metal-dielectric peapod-type nanowires with different functionalities.
Basides, SiO_2 NW-Au NPs composite systems are gaining a great scientific and technological interest for their potential applications, for example in electronic devices, biosensors, nanoscale

optical devices and sensors. In particular, these pea-podded structures are used as light waveguides or biosensors, in line with the results reported by Wang et. al. [93]. The authors report SP resonance enhanced molecular oxygen sensing by single Au NPs-SiOx NW under 532-nm illumination (visible light) at room temperature. Moreover, excellent selectivity of Au NPs-SiOx NWs to molecular oxygen in air has been demonstrated. To understand the electrical and opelectronic properties, they report the current-voltage (I-V) charactersistics, measured at room temperature in vacuum.

As shown in figure 1.12 (c), the I-V plots of both NWs are linear, indicating the ohmic nature of the e-beam defined contacts.

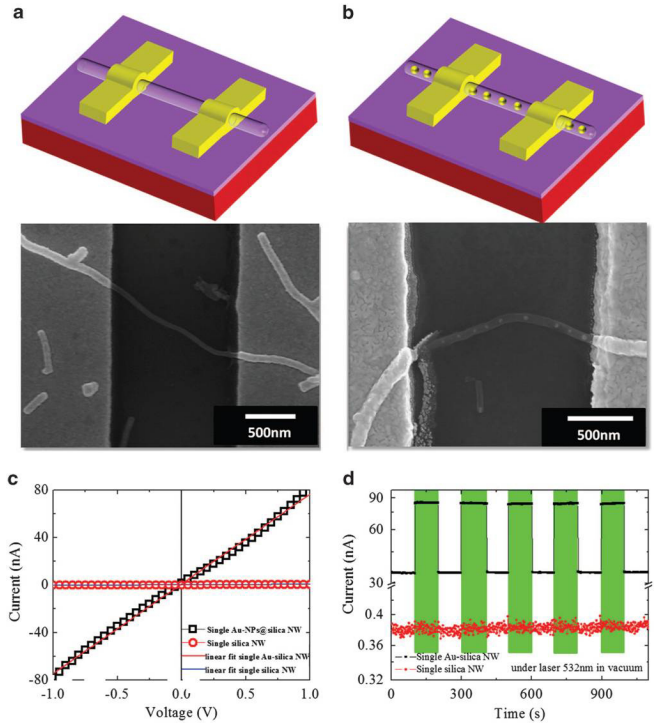

Figure 1.12 - Field-emission scanning electron microscopy images of single NW devices consisting of (a) plain silica NW (without the Au NPs) and (b) Au-NPs@silica NW. (c) Dark I–V characteristics of single NW devices, with and without Au NP peapods, measured in vacuum, and the corresponding linear fit to the data set. (d) Dark and photocurrent measured under vacuum in single NW devices, with and without Au NP peapods, as a function of time. The color bars indicate the duration of the 532-nm illumination. The measurement has been performed with a 1 V applied bias at room temperature. The bare silica NW showed no photoresponse, whereas the Au-NP@Silica NW showed strong photoresponse [93].

The slope of the I-V plot indicates that the electrical conductivity of the Au NPs-silica NW is higher than that of the bare silica NW. This trend occurs for the creation of more electron-hopping sites in the Au-NPs-silica NW leads to enhanced conductivity [94]. During the growth of Au NP-peapodded silica NWs, residual Au atoms may partially incorporate into the silica matrix of the wire during the peapod formation [80]. The incorporation of Au may produce impurities and/or defect-related hopping sites in the silica matrix [94].

The Au-embedded silica NW has higher conductivity than the plain silica NW, because of its shorter hopping length. Photoresponse measurements of the NW devices, conducted under alternating 532 nm illumination and dark conditions, is shown in figure 1.12 (d).

The plain silica NW device does not show any significant photoresponse; the ratio of photo and dark current is ~0.01. In contrast, the Au NPs-silica NW device presents a reversible photoresponse and a stable photocurrent, with a photo/dark current ratio of ~1.48. Assuming the band gap of silica NWs to be in the range of ~6.8 eV [95], and denying any absorption of the 532 nm light, these data suggest that the photocurrent can be attributed to the near-resonance SP absorption of the Au NPs (within the silica NWs) that has been reported at ~532nm [80].

Taking into account these optoelectronic properties, such complex systemscan be used as light waveguide. Indeed, the resonant coupling between the incident light and the plasmonic resonances of Au NPs can induce an enhancement of the output signal.

Taking into account the necessity to modulate the plasmonic properties for each specific application, in the following chapters the results of the synthesis and characterization of metallic nanostructures with complex shape and composition are reported.

Besides, the correlation between structural and optical parameters of other complex shape and composition metal nanostructures (gold nanoring and ring dimmers, disk dimmers, hematite-Au core-shell nanorice particles, nanoporous (np) gold film, np-Au nanowires and np-nano pillars structures) are reported in the appendix to this chapter.

References

[1] Fahlman BD., Mat. Chem., Vol. 1. Springer; Mount Pleasant, p. 282-283 (2007)
[2] Younan Xia, Yujie Xiong, Byungkwon Lim, Sara E. Skrabalak -Angew Chem Int Ed Engl.; 48(1): 60–103 (2009)
[3] Halperin WP., Rev Mod Phys., 58:533 (1986)
[4] Bawendi MG, Steigerwald ML, Brus LE. Annu Rev Phys Chem., 41:477 (1990)
[5] Weller H. Adv Mater., 5:88(1993)
[6] Alivisatos AP. Science., 271:933(1996)
[7] Murray CB, Kagan CR, Bawendi MG., Annu Rev Mater Sci. 30:545 (2000);
[8] Maheshwari V, Kane J, Saraf R. Adv Mater., 20:284 (2008)
[9] Mott NF. Rev Mod Phys., 40:677 (1968)
[10] Markovich G, Collier CP, Henrichs SE, Remacle F, Levine RD, Heath JR. Acc Chem Res., 32:415 (1999)
[11] Jeong U, Teng X, Wang Y, Yang H, Xia Y. Adv Mater., 19:33(2007)
[12] Angew Chem Int Ed Engl. 48(1): 60–103 (2009)
[13] Lewis LN. Chem Rev., 93:2693(1993)
[14] Davey NM, Seymour RJ. Platinum Met Rev., 29:2 (1985)
[15] Hamilton JF. Adv Phys., 37:359 (1988)
[16] Murray CB, Sun S, Doyle H, Betley T. MRS Bull., 26:985 (2001)
[17] Murray CB, Sun S, Doyle H, Betley T. MRS Bull., 26:985(2001)
[18] Maier SA, Brongersma ML, Kik PG, Meltzer S, Requicha AAG, Atwater HA., Adv Mater. 13:1501 (2001)
[19] Sanders AW, Routenberg DA, Wiley BJ, Xia Y, Dufresne ER, Reed MA. Nano Lett. 6:1822 (2006)
[20] Taton TA, Mirkin CA, Letsinger RL. Science. 289:1757 (2000);
[21] Chen J, Saeki F, Wiley BJ, Cang H, Cobb MJ, Li ZY, Au L, Zhang H, Kimmey MB, Li X, Xia Y. Nano Lett. 5:473 (2005)
[22] West JL, Halas NJ. Annu. Rev. Biom. Eng. (2003)
[23] Kottmann JP, Martin OJF, Smith DR, Schultz S. Phys. Rev B. 64:235–402 (2001)
[24] Valden M, Lai X, Goodman DW. Science. 281:1647 (1998)
[25] Narayanan R, El-Sayed MA. J Phys Chem B. 109:12663 (2005)
[26] Falicov LM, Somorjai GA. Proc Natl Acad Sci. 82:2207 (1985)
[27] Xia, Y., Xiong, Y., Lim, B., and Skrabalak, S.E. Angew. Chem., Int. Ed., 48 (1), 60–103. 2 (2009)
[28] Elechiguerra J.L., Reyes-Gasga J., and Yacaman M.J., J. Mater. Chem., 16 (40), 3906v (2006).
[29] Zhang J., Langille M.R., and Mirkin C.A., J. Am. Chem. Soc., 132 (35), 12502–12510 (2010)
[30] Liu M., Leng M., Yu C., Wang X., and Wang, C., Nano Res., 3 (12), 843–851 (2010)

[31] Zhang Q., Ge J., Pham T., Goebl J., Hu Y., Lu Z., and Yin Y., Angew. Chem., Int. Ed., 48 (19), 3516–3519 (2009)
[32] Zhou J., An J., Tang B., Xu S., Cao Y., Zhao B. Xu, W. Chang, J., and Lombardi J.R. Langmuir, 24 (18), 10407–10413 (2008)
[33] Zhang J., Li S., Wu J., Schatz G.C., and Mirkin C.A., Angew. Chem., Int. Ed., 121 (42), 7927–7931 (2009)
[34] Sau T. K. and Rogach A. L. - Complex-shaped Metal Nanoparticles- Wiley-VCH Verlag & Co. KGaA, Boschstr. 12, 69469 Weinheim, Germany (2012)
[35] Bratlie K.M., Lee H., Komvopoulos K., Yang P., and Somorjai G.A. Nano Lett., 7 (10), 3097–3101 (2007)
[36] Pastoriza-Santos, I. and Liz-Marz_an L.M., J. Mater. Chem., 18 (15), 1724 (2008)
[37] Tao A., Sinsermsuksakul P., and Yang P. Angew. Chem., Int. Ed., 45 (28), 4597–4601 (2006)
[38] Tao A., Sinsermsuksakul P., and Yang P. Nat. Nanotechnol., 2 (7), 435–440 (2007)
[39] Yoshida K.-I., Itoh T., Tamaru H., Biju V., Ishikawa M., and Ozaki Y., Phys. Rev. B, 81 (11), 115406 (2010)
[40] Mulvihill M., Tao A., Benjauthrit K., Arnold J., and Yang P., Angew. Chem., Int. Ed., 47 (34), 6456–6460 (2008)
[41] Maier S.A. - Plasmonic: fundamentals and Applications- Springer (2007)
[42] Krenn J. R., Dereux A., Weeber J. C., Bourillot E., Lacroute Y., and Goudonnet J. P., Phys. Rev. L ett. Vol. 82, 12 22 (1999)
[43] Maier Stefan A., Brongersma Mark L., Kik Pieter G., and Atwater, Harry A. Phys. Rev. B, 65:193408 (2002).
[44] Banaee M. G. and Crozier K. B., Opt. Lett., Vol. 35, No. 5 (2010)
[45] Novotny L. - Nature 455, 887 (2008)
[46] Kneipp K., Moskovits M., and Kneipp H., Surface- Enhanced Raman Scattering: Physics and Applications, Springer, (2006)
[47] Dieringer J. A., Lettan II R. B., Scheidt K. A., and Van Duyne R. P. - J. Am. Chem. Soc. 129, 16249 (2007)
[48] Kang J. H., Kim D. S., and Park Q. H. - Phys. Rev. Lett. 102, 093906 (2009)
[49] Barkey D., Oberholtzer F., and Wu Q., Phys. Rev. Lett. – vol. 75, n° 16 (1995)
[50] Hao E., Bailey R. C., Schatz G. C., Hupp J. T. and Li S. Y. - Nano Lett. 4 327–30 (2004)
[51] Chen S. H., Wang Z. L., Ballato J., Foulger S. H. and Carroll D. L. - J. Am. Chem. Soc. 125 16186–7 (2003)
[53] Herricks T., Chen J. Y. and Xia Y. N. - Nano Lett. 4 2367–71(2004)
[54] Teng X. W. and Yang H. - Nano Lett. 5 885–91 (2005)
[55] Ramirez E., Jansat S., Philippot K., Lecante P., Gomez M., Masdeu-Bulto A. M. and Chaudret B. - J. Organomet. Chem. 689 4601–10 (2004)
[56] Antonietti M. and Goltner C. - Angew. Chem. Int. Edn 36 910–28 (1997)
[57] Ewers T. D., Sra A. K., Norris B. C., Cable R. E., Cheng C. H., Shantz D. F. and Schaak R. E. - Chem. Mater. 17 514–20 (2005)

[58] Hoefelmeyer J. D., Niesz K., Somorjai G. A. and Tilley T. D. - Nano Lett. 5 435–8 (2005)
[59] Ould-Ely T., Amiens C., Chaudret B., Snoeck E., Verelst M., Respaud M. and Broto J. M. - Chem. Mater. 11 526–9 (1999)
[60] Vidoni O., Philippot K., Amiens C., Chaudret B., Balmes O., Malm J.O., Bovin J.O., Senocq F. and Casanove M. J.- Angew. Chem. Int. Edn 38 3736–8 (1999)
[61] Pelzer K., Vidoni O., Philippot K., Chaudret B. and Colliere V. - Adv. Funct. Mater. 13 118–26 (2003)
[62] Wang Z L - Annu. Rev. Phys. Chem. 55 159–96 (2004)
[63] Gao P X and Wang Z L - Appl. Phys. Lett. 84 2883–5 (2004)
[64] Cheng Y, Wang Y S, Chen D Q and Bao F - J. Phys. Chem. B 109 794–8 (2005)
[65] Yan H Q, He R R, Johnson J, Law M, Saykally R J and Yang P D - J. Am. Chem. Soc. 125 4728–9 (2003)
[66] Wang D, Qian F, Yang C, Zhong Z H and Lieber C M - Nano Lett. 4 871–4 (2004)
[67] Peng Z A and Peng X G - J. Am. Chem. Soc. 124 3343–3353 (2002)
[68] Manna L, Milliron D J, Meisel A, Scher E C and Alivisatos A P - Nat. Mater. **2** 382–5 (2003)
[69] Milliron D J, Hughes S M, Cui Y, Manna L, Li J B,l Wang L W and Alivisatos A P - Nature 430 190–5 (2004)
[70] Grebinski J W, Hull K L, Zhang J, Kosel T H and Kuno M - Chem. Mater. 16 5260–72 (2004)
[71] Lee S M, Jun Y W, Cho S N and Cheon J - J. Am. Chem. Soc. 124 11244–5 (2002)
[72] Jun Y W, Jung Y Y and Cheon J - J. Am. Chem. Soc. 124 615–9 (2002)
[73] Wang D L and Lieber C M - Nat. Mater. 2 355–6 (2003)
[74] Huang T., Meng F., and Qi L. - Langmuir 26(10), 7582–7589 (2010)
[75] Kaniyankandy S**.,** Nuwad J**,** Thinaharan C**,** Dey GK and Pillai C G S - Nanotech. 18 125610 (6pp) (2007)
[76] Claro F and Fuchs R - Phys. Rev. B **33** 7956 (1986)
[77] Link S and El-Sayed M A - J. Phys. Chem. B **103** 8410 (1999)
[78] Chen M C, Tsai S D, Chen M R, Ou S Y, Li W-H and Lee K C - Phys. Rev. B **51** 4507 (1995)
[79] Qiu T, Zhou Y, Li J, Zhang W, Lang X, Cui T and Chu P K - J. Phys. D: Appl. Phys. 42 175403 (5pp) (2009)
[80] Hu M-S, Chen H-L, Shen C-H, Hong L-S, Huang B-R, Chen K-H AND Chen L-C - Nature Mat. Vol. 5 (2006)
[81] Hache F., Ricard D. and Flytzanis C. - J. Opt. Soc. Am. *B* **3,** 1647–1655 (1986).
[82] Haglund R. F. *et al*. - Opt. Lett. 18**,** 373–375 (1993).
[83] Wang W. T. *et al*. - Appl. Phys. Lett. 83**,** 1983–1985 (2003).
[84] Dalacu D. and Martinu L. - Appl. Phys. Lett. 77, 4283–4285 (2000).
[85] Pardo-Yissar V., Gabai R., Shipway A. N., Bourenko T. and Willner I. - Adv. Mater. 13, 1320–1323 (2001).
[86] Dhara S. *et al*. - Chem. Phys. Lett. 370, 254–260 (2003)

[87] Yao B., Shi H., Zhang X. and Zhang, L. - Appl. Phys. Lett. 78, 174–176 (2001).
[88] Munekuni S. *et al*. - J. Appl. Phys. 70, 5054–5062 (1991)
[89] Yu, D. P. *et al*. - Amorphous - Appl. Phys. Lett. 73, 3076–3078 (1998).
[90] He H., Wang Y. and Tang H. - J. Phys. Condens. Matter 14, 11867–11874 (2002).
[91] Zhao J. *et al*. - Appl. Phys. Lett. 73, 1838–1840 (1998).
[92] Jana N. R., Gearheart L. and Murphy C. J. - Adv. Mater. 13, 1389–1393 (2003)
[93] Wang S. B., Huang Y. F., Chattopadhyay S., Chang S. J., Chen R. S., Chong C. W., Hu M. S., Chen L. C., Chen K. H. - NPG Asia Materials 5 (2013)
[94] Wang S. -B., Hu M. -S., Chang S. J., Chong C. -W., Han H. -C., Huang B. -R., Chen L. -C. and Chen, K. -H. - Nanoscale 4, 3660–3664 (2012)
[95] Pao C. -W., Wu C. -T., Tsai H. -M., Liu Y.- S., Chang C. -L., Pong W. F., Chiou J. -W., Chen C. -W., Hu M. -S., Chu M. -W., Chen L. -C., Chen C. -H., Chen K. -H., Wang S. -B., Chang S. -J., Tsai M. -H., Lin H. -J., Lee J. -F. and Guo J. -H. - Phys. Rev. B 84, 165412 (2011).

Appendix: other complex morphologies metal based materials

• **Gold nanoring and ring dimers**: the optical properties of gold nanorings fabricated by colloidal lithography were reported by Aizpurua *et al.* [A.1]. They showed that the LSPR frequency strongly depends on the ratio of the thickness to ring outer radius. This tunability, which is similar to that of nanoshells [A.2], allows tuning of the plasmon resonances from visible to near-IR wavelengths via reducing the ring thickness. The reduced amount of the metal in the ring geometry compared to disks of the same radius results in smaller absorption loss. Fabricating metallic rings with high-resolution methods such as electron beam lithography enables us to have great control of the periodic arrangement of the nanoparticles. Moreover, the ring geometry has an advantage over the nanoshell pattern in that molecules can attach to the inner wall as well as the outer wall, which is beneficial as substantial field enhancement occurs there. In addition to the conventional SERS, studying the field confinement in metallic rings could also have applications in optical corrals [A.3] and lasing spacers [A.4].
M. Banaee et al. [A.5] compare the SERS spectra related to single nanoring (fig. A.1 (a)) and nanoring dimmers (fig. A.1(b)) with that of an array of nanodisk dimmers (fig. A.1 (c)).

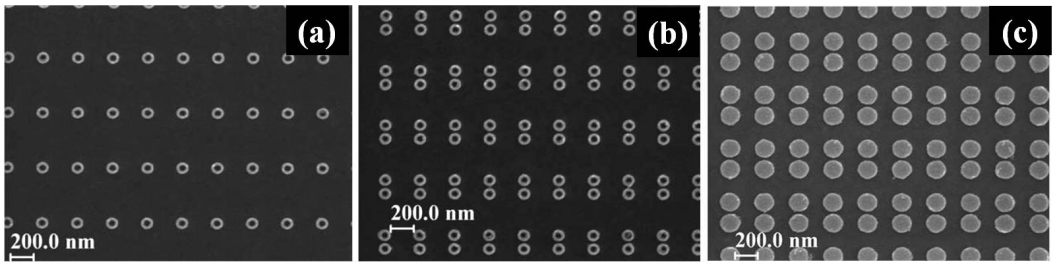

Figure A.1 - SEM images of arrays of gold (a) rings; (b) ring dimmers; and (c) nanodisk dimer [A.5].

Figure A.2 (a) reports the measured extinction spectrum, given by 1−T, where T is the light trasmission. The peaks in the spectrum correspond to the LSPRs and are 787 and 810 nm for the ring and ring dimer structures, respectively.
For SERS measurement, self-assembled monolayers of benzenethiol are formed on the gold nanostructures. Figure A.2 (b) shows SERS measurement from the ring and ring dimer samples. The vertical dashed lines in fig. A.2 (a) show the locations of the laser wavelengths and the Stokes Raman signal of benzenethiol at 1074 cm^{-1}. To compare SERS enhancements of ring and ring dimer structures with the disk dimmers, similar steps are taken for the measurement of the latter. The measured extinction spectrum is shown in fig. A.2 (c). In fig. A.2 (d), SERS spectrum is shown, obtained with a laser wavelength of 766 nm. The experimental SERS EFs for 1074 cm^{-1} line of benzenethiol for all patterns are shown in the last column of table in figure A.2 SERS EFs of the ring and dimer ring have the same magnitude, and they are roughly seven

times higher than the dimer disks. In addition, SERS EF of the ring structures is slightly higher than that of the ring dimers. In summary, SERS in ring and ring dimer geometries is studied. The result is compared with SERS from disk dimers. Although the peak field enhancement for ring dimers is found to be higher than that of rings through simulations, the measured SERS EFs are very similar (3.9×10^6 and 4.2×10^6). These are approximately seven times higher than that measured for disk dimers.

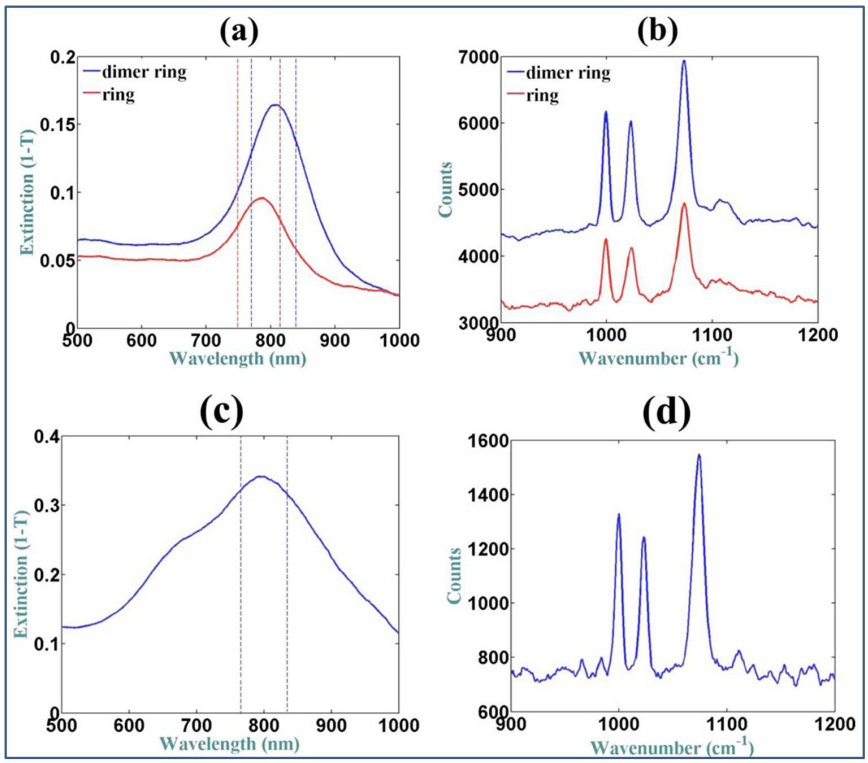

Table 1. Comparison between Calculated Average SERS Enhancement and Experimental Values for Ring, Dimer Ring, and Dimer Disk Patterns

Pattern	$\lvert E_{max}\rvert^4$	$(\lvert E(\lambda_r)\rvert^4)_{ave}$	$(\lvert E(\lambda_l)\rvert^2\lvert E(\lambda_s)\rvert^2)_{ave}$	SERS Measurement
Ring	2.3×10^6	1.8×10^5	5.3×10^4	4.2×10^6
Dimer ring	5.8×10^6	2.2×10^5	1.1×10^5	3.9×10^6
Dimer disk	9.2×10^5	3.5×10^4	2.9×10^4	5.8×10^5

Figure A.2 - (a) Measured extinction spectra (1-T) and (b) SERS spectra for ring and ring dimer structures. The vertical dashed lines in (a) show the locations of the laser wavelengths (749 nm for the ring and 770 nm for the ring dimer patterns) and the Stokes Raman signal of benzenethiol at 1074 cm^{-1}. (c) Measured extinction spectrum, and (d) SERS spectrum of the disk dimer structures. The laser wavelength (766 nm) and 1074 cm^{-1} benzenethiol vibrational mode are shown as dashed lines in (c) [A.5].

J.Aizpurua *et al.* [A.1] show that ring like nanoparticles (figs. A.3 (A) and A.3 (C)) exhibit tunable plasmon resonances in the near infrared that are not observed for solid particles of similar size (nanodisks in fig. A.3 (B)). The volume confined by the nanoring is empty and therefore accessible to various sensing and spectroscopy applications at the nanometer scale. The experimentally observed optical response of these structures is well described by numerical simulations (fig. A.3 (D)) and the main features can be qualitatively understood from simple models of the charge oscillation patterns. The predictive character of these calculations allows one to tailor the shape of a particle in order to achieve excitation spectra on demand with controlled field enhancement.

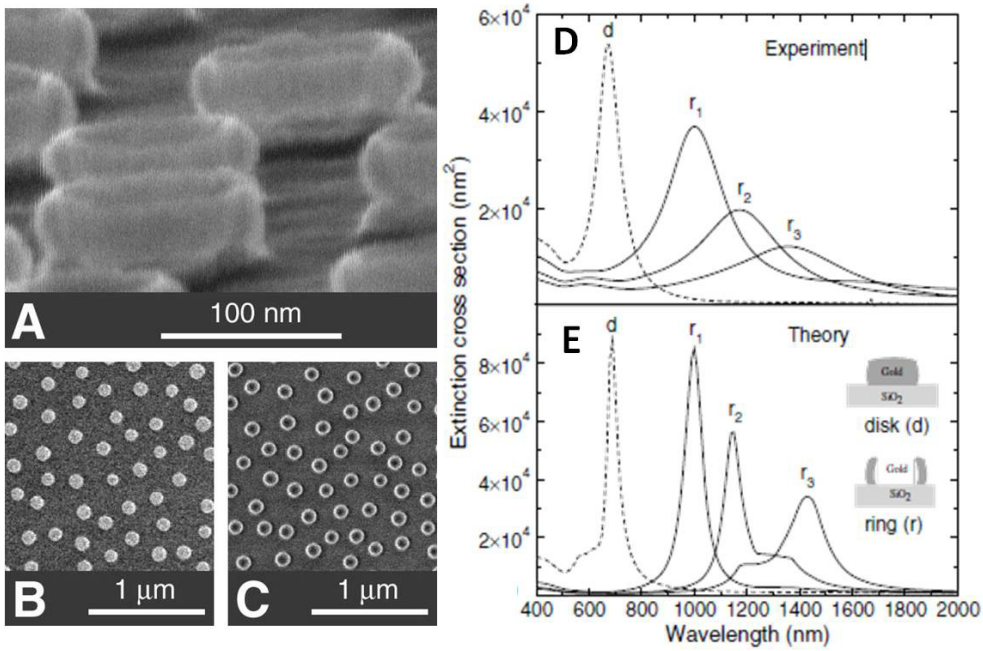

Figure A.3 - SEM images of gold nanorings and nanodisks prepared by colloidal lithography. (a) 80° tilt image of a ring structure. The walls of the rings are thin enough for the 30 keV electrons to pass through. (b), (c) Top views of disks and rings taken at an acceleration voltage of 1.5 keV. The heights of the disks and rings in the figure are ≈ 20 and ≈ 40 nm, respectively, whereas the radius is ≈ 60 nm in both cases. The thickness of the ring walls was estimated to 14±2 nm from sideview SEM images similar to (a). (d) Experimental extinction spectra of disks (d, dashed line) and rings (r, solid lines). The estimated wall thickness *d* of the rings is d = 14±2 nm (r_1), d=10±2 nm (r_2), and d = 9 ± 2 nm (r_3), respectively. (d) Calculated extinction spectra for the same particles as in (a). The rings exhibit near-infrared features at larger wavelengths for thinner walls. The disks show a dipolar excitation at around 700 nm [A.1].

• **Gold nanorice**: this new hybrid nanoparticle geometry combines the plasmonic properties of both nanorods and nanoshells in a single structure. This dielectric core-metallic shell prolate spheroid nanoparticle bears a remarkable resemblance to a grain of rice, inspiring the name "nanorice". H. Wang et al. [A.6] report nanorice (see fig. A.4) composed of a spindle-shaped hematite core coated with a continuous nanometer-thick Au shell. To apply the plasmon hybridization picture to analyze the resonances of this layered nanoparticle geometry, the authors analyze the plasmon resonances of a solid metallic nanorod and a nanocavity of arbitrary ellipticity as the parent plasmons which, when hybridized, give rise to the plasmon resonances of nanorice.

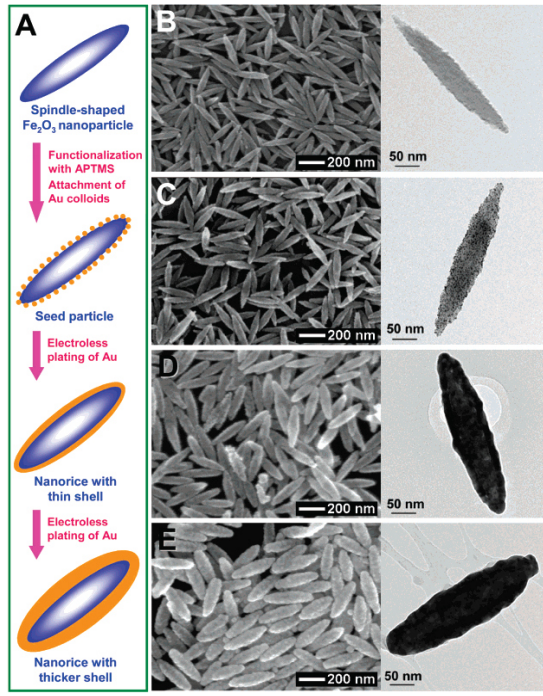

Figure A.4 - (A) Schematics of the fabrication of hematite-Au core-shell nanorice particles. SEM (left) and TEM (right) images of (B) hematite core (longitudinal diameter of 340±20 nm, and transverse diameter of 54 ±4 nm, (C) seed particles, (D) nanorice particles with thin shells (13.1±1.1 nm), and (E) nanorice particles with thick shells (27.5±1.7 nm) [A.6].

The fabrication of nanorice involves seeded metallization of spindle-shaped hematite nanoparticle cores (fig. A.4 (A)). Small Au nanoparticles (~2 nm in diameter) are immobilized onto the surface of (3-aminopropyl) trimethoxysilane (APTMS) functionalized cores at a nominal coverage of ~30%. The immobilized Au colloids act as nucleation sites for electroless Au plating onto the surface of core particles, leading to the gradual formation of a continuous and complete Au shell layer. This is essentially the same metallization procedure used in

silica-Au nanoshell synthesis [A.7] and shows that this approach is readily adaptable to produce uniform metallization layers on the surfaces of other oxide nanoparticles. Further metal deposition onto the nanostructure increases the thickness of the metal layer. Nanorice can be dispersed homogeneously in solvents such as water and ethanol to form colloidal solutions or be dispersed and immobilized on polyvinylpyridine (PVP)-coated substrates as individual, randomly oriented nanoparticles. Extinction spectra of nanorice with varying thicknesses of the shell layer are shown in fig. A.5 (A). Rrepresentative SEM image of the nanorice sample used to obtain these optical measurements is shown in fig. A.5 (B).

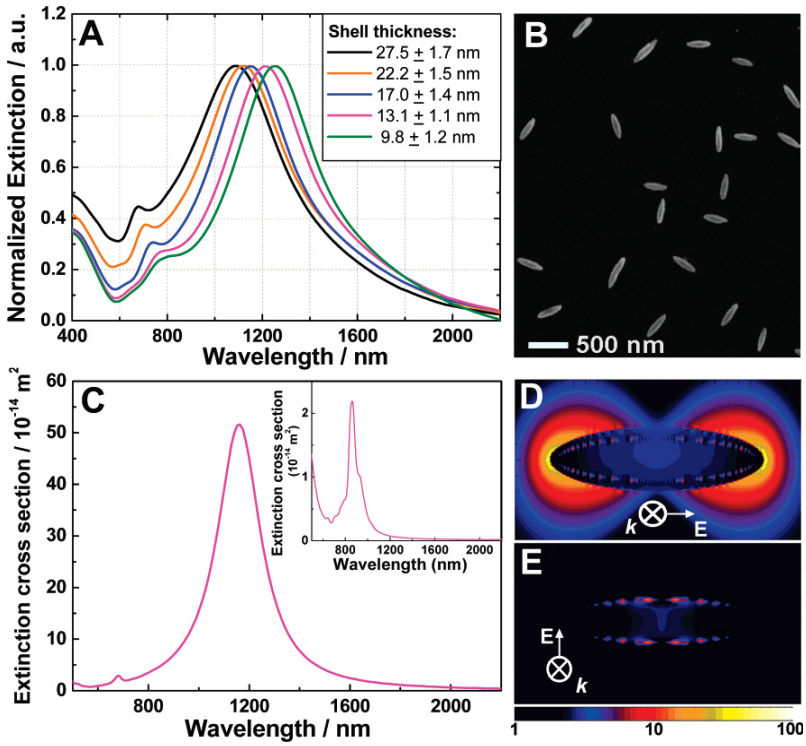

Figure A.5 - (A) Extinction spectra of hematite-Au core-shell nanorice with different shell thicknesses. Two plasmon peaks are observed for each sample. The plasmons at longer and shorter wavelengths are the longitudinal and transverse plasmons, respectively. The samples measured are monolayers of isolated nanoshells immobilized on PVP-glass slides. (B) A SEM image of a monolayer of nanorice particles (shell thickess of 13.1 (1.1 nm) on a PVP-glass slide. (C) Calculated far-field extinction spectra of the nanorice with incident polarization along the longitudinal and (inset) transverse axis of a nanorice particle using FDTD. The nanorice particle employed for the FDTD simulations is composed of a hematite core with longitudinal diameter of 340 nm and transverse diameter of 54 nm surrounded by a 13-nm-thick Au shell. Near-field profile of the nanorice under resonance excitations: (D) incident polarization along the longitudinal axis; (E) incident polarization along the transverse axis, λ_{ex}= 860 nm [A.6].

The strong plasmon resonance feature observed in the spectra in figure A.5 (A) arises because of the longitudinal plasmon of this layered structure and exhibits a highly sensitive structural dependence of its optical resonance, which blueshifts as the metal layer thickness is increased. A finite difference time domain (FDTD) analysis [A.8] of the far field extinction spectrum of this nanostructure reveals that the transverse plasmon mode (fig. A.5 (C) inset) has a much weaker extinction cross section than the longitudinal mode of this nanostructure (fig. A.5 (C)). The weaker, higher energy resonance observed in the spectrum of nanorice is attributable to the far weaker transverse plasmon mode, with a small additional contribution from a higher order longitudinal plasmon mode. The local fields associated with the longitudinal and transverse nanorice plasmons are shown in figs. A.5 (D) and (E). The asperities of this structure support very strong local field intensity enhancements (>7000 for this specific nanorice geometry) at wavelengths corresponding to the longitudinal plasmon resonance of the nanostructure. This intensity enhancement is several times larger than those reported for nanofabricated bowtie junctions [A.9] and what has been predicted and measured in scanning probe junctions [A.10, A.11]. Such strong, tunable local fields make this geometry highly attractive for use in designing substrates for surface-enhanced spectroscopy-based sensing. These large plasmon resonant local field enhancements are similar in magnitude to the localized plasmon resonant "hot spots" occurring in junctions between metallic nanoparticles when a dimer Plasmon resonance is excited [A.12, A.13]. The nanorice local fields should give rise to intense SERS enhancements with the added advantage that the hot spots are completely open to the surrounding medium in this geometry. From this point of view, each nanorice particle can potentially serve as a standalone, optically addressible nanoscale substrate for surface-enhanced spectroscopies. Moreover, because the enhanced near-field intensities can extend several tens of nanometers from the surface of the nanorice, these particles may exhibit unique advantages in the spectroscopic sensing and characterization of large biomolecules, such as proteins and DNA, biological samples, or materials placed directly adjacent to the nanoparticle.

• **Nonoporous gold (NPG) films**: porous materials have recently been attracting considerable attention because of a wide range of applications in catalysis, sensing, micro/nanoelectromechanical systems (MEMSs/NEMSs), and biotechnology [A.14]. One example is nanoporous gold formed by chemically or electrochemically dealloying silver-gold alloys [A.15-A.18], which possesses bicontinuousporosity and excellent electrical and thermal conductivities. Nanoporous Gold (NPG) offers an extensive surface where the analytes can connect and thereby an increased sensitivity and efficiency [A.19]. NPG may be formed by a spontaneous pattern-forming instability during the chemical etching of silver from gold-silver alloys [A.20]. The leaching of the less noble metal gives rise to a bicontinuous sponge-like structure of nanopores and gold ligaments [A.21] whose geometric features depend on the alloy composition and on the experimental conditions of the dealloying process [A.22]. The nanoporous structure affects also the optical properties: the plasma frequency ω_p exhibits red-shift due to the lower density in comparison with bulk gold and the material shows metallic behaviour for wavelengths above the near-IR range [A.23]. Nanoporous gold with excellent

thermal stability and chemical inactivity has recently been exploited as an attractive substrate for SERS applications because of its large surface area and bicontinuous porous structure in three dimensions [A.24]. These SERS-active substrates combines the selforganized and highly interacting nanoscale morphology of NPG with the advantages of reproducibly nanopatterned periodicstructures. Nevertheless, conventional nanoporous gold with a pore size of about tens of nanometers made by room temperature dealloying does not show a promising SERS enhancement although nanostructured gold, such as gold nanoparticles, are known to be SERS active for a number of organic and biological molecules [A.25]. Thus, optimizing the microstructure is crucial to the improvement of the SERS enhancements and thereby the SERS application of nanoporous gold, which has been made an effort by a few of research groups [A.26-A.28]. More recently, Kucheyev et al. [A.29] reported that the optimized SERS enhancement can be achieved in the annealed nanoporous gold with a coarsened pore size of ~250 nm. However, L.H. Qian [A.30] found that the strongest SERS enhancement takes place from the nanoporous gold with an ultrafine nanopore size of ~5-10 nm. The correlation between the structural parameters of the NPG films and the improvement of the optical properties drives the search to optimize the synthesis processes in order to obtain a greater control over the size of the nanopores structures. Following, we report same synthesis methods used to obtain porous materials with a greatly enhanced surface to volume ratio which is particularly suitable for the realization of plasmonic supports for sensing purposes.

X. Lang et al. [A.31], report the plasmonic properties of free-standing nanoporous gold films with an intricate bicontinuous nanostructure. $Ag_{65}Au_{35}$ (atomic ratio) leaves with a size of ~20 mm ×20 mm×100 nm in a 70% (mass ratio) HNO_3 solution at room temperature. Nanopore sizes can be tailored from 10 to 50 nm by controlling the corrosion time in the range of 5 min to 24 h (figs. A.6 (a)-(b)). Intermediate porous structure are quenched by distilled water and residual acid within nanopore channels is removed by water rinsing. UV-Vis extinction spectra of the NPG films with pore sizes of 10, 15, 20, 25, 30, 40, and 50 nm soaked into the water are shown in fig. A.6 (c). Regardless of nanopore sizes, two characteristic resonant bands can be detected in all the NPG samples. One at ~490 nm, resulting from the resonant absorption of gold films, is independent of nanopore sizes and dielectric surroundings. The other at ~550-650 nm, arising from the excitation of localized surface plasmon resonance, shows obvious band shift with the nanopore sizes and dielectric indices of surrounding media, suggesting that NPG is a promising candidate as plasmonic sensors for organic and biologic molecule detection. The spectral features of NPG are apparently different from those of other nanostructured gold. For instance, gold nanoparticles are characterized by an isolate SPR band and gold nanorods exhibit one transverse plasmon band at ~520 nm [A.32, A.33]. The low wavelength peak of NPG at 490 nm originates from the resonant absorption of gold films [A.34]. The resonant location mainly relies on film thickness rather than nanopore and ligament sizes. Thus, it is nearly independent of nanopore sizes. In contrast, the high wavelength band, arising from LSPR, represents the significant redshift with the increase in pore sizes, which expectedly results from the effective electron oscillation lengths that are determined by the gold ligament sizes.

Due to the excellent reproduction of absorption spectra and intense SPR peaks, the NPG films can be utilized as reliable plasmonic sensors. Figures A.6 (a)–(c) show the extinction spectra of the NPG films immersed into a series of organic dielectric media.

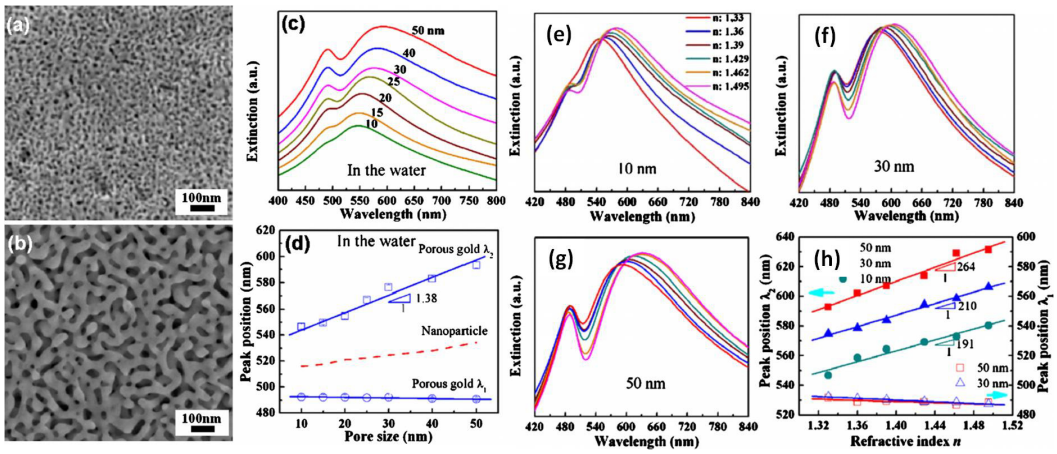

Figure A.6 - SEM micrographs of NPG synthesized by means of corrosion for 5 min (a) and 24 h (b). (c) UV-Vis extinction spectra and (d) the resonant peak position of λ1 and λ2 of NPG with the pore sizes of 10–50 nm in water. For comparison, the dashed line represents the size dependence resonant band of gold nanoparticles. UV-Vis extinction spectra of porous gold films with (e) 10 nm; (f)30 nm, and (g)50 nm are recorded by immersing them into various dielectric environments. Refractive index of these solution increases from left to right: water (n=1.33), ethanol (n=1.36), 3:1 ethanol/toluene (n=1.39), 1:1 ethanol/toluene (n=1.429), 1:3 ethanol/toluene (n=1.462), and toluene (n=1.495). (d) Dependence of resonance (λ_1), empty symbols and LSPR (λ_2, solid symbols) peaks of NPG films on refractive index. [A.31].

The SPR peak at 490 nm (λ_1) does not show detectable shift when the refractive indices of the media (n) increase from 1.33 to 1.495. In contrast, the SPR band at ~540 nm (λ_2) represents evident redshift with the refractive indices (see figs. A.6 (e)- (g)). The shift magnitude of λ_2 has a linear relationship with the refractive index as shown in fig. A.6 (h). For the λ_2 SPR band, the NPG films with larger pore sizes show more significant redshift with the refractive index. Thus, the refractive index sensitivity of NPG is comparable to those of other nanostructured gold, such as gold nanorods, hollow sphere and cylindrical holes.

L. H. Qian et al. [A.30] report, instead, the results of the characterization of two classes of $Ag_{35}Au_{65}$ (at.%, 50/50 by weight) films with the thicknesses of ~100 nm and ~60 μm, respectively, used to synthesize nanoporous gold by selective chemical and electrochemical dealloying in 70% HNO_3 aqueous solution at the temperatures of −20, 0, and 25 °C, respectively. By controlling the dealloying time and temperatures, the authors prove that the nanopore sizes can be tailored from ~5 to ~33 nm for 100 nm thick films (see SEM images in figs. A.7 (a),(b)). The 60 μm thick nanoporous gold with a pore size of ~55 nm, produced by

room-temperature dealloying for 48 h, is further annealed at 200, 300, 400, 500, and 600 °C for 2 h in air, which results in the coarsening of nanoporous gold with pore sizes ranging from 90 to 700 nm. The nanoporous gold specimens with various nanopore sizes were subjected to SERS experiments with rhodamine 6G (R6G) and crystal violet (CV) 10 B as the test molecules (see SEM images in figs. A.7 (c)-(f)). SERS enhancements of nanoporous gold for both R6G and CV molecules prove that ultrafine nanopores possess the strongest SERS enhancement. Although high enhancements can be obtained in the annealed samples with a large pore size of ~350 nm, this anomalous enhancement originates from the ultrafine pimple-type irregularities on the rough gold surfaces.

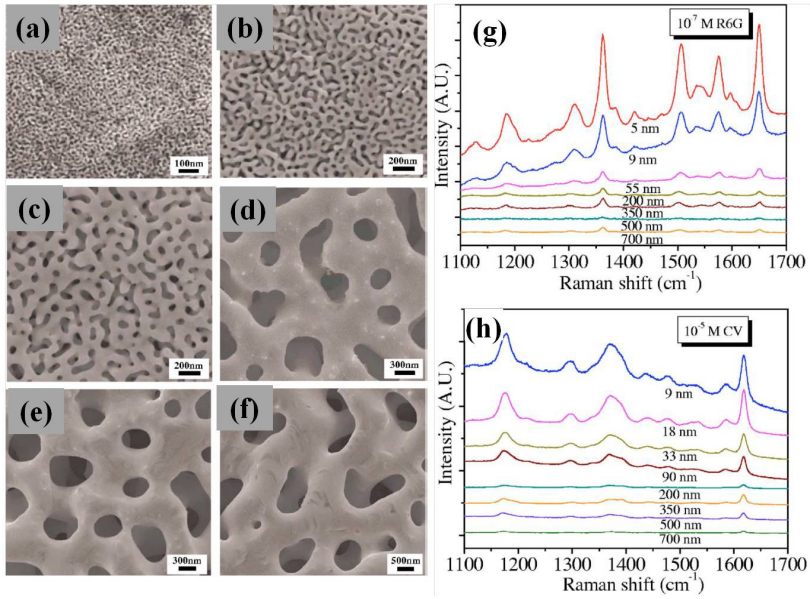

Figure A.7 - Representative SEM micrographs of nanoporous gold with various nanopore sizes. (a) Nanoporous gold film after 5 min dealloying at room temperature; (b) dealloyed at room temperature for 48 h; (c) thoroughly rinsed nanoporous gold annealed at 200 °C for 2 h; (d) 400 °C for 2 h; (e) 500 °C for 2 h, and (f) 600 °C for 2 h. SERS spectra of nanoporous gold with different pore sizes for (g) 10^{-7} mol/ l R6G aqueous solution and (h) 10^{-5} mol/ l CV methanol solution [A.30].

Thus, the observations of the SERS enhancements of nanoporous gold confirm that the high SERS enhancements result from smaller microstructure features, either smaller pore sizes or the rough gold ligament surfaces, which are believed to promote electromagnetic filed nhancements and provide more active sites for molecule adsorption [A.35, A.36]. Because the formation and coarsening of nanoporous gold are controlled by surface diffusion, the smaller pore sizes formed by a short dealloying time at low temperatures generally contain more or less residual silver.

It is known that the SERS effect of silver exceeds that of gold [A.37]. Thus, the stronger Raman scattering from the ultrafine nanoporous gold may also include the extra contribution from the residual silver. However, the fact that the annealed nanoporous gold (without detectable residual silver) containing a high density of surface irregularities exhibits the analogous enhancement as the ultrafine nanoporous gold indicates that the ultrafine structures, both small pore sizes and fine surface pimple-type irregularities, play the major role in the strong SERS enhancement of the nanoporous gold.

H.A. Che *et al.* [A.37] study the plasmonic properties of a 20-nm-thick nanoporous Au film by far-field and near-field optical techniques. The film is prepared sequentially by deposition of gold and copper, thermal annealing, and chemical etching, and has randomly distributed nanopores with sizes ranging between 20 and 350 nm . The nanoporous film has a different transmittance (fig. A.8 (a)) and a lower reflectance when compared with those of a 20-nm-thick plain Au film in the wavelength range between 400 and 1000 nm (fig. A.8 (b)).

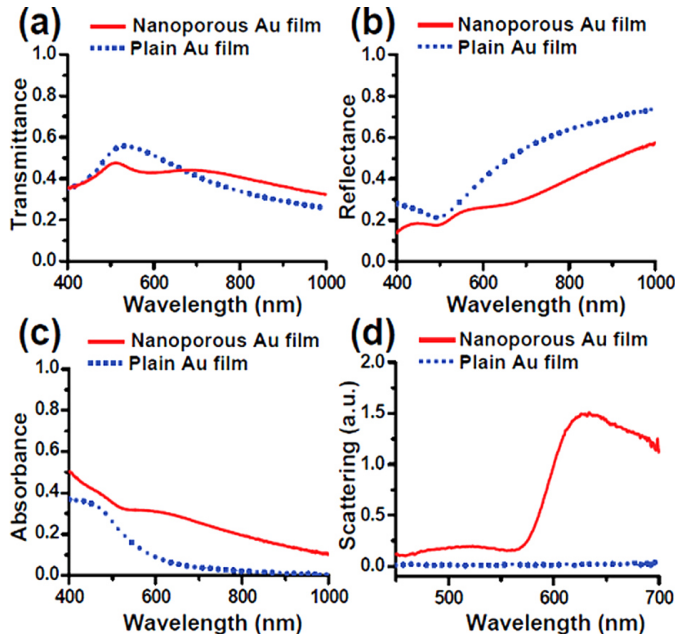

Figure A.8 - The (a) transmission, (b) reflection, (c) absorption, and (d) scattering spectra of the nanoporous (solid lines) and the plain Au (dashed lines) films [A.37].

As a result, the absorbance of the nanoporous film is much higher (fig. A.8 (c)) and can be attributed to the conversion of incident light into SPPs.

In the dark-field scattering spectrum, a broad peak appears at around 630 nm and confirms the presence of HPR [A.38] of the nanoporous film. With the aid of transmission mode NSOM, local field distribution on the film is observed and reveals the generation of SPPs. Furthermore,

two types of local field enhancement with spatial extents of around 200 nm and 1 lm are observed. The two types of enhancement correlate with strong and weak SPP localizations, respectively. The plasmonic properties reported in this work suggest a potentially use for future optical applications of nanoporous Au films.

The peculiar optical properties of this complex morphology structure are highlighted by the simulation reported by X.Y. Lang (fig. A.9), which use a discrete dipole approximation (DDA) [A.39].

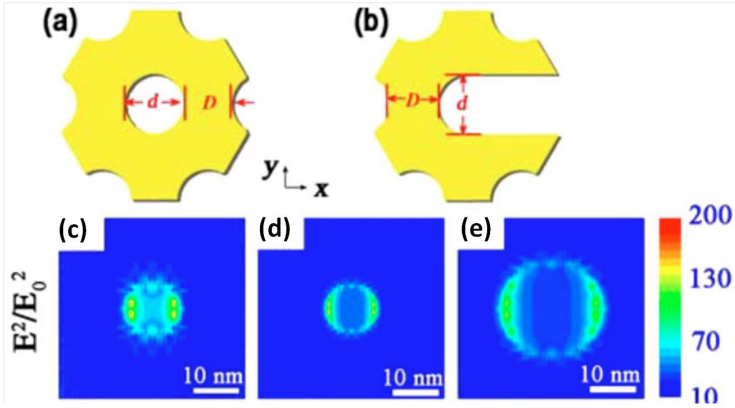

Figure A.9 – (a) and (b) schematic nanostructures used for DDA simulations. Calculated electric field distributions on the top surface of NPG: (c) total electric field E^2/E_0^2 for d =10 nm and D =30 nm; the distributions of (f) E^2/E_0^2 for d=D=10 nm; and the distributions of (i) E^2/E_0^2 *d*=*D*=20 nm. The incident light of 514 nm was polarized in the *x* direction [A.39].

A simplified nanostructure representing the key structural features of NPG (fig. A.9 (a)-(b)) is introduced to qualitatively simulate the optical properties of NPG with the bulk dielectric function of Au [A.40]. Under the plane wave with wavelength of 514 nm propagating along the direction normal to the top surface of the nanostructure, the total nearfield E^2/E_0^2 distributions are shown in figs. 1.13 (c), 1.13 (d), and 1.13 (e) for NPG films with *d*=10 nm and *D*=30 nm, *d*=*D* =10 nm, and *d*=*D*=20 nm, respectively, exhibiting that E^2/E_0^2 increases with the decrease in the *d*/*D* ratio. This is qualitatively in accordance with experimental measurements of the SERS enhancements reported in many works.

Apparently, the EM enhancements from near-field coupling dramatically increase as the ratio of d/D decreases compared to the NPG with the same pore size but large d/D ratios. Therefore, for SERS effect of GP-NPG (glod porous-NPG) films, in addition to the LSP, the weakening of plasmon damping with increasing ligament sizes obviously enhances the near-field coupling between neighboring ligaments, which gives rise to the observed SERS improvements with the decrease in the d/D ratios.

The following picture (fig. A.10) reports other nanoporous (np) materials, such as np-nanowires (fig. A.10 (a)), np-nanopillars (fig. A.10 (b)) and np-free standing beam (fig. A.10 (c)), studied in order to understand the strong correlation between structural, optical and electrical parameters [A.41].

• The **np-Au nanowires** (fig. A.10 (a)) **[**A.41, A.42**]** reveale significant impedance changes upon adsorption of thiolated-alkyl chains owed to comparable dimensions of nanowire diameter and pore sizes, exemplifying the potential of miniaturization in probing unique nanoscale phenomena. Liu et al. expanded the np-Au nanowire concept to fabricate a flow-through porous membrane. They electroplated Au-Ag into the channels porous alumina templates (~45–210 nm-diameter channels, ~10^8–10^{10} channels/cm^2) and later dealloyed the structures to form np-Au nanowires (pores and ligaments with ~20 nm characteristic size) within the channels. This is a promising method to fabricate flow-through catalysts or molecular sieves; however, the pressure-flow relationships with respect to membrane architecture need to be established in order to implement this structure in such applications.

• The **np-nano pillars structures** [A.41, A.42] (fig. A.10 (b)) are frequently fabricated using a focused ion beam (FIB) instrument to carve out pillars from bulk materials such as dealloyed Au-Ag ingots. Typical pillar dimensions are 1–8 μm and aspect ratios are 2–3. Accelerated ions lead to striations on the side surface of the pillars. It is speculated that such modifications on the surfaces of micron-size structures may have an effect on mechanical properties via arresting dislocations or creating dislocations. There has been limited research studying the potential effects of FIB on metallurgical and mechanical properties of pillars.
Powerful sensor applications of np-Au will likely find use in handheld devices that can identify -minute amounts of pollutants in water sources in remote settings or quantify disease-markers in blood for point-of-care applications. Such technologies will require successful integration of np-Au sensors with peripheral electronics or microfluidic channels, where the ability to produce np-Au sensor components with conventional microfabrication techniques is crucial. Photolithographic patterning techniques, employing photo-sensitive polymer coatings as stencil masks or etchant-resistant masks, are essential in producing np-Au patterns that can interface with peripheral interconnects of microprocessors.
In order to produce an array of **free standing Au-Ag alloy beams** [A.41] (fig. A.10 (c)), a combination of bulk- and surface- micromachining techniques were used. The ability to precisely pattern thousands of ~1 μm-thick beams with 5 to 50 μm widths and 50 to 500 μm lengths should enable studies elucidating size effects on porosity evolution and resultant mechanical properties.

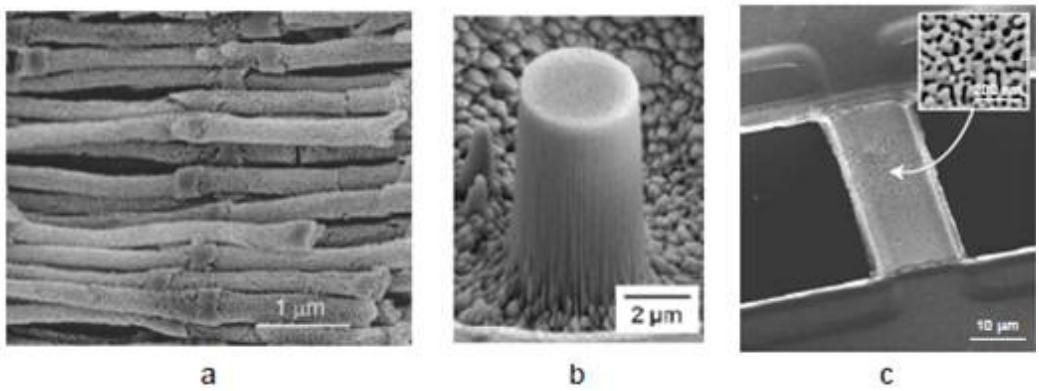

Figure A.10 -Examples of microfabricated np-Au structures: (a) nanowires produced by electroplating on a porous alumina template; (b) nano-pillar fabricated by focused ion beam and (c) freestanding beam fabricated by photolithography [A.41].

• In addition, precise thickness control offered by thin film deposition technology can create beams that are only a few pores thick, thereby allowing the study of quasi-two-dimensional ligament networks. As an alternative to sputter-deposition, Lee *et al.* followed a different strategy to prepare freestanding microbeams. They laminated a Au-Ag leaf onto a silicon wafer, patterned it by dry etching through nickel hard mask, and subsequently dry etched the silicon wafer to suspend the dog-bone shape structures. While it is possible to fabricate np-Au beams from micro-patterned Au-Ag beam, micro-patterned Au-Ag cantilevers warp catastrophically during dealloying, probably due to asymmetric dissolution rates, and hence stress generation, on opposite surfaces of the beams. However, it is possible to produce np-Au cantilevers by cutting np-Au beams with FIB microfabrication techniques are vital tools for high throughput sample production where a matrix of different structures (e.g., beams, pillars, stripes) with different properties (e.g., geometry, thickness, alloy composition) can be patterned on a single substrate. This allows for a highly parallel survey of alloy and final np-Au properties (e.g., mechanical, morphological, optical, electrochemical). This technology facilitates the optimization of np-Au properties for specific applications, most notably for sensors.

References

[A.1] Aizpurua J., Hanarp P., Sutherland D.S., Kall M., Bryant G.W., and Garcia de Abajo F.J., Phys. Rev. Lett. 90, 057401 (2003)

[A.2] Talley C.E., Jackson J.B., Oubre C., Grady N.K., Hollars C.W., Lane S.M., Huser T.R., Nordlander P., and Halas N.J. , Nano Lett. 5, 1569 (2005).

[A.3] Babayan Y., McMahon J.M., Li S., Gray S. K., Schatz G.C., and Odom T.W. , ACS Nano 3, 615 (2009).

[A.4] Zheludev N.I., Prosvirnin S. L., Papasimakis N., and Fedotov V. A., Nature Photon. 2, 351 (2008).

[A.5] Banaee M. G. and Crozier K. B., Opt. Lett., Vol. 35, No. 5 (2010).

[A.6] Wang H., Brandl D.W., Le Fei, Nordlander P., and Halas N. J. , Nano Lett., Vol. 6, No. 4, 827-832 (2006)

[A.7] Oldenburg, S. J., Averitt R. D., Westcott S. L., Halas N. J., Chem.Phys. Lett., 288, 243 (1998)

[A.8] Oubre C., Nordlander P., J. Phys. Chem. B, 108, 17740 (2004)

[A.9] Schuck P. J., Fromm D. P., Sundaramurthy A., Kino G. S., Moerner W. E., Phys. ReV. Lett., 94, 017402 (2005)

[A.10] Sanchez E. J., Novotny L., Xie X., S. Phys. ReV. Lett., 82, 4014 (1999)

[A.11] Hartschuh A., Sanchez E. J., Xie S. X., Novotny L., Phys. ReV. Lett., 90, 095503(2003)

[A.12] Michaels A. M., Jiang J., Brus L., J. Phys. Chem. B., *104*, 11965 (2000)

[A.13] Nordlander P., Oubre C., Prodan E., Li K., Stockman M. I., Nano Lett., *4*, 899 (2004)

[A.14] Qian L. H., and Chen M. W. , Appl. Phys. Lett. 91, 083105 (2007)

[A.15] Forty A. J., Nature _London_ 282, 597 (1979)

[A.16] Pickering H. W., Corros. Sci. 23, 1107 (1983)

[A.17] Oppenheim C., Trevor D. J., Chidsey C. E. D., Trevor P.L. , and Sieradzki K., Science 254, 687 (1991).

[A.18] J. Erlebacher, M. J. Aziz, A. Karma, N. Dimitrov, and K. Sieradzki, Nature –London- 410, 450 (2001).

[A.19] Biener J., Nyce G.W., Hodge A.M., Biener M.M., Hamza A.V., and Maier S.A., Adv. Mater. (Deerfield Beach Fla.) 20(6), 1211–1217 (2008).

[A.20] Senior N.A. and Newman R.C., Nanotechnology 17(9), 2311–2316 (2006).

[A.21] Fujita T., Qian L.H., Inoke K., Erlebacher J., and Chen M.W., Appl. Phys. Lett. 92(25), 251902 (2008).

[A.22] Ruffato G., Romanato F., Garoli D., and Cattarin S., Opt. Exp. Vol. 19, No. 14, 13164 (2011)

[A.23] Maaroof A. I., Gentle A., Smith G. B., and Cortie M. B., J. Phys. D Appl. Phys. 40(18), 5675–5682 (2007).

[A.24] Fujita T., Qian L. H., Inoke K., Erlebache J.r, and Chen M. W., Phys. Rev. Lett. (in press)

[A.25] Kneipp K., Haka A.S., Kneipp H., Badizadegan K., Yoshizawa N., Boone C., Shafer-peltier K. E., Motz J.T., Dasari R.R., and Feld M.S., Appl. Spectrosc. 56, 150 (2002).
[A.26] Dixon M. C., Ph.D. thesis, Pennsylvania State University, 2005.
[A.27] Kucheyev S. O., Hayes J. R., Biener J., Huse T., Talley C.E., and Hamza A.V., Appl. Phys. Lett. 89, 53102 (2006).
[A.28] Qian L.H., Yan X.Q., Fujita T., and M. W. Chen (unpublished).
[A.29] Qian L.H., Yan X.Q., Fujita T., Inoue A., and Chen M.W., Appl. Phys. Lett. 90, 153120 (2007)
[A.30] Lang X., Qian L., Guan P., Zi J., and Chen M., Appl. Phys. Lett. 98, 093701 (2011)
[A.31] Okamoto T., Yamaguchi I., and Kobayashi T., Opt. Lett. 25, 372 (2000)
[A.32] Marinakos S. M., Chen S.H., and Chilkoti A., Anal. Chem. 79, 5278 (2007)
[A.33] Kreibig U. and Vollmer M., Optical Properties of Metal Clusters -Springer, Berlin, (1995)
[A.34] Gersten J. and Nitzan A., J. Chem. Phys. 73, 3023 (1980)
[A.35] Jensen T., Kelly L., Lazarides A., and Schatz G.C., J. Cluster Sci. 10, 295 (1999)
[A.36] Kneipp K., Moskovits M., and Kneipp H., Surface-Enhanced Raman Scattering: Physics and Applications -Springer, Berlin, 103, p. 261(2006)
[A.37] Chen H.A., Long, J.L., Lin Y.H., Weng C.J., and Lin H.N, Jorn. of Appl. Phys. 110, 054302 (2011)
[A.38] Park T.H., Mirin N., Lassiter J.B., Nehl C.L., Halas N.J., and Nordlander P., ACS Nano 2, 25 (2008).
[A.39] Lang X.Y., Chen L.Y., Guan P.F., Fujita T., and Chen M.W., Appl. Phys. Lett. 94, 213109 (2009)
[A.40] Johnson P.B. and Christy R.W., Phys. Rev. B, 6, 4370 (1972)
[A.41] Seker E., Reed M.L. and Begley M.R., Materials, *2,* 2188-2215 (2009)
[A.42] Volkerta C.A. and Lilleodden E.T., Appl. Phys. Lett. 89, 061920 (2006)

Chapter 2

Structural and optical properties of branched metallic nanostructures for SERS applications

2.1 Metallic dendritic nanostructures: motivations and state of the art

2.1.1 Motivations

Surface-Enhanced Raman Scattering (SERS) is recognized as one of the most sensitive spectroscopic tools offering highly sensitive chemical and biological detection [1-3]. The fact that plasmon particles allows direct coupling of light to resonant electron plasmon oscillation has spurred efforts in the design and fabrication of highly SERS-active substrates in metallic nanostructured films and nanoparticles. For example, metallic nanostructures of "complex morphology" (see fig. 2.1 (a)) can be employed as SERS-active substrates [4–16]. The coupling between the incident field and metal nanoparticles (NPs) is responsible for the high amplification factors of electromagnetic field localized at far ends of NPs. In particular, for aggregates of metallic NPs, the plasmon normal modes are so localized that the enhancement, resulting from dipole-dipole interaction, is concentrated in very small regions of NPs (the so-called hot-spots) [4,15-18].

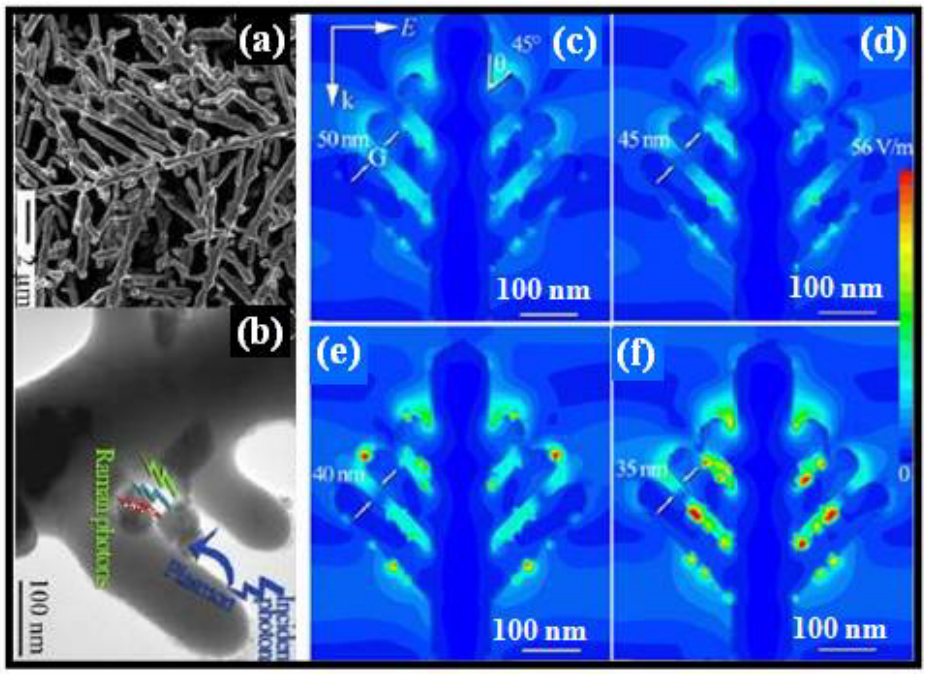

Figure 2.1 - (a) Magnified SEM image of silver nanodendrites. (b) Typical TEM image of C_{60} nanocluster coupled silver dendrite. (c)-(f) A simulated contour plot of the EM near-field distributions for a dendrite-like model pattern with inter-arm gap dimension *G*=50 nm (c), G=45 nm (d), G=40 nm (e) and G=35 nm (f) [1].

The Finite-Difference-Time-Domain (FDTD) approach has recently been demonstrated to be useful in the study of the electromagnetic (EM) properties of metallic nanostructures for almost arbitrary complexity. Indeed, Qui et al. [1], indicate that several hot spots exist into the interstitial regions of neighboring metallic nanostructures, and that the higher enhancement is obtained from the smaller inter-gap size. Figures 2.1 (c)-(f), show the contour plots of the EM near-field distributions for a dendrite-like model pattern with different inter-arm gap dimensions. The contour plots of the near EM field distributions highlight that several hot spots exist near the interstitial areas of the dendrite arms and the higher enhancement is obtained from the smaller inter-arm gap size. The SERS enhancement factor (EF) from FDTD calculation is simplified as the fourth power of the local electric field enhancement [1]: $EF = (E_{loc}/E_0)^4$, where E_0 represents the incident electric field enhancement. The authors report the values of EF related to C_{60} molecules placed in inter-arms gap of silver dendrites (fig. 2 1 (b), which vary from $2.66 \cdot 10^5$ to $6.27 \cdot 10^7$, reducing the inter-arms gap from 50 nm (fig. 2.1 (c)) to 35 nm (fig. 2.1 (f)). Therefore, the hot spots are responsible for the SERS giant enhancement ($\sim 10^{14}$) [6, 18–20], as a consequence of the high overlap between both the incident and scattered light with the absorption band of the metal surface plasmon resonances (SPR).

To sum up, the structural symmetry breaking in metallic nanostructures determines the enhancement of the incident electromagnetic field close to the nanostructures and in the gaps between the sharper regions [4, 15, 16]. Due to their morphological complexity, these branched structures are expected to have a wide range of applications as SERS-active substrates with respect to nanospheres, nanowires and nanodiscs.

On the basis of the above considerations, a large strand of current research is focused on the design and fabrication of complex geometry metallic nanostructures. In particular, crucial is the fine control of their structural characteristics towards functional applications in optical, opto-electronics and magnetic devices [21–26]. In the following subsection, we report the current employed synthesis methods to obtain the complex morphology metallic nanostructures for SERS applications.

2.1.2 State of the art: synthesis techniques and growth kinetic

In recent years, a variety of wet chemical methods have been developed to fabricate metal nanostructures with various shapes such as branched nanoparticles. In this subsection, we review the main literature works describing the most common synthesis processes and the growth kinetics of metallic nanostructures with complex morphology.

Metallic nanodendrites (dendritic structures are defined as large fractal aggregates) with hyperbranched architectures have attracted much attention due to their importance in understanding the fractal growth phenomena (researchers have modelled the optical properties for fractal structures formed from aggregates of metal nanoparticles [20, 27–29], distinguishing these from non-fractal structures such as compact or periodic geometries) and their potential applications in functional devices, plasmonics, biosensing, and catalysis. Recent examples

include the solution-phase synthesis of dendritic nanostructures of Ag [30], Cu [31], Pd[32] and Pt [33]. However, there are rare reports on the dendritic hyperbranched gold nanostructures. Figures 2.2 (a)-(i) show some examples of multibranced structures obtained by using chemical synthesis methods. In particular, we report in figs. 2.2 (a), (b) and (c) the representative SEM images of well-defined planar Au nanodendrites with a symmetric single-crystalline structure consisting of trunks and side branches grown along the <211> directions [34].

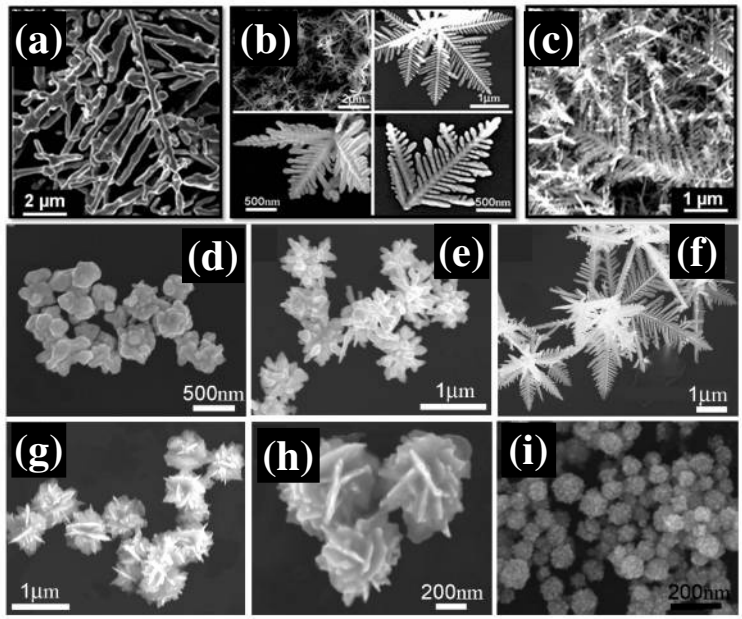

Figure 2.2 - (a)-(i) Representative SEM images of Au nanodendrites. The complex nanostructures with different morphology are obtaitened at various molar ratios of CD-to DTBA used in the chemical solutions [34].

The controlled synthesis of the Au dendritic structures is obtained by Huang et al. [34] by reducing chloroauric acid in aqueous mixed solutions of dodecyltrimethylammonium bromide (DTAB) and β-cyclodextrin (β-CD). The process reveales that the formation of supramolecular complexes of DTAB with β-CD, due to host-guest interactions, is indispensable for the fabrication of these Au planar nanodendrites, and that a proper CD-to-DTAB molar ratio is essential for their formation. The experimental results show that various molar ratios of CD-to DBA induce the growth of dendritic structures with different morphology, as reported in figs. 2.2 (d)-(i). Figure 2.3 reports a schematic illustration of the possible formation mechanism of Au nanostructures obtained at various molar ratios of CD-to DTBA in the mixed DTBA β-CD solutions. As illustrated in fig. 2.3 (a), as long as the DTAB concentration was fixed, irregular particles exhibiting faceted surfaces were the predominant product in the absence of

β-CD. The gradual addition of β-CD in the solution induces the growth of Au nanostructures with more complex geometry such as planar dendrites (fig. 2.3 (c)) or flower-like particles (fig. 2.3 (d)).

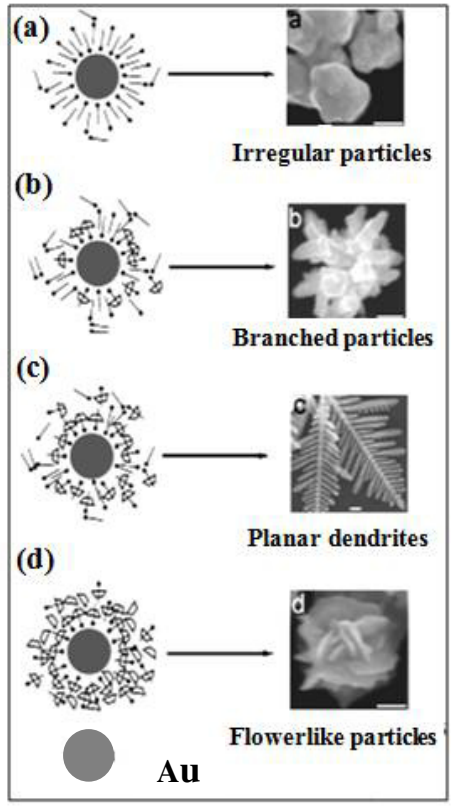

Figure 2.3 - Schematic illustration of the possible formation mechanism of Au nanostructures obtained at various molar ratios of CD-to-DTAB. [β-CD]/[DTAB]: (A) 0; (B) 0.3; (C) 0.5; (D) 2.0. All scale bars are 200 nm in panels (a)-(d) [34].

Huang et al. [34], in their work, conclude that in the mixed DTAB/β-CD solutions with suitable compositions, the DTAB/β-CD complexes and the DTAB molecules may interact with growing Au crystals in a synergistic way, which may result in a delicate balance between the diffusion rate and the reaction rate under nonequilibrium conditions, favoring the formation of the planar Au dendrites with a symmetric single-crystalline structure. Therefore, this work reports the shape-controlled synthesis of Au nanostructures with the assistance of supramolecular complexes of surfactants with CDs. These Au nanodendrites exhibited both a good electrocatalytic activity and a good SERS sensitivity for detecting p-aminothiophenol (PATP) molecules, indicating their potential applications such as catalysis, biosensing and nanodevices.

Song et al. [35] report on the controlled synthesis of two- and three-dimensional dendritic platinum nanostructures, obtained by reduction of platinum salt in acqueous surfactant solution using ascorbic acid as reductant. In micellar surfactant solutions, spherical dendritic metal nanostructures are obtained, and the smallest of these nanodendrites resembles aggregates of joined nanoparticles and where the nanodendrites are single crystals. The platinum dendrites are formed by interfacially directed growth and restricted access of nutrients due to the surfactant on the surface of the growing nanostructure.

Besides, Qui et al. [36] obtain silver nanodrendites starting from a p-type, B-doped silicon <100> cleaned by acetone to decrease the Si surface, and then etched in a diluted aqueous HF (~10 wt%) solution for 10 min. Subsequently, the cleaned silicon wafers are etched in a 5.0M HF solution containing 0.02 M silver nitrate at 60 °C for 20 min. After the etching process, the thick silver dendrites cover the silicon wafers. Also, the well-defined planar gold nanodendrites with a single-crystalline nature are ideal candidates for investigating the electrical and photonic properties of hierarchical architectures of one-dimensional metal nanostructures and may find potential applications including catalysis, biosensing, and nanodevices.

Another commonly used method for obtaining metallic dendritic nanostructures is the electrodeposition technique. Indeed, Kaniyankandy et al. [37] report the structural properties of silver nanodendrites synthesized by electrodeposition using $AgNO_3$ as the source in ammoniacal solution. The electrodeposition is carried out using a typical electrodeposition set-up consisting of a potential source with a Si <111> cathode (substrate) and a graphite plate anode. The total electrolyte volume is 20 ml and the electrodeposition is carried out at 20 V for a deposition time of 5 min. The electrolyte solution consisted of 0.1 M $AgNO_3$ electrolyte. The formation of dendritic structure is confirmed by SEM analysis, which indicates the growth of a hyperbranched silver nanostructure with lengths of the order of few micrometres. In this study, the authors use an applied potential that is much higher than the standard reduction potential of the metal itself, therefore the nonequilibrium condition prevails during the deposition. The well known growth mechanism under non-equilibrium conditions are explained on the basis of a DLA model [38, 39] and CCA model [40]. In a diffusion-limited aggregation regime, the growth takes place by bonding of the individual atoms to the growing surface after the reduction of the metal ions, whereas according to the CCA model, the individual metal clusters aggregate to form a branched morphology. Barkey et al. [41] explained the formation of dendritic morphology based on the anisotropy created by the elementary chemical reaction equilibrium involved in the deposition. Besides, the XRD analysis indicate the increase in the Ag peak width with decreasing particle size, explained on the basis of the intrinsic size effect. These SPR band spreads throughout the entire visible region of the electromagnetic spectrum. This result suggests the applicability of these structures in SERS studies, because of an enhancement based on an electromagnetic mechanism where high overlap of the incident and the scattered light with a metal SPR absorption band is important. The greater the overlap, the higher the enhancement. In this case, since the SPR band extends throughout the entire visible region, the light of any wavelength in the visible region will be enhanced, thereby giving more

flexibility with respect to the application in SERS. Besides, the highly branched dendritic structure has a higher surface area, enabling an increase in the sensitivity of SERS [42,43].
Even if microwave irradiation, photoreduction, and colloidal methods [1,44–47] have been employed for the production of controlled synthesis of two- and three-dimensional dendrites, a limit of these synthesis techniques, for direct solid state devices applications, is the growth of the branched structures in solutions. For solid state devices functional applications the controlled transfer of the nano-structured materials on functional substrates is required. Therefore, the development of alternative and low-cost strategies for the direct fabrication of the metallic dendrities directly on surfaces (providing reproducibility and control over shape, size and optical properties) could be a key step towards direct solid state-devices applications.

2.2 Multibranches structures: the physics of the snow crystal

To understand the processes involved in the transiction from faceting to branching, we report in this subsection the physics of a snow crystal.
The basic structures of an ice crystals are hexagonal prisms that appear when the crystal growth is not so strongly limited by particle diffusion, i.e. when the vapor supersaturation is low, the crystal size is small, and/or the background gas pressure is low [48]. As long as one of these parameters is small enough, the growth is dominated by attachment kinetics, resulting in faceted crystals (fig. 2.4 (a)).

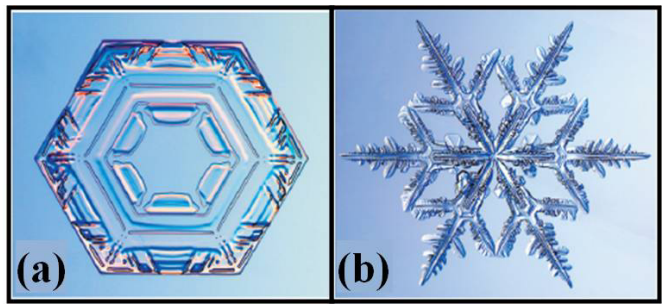

Figure 2.4 - Examples of several different morphological types of snow crystals found in natural snowfalls in temperate climate. (a) A relatively simple plate-like crystal, 1.4 mm from tip to tip. (b) A multi-branched stellar dendrite crystal, 3.0 mm from tip to tip [48].

These typically form at higher humidities and only when the temperature is near to T = −15°C. [48]. When some combinations of these parameters is increased sufficiently, then particle diffusion dominates the crystal growth dynamics, and at some point branching occurs. When the crystal morphology exhibits numerous branches and side-branches, then the growth is dendritic, which literally means “tree-like” (fig. 2.4 (b)). Dendritic crystal growth is one

example of the more general phenomenon of pattern formation in non-equilibrium growing systems.

• **Transition from faceting to branching**: when the solidification process is limited by the diffusion, the growth of a flat interface is unstable. This is true if the growth is limited by particle diffusion that brings material to the interface or by heat diffusion that removes latent heat generated at the interface. To highlight the origin of this instability, it is considered the case in which the particle diffusion is the dominant factor and the attachment kinetics are negligible. If a small bump is added to a flat, growing surface, the bump will effectively stick out farther into the supersaturated medium above the surface. Thus, particle diffusion will bring material to the top of the bump at a faster rate than to the surrounding flat surface. With a greater supply of material, the bump grows larger, which increases its supply even more. This effect is often called the Mullins-Sekerka instability [49-51], and it is a common feature of the diffusion-limited aggregation, DLA (in DLA the exposed ends of the clusters grow more rapidly than the interior because the random walkers are captured before they reach the interior [52]. Much of the structure in snow crystals derives from this instability. If the attachment kinetics at the interface is considered, the picture becomes more complex. A simple faceted morphology can grow stably, but no for so long. Consider the case in figs. 2.5 (a),(b), in which a faceted plate-like crystal sprouts branches as it grows larger.

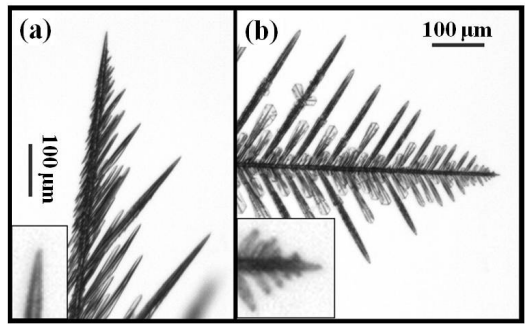

Figure 2.5 - (a) An ice dendrite growing at T = −5°C, showing the characteristic 'fishbone' structure. The tip growth is not along a well-defined crystal axis, but varies depending on supersaturation. (b) A "fern-like" ice dendrite growing at T = −15°C. Here the tip growth is along the *a*-axis of the crystal, so each side-branch makes a 60° angle from its main branch. Growth of the basal facet is slow at −15°C, so again this is a planar structure. The insets are 4× magnified views of the growing tips. [48]

The growth of the prism facets requires that v_n (x) ≈ const., where this is the perpendicular growth velocity as a function of position along the facet. Taking into account the growth kinetic, the growth velocity is given by:

$$v_n = \alpha \cdot v_{kin} \cdot \sigma_{surf} \quad (2.1)$$

where α is known as the condensation coefficient (α embodies the surface physics that governs how water molecules are incorporated into the ice lattice, collectively known as the attachment kinetics) and σ_{surf} is the vapor supersaturation at growing surface.

Besides, a solution of the diffusion equation reveals that the supersaturation, σ_{surf} (x), varies across the facets, being lowest at the facet centres. Therefore, the condensation coefficient (α) must also vary across the facets, being highest at the facet centres. Since the surface diffusion lengths are small compared to the crystal size, this simple analysis reveals that the prism facets cannot be perfectly flat, but are slightly concave. The curvature induces the variation in α (x) across the facet. The curvature is so slight, however, that the facets remain flat in appearance. As long as this growth mechanism can continue, the crystal growth remains faceted in appearance, with the costant facet curvature as the crystal grows larger. With time, the step density reaches its maximum value at the facet centres, at which point the surface is essentially rough on a molecular scale. If α reachs its maximum value ($\alpha \approx 1$), σ_{surf} continues to decline at the facet centres as the crystal continues to grow. When this condition is obtained, we can no longer have $v(x) \approx$ const. across the facet, and the crystal then sprouts branches as shown in fig.

The transition from the growth of simple prism crystals to more complex dendritic structures is fairly well understood at a qualitative level, and some attempts have been made to model this transition in detail [48, 53].

Taking into account the mechanism involved in the pattern formation in non equilibrium systems, we report (see subsection 2.3.5), a phenomenological growth model related to the physical synthesis of Au dendritic structures.

2.3 Structural and optical properties of solid-state synthesized Au dendritic structures

2.3.1 Introduction

In comparison with the methods reported in Subsection 2.1.2, this work describes a simple and versatile process for obtaining Au dendritic structures (Au Ds), reminiscent of fractal structures, on sample surfaces. This process arises from the consideration that a Au film, deposited on a Si surface, partially dewets, forming Au-Si islands (Au-Is) on a smooth Au wetting layer [29, 30], during thermal annealing at 1073 K (800 °C). In particular, we observed a peculiar structural evolution of the Au film on Si substrate from a continuous coating to Au Ds as a consequence of thermal treatment at 1373 K (1100 °C), in the presence of fast heating and cooling stages (1373 K/min). Figure 2.6 reports an example: (a) shows a SEM image of the sample surface on a large scale, while (b) is a SEM image of a single dendritic structure on the sample surface. In order to study the morphological evolution and chemical composition of the samples, SEM, TEM, RBS, EDX and AFM were performed. The size of the Ds suggests that these structures should be formed by Si atoms originating from the substrate and covered by crystalline Au nanostructures. The optical analyses highlight the efficient behavior of the Au Ds as scattering centers, and the SERS spectra the enhancement of the Raman signals related to methylene-blue (MB) and thiophenol molecules. Furthermore, in contrast to the results discussed in this chapter, the suppression of Au Ds growth and the promotion of amorphous SiO_2 NWs synthesis occur for the same samples when the thermal process at 1373 K is performed using slow heating and cooling ramps (283 K/min). So, in order to explain the kinetic processes of the Au-Si interface and the role of temperature and substrate in the growth dynamic and the evolution of dendritic morphologies, a phenomenological growth model has been drafted.

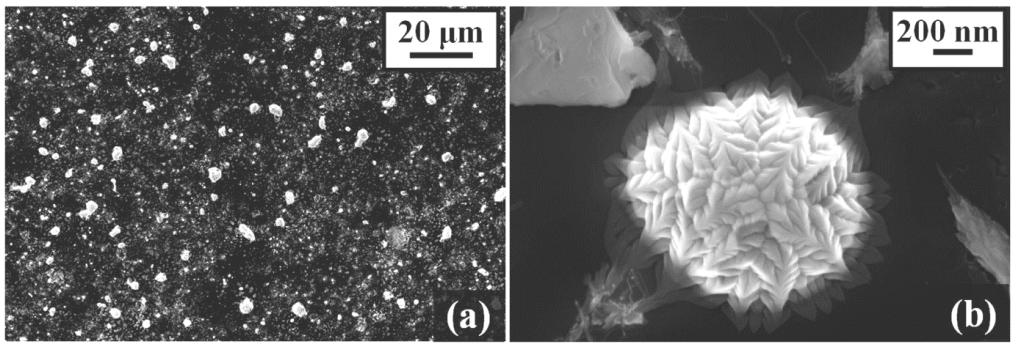

Figure 2.6 - SEM images of the sample thermal treated at 1373 K-60 min. (b) is an enlargement of (a) to highlight the morphological structure of a single dendrite.

2.3.2 Experiment

The samples were prepared by using three different silicon substrates: CZ <100> Si wafer (c-Si, previously etched in 10% aqueous HF solution to remove the native oxide); polycrystalline-Si wafer (poly-Si, 120 nm-thick Si film sputter deposited on SiO_2 by UHV AJA Confocal Magnetron Sputtering from a 99.999% purity Si target, working pressure of 5×10^{-3} mbar and heated substrate at 673 K (400 °C)); Silicon on Sapphire, SOS, (700 nm-thick Si film on Al_2O_3, by MolTech 95 GbH). The sets of samples were fabricated by depositing 20 nm-thick Au films on the starting substrates. The Au depositions were carried out by using an Emitech K550X sputter coater from an Au target source of 99.999% purity. The electrodes were laid at a distance of 40 mm under Ar flow keeping a pressure of 2×10^{-2} mbar in the chamber. The thickness of the deposited Au film was checked by RBS analyses. Then, the samples were annealed using a standard Carbolite horizontal furnace (provided by a pre-chamber) in dry N_2 (2.5 l/min) at temperatures of 1073 K, 1273 K and 1373 K. The samples were introduced in the pre-chamber and then transferred, in few seconds, into the furnace previously heated up to the desired temperature. The heating rump depends on the thermal conductivity of the sample holder (a quartz boat 10 cm×20 cm) and it can be estimated in the order of few seconds. The same consideration can be taken into account for the cooling ramp. The annealing time was of 60 min for all the processes. The RBS analyses were performed by using 2 MeV $4He^+$ backscattered ions at 165°. In order to study the evolution of the samples morphology, SEM analyses were performed by a Zeiss FEG-SEM Supra 25 Microscope operating at 5 kV. The SEM images were analyzed by the Gatan Digital Micrograph software. TEM analyses were performed with a 200 keV 2010 JEOL instrument. Cross-section TEM (X-TEM) samples were prepared by means of a standard X-TEM preparation with mechanical grinding and ion milling. The latter process was performed in a GATAN-PIPS apparatus at low energy (5 keV Ar^+) and low incidence (7°). AFM analyses were performed by a Veeco-Innova microscope operating in high amplitude mode, and ultra-sharpened Si tips (MSNL-10 from Veeco instruments) were used. The AFM images were analyzed by SpmLab Analysis V.7.1. Finally, the optical measures were performed by a UV–Vis. Lambda 40 spectrophotometer in the spectral range between 200 and 1100 nm and by a Spectrum 1000 instrument in the IR region (1500 and 3500 nm).

2.3.3 Results

2.3.3.a General effects of the thermal processes

The description reported in this subsection concerns the process performed on the c-Si <100> substrate, while in the next subsection we will extend the analysis to the other substrates. Figure 2.7 (a) reports the RBS spectrum of the as-deposited sample (20 nm-thick Au film on the c-Si <100> substrate).

The Au atomic concentration was evaluated by measuring the peak area of the Au signal (using the XRump simulation software [54], resulting in $Q_{Au} = 11.4\times10^{16}$ at/cm^2 (within a statistical error of 5%). The equivalent thickness of the deposited Au film is (20±1) nm. Figure 2.7 (b) shows the RBS spectra of the annealed samples (1073 and 1373 K). The spectra were acquired by the He beam channeled along the <100> crystal axis of the substrate in order to enhance the signal of eventual impurities with atomic number lower than Si. The annealing at T = 1073 K induces a spreading of the Au peak due to the Au-Si intermixing that occurs during the thermal treatment (black curve in fig. 2.7 (b)). In addition, by increasing the temperature at 1373 K (red curve), the RBS spectrum of the sample displays the presence of nitrogen atoms at the surface.

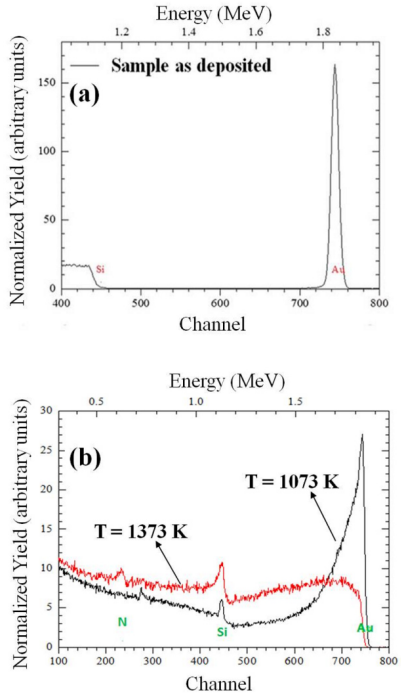

Figure 2.7 - (a) 2 MeV He RBS spectrum of gold-coated c-Si substrate. Surface Si and Au signal positions are indicated. (b) 2 MeV He RBS spectra of gold-coated c-Si substrates thermal treated at 1073 K (black curve) and 1373 K (red curve) for 60 min. Surface Si, N and Au signal positions are indicated.

In particular, as regards the sample thermal treated at 1373 K, the simulation of RBS spectrum (by XRump analysis software) in fig. 2.8 (a), suggests the formation of an Au-Si-N alloy with thickness of about 1.3–1.4 μm, whose composition is reported in the table below (fig. 2.8). From the analysis of the nitrogen peak, the estimated atomic density is $Q_N = 1.45\times10^{17}$ at/cm^2 (see fig. 2.8 (b)).

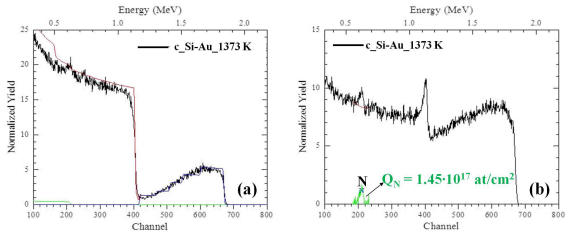

X-Rump Simulation				
Layer	**Thick (1e15 at/cm²)**	**Elements**		
1	100	Si 0.95	N 0.05	Au 0.00
2	2000	Si 0.891	N 0.1	Au 0.009

Figure 2.8 - (a) Random RBS spectrum of the sample thermal treated at 1373 K-60 min. XRump simulation suggests the formation of the Au-Si-N alloy with thickness of about 1.3–1.4 μm, whose composition is reported in the table. (b) the RBS spectrum in channeling, related to the sample thermal treated at 1373 K-60 min, is enlarged to highlight the N peak on the sample surface. The estimated atomic density is $Q_N = 1.45 \times 10^{17}$ at/cm^2.

The question that naturally arises about these Au Ds concerns their chemical composition. To clarify this point, we performed EDX measurements. Figure 2.9 (a), (b) shows the EDX spectra, which report the characteristic peaks of the chemical elements present on the samples surfaces treated at higher temperature (1373 K). The N peak in fig. 2.9 (a) confirms that the nitrogen contamination is due to the annealing at higher T (1373 K). Besides, fig. 2.9 (b) shows the EDX maps of aggregate of NDs on the sample surface. We use the overlap of the Au (pink), Si (blue), and N (green, the gas carrier used during the annealing processes) to highlight the chemical composition of the sample surface.

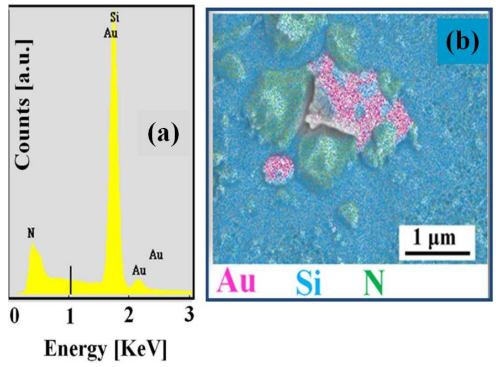

Figure 2.9 – (a) EDX spectrum related to sample thermal treated at 1373 K (Au Ds). (b) EDX map of the Au, Si, and N relative to a SEM image of the Au NDs aggregate.

Figure 2.10 shows, in the infrared region (8–12 μm), the transmittance spectrum (T%) of the Au-coated c-Si substrate thermal treated at 1373 K. The two characteristic peaks, visible at about 9 μm and 11 μm, are due to the formation of SiO_2 and Si_3N_4 on the sample surface. This result confirms the interaction between Si and N, with the consequent formation of stoichiometric silicon nitride (Si_3N_4) in the sample.
By analyzing the results of structural and optical characterizations, we can conclude that the surface of the sample with dendritic structures is formed by Si (the substrate) with some inclusion of N (formation of Si_3N_4 by the reaction of Si and N during the annealing), while the Ds are mainly formed by Au with some Si inclusion.

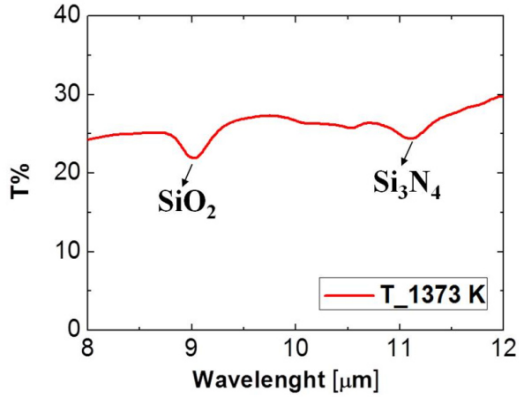

Figure 2.10 - Transmittance spectrum in the infrared region of the gold-coated c-Si substrate thermal treated at 1373 K. The trend of transmittance values shows two characteristic peaks, visible at about 9 μm and 11 μm, due to the formation of SiO_2 and Si_3N_4 on the sample surface.

In fig. 2.11 the representative SEM and AFM images show the structural evolution of the samples as result of the thermal processes. Starting from a continuous Au film (fig. 2.11 (a)), the thermal annealing at T = 1073 K leads to the formation of Au-Si islands (Is) on the sample surface, fig. 2.11 (b). When the temperature of the process is raised to 1373 K (fig. 2.11 (c)), these structures evolve into larger aggregates characterized by a surface morphology that reminds the dendritic one. The height and number of dendrites, as well as the surface roughness of the samples, were estimated by averaging the values obtained from the analyses of the structures located in different scanned areas. These analyses indicated a value of surface roughness equal to δ_{Is} = 74.2± 11 nm for the sample processed at 1073 K (sample with Au-Si Is), and δ_{Ds} = 68.4 ±10 nm for the sample processed at 1373 K (sample with Au Ds). Figure 2.12 shows the representative two- and three-dimensional AFM images of the samples thermally processed at 1073 K and 1373 K.

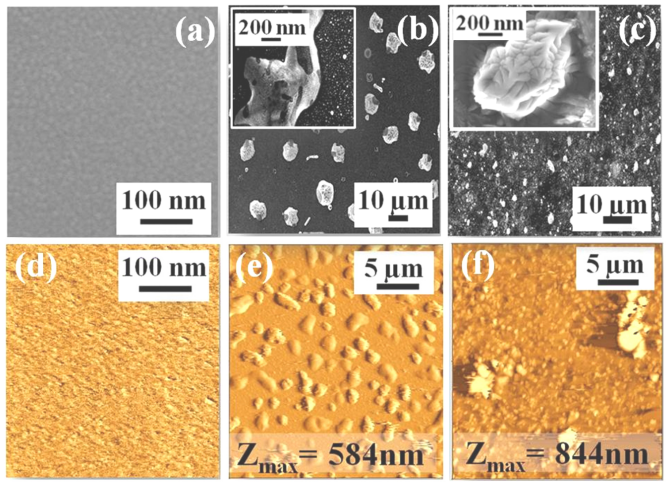

Figure 2.11 - Representative SEM ((a)–(c)) and AFM ((d)–(f)) images of as deposited and thermal treated samples: (a)–(d) as-deposited; (b)–(e) thermal treated at 1073 K; (c)–(f) thermal treated at 1373 K. The insets of (b) and (c) are high-resolution SEM images showing a single Au-Si island and a single Au-dendrite.

In particular, fig. 2.12 (a) reports a 3.5 µm×3.5 µm AFM image of a single Au-Si island. By AFM cross-sectional profile (also reported), its height is quantified in h_I =233± 35 nm. In figure 2.12 (b), 4.0 µm×4.0 µm AFM images of a single Au dendrite are reported. The estimated height of the structure, from the section profile, is h_D = 460±69 nm.

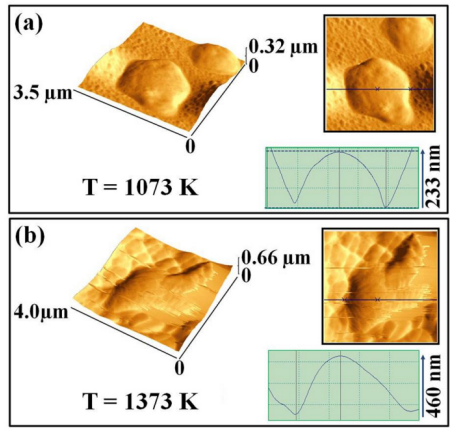

Figure 2.12 - Representative AFM images of Au-Si island and Au-dendrite: (a) 3D, 2D images and line section profile for a single Au-Si island; (b) 3D, 2D images and line section profile for a single Au-dendrite.

From statistical analysis of AFM images, the sample (thermally treated at 1073 K by direct counting and averaging on several scans) surface density of Au-Si Is was estimated in $\langle N_{Is} \rangle = (3.5 \pm 0.5) \times 10^{7} cm^{-2}$. Similarly, the average height of the Au-Si Is was $\langle h_{Is} \rangle = 169 \pm 25$ nm (by averaging several values obtained by cross-sectional profile analyses). The mean values of the surface density and height of the Au Ds (sample thermal processed at 1373 K) were estimated in $\langle N_{Ds} \rangle = (3.0 \pm 0.4) \times 10^{6} cm^{-2}$ and $\langle h_{Ds} \rangle = 605 \pm 91$ nm. The high value of $\langle h_{Ds} \rangle$ led us to check the variation of the Au surface density (atoms cm^{-2}) after the thermal treatment with respect to the value of the as-deposited sample. The value ρ_{Au_Ds} of the atomic surface density of the samples with Au dendritic structures on the surface was derived by:

$$\rho_{Au\_Ds} = \frac{\rho_{asdep} \cdot S \cdot t_{Au}}{N \cdot A \cdot \langle h_{Ds} \rangle} \tag{2.2}$$

where S is the scanned area on the sample, t_{Au} is the thickness of the sputter-deposited Au film, N is the number of counted structures, A is the average area covered by a single structure, $\langle h_{Ds} \rangle$ is the average height of the dendritic structures and $\rho_{as\text{-}dep}$ is the atomic surface density related to the as-deposited 20 nm-thick Au film ($\rho^{vol}_{Au} / t_{Au} = (1.18 \pm 0.06) \times 10^{17} cm^{-2}$). The value obtained of $\rho_{Au\text{-}Ds} = (5.11 \pm 0.76) \times 10^{17}$ cm^{-2}, which is about five-fold more than $\rho_{as\text{-}dep}$, suggests that the Ds structures, in addition to Au atoms, are also formed by Si atoms originating from the substrate (this point will be further discussed by cross-sectional TEM analyses).

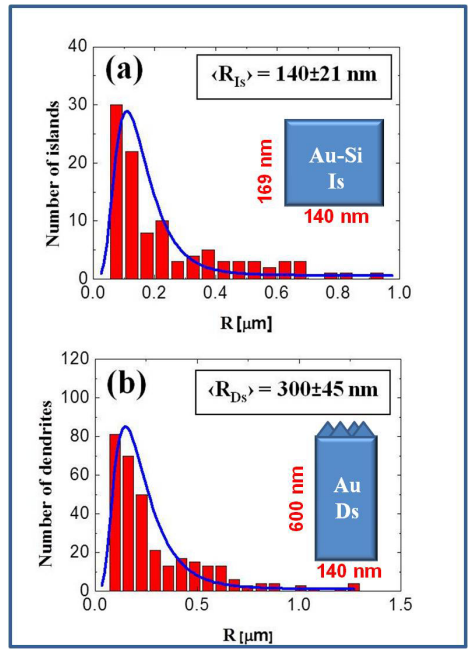

Figure 2.13 - Size distribution (radius R) of (a) Au-Si islands; (b) Au-dendrites.

Further structural informations were obtained by analyses of SEM images. In particular, SEM images were processed by Gatan Digital Micrograph software in order to determine the planar size distributions of the examined structures. Assuming a spherical shape structure, the size distributions for Au-Si Is and Au Ds were calculated on a statistical population of about 300 structures.

The distribution of radii R of the Is in the first sample and of the Ds in the second was fitted (continuous line in fig. (a and b)) by using the log-normal function [55]

$$f(R) = \left\{ \left(1 + 2\sqrt{2\pi\sigma}\right) \cdot \exp\left[- \left(\ln^2 \left(R/R_c \right) / 2\sigma^2 \right) \right] \right\} \qquad (2.3)$$

where σ is the standard deviation on R. The fit parameters are R_c and σ. The mean radius is obtained by $\langle R \rangle = \langle R_c \rangle \times \exp(\sigma^2/2)$. For the Au-Si Is, the mean value of the radius is $\langle R_{Is} \rangle$= 140 ±21 nm, (fig. 2.13 (a)). The Au Ds have a wider size distribution, and the average radius is equal to $\langle R_{Ds} \rangle$ = 300 ± 45 nm (fig. 2.13 (b)).

In order to investigate the internal structure of the Ds, cross-sectional TEM analyses were performed on the 1373 K-annealed sample.

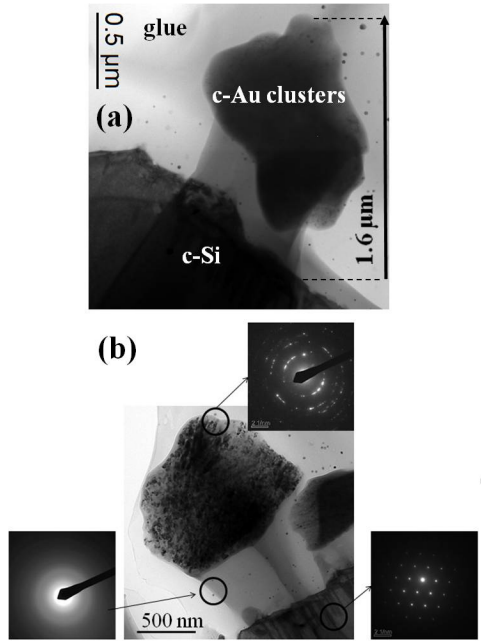

Figure 2.14 - Cross-sectional bright field-TEM images of the sample thermal treated at 1373 K: (a) image of an Au dendritic structure (height of about 1.6 µm); (b) aggregate of Au dendritic structures. In the insets, diffraction patterns are reported.

Figure 2.14 shows representative bright-field TEM (BF-TEM) images of the dendritic structures. On the c-Si substrate, diffraction patterns (see inset in fig.) highlight amorphous Si protusions (bright region) covered by crystalline Au nanostructures at the upper end (dark region). So, the dendritic structures are formed by amorphous Si micro-pillars (originating from the substrate) covered on the surface by nano-dentritic structured crystalline Au.

2.3.3.b Effects of substrate and temperature

As reported in Subsection 2.3.2, the samples thermal treated at 1373 K exhibit the presence of Au dendrites, under condition of rapid heating and cooling stages. In order to understand the formation mechanism of the dendritic structures, the role of the substrate in the growth process was investigated using three different substrates (c-Si, poly-Si and SOS). Figure 2.15 shows the schematic representations of the samples and the representative SEM images of the sample surface after the thermal annealing at 1373 K. Each substrate exhibits the formation of Au Ds covering the entire surface.

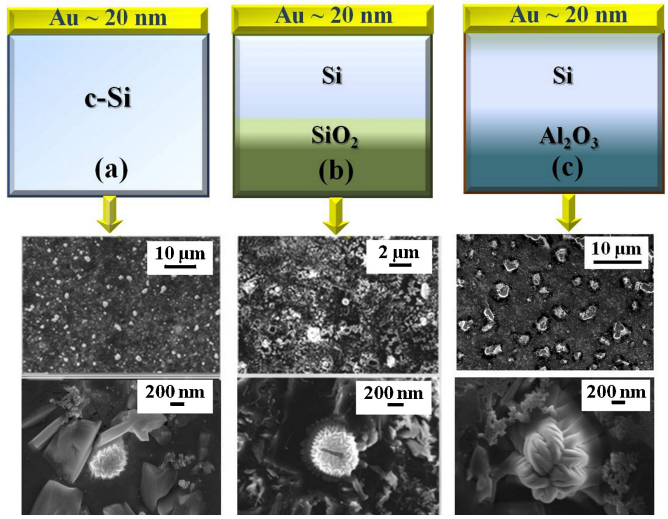

Figure 2.15 - Schematic picture of the samples with tree different gold-coated substrates and related SEM images with different magnification factors of the same samples after the thermal annealing at 1373 K: (a) c-Si substrate; (b) poly-Si substrate and (c) SOS substrate. Each substrate exhibits Au Ds formation after the thermal annealing.

Therefore, the experimental results suggest that the Au Ds growth is independent of the substrate crystal structure, and that it is only related to the Au-Si intermixing during the thermal treatment, as explained in the next subsection.
It remains to consider the role of temperature in the growth dynamics and the evolution of the Au dendritic structures. To this aim, the samples were processed at three different temperatures,

T_1 = 1073 K, T_2 = 1273 K and T_3 = 1373 K. Figure 2.16 reports the representative SEM images of the Au-coated c-Si substrate after the thermal annealing at T_1, T_2 and T_3. The images show the evolution from Au-Si Is (fig. 2.16 (a)) to dendritic structures (fig. 2.16 (c)) when the temperature is increased from 1073 K to 1373 K. It is clearly visible in fig. 2.16 (b) that the process at 1273 K, induces the formation of structures characterized by an incomplete developed dendritic morphology. Hence, the annealing at high temperature (>1273 K) is necessary to induce the complete development of the Au dendritic structures when fast heating and cooling ramps are performed.

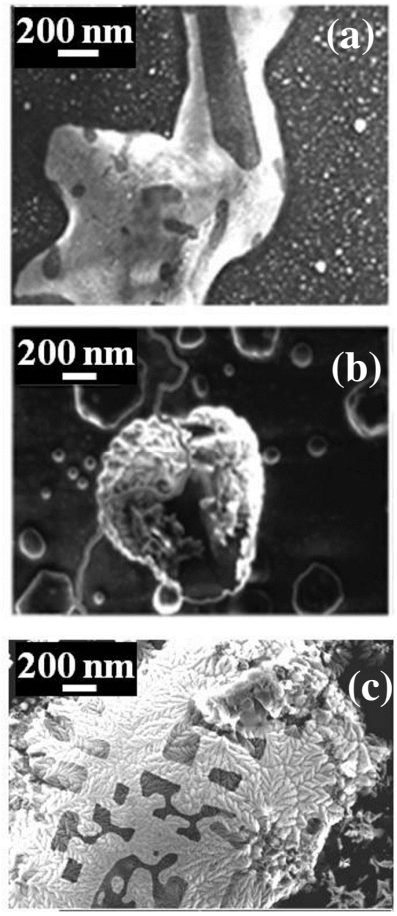

Figure 2.16 - Representative SEM of the gold-coated c-Si substrates submitted to thermal annealing at three different temperatures: (a) 1073 K; (b) 1273 K and (c) 1373 K. The increased T of the thermal process induces sample surface evolution from Au-Si islands to Au dendritic structures.

2.3.4 Optical measurements

This subsection reports the optical characterizations of the samples treated at the two different temperatures at which Is or Ds are present (1073 and 1373 K). Figure 2.17 shows the percentage values of the specular reflectivity (R%), obtained in the range between 200 nm and 1000 nm (visible range), for the following samples: a reference c-Si (substrate); the same substrate covered with 20 nm thick Au film (as-dep sample); the Au-Si samples annealed at T = 1073 K and T = 1373 K. The R% values of substrate and as-dep samples are significantly reduced after the thermal annealing at 1073 and 1373 K in all the wavelength range. The characteristic peaks at 279 and 370 nm, clearly visible in the spectrum of c-Si substrate, are also visible after the heat treatment at lower temperature. As described in subsection 2.3.3a, the rapid heating and cooling at T = 1073 K induces the formation of Au-Si Is. Such a morphological change of the sample explains the variations in the reflectivity values. Indeed, due to the heating stage, the breaking of the Au film determines the presence of Si regions that are no longer covered with metal. Thus, the corrugation of the sample surface produces the reduction of the reflectivity with respect to the as-dep sample. The R% is further reduced as a result of heat treatment at 1373 K. The formation of dendritic structures on the sample surface determines a considerable increase of the diffused radiation with consequent reduction of the reflected component (see fig. 2.17).

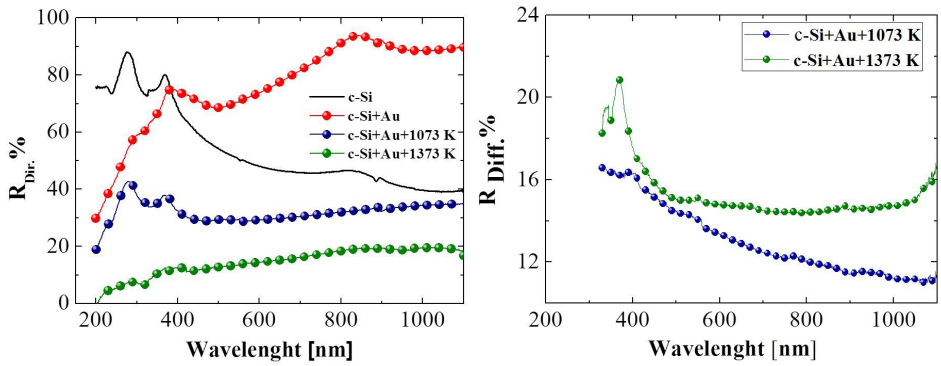

Figure 2.17 - Specular reflectivity (R_{Dir}.%) in the visible range (200–1000 nm) for the following samples: c-Si substrate (black curve); gold-coated c-Si substrate (red curve); gold-coated c-Si substrate thermal treated at 1073 K (blue curve) and gold-coated c-Si substrate thermal treated at 1373 K (green curve). (b) Diffused reflectivity related to the sample submitted to thermal treatments at T: 1073K (blue curve); 1373 K (green curve).

The μm-scale size of the dendrites suggested to study the optical properties of the samples annealed in the infrared region. Indeed, in this spectral range it is possible to analyze the scattering of radiation from sub-wavelength structures. Figure 2.18 reports the extinction spectra (i.e. the sum of absorbance and diffusion components calculated as 100– R_{tot}% – T_{tot}%) for the two samples annealed at 1073 and 1373 K.

The extinction values are much higher for the sample thermal treated at 1373 K than that of the sample processed at 1073 K.

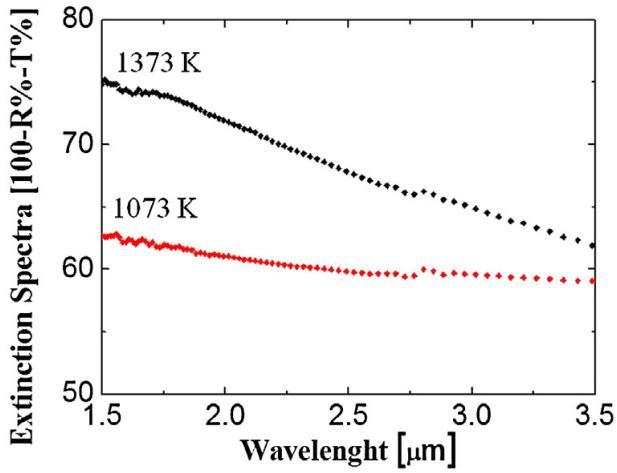

Figure 2.18 - Extinction spectra (diffusion + absorption, i.e. 100-R%-T%) for the gold coated substrates submitted to thermal annealing at increasing T. The red curve refers to the sample after the annealing at 1073 K. The black curve, instead, refers to the sample after thermal treatment at 1373 K.

This result can be explained by considering the different surface structure of the samples. Indeed, according to the SEM images reported in figs. 2.11 (b) and 2.11 (c) and using the Gatan Digital 305 Micrograph software, we determined the average values of the surface area covered by the Is or by Ds. These values were calculated by

$$FA\% = (N \times A/S) \times 100 \qquad (2.4)$$

where N is the average number of counted structures, A is the average area covered by a single structure and S is the scanned. The resulting filled areas for the sample annealed at 1073 and 1373 K are: filled area Au-Si Is = 26%; filled area Au Ds = 12%. So, assuming that the absorbed component is strictly related to the fraction of covered area, the sample covered by Au-Si Is absorbs a greater fraction of the incident radiation with respect to the sample covered by Au Ds. Therefore, the high extinction values of the incident field for the 1373 K annealed sample are attributable to a larger increase in the fraction of diffused radiation by the dendrites present on its surface.

As a conclusion, the optical analyses in infrared region suggest the ability of dendritic structures as scattering centers.

2.3.5 Phenomenological growth model

A phenomenological model for the growth of the dendritic structures can be drawn by considering the kinetic processes that occur at the Au-Si interface in a far from equilibrium condition. In the heating stage upon 1073 K, the Au layer deposited on Si, partially dewets leading to the formation of Au-Si droplets on a smooth Au wetting layer [56, 57]. When the temperature of the thermal treatment is increased to 1373 K, the morphology of the resulting droplets evolves towards the dendritic one. This is related to the high temperature of the thermal process. As mentioned in Subsection 2.3.3b, each sample presents an Au-Si interface. The presence of the Au-Si system allows to deduce that the formation of dendritic structures is correlated to the Au-Si phase diagram (fig. 2.19). Accordingly, different stages leading to nanostructures formation are schematically represented in figure 2.19.

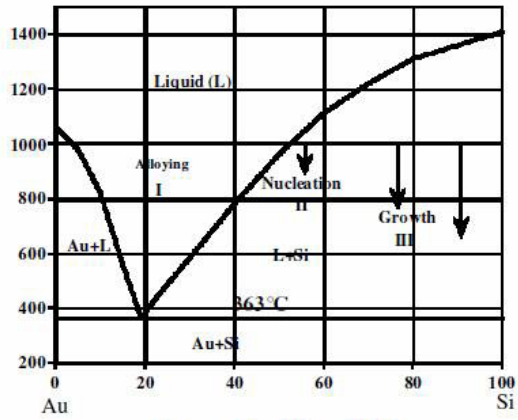

Figure 2.19 - Phase diagram of gold-silica system. The different stages leading to nanostructures formation are highlighted. [58]

The eutectic temperature of the silicon-gold system is 636 K (363 °C) at a composition of 19.1 at% in silicon [59]. Below the eutectic temperature, Au atoms diffuse into Si giving origin to a Au_3Si alloy. However, above the eutectic temperature, Si atoms can diffuse in the Au layer, forming an eutectic gold-silicon phase [60, 61]. Condition to obtain the eutectic alloy, is that the Si-Au wafer temperature is so high to induce the Si diffusion into the Au layer. Indeed, at 1373 K enough silicon atoms diffuse into the gold layer to form a melt alloy. This melt takes the form of droplets due to the surface tension minimization. With time, more Si from the substrate diffuses into the droplets, making them supersaturated with Si [58]. During the cooling stage, then, a phase separation between Au and Si occurs. At the end of the cooling process, we observe the formation of the Si protusions with Au dendritic surfaces.

The dendritic morphology is a common form of solidification for a DLA process [4, 37]. The condition for occurring such a process is that the molten material is undercooled below the freezing point of the solid. During the cooling, a spherical solid nucleus, which grows in the undercooled melt, becomes unstable as it increases in size and the symmetrical shape becomes perturbed. Therefore, the solid shape begins to express preferred growth directions. These growth directions may be due to anisotropy in the surface energy of the solid–liquid interface [62]. The resulting dendrite, then, exhibits sharp tips as it grows and the micro-structural length scale [63] is determined by the balance between the surface energy and the temperature gradient in the liquid at the interface [64]. So, the rapid heating and cooling processes play a significant role in the growth of dendritic structures.

Based on the considerations above, the following scheme for a growth model of dendritic structures (Au Ds) is drafted. The insertion of the Au-Si substrate from room-temperature environment directly into the pre-heated 1373 K oven chamber determines a far-from-equilibrium condition. As reported in fig. 2.20 (a), during the fast heating stage, the surface tension induces the formation of thermodynamic instable alloy droplets with high Si concentration. After the 60 min thermal annealing, the rapid cooling under the eutectic temperature (636 K) produces the phase separation between Au and Si. As a result, the Si is now rejected towards the substrate, while the gold segregates on the drop surface (fig. 2.20 (b)). In the fast solidification process the symmetrical shape of alloy droplets becomes unstable, and the structures exhibit the preferred growth directions (sharp tips) induced by anisotropy in the surface energy of the solid–liquid interface. As shown in fig. 2.20 (c), at the end of the solidification process the resulting structures show a morphology that is reminiscent of fractal structures. Furthermore, our structural characterizations of Au Ds suggest that the sample surface contains nitrogen contamination due to the interaction between Si and N in the phase of the sample heated at 1373 K (RBS in fig. 2.8).

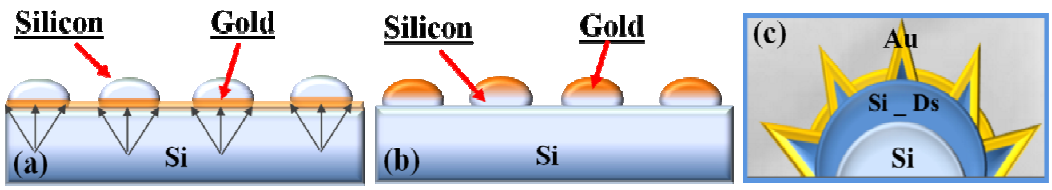

Figure 2.20 - Schematic stages in the formation of the Au Ds: (a) rapid heating stage, (b) rapid cooling stage and (c) morphology of the resulting dendritic structure.

2.4 Application: Au dendrites as SERS-active substrates

Sensitive Raman spectroscopy has been carried out with a Jobin-Yvon HR 800 micro-spectrometer coupled to a linearly polarized HeNe laser emitting at 633 nm. The excitation power is set between 0.8 and 80 μW. Light is focused on a spot of ~800 nm diameter via a 100X microscope objective (NA 0.9). The same objective is used to collect the backscattered radiation. A silicon CCD camera is used for light detection. Typical integration times range from 10 to 30 sec. A polarization analyzer is mounted on a rotating mount and placed in front of the monochromator slits. Spectral analysis is accomplished with a 600 l/mm grating, featuring a 10% difference in the polarization response to the two Transverse Electric and Transverse Magnetic components. A polarization scrambler is used to compensate for such effect.
Figure 2.21 (a) shows the image of the sample with Au dendrites on the surface, while in fig. 2.21 (b) the shape of the laser spot is impinging on the sample surface.

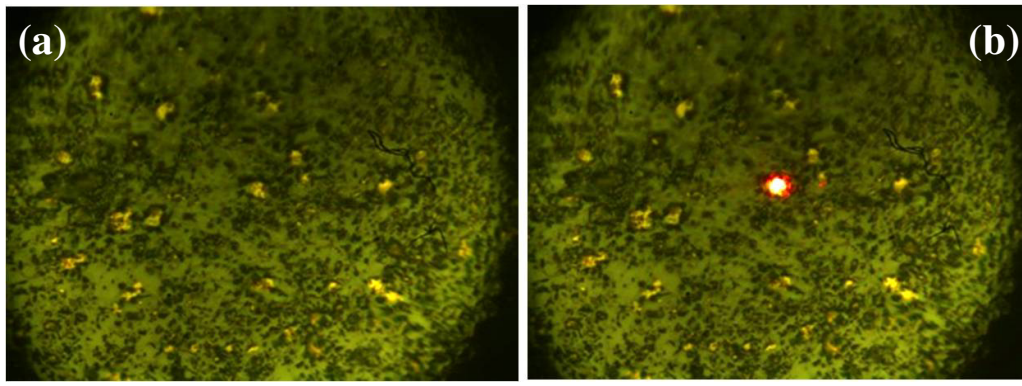

Figure 2.21 – (a) Optical microscope image of the Au dendrites on c-Si substrate; (b) red spot: laser spot impinging on the sample surface.

We have used Methylene Blue (MB) as a probe molecule for SERS (MB chemical formula: $C_{16}H_{18}ClN_3S$). MB is a suitable probe for SERS for several reasons: (i) the presence of two electron doublets on the sulfur atom fosters the formation of stable chemical bonds of MB with gold and silver substrates on which it adsorbs as a monomer, dimer or as a layer of aggregates; (ii) the monomer has a low fluorescence quantum yield (η = 0.03), while the dimer has no fluorescence; (iii) the presence of delocalized π electrons improves the optical coupling with plasmon modes; (iv) the excitation at 633 nm leads to a further resonant amplification of Raman emission [39].
At concentration of 10^{-6} M the MB molecules appear in monomer or dimer form, with absorption maxima at 670 nm and 620 nm (as shown in fig. 2.22 (a)). Binding of the gold nanostructures is achieved by immersion of the metal nanostructure substrate for 1h in the

solution and, after rinsing in water, drying in air for 1 hour. During the drying procedure, the glass substrate is held vertically to avoid the formation of droplets that could induce local accumulation of MB.

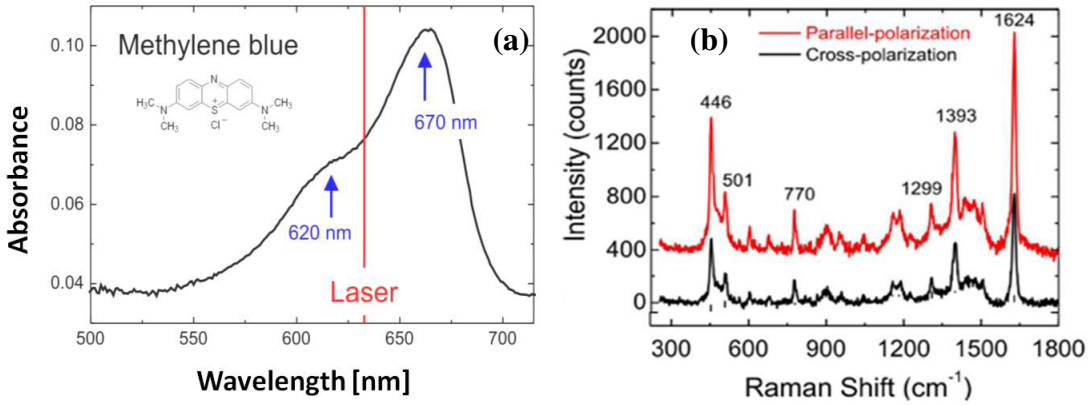

Figure 2.22 - (a) Absorption spectrum of MB aqueous solution at 10^{-4} M. The red vertical line indicates the spectral position of the laser excitation for RRS and SERRS. (b) Resonant Raman spectra of MB molecules cast on glass detecting the parallel polarized (red line) and the cross-polarized (black line) component of the scattering with respect to laser polarization. Spectra are offset for clarity. Laser power 50 μW. Integration time 30sec.

Figure 2.22 (b) shows the Resonant Raman Spectra (RRS) acquired on a drop of MB solution cast on glass substrate after evaporation of the solvent. Measurements have been acquired on the dense bluish external annular region of the drop, assuring a sufficient concentration, so to obtain a good signal to noise (S/N) ratio, even without plasmonic enhancement and using a laser power (50 μW) that does not alter the molecule.

The SERS spectra related to different Au dendrites (Au Ds spectra are offset for clarity), grown on c-Si substrates, have been compared with the SERS spectrum of the Au-coated c-Si substrate (sample as deposited), as shown in fig. 2.23. All spectra exhibit the characteristic Si peak at 521 cm^{-1}. The comparison allows us to estimate the EF for each Raman mode, calculated by normalizing the intensities to the incident power (P) and integration time (t). Therefore, the EF (without SERS-active areas normalization) can be calculated through the relationship:

$$EF = \frac{I_{SERS}}{I_{Raman}} \cdot \frac{P_{raman}}{P_{SERS}} \cdot \frac{t_{Raman}}{t_{SERS}} \qquad (2.5)$$

We obtained the following EF values for the best intensity of MB peaks at 450 and 1625 cm^{-1}:

- EF_450 = ($\frac{1140 cts}{140 cts} = 10$) for the best intensity of MB peak at 450 cm^{-1} ;

- EF_1625= ($\frac{900cts}{180cts} = 5$) for the best intensity of MB peak at 1625 cm^{-1}.

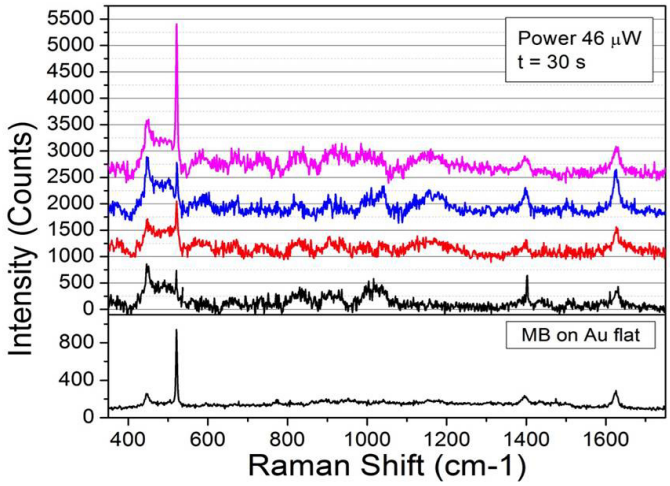

Figure 2.23 - Comparison between Raman spectrum related to MB on Au-coated c-Si substrate (Au flat) and MB on the different Au dendritic structures.

The average value of the enhancement factor for the MB peak at 450 cm^{-1}, <EF_450> = (7.0±1.4), is estimated by averaging the values obtained from the analyses of the four Raman spectra related to the Au dendrites on c-Si substrates (see fig. 2.23). Using the procedure described above, the average value of the enhancement factor for the MB peaks at 1625 cm^{-1} is <EF _1625> = (3.5±0.7).
Assuming a spherical shape structure, the average radius of dendrites is $<R_{Ds}>$ = (300 ± 45) nm, and we can derive the $<EF^{norm.}>$ with SERS-areas normalization, using the following formula:

$$EF = \frac{I_{SERS}}{I_{Raman}} \cdot \frac{P_{raman}}{P_{SERS}} \cdot \frac{t_{Raman}}{t_{SERS}} \cdot \frac{A_{Raman}}{A_{SERS}} \qquad (2.6)$$

where A_{Raman} = 502.400 nm^2 is the sample region covered by the laser spot, and A_{SERS} = 282.200 nm^2 is the SERS area.

- $<EF^{norm.}\_450>$ = 12 for the intensity of MB peak at 450 cm^{-1};
- $<EF^{norm.}\_1.625>$ = 6 for the intensity of MB peak at 1625 cm^{-1}.

To obtain information about the role of the substrate on SERS measurements, we study the Raman signals deriving from MB molecules Au dendrites synthesized on different substrates. In particular, fig. 2.24 shows a large aggregate of Au dendritic structures grown on SOS.

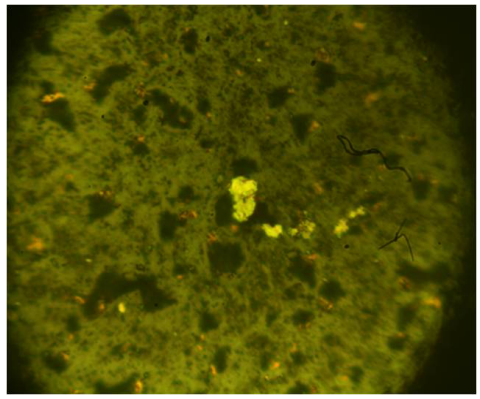

Figure 2.24 - Optical microscope image of a large aggregate of Audendrites on the SOS substrate.

The SERS spectra related to seven different Au dendrites on the SOS substrate surface are reported in fig. 2.25 .

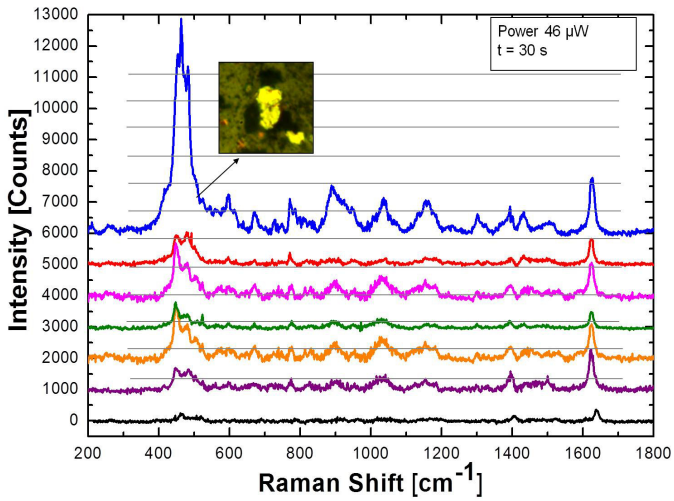

Figure 2.25 - Comparison between Raman spectrum related to MB adsorbed on the seven different Au dendritic structures grown on SOS substrate.

By eq. (2.6), we estimate the EF values for the best intensity of MB peaks at 450 and 1.625 cm^{-1}.

- $<EF^{norm.}\_450> = 257$ for the intensity of MB peak at 450 cm^{-1};
- $<EF^{norm.}\_1.625> = 17$ for the intensity of MB peak at 1625 cm^{-1}

The comparison between the EF values related to Au dendrites obtained on the two different substrates, shows an improvement of the enhancement signals related to the dendritic structures on the SOS substrate. Given that the Au Ds growth is independent of the substrate crystal structure, and that it is only related to the Au-Si intermixing during the thermal treatment (see results in Subsection 2.3.3b), we deduce that the higher EF are due to the larger size of the analysed dendrites aggregate. Indeed, if the size of laser light (focused on a spot of ~800 nm) is comparable with the larger planar dimension of the Au dendrites, all the incident light interacts with the dendritic aggregates (the effective SERS active substrate) and there is no loss of signal due to the interaction with the Si substrate. The lower intensity of the characteristic Si peak at 521 cm^{-1}, highlighted by the SERS spectra in fig. 2.26, confirms this assertion. Therefore, we conclude that to obtain higher EF, the planar size of the Au dendrites and then, the SERS-active area, must be comparable with the laser spot size and the dendrite surface must be uniformly covered by Au such that most MB molecules are adsorbed to the dendritic structures.
Another important result, highlighted by SERS measurements, is illustrated in fig. 2.26. The light scattered from non-spherical particles is generally partially depolarized [21], i.e. there is a non-zero intensity component with a polarization orthogonal to the incident one (linearly polarized excitation is assumed). To quantify this effect, we report in fig. 2.26 the depolarization factor ($I_{\parallel} : I_{\perp}$) related to the silicon signals detected out of the dendrites (fig. 2.26 (a)), or after the interaction with the dendritic structures (fig. 2.26 (b)).

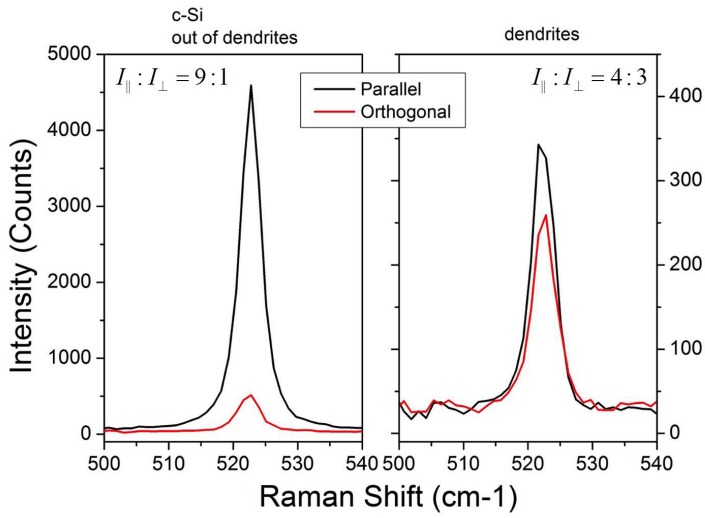

Figure 2.26 - Intensity of the Si signal detected: (a) out of the dendritic structure or (b) after the interaction with Au dendrite.

The changes of the characteristic ratio between the polarized components of the Si signal suggests the depolarization effect due to Au dendritic structures that act as micro-antennas.

2.5 Conclusions

Our results show that high-temperature treatments of thin Aufilms on a Si layer induce the growth of Au dendritic structures when fast heating and cooling stages (1273 K/min) are performed. The structural characterizations suggest that the Au DS synthesis is independent of the substrate crystal structure, on which Au was deposited and that it is only a consequence of the Au-Si intermixing during the thermal treatment at 1373 K. The role of temperature in the dynamic growth of dendritic structures has been investigated. The analyses of the sample surfaces evidence the evolution from Au-Si Is to the Au Ds, when the temperature of the hermal treatment is increased from 1073 K to 1373 K. The resulting structures exhibit a dendritic surfaces covered by crystalline Au nanostructures at the upper end. The TEM analyses suggest that, below the dendritic surface, these structures are formed by Si atoms originating from the substrate. In order to explain the kinetic processes of the Au-Si interface and the role of temperature and substrate in the growth dynamic and the evolution of dendritic morphologies, we have drafted a phenomenological growth model in which the rapid heating stage at 1373 K is responsible for the composition of the dendritic structures. The peculiar surface morphology and μm-scale size of Au Ds have revealed their ability as scattering centers in the infrared region of the spectrum. For their optical properties, these structures may be of great interest for the application in optical, opto-electronics and magnetic devices.
Besides, the SERS measurements, performed by using MB or thiophenol as probe molecules, have highlighted that the dendritic nanostructures can be used as SERS active substrate to obtain amplification factors of electromagnetic field due to the resonant coupling between the Raman signal and plasmonic oscillations related to sharp tipo of Au Ds.

References

[1] T. Qiu, Y. Zhou, J. Li, W. Zhang, X. Lang, T. Cui and P. K Chu - J. Phys. D: Appl. Phys. - 42 175403 (2009)

[2] M. Moskovits - Rev. Mod. Phys. **57** 783 (1985)

[3] K. Kneipp, H. Kneipp, I. Itzkan, R.R. Dasari and Feld M S J. Phys.: Condens. Matter 14 R597 (2002)

[4] T. Qiu, Y. Zhou, J. Li, W. Zhang, L. Xianzhong, C. Tiejun, P.K. Chu - J. Phys. D: 425 Appl. Phys. 42 426 175403 (2009)

[5] G. Lu, C. Li, G. Shi - Chem. Mater. 19 427 3433 (2007)

[6] H. Xu, E.J. Bjerneld, M. Kall, M. Borjesson - Phys. Rev. Lett. 83 428 4357(1999)

[7] T. Huang, F. Meng, L. Qi - Langmuir 26 429 7582 (2010)

[8] W. Song, Y. Cheng, H. Jia, W. Xu, B. Zhao - J. Colloid Interface Sci. 298 765 (2006)

[9] S. Joon Lee, A.R. Morrill, M. Moskovits, J. Am. Chem. Soc. 128 432 2200 (2006)

[10] Y.K. Mishra, D. Kabiraj, I. Sulania, J.C. Pivin, D.K. Avasthi - J. Nanosci. 433 Nanotech. 7 434 1878 (2007)

[11] Y.K. Mishra, S. Mohapatra, D. Kabiraj, A. Tripathi, J.C. Pivin, D.K. Avasthi - J. Opt. A: Pure Appl. Opt. 9 436 S410 (2007)

[12] Y.K. Mishra, R. Adelung, G. Kumar, M. Elbahri, S. Mohapatra, R. Singhal, A. Tripathi, D.K. Avasthi - Plasmonics 8 811 (2013)

[13] Y.K. Mishra, S. Mohapatra, R. Singhal, D.K. Avasthi, D.C. Agarwal, S.B. Ogale - Appl. Phys. Lett. 92 043107 (2008)

[14] Y.K. Mishra, V.S.K. Chakravadhanula, V. Hrkac, S. Jebril, D.C. Agarwal, S. Mohapatra, D.K. Avasthi, L. Kienle, R. Adelung, J. Appl. Phys. 112 064308 (2012)

[15] J. Ye, L. Lagae, G. Maes, G. Borghs, P. Van Dorpe, Opt. Exp. 17 23765 (2009)

[16] E. Prodan, C. Radloff, N.J. Halas, P. Nordlander, Science 302 419 (2003)

[17] K. Kneipp, Y. Wang, H. Kneipp, L.T. Perelman, I. Itzkan, R.R. Dasari, M.S. Feld, R. George, Phys. Rev. Lett. 78 1667(1997)

[18] S. Nie, S.R. Emory, Science 275 1102 (1997)

[19] K.A. Bosnic, J. Jiang, L.E. Brus, J. Phys. Chem. B 106 8096 (2002)

[20] M.I. Stockman, L.N. Pandey, L.S. Muratov, T.F. George, Phys. Rev. Lett. 72 2486 (1994)

[21] L. Manna, D.J. Milliron, A. Meisel, E.C. Scher, A.P. Alivisatos, Nat. Mater. 2 416 382 (2003)

[22] D.J. Milliron, S.M. Hughes, Y. Cui, L. Manna, J.B. Li, L.W. Wang, A.P. Alivisatos - Nature 419 190 (2004)

[23] J.W. Grebinski, K.L. Hull, J. Zhang, T.H. Kosel, M. Kuno, Chem. Mater. 16 5260 (2004).

[24] S.M. Lee, Y.W. Jun, S.N. Cho, J. Cheon - J. Am. Chem. Soc. 124 11244 (2002)

[25] Y.W. Jun, Y.Y. Jung, J. Cheon - J. Am. Chem. Soc. 124 615 (2002)

[26] D.L. Wang, C.M. Lieber, Nat. Mater. 2 355 (2003)

[27] V. M. Shalaev, R. Botet, J. Mercer and E. B. Stechel - Phys. Rev. B 54 8235 (1996)

[28] M. I. Stockman - Phys. Rev. E 56 6494(1997)

[29] V. M. Shalaev and A. K. Sarychev - Phys. Rev. B **57** 13265 (1998)
[30] Y. Zhou; S. H Yu, C. Y. Wang, X. G.Li, Y. R. Zhu, Z. Y. Chen - Adv. Mater. 11, 850 (1999)
[31] R. Qiu, H. G. Cha, H. B. Noh, Y. B. Shim, X. L. Zhang, R. Qiao, D. Zhang, Y. Kim, U. Pal, Y. S.Kang - J. Phys. Chem. C 113, 15891 (2009)
[32] Y.J Song, J.Y.Kim, K.W. Park - Cryst. Growth Des. 9, 505 (2009)
[33] Y. Song, Y. Yang, C. J. Medforth, E. Pereira, A. K. Singh, H. Xu, Y. Jiang, C. J. Brinker, F. van Swol, J. A.Shelnutt - J. Am. Chem. Soc. 126, 635 (2004)
[34] T. Huang, F. Meng, and L. Qi - Langmuir 26(10), 7582–7589 (2010)
[35] Y. Song1, Y.B. Jiang, H. Wang, D. A Pena, Y. Qiu, J. E. Miller and J. A. Shelnutt - Nanotechnology **17** 1300–1308 (2006)
[36] T. Qiu, X.L.Wu, Y.F. Mei, P.K. Chu, G.G. Siu - Appl. Phys. A 81, 669–671 (2005)
[37] S. Kaniyankandy, J Nuwad, C Thinaharan,GK Dey and C G S Pillai - Nanotechnology 18 125610 (6pp) (2007)
[38] F. Claro and R, Fuchs - Phys. Rev. B 33 7956 (1986)
[39] S. Hayashi, R. Koga, M. Ohugi, K. Yamamoto and M. Fujii - Solid State Commun. 76 1067 (1990)
[40] T. A Witten Jr and L. M Sander - Phys. Rev. Lett. 47 1400 (1981)
[41] D. Barkey, F. Oberholtzer and Q. Wu - Phys. Rev. Lett. 75 2980 (1995)
[42] M. C. Chen, S. D. Tsai, M. R. Chen, S. Y. Ou, W-H Li and K. C. Lee - Phys. Rev. B 51 4507 (1995)
[43] Y. Y. Teng and E. A. Stern - Opt. Commun. 67 119 (1988)
[44] I. Pastoriza-Santos, L. Marzan, Langmuir 18 2888. 453(2002)
[45] F. Mafune, J.Y. Kohno, Y. Takeda, T. Kondow - J. Phys. Chem. B 104 8333. 454 (2000)
[46] L.N. Lewis, N. Lewis - J. Am. Chem. Soc. 108 7228. 455 (1986)
[47] R. He, X. Qian, J. Yin, Z. Zhu - Chem. Phys. Lett. 369 454 (2003)
[48] K. G. Libbrecht - Rep. Prog. Phys. 68 855–895 (2005)
[49] Y. Saito - Statistical Physics of Crystal Growth (Singapore: World Scientific) (1996)
[50] J. S. Langer - Rev. Mod. Phys. 52 1–28 (1980)
[51] WWMullins and R F Sekerka - J. Appl. Phys. 35 444–51 (1964)
[52] T.A. Witten, L.M. Sander – Phys. Rev. B 27, No.9, 1 (1983)
[53] E. Yokoyama and T. Kuroda - Phys. Rev. A 41 2038–49 (1990)
[54] L. R. Doolittle and M. O. Thompson, RUMP, Computer Graphics Service (2002)
[55] C.G. Granqvist, R.A. Buhrman - J. Appl. Phys. 47 (1976) 2200.
[56] F. Ruffino, A. Canino, M.G. Grimaldi, F. Giannazzo, F. Roccaforte, V. Raineri - J. Appl. Phys. 104 024310. 458 (2008)
[57] B. Ressel, K.C. Prince, S. Heun, Y. Homma - J. Appl. Phys. 93 3886 (2003)
[58] M. Paulose, O. K. Varghese, and C. A. Grimes - J. Nanosci. Nanotech. 3, 341–346 (2003)
[59] R.F. Wolffenbuttel, Sens. Actuators A 62 680 (1997)
[60] P.H. Chang, G. Berman, C.C. Shen - J. Appl. Phys. 63 1473. 467(1988)
[61] W. Gerlach, B. Goel - Solid-State Electron. 10 589 (1967)

[62] D.R. Askeland, The Science and Engineering of Materials, Chapman and Hall, 475 476 (1990)
[63] A.J. Dougherty, F.S. Stinner, http://arxiv.org/pdf/1206.4030.pdf 477 (2012).
[64] M.C. Fleming - Metall. Trans. 22 B 269 (1991).

Chapter 3

SiO_2 Nanowires-Au Nanoparticles pea-podded composites: synthesis and structural analyses

3.1 SiO_2 nanowires-Au nanoparticles pea-podded composites: motivations and state of the art

Oxide-based semiconductor nanostructured materials have been widely investigated for chemical and biosensing applications, biocompatibility, relatively easy large-scale synthesis, superior thermal and chemical stabilities and high surface-to-volume ratios [1, 2]. Because of their large surface areas, nanostructures such as nanowires (NWs) [3], nanotubes [4, 5], nanorods [6] and nanoparticles (NPs) [7] offer large reaction cross sections for signal generation [8]. Among Si-based nanostructures, SiO_2 nanowires (NWs) are gaining a great scientific and technological interest due to their potential applications, such as new electronic devices, biosensors, nanoscale optical devices and sensors [9-14]. For example, amorphous silicon oxide nanowires prepared by laser ablation [15, 16] have shown intense blue light emission, making them a promising material for optoelectronic devices. Laser ablation [17, 18], chemical vapor deposition [19, 20], physical vapor deposition [21, 22] and thermal annealing [23] are used to synthesize bulk quantities of silicon nanowires, the majority of which have an inner silicon core surrounded by an outer silicon oxide shell.

Another important trend of the research in the field of biosensing and optoelectronic devices is focused on the study of the structural and optical properties of metallic nanoparticles (NPs) embedded in the dielectric matrix. Noble metal nanoparticle-dielectric matrix composite systems are considered to have practical applications in ultrafast all-optical switching devices owing to their enhanced third-order nonlinear susceptibility, especially near the SPR frequency [24]. Therefore, metal-dielectric nanocomposites (see SiO_2 nanowires-Au nanoparticles pea-podded composites in fig. 3.1) have been applied in optical switching devices for nonlinear and fast optical response near the SPR [25, 26]. It has been recognized that the electronic, optical and magnetic properties of metal NPs embedded in a dielectric matrix depend on the size and shape of NPs, the interparticles distance and the dielectric costant of the surrounding medium.

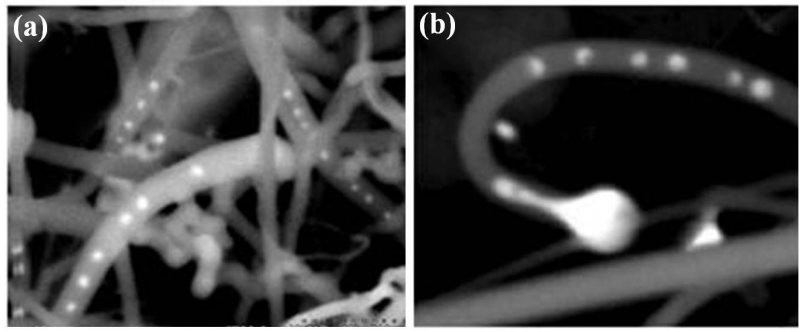

Figure 3.1 - (a)-(b) Typical nearly regular growth of gold bead-strings within silica nanowires. The width of the image is 2 μm. [27]

Several approaches, such as the sol-gel process, metal-dielectric co-sputtering deposition, metal-ion implantation into a dielectric matrix and pulsed laser deposition, have been used to prepare metal-dielectric nanocomposites [24].

Recently, a simple and versatile method for the direct growth of SiO_2 NWs on Si surface was reported (a method, so, allowing direct applications in Si-based solid state devices): it was observed that amorphous SiO_2 NWs can be grown on a crystalline Si substrate by first deposting a thin metal film (Au, for example) on its surface and then heating the system to elevated temperatures (>1273 K) in an inert ambient (e.g. N_2 or Ar) containing trace amounts (3–5 ppm) of oxygen [10, 11, 15 28-35]. Considering, for example, a thin Au film on the Si substrate, it is widely recognized [15, 27] that, during the heating, the film breaks up into nanometer-scale islands and reacts with the Si substrate to form molten droplets of Au–Si eutectic composition. These droplets absorb gas-phase reactants in the form of O_2 and SiO, produced by the reaction between O_2 and Si wafer, until they become supersaturated. Due to this reaction, solid precipitates of secondary phases (e.g. Si or SiO_2) can form within the droplets. These precipitates then grow and extend from the droplets to form nanowires. During the subsequent growth, the liquid eutectic droplets simply act as preferential absorption sites for the gas-phase reactants and as rapid transport media for the diffusion to the growing nanowire. The diameter of the nanowires depends on the size of the gold droplets, which is determined by the thickness of the original Au film. In these experiments, it was frequently observed that such SiO_2 NWs develop a pea-pod structure with a string of nano-sized Au beads distributed with nearly regular spacing along its axis [15, 28, 29, 27, 36-38]. Typical annealing conditions for the growth of such a structure are 60 min at 1373 K. The prevalence of such bead strings in the SiO_2 nanowires depend critically upon growth conditions and may vary between about 1% and 80% even on a single wafer. Explaining exactly how such a pea-pod develops is currently a matter for conjecture and, until now, the more detailed and reliable explanation model was given by Fletcher et al. [27] based on a simple diffusion mechanism that produces individual nano-beads, but in regular succession in the SiO_2 nanowire. According to the theoretical results of Fletcher et al. [27], the beads formation process does not depend on instabilities developed in a considerable length of cylindrical liquid gold core (as in the case of models based on the Rayleigh instability), but rather on a simple diffusion mechanism. On the other hand, Wu et al. [39] invoke as a possible formation mechanism for the beads, the instability phenomena, due to thermodynamic fluctuations, of a liquid Au-Si core embedded in the SiO_2 NW. It is a matter of fact, however, that such SiO_2 NWs-Au nanoparticles (NPs) composites show interesting optical, electrical and plasmonic properties tunable by structuralones. For example: Wu et al. [39] observed a sharp photoluminescence peak around 683 nm for such peapodded nanostructures; Hu et al. [36] showed an enhanced photoresponse behavior in these composite materials; Wang et al. [37, 38] highlighted the strong dependence of the conductivity of the single SiO_2 NW on the number of embedded Au NPs. Corcerning the fied of applications, Hung et al. report Au NPs-embedded silica nanowires devices as wavelength selective nanoswitches [36]. Wang et al. [8] demonstrated how Au NPs embedded in single amorphous silica NW can be used as an oxygen gas sensor by amperometric routes. The silica shell of NW is amorphous, containing

various defects within NW, such as nonbrinding oxygen atoms, dangling bonds, strain bonds and oxygen vacancies, and the silica matrix is nonstoichiometric (SiO_x). These Au NPs-silica NW properties make the composite system sensitive to oxygen molecules, which change the conductance of a single NW system to enable sensing. Although silica NWs are nonconducting, photoconductance is observed via the SPR absorption of visible light at ~532 nm. The photocurrent of Au NPs-silica NWs shows an enhancement of ~15% when the incident polarization is transverse over that of longitudinal polarization. This enhanced photocurrent suggests that photogenerated carriers affect the surface-carrier concentration and would be critical in gas sensing, because adsorption would be solely on the surface of the NW. Such an observation opens up the possibility of using photocurrent behavior in oxygen sensing rather than monitoring dark current. Oxygen sensing is an important issue in many fields, such as the environment, medicine, transportation, etc. For example, oxygen sensors can monitor the environmental oxygen concentration of an industrial clean room; they are also widely used to control the air/fuel ratio in automobile engines, which enhances combustion efficiency and reduces the emission of pollutants [8].
For all the technological applications, new insights on the formation mechanism of such structures are crucial to improve the structural control towards the functional tuning of their physical properties. In the following subsection, we report the common synthesis methods used to obtain composite systems Au NPs-silica NWs.

3.1.1 Synthesis techniques and growth kinetics

3.1.1.a Vapor Liquid Solid (VLS) growth mechanism

Many works in the literature report the formation of silicon-based nanowires following the vapor-liquid-solid (VLS) growth mechanism and using a metal catalyst, because metals play a major role in the catalytic action.
Gold is the most widely used catalyst in the VLS growth of silicon-based nanowires, since the Au-Si system is a simple eutectic with the eutectic point at 363°C at about 19 at.% silicon. VLS growth of nanowires with silicon core and oxide as cladding layer has been reported both by thermal evaporation [21] and laser ablation [40] techniques at high temperature (1.200 °C) and low pressure (100-500 torr) in a quartz tube furnace.
One-dimensional crystalline nanowires are then grown by a liquid metal-alloy droplet-catalyzed chemical or physical vapor deposition process, which takes place in a vacuum deposition system (see growth diagram in fig. 3.2). Au-Si droplets on the surface of the substrate act to lower the activation energy of normal vapor-solid growth. For example, Si can be deposited by means of a $SiCl_4$:H_2 gaseous mixture reaction (chemical vapor deposition), only at temperatures above 800 °C, in normal vapor-solid growth. Moreover, below this temperature almost no Si is deposited on the growth surface. However, Au particles can form Au-Si eutectic droplets at temperatures above 363 °C and adsorb Si from the vapor state (because Au can form a solid-

solution with all Si concentrations up to 100%) until reaching a supersaturated state of Si in Au. Furthermore, nanosized Au-Si droplets have much lower melting points because the surface area-to-volume ratio is increasing, becoming energetically unfavorable, and nanometer-sized particles act to minimize their surface energy by forming droplets (spheres or half-spheres).

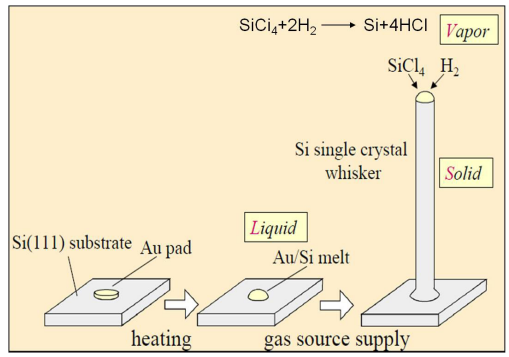

Figure 3.2 – Schematic diagram of the VLS growth of silicon-based NWs. Si is deposited by means of a $SiCl_4$:H_2 gaseous mixture reaction (chemical vapor deposition) [available on line].

The vapor-liquid-solid (VLS) mechanism suggested by Wagner et al. [41] for the growth of single-crystal silicon nanowires is a widely cited mechanism for silicon nanowire growth. In this growth mode, a liquid metal cluster acts as an energetically favored site for the absorption of gas-phase reactants. The cluster supersaturates and grows into a one-dimensional wire of the material with the alloy cluster at top the wire (see fig. 3.3); the resulting wire morphology depends on experimental parameters such as temperature, pressure, and the nature of the metal catalyst.

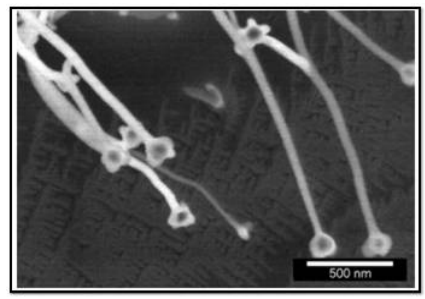

Figure 3.3 - Field emission Scanning Electron Microscopy (FESEM) image of flower-like morphology of nanowires obtained by VLS growth mechanism [29].

Wun et al. [39] study the growth mechanism and the optical properties of self-organized Au_2Si nanosphered pea-podded in a silicon oxide nanowire. These nanocomposites are obtained by thermal annealing of gold/amorphous silicon (Au/a-Si) bilayer at 1030 °C in a nitrogen ambient

atmosphere. Since there are no oxygen source during the growth process, the oxygen in the NWs is originated from the residual oxygen in the furnace and from the ambient after the samples are taken out of the furnace tube. The formation silicon based NWs follows the VLS growth mechanism. figure 3.4 shows a schematic diagram of the Au NPs-silica NWs growth mechanism. At high temperature (1030 °C), an Au/a-Si bilayer forms an silicide alloy owing to the interdiffusion of Au in silicon. Molten gold silicide is formed as droplet, as the the silicide surface energy is lower than both elemental gold and silicon (fig. 3.4 (a)). This alloy composition, at elevated temperature is supersatured with silicon as it abundant in the system. Indeed, nanometer-scale a-Si can be vaporizedabouve 1000°C owing to the effect of lowerin melting point of NPs. This constitutes the vapor-liquid interface. During the cooling stage, silicon can precipitate, leaving Au-Si alloy in the core of the NW (fig. 3.4 (b)).

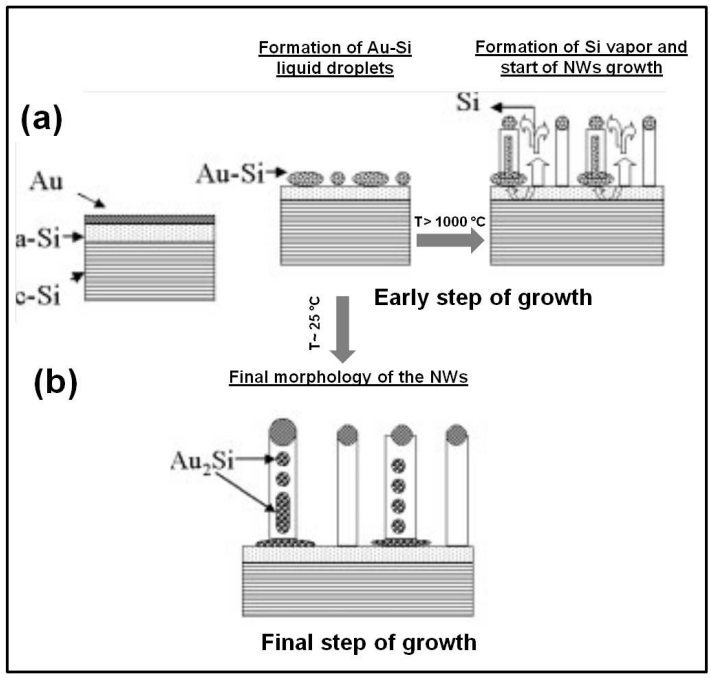

Figure 3.4 - Schematic diagram of (a) the early stage of formation of nanowires that embed Au_2Si nanoparticles and (b) the final stage of the growth and the formation of the nanoparticles in the NW core [39].

Due to its high surface area to volume ratio, the silicon NWs oxidize immediately upon exposure to ambient air. The authors observe that the NWs diameters increases by increasing the gold layer thickness, whereas the NWs length increases by increasing the a-Si layer thickness. This can be explained taking into account that the NWs diameter depends on the Au-Si islands grain size that improves by increasing the starting gold thickness. Indeed, with

increasing gold layer thickness, the nucleation density of Au-Si islands is expected to decrease by increasing the grain size. The increasing length of the NWs is correlated to the abundance of silicon vapor source taking part in the VLS process with the increase in the a-Si layer thickness. The number density of SiOx NWs is a function of the growth time, but by improving the time of the thermal process rare gold silicide nanoparticles are embbeded in the NWs.

3.1.1.b Solid Liquid Solid (SLS) growth mechanism

Yan et al. [42] propose an alternative growth method to obtain Au NPs-silica NWs composite systems. The authors grew amorphous silicon nanowires by heating nickel-coated silicon substrates at high temperature in an argon and hydrogen environment. They postulated that growth occurred through silicon diffusion from the substrate into the metal/silicon melt formed on the surface at high temperature where, with the saturation of silicon, precipitation occurred in the form of wires. Since this process goes from solid-phase silicon to liquid phase and finally to solid nanowire form, it was termed solid liquid-solid (SLS) mechanism of growth.
Paolose et al. [15], instead, report the SLS growth mechanism to synthesize silicon owide nanowires with embedded gold silicide NPs (see fig. 3.5), by using gold as catalyst.

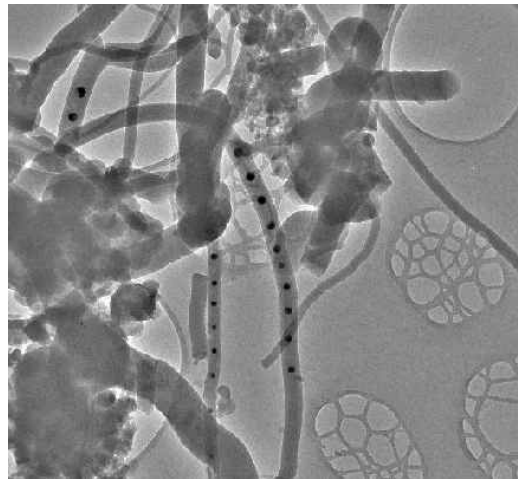

Figure 3.5 - TEM micrograph showing the amorphous silicon oxide nanowires, several of which contain spherical gold silicide nanoparticles. [15].

In both the works reported above, the nanowire growth mechanism can be related to metal-silicon phase diagram. At elevated temperature, diffusion of silicon into gold leads to the formation of pockets of gold silicide nanoparticles at the Au/Si interface. When the temperature reaches 1000 °C, the continued silicon diffusion increases the concentration of silicon in gold, resulting in formation of the liquid alloy phase. This melt takes the form of droplets because of

the surface tension (stage I in fig. 3.6). The continued silicon diffusion takes the droplet supersaturated with Si. At this point, silicon segregation begins (stage II in fig. 3.6). Then, the diffusion of silicon from the wafer to the droplet makes the droplet sink into the wafer, as nanowire growth continues (stage III in fig. 3.6).

As silicon is precipitated in the form of a thin wire, it is immediately oxidized because of the presence of trace amounts of oxygen in the tube at high temperature. The pitting in the silicon wafer surface, upon which the nanowires were grown, are evidence of out-diffusion of silicon from the substrate. The authors noted the inability of the system to form an alloy droplet below 1000 °C, and then the nanowire growth.

The growth mechanism is "root growth," with the alloy droplet remaining on the substrate, allowing more silicon to diffuse into it. This is in contrast to VLS growth, where silicon is collected by the droplet atop the wire from the vapor phase.

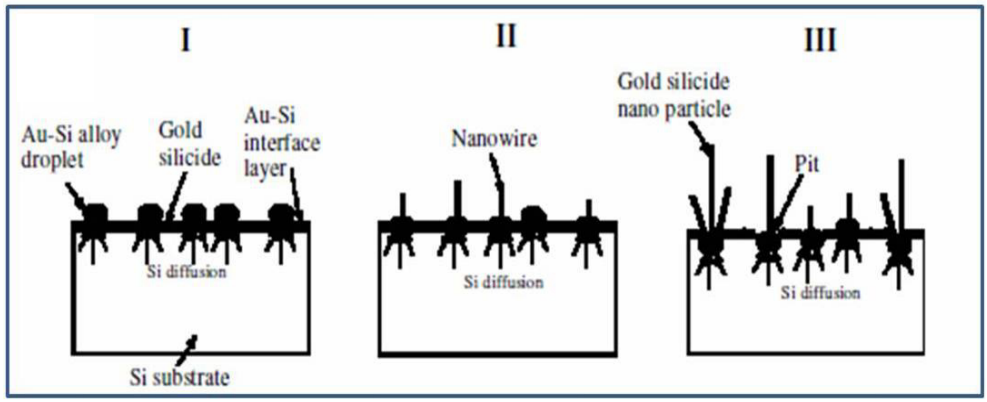

Figure 3.6 - Schematic representation of the corresponding changes on the gold-coated silicon wafer where nanowire growth occurs [15].

3.1.2 Rayleight Instability

The concept of Rayleigh instability originates from the instability of liquid cylinders due to surface tension. A liquid cylinder tends to undulate its free surface with a wavelength (λ), which is larger than the circumference of the cylinder. The driving force for the surface undulation is the decrease of the surface area and thus the total surface energy [43]. Plateau initiated this study over a century ago [44]. Lord Rayleigh continued with theoretical studies on the instability of liquid jets, and explained the regular spacing of the formed drops [45]. Nichols and Mullins extended Rayleigh's perturbation approach to solids [46]. Recently, more effort has been put into this study in both theoretical and experimental fields leading to significant progress [47-50]. Cu and Au nanowires on a SiO_2 substrate were observed to undergo various

configurational changes to finally break up into chains of nanospheres due to Rayleigh instability with gradually increased annealing temperature [51, 52] Besides, Rayleigh instability in polymers confined within nanoporous alumina membranes was studied, which results in the formation of polymer nanorods with periodically encapsulated holes [53]

Corcening Rayleigh instability, the filaments, or liquid metal nanowires, can then split into droplets. It is widely recognised that the mechanism of thin-film dewetting relies on the formation of capillary instabilities [54-56]. Considering a cylindrical NW of radius L, the maximum tension that the wire can sustain before the onset of plastic flow is given by the yield strength, σ_Y. If the surface tension, σ_S, is larger than the yield strength, i.e. $\sigma_S > \sigma_Y$, the NW undergoes plastic flow and if $\lambda > 2\pi L$, it is expected to break up into smaller fragments. Therefore, the liquid cylinders are unstable to small perturbations, which wavelengths $\lambda > 2\pi L$, where L is the radius of the liquid cylinder (fig. 3.7 (a)). As a result, they spontaneously decomposed into a collection of liquid droplets (fig. 3.7 (c)). Figure 3.7 reports a sketch of such a process: it schematically shows a few tiny perturbations in breaking liquid column. The thermal perturbations that are always present at any smooth liquid stream can be resolved into sinusoidal components with different wavelengths and amplitudes. Some components grow with time while others decay with time. A fastest growing wave exists among those that grow with time and the growth rate related to its wavelength and the radius of the original cylindrical stream.

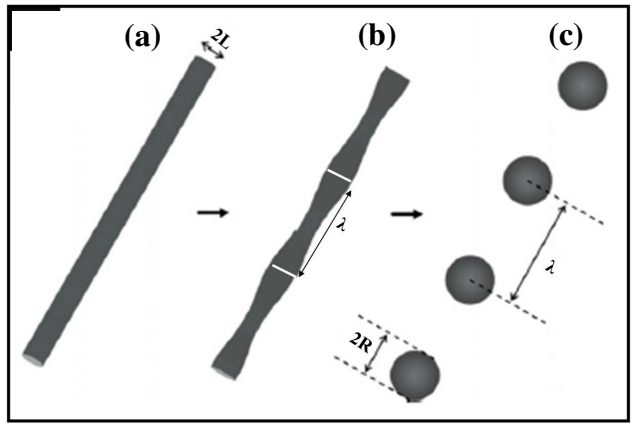

Figure 3.7 - Sketch of the decay of an infinite liquid cylinder into a collection of droplets via Rayleigh instability [57].

As time progresses, the fastest growing wavelength will dominate and eventually determine the size of the final droplets [58]. According to the Rayleigh equation, the particle diameter D is determined by the radius R of the starting wires, namely D = 3.78 R. Rayleigh also predicted that the perturbations with a wavelength $\lambda = 9.016L$ are expected to dominate the above process. Nichols and Mullins [59] studied the stability of solid circular cylinders free of contact

with any substrate. They found results identical to Rayleigh. The solid wires were unstable to perturbations with $\lambda > 2\pi L$ and the wavelength of the dominant perturbations depended on the specific mass-transport mechanism. For surface diffusion, which is expected to dominate in most cases [59]

$$\lambda = 8.89L \tag{3.1}$$

Assuming that the volume between two consecutive minima forms an island (fig. 3.6), the average diameter of the dewetted NPs can be calculated as [54]

$$\langle D \rangle = 2\langle R \rangle = 3.78L \tag{3.2}$$

If λ is interpreted as the mean centre-to-centre distance between the NPs ($\lambda = \langle s \rangle + 2\langle R \rangle$), from (3.1) and (3.2)

$$\frac{\lambda}{\langle R \rangle} = \frac{\langle s \rangle + 2\langle R \rangle}{\langle R \rangle} = 4.7 \tag{3.3}$$

According to the above results, one-dimensional structures with radius L can spontaneously decay because of small variations in their initial radius with $\lambda > 2\pi L$. They will form arrays of NPs with average radius of $\langle R \rangle = 1.89L$ and average spacing of $\lambda = 8.89L$. The annealing promotes atomic diffusion, and perturbations can grow in a reasonable amount of time [27].

3.2 SiO_2 nanowires-Au nanoparticles pea-podded composites: synthesis and structural analyses

On the basis of the considerations reported in the previous subsections, the purpose of the present work is a systematic and quantitative analysis of the structural characteristic of such SiO_2 NWs-Au NPs composites.
In particular, after the growth of SiO_2 nanowires-Au nanoparticles pea-podded composites, using TEM analyses, we proceeded to the quantification of the SiO_2 NWs diameters (D_{NWs}) and Au NPs diameters (d_{NPs}) embedded in them, in order to establish a specific correlation between D_{NWs} and d_{NWs}. A further correlation was established between the diameter of Au NPs embedded in a single NW and their center-to-center distance (s_{NPs}). From the experimental correlations of such parameters, information on the characteristics of the mechanisms governing the formation of the SiO_2 NWs-Au NPs pea-podded structures can be inferred. In particular, our results indicate the likely co-existence of both diffusion and thermodynamic instability phenomena in the determination of the formation process.

3.2.1 Experimental

The samples were prepared using a CZ-<100> Si wafer as a substrate. Some slides (2 cm×2 cm) were cut from the wafer and etched in 10% aqueous HF solution to remove the native oxide. The set of samples were fabricated by depositing 20 nm-thick Au film on the slides. The Au depositions were carried out on several Si slides using an Emitech K550X sputter coater from an Au target source of 99.999% purity. The electrodes were laid at a distance of 40 mm under Ar flow keeping a pressure of 2 Pa in the chamber. The thickness of the deposited Au film was verified by Rutherford back-scattering spectrometry analyses. The samples were then annealed by using a standard Carbolite horizontal furnace (provided by a pre-chamber) in dry N_2 (2.5 liters/minute) at a temperature of 1100°C for 60 minutes. The samples were charged in the pre-chamber, and the system was then evacuated with a turbo pump and subsequently filled with dry N_2. Then, the samples were transferred into the chamber and exposed to heating and cooling ramps with rates of 10 °C/minute between 293 K and 1273 K (or between 1273 and 293 K) and of 5 °C/minute between 1273 and 1373 K (or between 1373 and 1273 K). A first inspection of the sample surface was conducted by SEM analyses. The detailed inspection of the SiO_2 NWs was conducted by TEM analyses. The SEM analyses were performed using a Zeiss FEG-SEM Supra 25 Microscope operating at 5 kV. Concerning TEM analyses, the SiO_2 NWs were mechanically scraped from the Si surface to a standard TEM grid, and the analyses were performed by a 200 keV 2010 JEOL instrument. TEM images were analyzed by using the Gatan Digital Micrograph software. Besides, EFTM analyses were used to study the chemical composition of the pea-podded nanostructures.

3.2.2 Results and discussion

Figure 3.8 shows some representative SEM images of the Si surface after Au deposition and thermal treatment at high temperature for 20 (fig. 3.8 (a)), 60 (fig. 3.8 (b)) and 80 (fig. 3.8 (c)) minutes. As usually recognized [10, 11, 15, 28, 29], the sample surface shows a grass-like array of nanowires which surface density increases with increasing growth time.

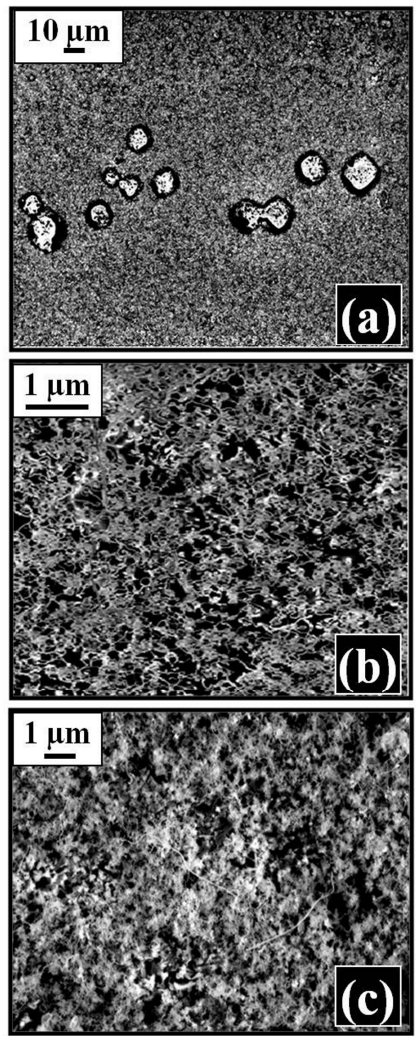

Figure 3.8 - Representative SEM images with different magnification factors of the gold-coated c-Si substrates submitted to the thermal annealing at 1373 K for: (a) 20 minutes; (b) 60 minutes; (c) 80 minutes. The sample surface shows a grass-like array of nanowires which surface density increases with increasing growth time.

The obtained NWs are well-defined, with diameters of about 40-200 nm and lengths up to 20 μm. These results are in agreement with those obtained by Paulose et al. [15] and Elechiguerra et al. [29]. Paulose et al. [15] used a cleaned p-type Si substrate coated with a 50-nm-thick Au. They annealed the samples from 1273 to 1473 K for 0.5, 1, or 3 h in ambient of Ar or N_2 using heating and cooling ramps with rates of 5 K/minute. Their SEM and EDX (Energy Dispersive X-ray spectroscopy) images of the 1373 K-1 h sample revealed a dense mat of entangled SiO_2 NWs (from 30 to 150 nm in diameters and until 1mm in length) covering the entire surface of the substrate. Elechiguerra et al. [29] used cleaned Si wafers to deposit 1:1 Pd/Au 15 nm thick film. These samples were placed at the center of a quartz tube, which was then slowly heated up to 1373 K. Once thermally stabilized, a continuous N_2 flow was allowed to run through the tube for 40 min. The tube was then cooled down to room temperature in about 3 h.

Their SEM analyses revealed the presence of a grass-like array of SiO_2 NWs covering the entire surface of the Si substrate. Concerning the mechanism for the SiO_2 NWs growth, it is recognized that the first step towards the NWs formation is the Au-Si intermixing due to the heating cycle, with consequent formation of silicide at the interface. It is known that the annealing of the Au-Si system above the eutectic temperature induces the formation of Au-Si liquid alloy droplets [15] (eutectic temperature of 363°C at a composition of 19.1 at. % silicon). Instead of a continuous layer, pockets of Au silicide phase commonly appear at the Au-Si interface [15, 29]. There is not an equilibrium Au-silicide phase in the phase diagram of the Au-Si system. However, many reports highlight non-equilibrium Au-silicide phases formed by quenching and subsequent annealing processes. For example, Chang et al. [60] reported that below the eutectic temperature, Au diffuses into Si forming Au-silicide (Au_3Si), while above the eutectic temperature Si diffuses into Au, forming an eutectic Au-Si phase. So, during the heating stage at elevated temperature (<1100 °C), the Si diffusion into Au leads to the formation of Au silicide nanoparticles at the Au-Si interface. When the temperature reaches 1100 °C, the continued diffusion of Si raises the concentration of Si in Au, resulting in the formation of the liquid alloy phase rich in silicon. This melt takes the form of droplets because of surface tension. The persistent Si diffusion takes the droplets to the second liquidus line in the phase diagram. At this point, Si segregation begins. Then, the diffusion of Si from the wafer toward the droplets makes them sinking into the wafer. When the Si is precipitated in the form of a thin wire, it is immediately oxidized because of trace amounts of oxygen present in the tube and high oxidation rate of Si at high temperature. Thus, the growth of SiO_2 NWs from the Si surface starts and continues for all the annealing time (60 minutes in our case). As this process goes from solid-phase silicon to liquid phase and finally to solid nanowire form, it was termed a solid-liquid-solid (SLS) mechanism of growth (see subsection 3.1.1.b). However, several authors observed, a fraction of the so-formed SiO_2 NWs having a pea-pod structure with a string of nano-sized Au beads distributed with nearly regular spacing along their axis [15, 28, 29, 61-64]. The prevalence of such bead strings in the SiO_2 nanowires depends critically upon growth conditions and may vary between about 1% and 80%. Using TEM analyses (fig. 3.9), in

our case we, also, were able to find SiO_2 NWs embedding Au NPs, roughly the 2%-3% of the entire NWs population.

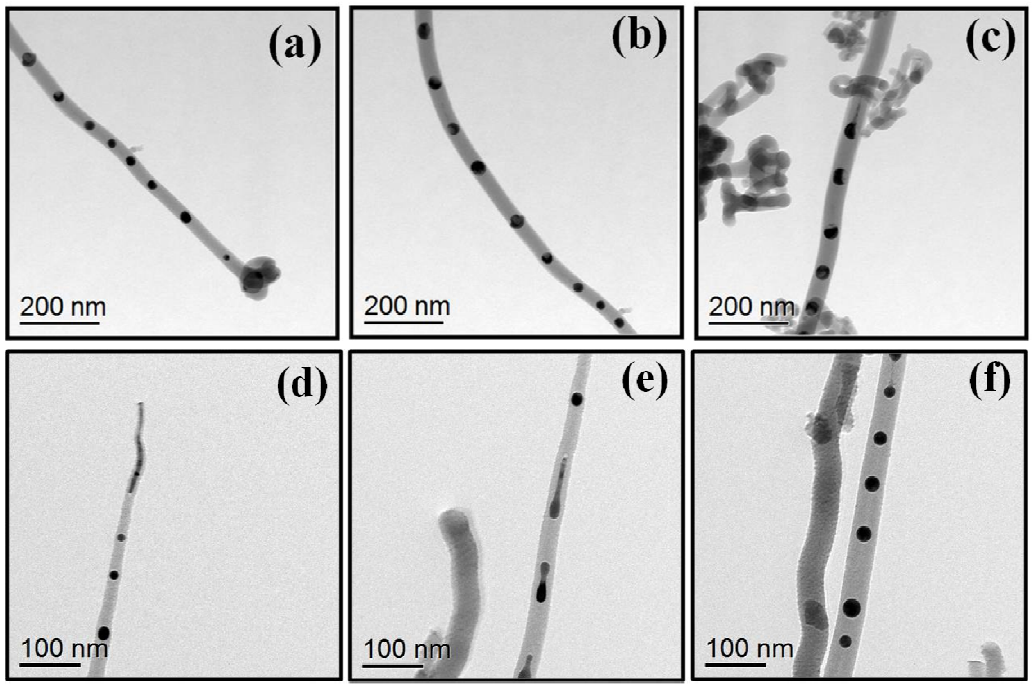

Figure 3.9 - (a)-(f) TEM images of SiO_2 nanowires-Au nanoparticles pea-podded composites. The images highlight a pea-podded stream of non-uniform nano-size particles distributed with non-regular spacing. In particular, figs. 3.8 (d) and (f) provide information about the formation mechanism of the Au NPs from the cylindrical liquid core embedded in the growing NW. In addition, figs. 3.9 (a)-(f) report representative High Resolution-TEM images of some NWs embedding NPs.

The images highlight a pea-podded stream of non-uniform nano-size particles distributed with non-regular spacing. In particular, figs. 3.9 (d) and 3.9 (f) provide information about the formation mechanism of the Au NPs from the cylindrical liquid core embedded in the growing NW.
In addition, figs. 3.10 (a)-(f) report representative High Resolution-TEM images of some NWs embedding NPs.
To verify the chemical nature of the NWs and NPs, figs. 3.110 (b) and 3.11 (c) show the EFTEM images of NW reported in fig. 3.11 (a). The results of the EELS highlight the presence of oxygen (bright regions in fig. 3.10 (b)) and silicon (bright regions in fig. 3.11 (c)) in

the NW matrix. Indeed, this spectroscopy involves measurement of the energy distribution of electrons that have interacted with a specimen and lost energy due to inelastic scattering.

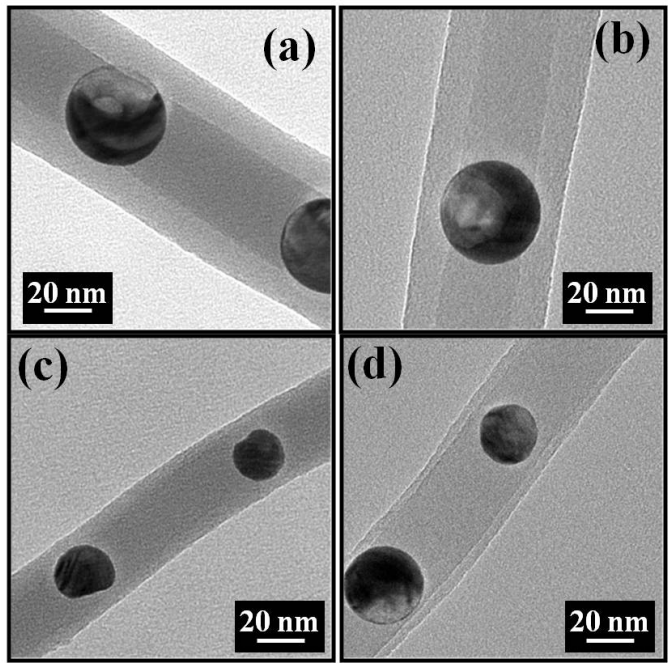

Figure 3.10 - High resolution TEM images of SiO_2 NWs with embedded Au nanoparticles.

The values of the energy reported in figs. 3.11 (a) and 3.11 (b) represents, thus, the characteristic bonding energies related to K inner-shell-electrons of the oxygen (E_{O2}=532 eV) and L_2 inner-shell-electrons of the silicon (E_{Si}=99 eV). Therefore, this analysis suggest the peculiar morphology of this composed structures: an external non stochiometric silicon oxide shell and an internal Si-O-Au liquid core that includes Au NPs.

The favored view [27] for the formation of the Au NPs embedded in the SiO_2 NWs is based on thermodynamic instability phenomena such as the Rayleigh instability [56], in which a cylindrical core of liquid Au is included in the growing Si wire. In the growing NW, this core develops a Rayleigh instability (see subsection 3.1.2), and it is converted to a stream of uniform droplets by the process of minimization of the surface free energy. The separation of nano-beads should be close to that which is expected from this process, namely about two to three times the original core diameter.

However, Fletcher et al. [27] evidenced some weaknesses of this simple model (for example the need for the development of a long uniform cylindrical Au core within the wire). On the basis of theoretical calculations, they instead propose an instability mechanism that is governed by simple diffusion, and that generates isolated beads in an uniform succession as the growth

proceeds. Now, we focus our attention on the SiO_2 NWs embedding Au NPs prepared by us, and proceed to the statistical evaluation of D_{NWs}, d_{NPs} and s_{NPs} in order to establish the experimental correlations between such parameters and infer information about the formation mechanism.

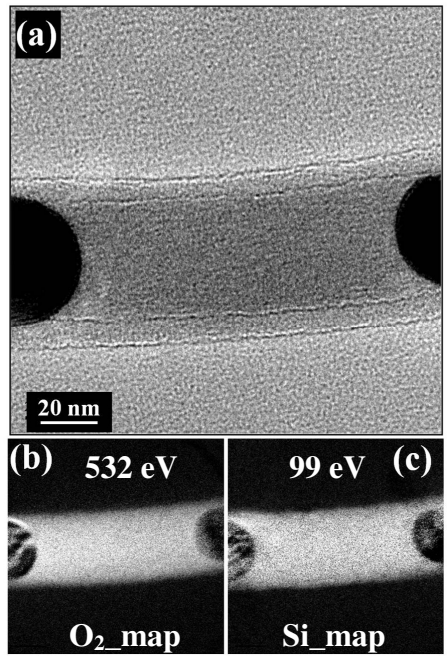

Figure 3.11 – (a) High resolution TEM images of SiO_2 nanowire-Au nanoparticles pea-podded composite; (b)-(c): EFTEM (Energy Filtered Transmission Electron Microscopy) images of NW shown in (a). The images (b) and (c) report the characteristic values of the bonding energy related to K inner-shell-electrons of the oxygen (E_{O2}=532 eV) and L_2 inner-shell-electrons of the silicon (E_{Si}=99 eV).

Figure 3.12 illustrates the evaluation procedure: the mean NW diameter, $\langle D_{NW} \rangle$, was obtained by averaging the different values measured along its axis. Similarly, it was estimated the mean diameter of the nanoparticles embedded in it, $\langle d_{NPs} \rangle$, as well as the average center-to-center between neighboring nanoparticles, $\langle s_{NPs} \rangle$ (by averaging the values measured for several NPs along the NW). This procedure was repeated for several pea-podded NWs, and in order to obtain information about the growth mechanism of such structures, we calculated the following ratios between the structural parameters: $\langle D_{NW} \rangle / \langle d_{NPs} \rangle$ and $\langle D_{NW} \rangle / \langle s_{NPs} \rangle$. For example, concerning the pea-podded NW in fig. 3.12, we obtain $\langle D_{NW} \rangle / \langle d_{NPs} \rangle = 1.6 \pm 0.3$ and $\langle D_{NW} \rangle / \langle s_{NPs} \rangle = 0.6 \pm 0.1$.
Figure 3.13 (a) shows the experimental data correlating $\langle d_{NPs} \rangle$ with $\langle D_{NW} \rangle$: chosen some random pea-podded NWs for each was calculated $\langle D_{NW} \rangle$ and $\langle d_{NPs} \rangle$. Figure 3.13 (a) reports

the calculated $<d_{NPs}>$ as a function of the calculated $<D_{NW}>$ evidencing a linear trend of $<d_{NPs}>$ as a function of $<D_{NW}>$ so that $<d_{NPs}>=(0.6\pm0.1)\ <D_{NW}>$. Such a linear correlation can be understood, according to Wu et al. [61], assuming that the embedded NPs arise from the clustering, due to thermodynamic instability phenomena (such as Rayleigh instability), of an embedded Au liquid wire inside the growing SiO_2 NW.

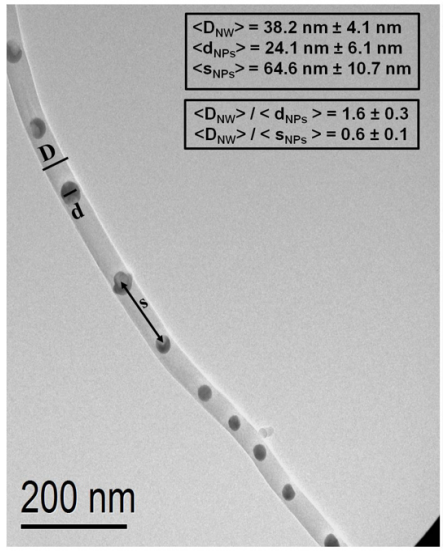

NW length: L_{NWs}	L = 710 nm
NW diameter: D_{NWs}	D_1 = 42.7 nm
	D_2 = 42.6 nm
	D_3 = 42.5 nm
	D_4 = 40.0 nm
	D_5 = 38.5 nm
	D_6 = 35.3 nm
	D_7 = 32.3 nm
	D_8 = 33.5 nm
	D_9 = 31.2 nm
	D_{10} = 39.5 nm
Number of NPs	N=10
NPs diameter: d_{NPs}	d_1 = 31.3 nm
	d_2 = 27.7 nm
	d_3 = 32.3 nm
	d_4= 30.7 nm
	d_5 = 23.0 nm
	d_6 = 20.9 nm
	d_7 = 16.8 nm
	d_8 = 18.7 nm
	d_9 = 16.5 nm
	d_{10} = 24.5 nm
NPs inter gap size: s	$S_{1,2}$ =50.4nm
	$S_{2,3}$ =60.7 nm
	$S_{3,4}$ = 81.5 nm
	$S_{5,6}$ = 76. 2 nm
	$S_{6,7}$ = 58.8 nm
	$S_{7,8}$ = 57.1 nm
	$S_{8,9}$ = 60.2 nm
	$S_{9,10}$ = 72.4 nm

Figure 3.12 - TEM image and evaluation procedure of the NW structural parameters: the average diameter of NW ($<D_{NW}>$); the average diameter of nanoparticles ($<d_{NPs}>$); the average spacing between neighboring nanoparticles ($<s_{NPs}>$). In figure are also reported the following ratios between the structural parameters: $<D_{NW}>/<d_{NPs}>$ and $<D_{NW}>/<s_{NPs}>$.

Increasing the NW diameter D_{NW}, increases, also, the diameter of the embedded Au wire and so, also, the diameter of the NPs originating from the clustering of the wire. The experimental data (dots, while the continuous red line is only a guide for the eyes) in fig. 3.13 (b) show the plot of $<s_{NPs}>$ as a function of $<d_{NPs}>$. Also in this case, chosen some random pea-podded NWs for each of them, the mean diameter $<d_{NPs}>$ and mean surface-to-surface distance $<s_{NPs}>$ were calculated for the embedded NPs. From this plot, we can distinguish two different growth regions for the NPs. To the first regions belong values of $<d_{NPs}>$ up to 25 nm. In this region, the center-to-center distance between NPs ($<s_{NPs}>$) increases by increasing $<d_{NPs}>$. In this region, the distance between the surface of the neighboring nanoparticles, $<L>=<s_{NPs}>-<d_{NPs}>$, is lower than the Au diffusion length in SiO_2 at 1100°C. In fact, according to Collins et al. [65] and Ruffino et al. [66] the temperature-dependent diffusion coefficient for Au atoms in SiO_2 matrix can be expressed by $D(T)=D_0[\exp(-E_A/kT)]$ being $D_0\approx5\times10^{-7}$ cm^2/s and $E_A\approx2.15$ eV/atom (k the Boltzmann constant and T the absolute temperature).

So, for the 60 minutes annealing at 1100 °C, the Au atoms length diffusion inside the SiO_2 NWs should be about L_{diff} =60 nm. So, if the growth of the embedded Au NPs is limited by a diffusion-limited ripening, the Au NPs can increase their mean diameter until their mean surface-to-surface distance L does not exceed 60 nm, i. e. in our case $\langle s_{NPs} \rangle = \langle L \rangle + \langle d_{NPs} \rangle$ does not exceed about 75 nm, consistently with the data in fig. 3.13 (b).

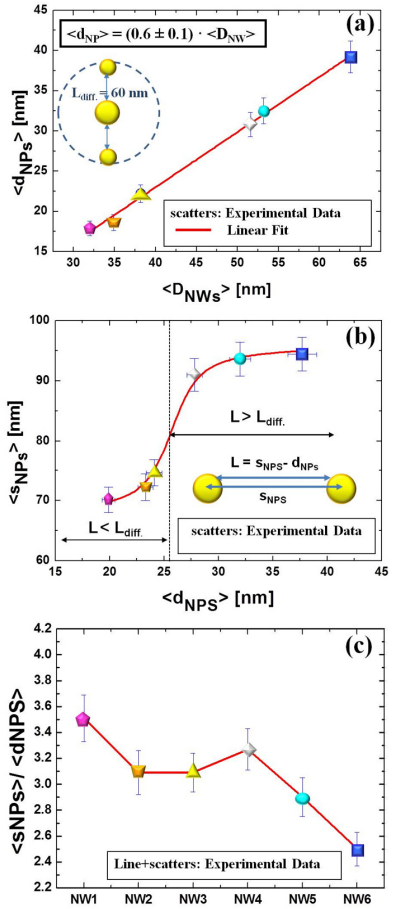

Figure 3.13 - (a) Linear trend of $\langle d_{NPs} \rangle$ as a function of $\langle D_{NW} \rangle$ so that $\langle d_{NPs} \rangle = (0.6 \pm 0.1) \langle D_{NW} \rangle$. The size of Au-Si nanoparticles increases by increasing the diameter of the nanowire that embeds the unstable liquid core. The inset shows the NPs intervals equal to the diffusion length of Au in SiO_2 (60nm); (b) the trend of $\langle s_{NPs} \rangle$ in function of $\langle d_{NPs} \rangle$. It is possible to subdivide the chart into two regions: for $L < L_{diff.}$ ($\langle d_{NPs} \rangle$ up to 25 nm) the distance between NPs ($\langle s_{NPs} \rangle$) increases by increasing $\langle d_{NPs} \rangle$ and the trend of experimental data is shown by the red line. For values of $\langle d_{NPs} \rangle$ above 25 nm, the average spacing between NPs is saturated. The inset explains the difference between the parameters L and s_{NPs}; (c) value of the ratio $\langle s_{NPs} \rangle / \langle d_{NPs} \rangle$ calculated for six different NWs. In contrast with the specific constant value (i.e $\langle s_{NPs} \rangle / \langle d_{NPs} \rangle = 2.47$) prescribed from the Rayleigh instability model, our experimental data show values ranging between about 2.4 and 3.5.

Furthermore, in the second region, corresponding to values of $<d_{NPs}>$ above 25 nm, the average spacing between NPs is saturated. It is, yet, consistent with a diffusion-limited ripening growth of the Au NPs. In this llkkregion, indeed, the mean surface-to-surface distance between neighboring NPs L is higher than the Au length diffusion L_{diff}, so that the NPs no longer can increase their mean diameter and mean spacing.

Finally, fig. 3.13 (c) shows the values of the ratio $<s_{NPs}>/<d_{NPs}>$ calculated for six different NWs. If the NPs formation is purely due to a Rayleigh instability phenomenon of an embedded Au wire, the standard theory model prescribes a specific constant value of 2.47 for such a ratio [56, 67, 68]. In contrast, our experimental data in figure 3.11(c) show values changing on the base of the chosen NWs and values ranging between about 2.4 and 3.5. This evidence suggests that the formation and growth of the embedded NPs is, probably, not exclusively due to the Rayleigh instability process but may be induced by the coexistence of instability processes and transport phenomena, such as the diffusion-limited ripening invoked in the discussion of the data in fig. 3.12(b).

So, on the basis of the experimental data in fig. 3.13, we propose the following phenomenological model for the formation and time evolution of the SiO_2 NWs/Au NPs pea-podded structures, based on the coexistence of instability and diffusion processes**:** in the first step of the growth process (fig. 3.14 (a)), the liquid Au core develops a thermodynamic instability such as a Rayleigh instability. The driving force for the surface undulation of the core is the decrease of the surface area and thus the total surface energy. Therefore, such type of instability converts the Au liquid core into regular succession of isolated Au NPs with non-uniform size. Indeed, the diameter of nanoparticles (d_{NPs}) depends on the liquid core diameter (D_{core}) whose values vary with varying the diameter of the nanowire (D_{NW}). In the second growth stage (fig. 3.14 (b)), the diffusion-limited ripening drives the Au NPs evolution (fig. 3.14 (b)) when the surface-to-surface distance between NPs is smaller than the Au diffusion length in SiO_2 ($L_{diff.}$) at the used annealing temperature and time. According to the ripening mechanism, NPs with a diameter smaller than a critical one dissolve in the constituent atoms which diffuse through the SiO_2 to be incorporated by the neighboring NPs with diameter larger than the critical one. This process reduces the linear density of the embedded Au NPs, but increases their mean size and mean spacing. When the surface-to-surface distance becomes greater than 60 nm (which is the Au diffusion length in SiO_2 in our experimental conditions), a further increase in the Au NPs size does not occur. At the end of the diffusion process, the NWs exhibit a resulting pea-podded stream of non-uniform nano-size particles distributed with non-regular spacing (s_{NPs}), as shown in figure 3.11. Therefore, the formation and evolution of Au NPs embedded in the SiO_2 NWs may be a consequence of the coexistence of instability and diffusion processes**.**

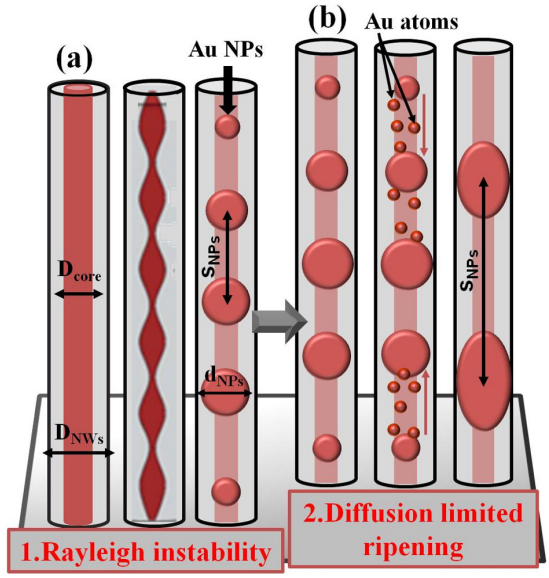

Figure 3.14 - Scheme for the growth model: (a) in the first step of the growth process, the liquid core develops the Rayleigh instability that induces the formation of Au NPs in order to minimize the surface energy. The diameter of pea-podded NPs depend on the liquid core diameter; (b) in the second growth stage, the ripening mechanism dissolves the small particles and re-deposits the Au atoms on the surface of larger nanoparticles. At the end of the diffusion process, the NWs exhibit a resulting pea-podded stream of non-uniform nano-size particles distributed with non-regular spacing (s_{NPs}).

3.3 Range of applications

As mentioned in subsection 3.1, SiO_2 NW-Au NPs composite systems are gaining a great scientific and technological interest due to their potential applications, for example in electronic devices, biosensors, nanoscale optical devices and sensors. In particular, we are interested to use these pea-podded structures as light waveguides or biosensors in line with the results reported by Wang et al. [38]. The authors report SP resonance enhanced molecular oxygen sensing by single Au NPs-SiOx NW under 532-nm illumination (visible light) at room temperature. Besides, excellent selectivity of Au NPs-SiOx NWs to molecular oxygen in air has been demonstrated. As reported in Chapter 1, this work reports the current-voltage (I-V) charactersistics, measured at room temperature in vacuum.

As shown in figure 3.15 (c), the I–V plots of both NWs are linear, indicating the ohmic nature of the e-beam defined contacts. The slope of the I–V plot indicates that the electrical conductivity of the Au NPs-silica NW is higher than that of the bare silica NW. This trend occurs for the creation of more electron-hopping sites in the Au-NPs-silica NW leads to

enhanced conductivity [37]. During the growth of Au NP-peapodded silica NWs, residual Au atoms may partially incorporate into the silica matrix of the wire during the peapod formation [24]. The incorporation of Au may produce impurities and/or defect-related hopping sites in the silica matrix [37].

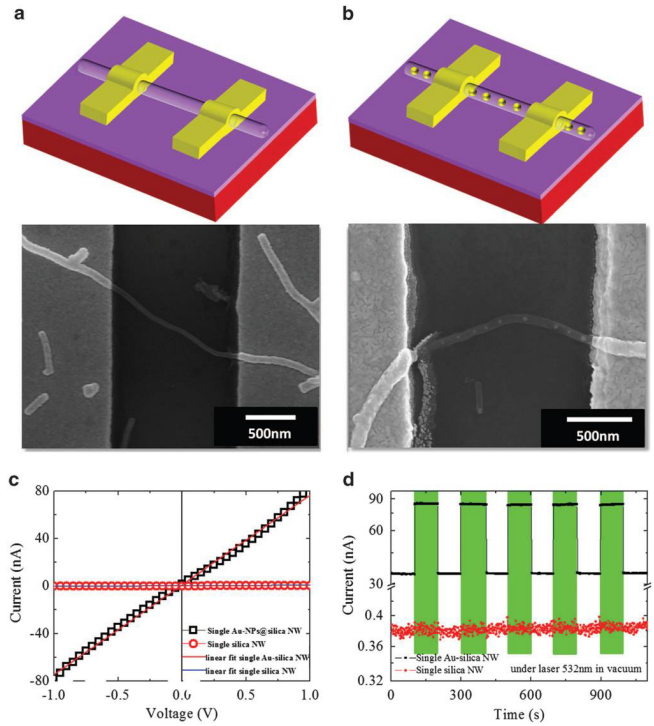

Figure 3.15 - Field-emission scanning electron microscopy images of single NW devices consisting of (a) plain silica NW (without the Au NPs) and (b) Au-NPs@silica NW. (c) Dark I–V characteristics of single NW devices, with and without Au NP peapods, measured in vacuum, and the corresponding linear fit to the data set. (d) Dark and photocurrent measured under vacuum in single NW devices, with and without Au NP peapods, as a function of time. The color bars indicate the duration of the 532-nm illumination. The measurement was performed with a 1-V applied bias at room temperature. The bare silica NW showed no photoresponse, whereas the Au-NP@Silica NW showed strong photoresponse [38].

The Au-embedded silica NW has higher conductivity than the plain silica NW, because of its shorter hopping length. Photoresponse measurements of the NW devices, conducted under alternating 532 nm illumination and dark conditions, is shown in figure 3.15 (d).
The plain silica NW device does not show any significant photoresponse; the ratio of photo and dark current is ~ 0.01. In contrast, the Au NPs-silica NW device presents a reversible

photoresponse and a stable photocurrent, with a photo/dark current ratio of ~1.48. Assuming the band gap of silica NWs to be in the range of ~6.8 eV [69], and denying any absorption of the 532 nm light, these data suggest that the photocurrent can be attributed to the near-resonance SP absorption of the Au NPs (within the silica NWs) that has been reported at ~532nm [37].
Taking into account these optoelectronic properties, such complex systemscan be used as light waveguide. Indeed, the resonant coupling between the incident light and the plasmonic resonances of Au NPs can induce an enhancement of the output signal.
Besides, Au NPs with interparticles size of about ten nanometers allow the coupling between localized plasmon normal modes such that the enhancement, resulting from dipole-dipole interaction, is concentrated in very small regions close to the NPs. This effect induces the near-field enhancement of the electromagnetic field (see FDTD simulation in fig. 3.16).

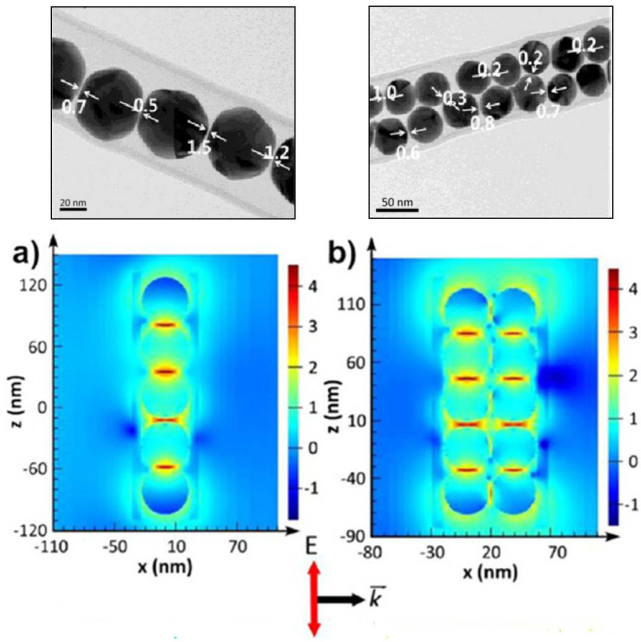

Figure 3.16 - TEM images and Finite dimension time domain (FDTD) calculations of (a) single-line linear, (b) double-line linear of Au Nps encapsulated in silica nanopeapods [70].

Indeed, Cong et al. [70] show high enhancement factors (EF) related to SERS spectra of p-MBA-coated AuNPs embedded in silica nanopeapods.
The experimental results suggest that the intensity of the EF depend on the structural parameters of the Au NPs chain encapsulated in the silica nanopeapod.
Taking into account these results, the purpose of the synthesis and characterization of our complex systems is the optimization of the structural parameters, during the synthesis growth, in order to modulate their optoelectronic properties. The optimization of dimension and the density of the Au NPs and the inter-particles size is required for the application of SiO_2

Nanowires-Au Nanoparticles pea-podded composites, as highly SERS-active substrates or biosensors.

3.4 Conclusions

Our results have shown that SiO_2 nanowires-Au NPS pea-podded composites can be grown on a crystalline Si substrate by first depositing a thin metal film (Au, for example) on its surface and then heating the system to elevated temperatures (>1100°C 60 min.) in an inert ambient (e.g. N_2 or Ar) containing trace amounts (3–5 ppm) of oxygen. The sample surface, after 60 minutes thermal annealing, is entirely covered by a grass-like array of nanowires. The NWs are well-defined with diameters of about 40-200 nm and lengths up to 20 μm.
Using TEM analyses, we were able to find SiO_2 NWs embedding Au NPs, roughly the 2%-3% of the entire NWs population. The results of EFTEM analyses highlighted the presence of oxygen and silicon in the NWs matrix and suggested the peculiar morphology of this composed structures: an external non stochiometric silicon oxide shell and an internal Si-O-Au liquid core that includes Au NP_S. The statistical evaluation of the structural characteristics (D_{NWs}, d_{NPs} and s_{NPs}) was developed in order to establish the experimental correlations between parameters and infer information about the formation mechanism.
The quantitative analyses of SiO_2 NWs embedding Au NPS suggested that: *i*) the size of Au-Si nanoparticles increases by increasing the diameter of the nanowire that embeds the unstable liquid core; *ii*) the distance between NPs ($<s_{NPs}>$) increases by increasing the nanoparticles diameter ($<d_{NPs}>$), when the distance between the surface of the neighboring nanoparticles is lower than the Au diffusion length in SiO_2 (for values of $<d_{NPs}>$ up to 25 nm); *iii*) the spacing between nanoparticles becomes constant for values of $<d_{NPs}>$ above 25 nm. In this range, the aggregation mechanism is limited by NPs intervals higher than the Au diffusion length; *iv*) The value of the ratio $<s_{NPs}>/<d_{NPs}>$ (different from the one established by Reyleigh criterion, i.e. $<s_{NPs}>/<d_{NPs}> = 2.47$) suggested that the formation of pea-podded Au NPs is not exclusively due to the Reyleigh instability, but may be induced by the co-existence of transport and instability processes.
We reported the scheme of growth model to explain how these mechanisms (instability+ transport) induce the evolution of resulting composite structures.

References

[1] Banan, Sadeghian R. & Islam M. S. - Nat. Mater. 10, 135–140 (2011)

[2] Wang S. B., Hsiao C. H., Chang S. J., Lam K. T., Wen K. H., Young S. J., Hung S. C. & Huang B. R. - IEEE Sens. J. 12, 1884 (2012)

[3] Chen R. S., Wang S. W., Lan Z. H., Tsai J. T. H., Wu C. T., Chen L. C., Chen K. H., Huang Y. S., & Chen C.C. - Small 4, 925–929 (2008).

[4] Liu S. & Guo X. - NPG Asia Mater. 4, 1–10 (2012).

[5] Jana D., Chen L. C., Chun-Wei C., Chattopadhyay S. & Chen K. H. - Carbon NY 45, 1482–1491 (2007).

[6] Lin Y. G., Hsu Y. K., Chen S. Y., Chen L. C. & Chen K. H. - J. Mater. Chem. 21, 324–326 (2011).

[7] Burda C., Chen X., Narayanan R. & El-Sayed M. A. - Chem. Rev**.** 105, 1025–1102 (2005).

[8] Wang S. B., Huang Y. F., Chattopadhyay S., Chang S. J., Chen R. S., Chong C. W., Hu M. S., Chen L. C. and Chen K. H. - NPG Asia Materials 5, e49(2013)

[9] Bilalbegović G. - J. Phys.: Condens. Matter. 18 3829-3836 (2006)

[10] Elliman R. G., Wilkinson A. R., Kim T. H., Sekhar P. K., Bhansali S. - J. Appl. Phys. 103 104304 (2008)

[11] Elliman R. G., Wilkinson A. R., Kim T. H., Sekhar P. K., Bhansali S. - Meth. Phys. Res**.** B 266 1362-1366 (2008)

[12] Kang M., Trofin L., Mota M. O., Martin C. R. - Anal. Chem. 77 6243-6249 (2005)

[13] Kohli P., Martin C. R. - Curr. Pharm. Biotech. 6 35-47 (2005)

[14] Sekhar P., Ramgir N. S., Bhansali S. - J. Phys. Chem. C 112 1729- 1734 (2008)

[15] Paulose M., Varghese O. K., and Grimes C. A. **-** J. Nanosci. Nanotech. 3, 341–346 (2003)

[16] Yu D. P., Hang Q. L., Ding Y., Zhang H. Z., Bai Z. G., Wang J. J., Zou Y. H., Qian W., Xiong G. C., and Feng S. Q. - Appl. Phys. Lett. 73, 3076 (1998)

[17] Morales A. M. and Lieber C. M. - Science 279, 208 (1998)

[18] Wang N., Zhang Y. F., Tang Y. H., Lee C. S., and Lee S. T., Appl.Phys. Lett**.** 73, 3902 (1998)

[19] Westwater J., Gosain D. P., Tomiya S., Usui S., and Ruda H., J. Vac.Sci. Technol*., B* 15, 554 (1997)

[20] Hwang N. M., Cheong W. S., Yoon D. Y., and Kim D.Y., J. Cryst. Growth 218, 33 (2000).

[21] Yu D. P., Bai Z. G., Ding Y., Hang Q. L., Zhang H. Z., Wang J. J., Zou Y. H., Qian W., Xiong G. C., Zhou H. T., and Feng S. Q., Appl. Phys. Lett. 72, 3458 (1998).

[22] Pan Z. W., Dai Z. R., Xu L., Lee S. T., and Wang Z. L. - J. Phys. Chem. B105 (13), pp 2507–2514 (2001)

[23] Jin S., Li Q., and Lee C. S., Phys. Stat. Sol. A 188, R1-R2 (2001)

[24] Hu M. S., Chen H. L., Shen C. H., Hong L. S., Huang B. R., Chen K. H. AND Chen L. C. - Nat. Mat. Vol. 5 (2006)

[25] Hache F., Ricard D. & Flytzanis C. - J. Opt. Soc. Am. B 3**,** 1647–1655 (1986).

[26] Haglund R. F. *et al*. - Opt.Lett. 18**,** 373–375 (1993).

[27] Fletcher N. H., Elliman R. G. and Kim H. – Nanotech. 20 085613 (5pp) (2009)
[28] Hu J. Q., Jiang Y., Meng X. M., Lee C. S., Lee S. T. - Chem. Phys. Lett. 367 339-343 (2003)
[29] Elechiguerra J. L., Manriquez J. A., Yacaman M. J. - Appl. Phys. A 79 461-467(2004)
[30] Sekhar P. K., Sambandam S. N., Sood D. K., Bhansali S. - Nanotech. 17 4606-4613 (2006)
[31] Wang C. Y., Chan L. H., Xiau D. Q., Lin T. C., Shih H. C. - J. Vac. Sci. Technol. B 24 613-617 (2006)
[32] Kim J. H., An H. H., Woo H. J., Yoon C. S. - Nanotech. 19 125604 (2008)
[33] Bettge M. , MacLaren S., Burdin S., Wen J. G., Abraham D. , Petrov I., Sammann E., Nanotech. 20 115607 (2009)
[34] Ruffino F., Romano L., Pitruzzello G., Grimaldi M. G. - Appl. Phys. Lett. 100 053102 (2012)
[35] Ruffino F., Grimaldi M. G. - J. Nanopart. Res. 15 1909 (2013)
[36] Hu M. S., Chen H. L., Shen C. H. , Hong L. S., Huang B. R., Chen K. H., Chen L. C. - Nat. Mater. 5 102-106 (2006)
[37] Wang S. B., Hu M. S., Chang S. J., Chong C. W., Han H. C., Huang B. R., Chen L. C., Chen K. H. - Nanoscale 4 3660-3664(2012)
[38] Wang S. B., Huang Y. F., Chattopadhyay S., Chang S. J., Chen R. S., Chong C. W., Hu M. S., Chen L. C., Chen K. H. - NPG Asia Materials 5 (2013)
[39] Wu J. S., Dhara S., Wu C. T., Chen K. H., Chen Y. F., Chen L. C. -, Adv. Mater. 14 1847-1850 (2002)
[40] Zhang Y. F., Tang Y. H., Wang N., Yu D. P., Lee C. S., Bello I., and Lee S. T. - Appl. Phys. Lett. 72, 1835 (1998)
[41] Wagner R. S. and Ellis W. C. - Appl. Phys. Lett. 4, 89 (1964).
[42] Yan H. F., Xing Y. J., Hang Q. L., Yu D. P. , Wang Y. P., Xu J., Xi Z. H., and Feng S. Q., Chem. Phys. Lett. 323, 224 (2000)
[43] Qin Y., Lee S. M., Pan A., Go1sele U., and Knez M. - Nano Lett., Vol. 8, No. 1, 115 (2008)
[44] Plateau J. - Transl. Annual Reports of the Smithsonian Institution p. 1863 (1873)
[45] Rayleigh L. - Proc. London Math. Soc. 10, 4 (1878)
[46] Nichols F. A., Mullins W. W. - Trans. Metall. Soc. AIME *233*, 1840 (1965)
[47] De Gennes P. G., Brochard-Wyart F., Quere D. - Capillarity and Wetting Phenomena - Springer: New York, (2004)
[48] Lian J., Wang L., Sun X., Yu, Q., Ewing R. C. - Nano Lett. 6, 1047 (2006)
[49] Park J., Suh K. Y., Seo S., Lee H. H. - J. Chem. Phys. 124, Art. No. 214710 (2006)
[50] Kolb F. M., Hofmeister H., Zacharias M., Gosele U. - Appl. Phys. A 80, 1405-1408 (2005)
[51] Toimil-Molares M. E., Balogh A. G., Cornelius T. W., Neumann R., Trautmann C. - Appl. Phys. Lett. *85*, 5337 (2004)
[52] Karim S., Toimil-Molares M. E., Balogh A. G., Ensinger W., Cornelius T. W., Khan E. U., Neumann R. - Nanotech. 17, 5954 (2006)

[53] Chen J. T., Zhang M. F., Russell T. P. - Nano Lett. 7, 183 (2007)
[54] Frantzeskakis E.: Analysis of the potential applications for the template dewetting of metal thin films', Dipl. Eng. Mining Engineering and Metallurgy, National Technical University of Athens (2003). Available at http://www.dspace.mit.edu/handle/1721.1/33625
[55] Wu Y.: 'Nanoscale metal thin film dewetting via nanosecond laser melting: understanding instabilities and materials transport in patterned thin films'. PhD Dissertation, University of Tennessee (2011). Available at http://www.trace.tennessee.edu/utk_graddiss/1240
[56] Rayleigh L.:, Proc. London Math. Soc., 10, pp. 4–13 (1879)
[57] Rauber M., Muench F., Toimil-Molares M. E. and Ensinger W. – Nanotech. 23 475710 (2012)
[58] Ruffino F., Carria E., Kimiagar S., Crupi I., Grimaldi M. G. - Micro & Nano Letters Vol. 8, Iss. 3, pp. 127–130 (2013)
[59] Nichols F.A., Mullins W.W. - Trans. Metall. Soc. AIME 233, p. 1840 (1965)
[60] Chang P. H., Berman G., Shen C. C. - J. Appl. Phys. 63 1473 (1988)
[61] Wu J. S., Dhara S., Wu C. T., Chen K. H., Chen Y. F., Chen L. C. - Adv. Mater. 14 1847-1850 (2002)
[62] Hu M. S., Chen H. L., Shen C. H., Hong L. S., Huang B. R., Chen K. H., Chen L. C. - Nat. Mater. 5 102-106 (2006)
[63] Wang S. B., Hu M. S., Chang S. J., Chong C. W., Han H. C., Huang B. R., Chen L. C., Chen K. H. - Nanoscale 4 3660-3664 (2012)
[64] Wang S. B., Huang Y. F., Chattopadhyay S., Chang S. J., Chen R. S., Chong C. W., Hu M. S., Chen L. C., Chen K. H. - NPG Asia Materials 5 e49 (2013)
[65] Collins D.R., Schroder D.K., Sah C.T. -, Appl. Phys. Lett. 8 323(1966)
[66] Ruffino F., Grimaldi M. G., Bongiorno C., Giannazzo F., Roccaforte F., Raineri V. - Superlattices and Microstructures 44 588 (2008)
[67] Nichols F. A., Mullins W. W. - Trans. Metall. Soc. AIME 233 1840 (1965)
[68] Xu J., Zhu Y., Zhu J., Jiang W. - Nanoscale 5 6344 (2013)
[69] Pao C. -W., Wu C. -T., Tsai H. -M., Liu Y.- S., Chang C. -L., Pong W. F., Chiou J. -W., Chen C. -W., Hu M. -S., Chu M. -W., Chen L. -C., Chen C. -H., Chen K. -H., Wang S. -B., Chang S. -J., Tsai M. -H., Lin H. -J., Lee J. -F. and Guo J. -H. - Phys. Rev. B 84, 165412 (2011).
[70] Cong V. T., Ganbold E. O., Saha J. K., Jang J., Min J., Choo J., Kim S., Song N. W., Son S. J., Lee S. B., and Joo S. W. – J. Am. Chem. Soc. 136, 3833-3847 (2014)

Chapter 4

Nanoscale structuration, optical and electrical properties of thin gold films on textured FTO substrates for photovoltaic applications

4.1 Electronic device for solar energy conversion

At present, the research in the photovoltaic (PV) devices field is mainly focused on the design and fabrication of electronic devices efficient in creating and separating photogenerated charge carriers before they recombine. This requires a strong built-in electric field within the electronic device. Therefore, a PV device is constituted by one or more interfaces created by using proper semiconductors and two electrical contacts to extract charge carriers from the device. The most basic interface, used in a PV device, is the p-n junction formed within one semiconductor material having p-type and n-type electrical conduction in two adjacent regions. These types of junctions are generally known as homo-junctions. When photons with energy (h_f) greater than the bandgap of the semiconductor ($h_f \geq E_g$) reach the depletion region, they are absorbed and the bonds between the atoms are broken to create free e-h pairs. The internal electric field separates these photo-generated charge carriers and forces them in opposite directions, towards the two electrical contacts on both sides of the junction. If the built-in electric field is weak, the photo-generated charge carriers will recombine again and the photo-current will be low. Therefore, the key to improve the PV efficiency is to optimize the device depletion region by using a semiconductor with high optical absorption properties and low recombination centers. One improvement, generally used in the fabrication of PV device, is the incorporation, in the overall device, of a p-i-n semiconductor junction whose structure is reported in the following subsection.

4.1.1 p-i-n junction

The production of a wide depletion region depends on the doping concentration of the two semiconductor regions used to fabricate the junction. Low doping concentrations produce a wide depletion region, and heavy doping concentrations create a thin depletion layer, which are not helpful for PV conversion. A method used to obtain the best device performance is the optimization of the doping concentration to create a depletion region width comparable to the thickness of a thin film solar cell (typically in the order of 2 μm). At this purpose, p-i-n interfaces are introduced in the PV devices. Figure 4.1 shows the energy band diagram of a p-i-n device containing an intrinsic semiconductor (i.e. i-layer) between p and n-type semiconductor contacts (S/C) [1]. The p-type and n-type regions are typically heavily doped because they are used for ohmic contacts. A such structure induces the alignment of the the Fermi levels (related to the two semiconductors) through the intrinsic layer to create a strong internal electric field throughout the i-layer and then control the width of the depletion region. This method is also used to form a potential barrier comparable to the bandgap of the semiconductor ($E_g \approx \varphi_B$). Therefore, the advantage of using a p-i-n structure over conventional semiconductor junction is the better long wavelength response. In case of long wavelength irradiation, photons penetrate deep into the cell, but only the electron-hole pairs generated near the depletion region contribute to current generation. The wider depletion region of the p-i-n

structure enables electron-hole pair generation deep within the device and this increases the quantum efficiency of the cell [1].

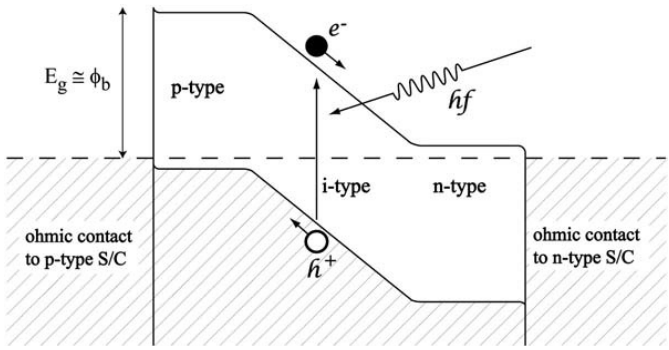

Figure 4.1 - The energy band diagram of a p-i-n diode and themechanisms of PV activity within the device [1].

4.1.2 Metal/Semiconductor (Schottky) contacts

As reported above, a solar device requires one or more interfaces (creating its depletion region and hence the built-in electric field) and two electrical contacts on either side to collect the photo-generated charge carriers and transport them through an external circuit. These electrical contacts are usually formed using metal/semiconductor (MS), or Schottky, contacts. The front electrical contact should either take the form of a grid contact to minimise the effect of shading or be transparent to incoming light. The ohmic or rectifying properties of MS interface depend on the design of the solar cell device. Figure 4.2 presents the energy band diagram of a metal/n-type semiconductor interface.

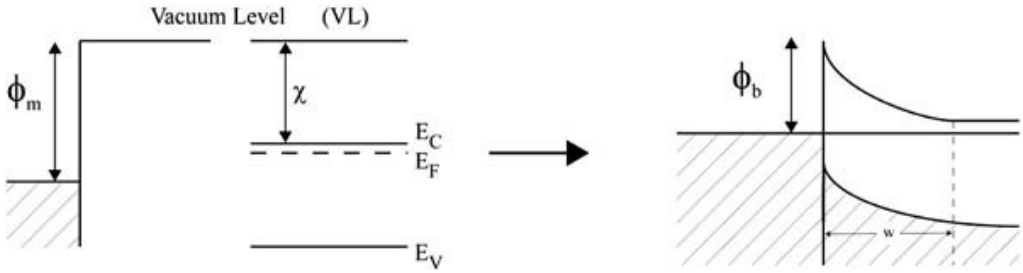

Figure 4.2 - Schottky barrier formation at a metal/n-type semiconductor when an ideal interface is formed between the two materials [1].

When a metal having a work function φ_m is placed in contact with a n-type semiconductor, having an electron affinity χ, a potential barrier height (φ_B) is formed at the interface. If there are no surface states or other defects arising from the material, the φ_B formed at the interface is given by [1]:

$$\varphi_B = \varphi_m - \chi \tag{4.1}$$

The formation of potential barriers at the metal/p-type semiconductor is very similar, but the band bending will be in the opposite direction, forming potential barriers for the flow of holes. The above description is valid only for ideal interfaces, but the situation is very different for interfaces affected by semiconductor defects, surface or interface states. In these situations, the Fermi level will be pinned by the defect states, and hence φ_B is independent of the metal used for the formation of the electrical contact. The nature of the potential barrier at the MS interface will govern the electrical properties of this interface. If the φ_B is more than ~ 0.40 eV, the interface will have rectifying electrical properties described by Eq. 4.2 [2,3]:

$$I_D = SA^*T^2 \cdot \exp\left(\frac{-e\varphi_B}{kT}\right) \cdot \left[\exp\left(\frac{eV}{nkT}\right) - 1\right] \tag{4.2}$$

where I_D is the current in dark condition, V the applied potential, S is the contact area, A* is the Richardson costant for thermoionic emission, T is the absolute temperature, e is the electron charge, φ_B is the potential barrier height, k is the Boltzmann costant and n the ideality factor of the diode.

These types of potential barriers are formed when the semiconductor has moderate doping concentration (~10^{15}–10^{17} cm^{-3}). When the φ_B is less than ~ 0.40 eV or the depletion region is thin, the electrical conduction through the interface will exhibit linear (ohmic) behaviour due to the ease of electron transfer in both directions. Heavy doping, in excess of 10^{18} cm^{-3}, will form a thin enough depletion layer, enabling charge carriers to tunnel through the interface. Both rectifying and ohmic electrical contacts can be incorporated in PV solar cells in order to maximise the internal electric field present in these devices [1].

4.1.3 Electron transport at metal-semiconductor (MS) interface

The formation mechanism of the Schottky barrier (SB) at MS interfaces is still is currently a matter for conjecture depite decades of intensive investigations. The most popular proposal of SB formation seems to be Fermi-level (FL) pinning by electronic states at MS interface, such as metal-induced gap states (MIGS's) and defect-realeted states [4]. According to the FL pinning

proposals, the Shottchky barrie height (SBH) of a MS system should be uniform. If the SBH is uniform, the current-voltage (I-V) relationship of SB junction is described by the thermoionic emission theory as [4]

$$I(V_a) = I_s\left[\exp\left[\frac{qV_a}{nk_BT}\right]-1\right] \tag{4.3}$$

Questa equazione non è sempre la 4.2? where q is the electron charge, k_B is the Boltzmann costant, T is the absolute temperature, V_a is the applied bias and I_s is the saturation current given by [4]

$$I_s = A^*AT^2\exp\left(-\frac{q\varphi_B}{k_BT}\right) \tag{4.4}$$

where A* is the Richardson costant of the semiconductor and A is the diode area. The ideality factor n in Eq. 4.3 is a fit to slope of the experimental (semilogarithmic) current- voltage (I-V) curve (see subsection 4.1.4) Therefore, if Eqs. 4.3 and (4.4) are used to analyze any I-V data that have semilogarithmic relationship, we obtain a single parameter (φ_B), which is then regarded as SHB.

In the recent years, several experimental and theoretical results have suggested that the SBH depends on the structure of the MS interface. Such a dependence implies that the SBH of nonepitaxial MS interface may be inhomogen junctions. Tradionally, electron transport at MS junction is trated by a parallel conduction model, namely, the current is assumed to be a sum of the currents flowing in all individual patches (I_i) each with its own area (A_i) and SBH (φ_i):

$$I(V_a) = \sum_i I_i = A*T^2\left[\exp\left(\frac{qV_a}{k_BT}\right)-1\right]\exp\left(\frac{-q\varphi_i}{k_BT}\right)A_i \tag{4.5}$$

The parallel conduction model is in significant error when the SBH varies spatially on a scale less than, or comparable to the depletion region width. Tung explains, in his model on the electron transport at MS interface, that such an error arises from considering the interaction between neighboring patches with different SB height. Indeed, Tung depicts an inhomogeneous contact as a distribution of regions (patches) with different low barrier height values and areas embedded in a uniform higher Schottky barrier area. In particular, the of SBH inhomogeneity is taken into in account by the presence of small regions with low SBH, φ_B^0-Δ, embedded in an interface with an otherwise uniform high SBH, φ_0. The geometries used in the Tung's model for the low SBH region are small circular patches, as shown schematically in fig. 4.3.

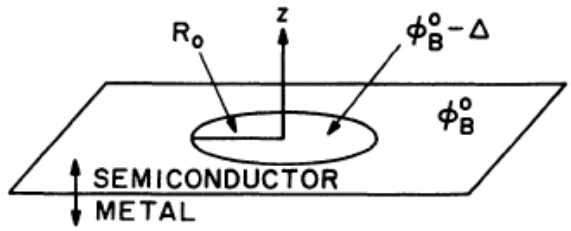

Figure 4.3 - Geomety and coordinates of a patch used in the Tung model to describe an inhomogeneous MS contact. [4]

For a low-SBH circular patch with radius R_0, which is small compared with the depletion width (W), the potential in any point (ρ, z) may be written using the following equation [4]

$$V(x,y,z) = V_{bb}\left[1-\frac{z}{W}\right]^2 + V_n + V_a + \int \frac{\delta(x_1,y_1)}{2\pi}\cdot\frac{z}{\left[z^2+(x_1-x)^2+(y_1-y)^2\right]^{3/2}}dx_1dy_1 \qquad (4.6)$$

where V_{bb} is the bend bending corresponding to a MS junction with a uniform SBH of $\varphi_B{}^0$, W is the depletion region width, and V_n is the difference between the FL and conduction-band minimum (CBM) for neutral semiconductor. The first three terms on the right-hand side of the Eq. 4.6 represent the potential due to a uniform SBH of $\varphi_B{}^0$. The last term is the variation of the potential due to the presence of SBH inhomogeneity. Eq. 4.6 suggests that the potential at the MS interface highly depends on the circular patch radius and the SBH difference. Also, in the Tung's model the current through a small patch is influenced by the surrounding area with a higher SBH, thus resulting in an effective Schottky barrier and an effective area depending on the patch parameter and bias. Hence, Tung gives the following form of the total current through an inhomogeneous Schottky contact [5]:

$$I = AA^*\exp\left(-\beta\varphi_B^{ohm}\right)\left[\exp\left(\beta\left(V-IR_s\right)\right)-1\right](1+P) \qquad (4.7)$$

which also consists of $V \le 3kTq^{-1}$ values (and, where $\beta = q/kT$). The other terms except for (1 + P) on the right-hand side of Eq. 4.7 are the thermoionic emission current of a homogeneous Schottky contact of area A, series resistance R_S, and barrier height $\varphi^B{}_{ohm}$. The additional current term P is the patch function and depends on the patch density (N) and strength factor (γ) of the patches. The γ parameter of a given patch is related to its radius R_0 and decreases in barrier at the interface ΔP (the local lowering of the SBH at the saddle point in front of a circular patch of radius $R_P = \langle R \rangle$). The comparison of Eq. 4.7 with the usual espression for junction current from the thermionic emission theory, Eqs. 4.3-4.4, shows that a low-SBH patch may be considered as having an effective SBH, φ_{eff}, and an effective area, A_{eff}. The effective SBH is simply the potential at the saddle point. Since V_{bb} decreases linearly with V_a, the applied bias

voltage affects the current through both the usual exponential factor and the variation of φ_{eff} with $V_{bb.}$ This dependence of potential barrier on the applied bias leads to an ideality factor greater than 1 [1]. Then, according to Tung's model, the presence of the inhomogeneities at the MS interface of the Schottky diode can be approximated to a circular patch with same effective radius. The continuous spatial distribution of the barrier induces a total current across a Schottky diode, obtained by integrating the thermoionic emission current with an individual barrier height and weighted by using the Gaussian distribution function.

4.1.4 I-V characteristics of the solar cell under dark or light condition

In this subsection, we report a simple solar cell device structure (based on a rectifying Schottky diode formed on an n-type semiconductor) in order to illustrate the characteristics of the device (in dark/light condition) and its conversion efficiency. Figure 4.4 shows a schematic diagram of the solar cell and the corresponding energy band diagram. The front contact can be fabricated using a transparent electrical contact or grid type contact to minimise the effect of shading. The back electrical contact is a usual ohmic contact to collect charge carriers [1].

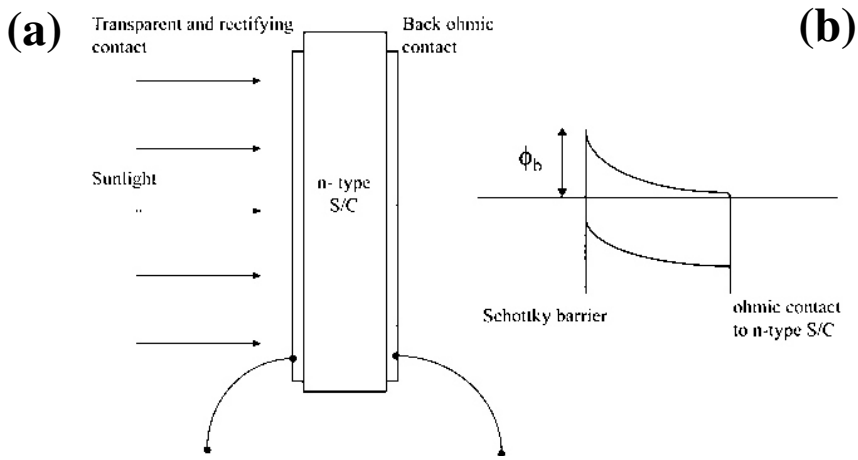

Figure 4.4 - (a) schematic diagram of a PV solar cell based on a rectifying Schottky contact and an ohmic back contact formed on an n-type semiconductor. (b) device energy band diagram. [1].

Therefore, by using the schematic diagram in fig. 4.4 (a), we illustrate the behavior of the solar device under dark or light condition in agreement with the thermoionic emission theory.

(a) I-V characteristic under dark condition: The current-voltage (I-V) characteristics of a Schottky diode can be expressed by the following equation [1]:

$$I_D = I_s\left[\exp\left(\frac{eV}{nkT}\right) - 1\right] \tag{4.8}$$

Taking into account that for external applied voltage across the diode above 75 mV the exponential term is most higher than 1, the Eq. 4.8 can be espressed by

$$I_D = I_s \exp\left[\frac{eV}{nkT}\right] \tag{4.9}$$

Rearranging Eq. 4.9, a useful relation to analyse the I-V data (measured under dark conditions) is obtained:

$$\log_{10}(I) = \left(\frac{e}{2.303nkT}\right)\cdot V + \log_{10}(I_D) \tag{4.10}$$

Figure 4.5 reports a plot of $\log_{10}(I_D)$ versus the voltage applied (V) for a practical device. The forward and reverse currents are plotted in the same quadrant by changing the sign of the reverse voltages [1].

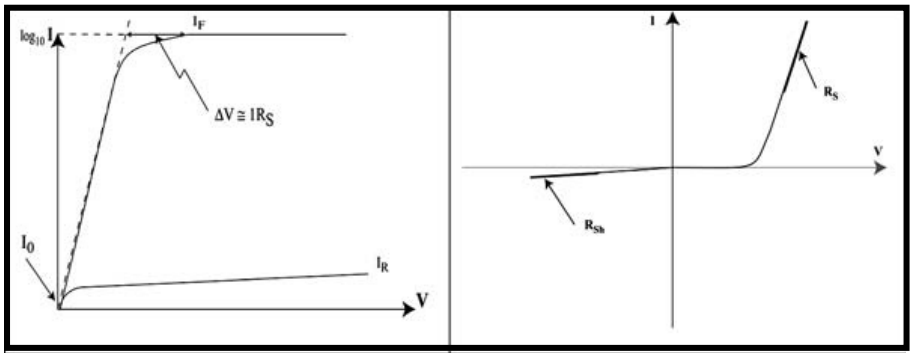

Figure. 4.5 -The log-linear and linear-linear graphs plotted for detailed analysis of dark I-V characteristics of PV solar devices [1].

For an ideal diode, the current transport occurs only through thermionic-emission over the potential barrier and n is equal to one (n = 1.00). If the depletion region and the interface contain many recombination and generation (R&G) centers, the current transport is dominated

by the R&G process and the value of n becomes 2.00 (n = 2). In practical devices, both these transport mechanisms take place and, therefore, n takes values between 1.00 and 2.00 (1<n< 2). The situation becomes more complicated when there is a large series resistance (R_s) in the device structure. Large values of R_s induce the reduction of the gradient of the log-linear curve at the high forward-bias region and, hence, the n value is increased. Tunnelling processes through the device can also increase the low forward bias current, decreasing the gradient of the log-linear I-V curve and, hence, increasing n. When both effects are present in one device, the log-linear curve deviates accordingly, making the analysis more complicated. The largest gradient of the I-V curve should be used to evaluate the smallest value of n and other parameters for accurate analysis of the device. For example, the intercept of the straight line with the highest gradient provides a more accurate value for I_0, and thus the φ_B can be evaluated from the following equation:

$$I_S = SA^{*}T^2 \cdot \exp\left(\frac{-e\varphi_B}{kT}\right) \tag{4.11}$$

The saturation current (I_s) is a key parameter for the production of an interface with a large φ_B. Large values of SB are desirable to obtain an efficient PV device and then the Is values must be low. By plotting I-V data (measured under dark conditions) in a linearlinear graph, series resistance (R_s) and shunt resistance (R_{sh}) can also be estimated from the forward and reverse current portions, respectively. Therefore, the dark I-V measurements provide the most important device parameters (n, φ_B, R_s, and R_{sh}) and provide the quality of the depletion region and the information on current transport mechanisms in the device (by using the parameter n). These parameters then help to establish an equivalent circuit for the solar cell device, as shown in figure 4.6 (b).

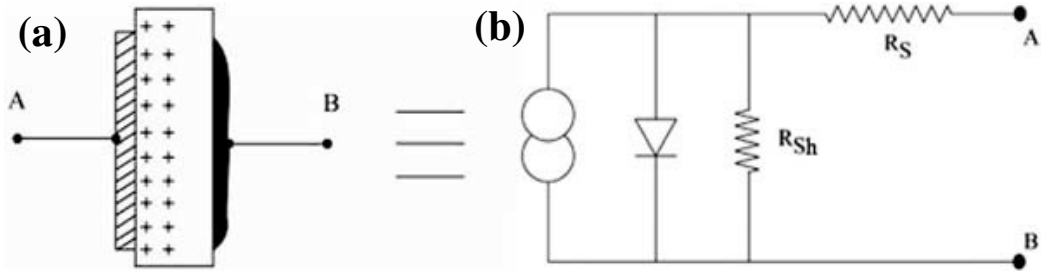

Figure 4.6 - (a) schematic diagram of a Schottky barrier solar cell and its equivalent circuit (b) [1].

(b) I-V characteristic under light condition: the band diagrams, in Fig. 4.7, highlight the directions of electron flow under dark (a) and illuminated conditions (b).

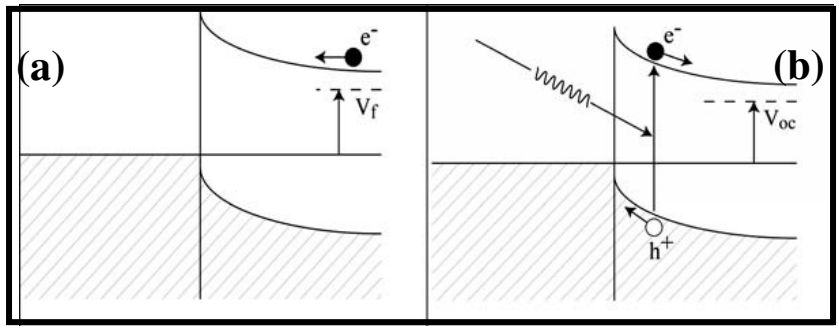

Figure 4.7 - The direction of electron flow during forward bias under dark conditions and when used as a solar cell device under illuminated conditions [1].

The picture shows that the photo-generated current flows in the opposite direction to the forward current under dark conditions. Therefore, the current through the diode under illumination is given by [1]

$$I_L = I_D - I_{SC} = I_0 \exp\left(\frac{eV}{nkT}\right) - I_{SC} \tag{4.12}$$

where I_{sc} denotes the short circuit current produced by the solar cell under illumination.
The I-V characteristics described by Eq. 4.12 can then be plotted in a linear-linear graph, as shown in figure 4.8.

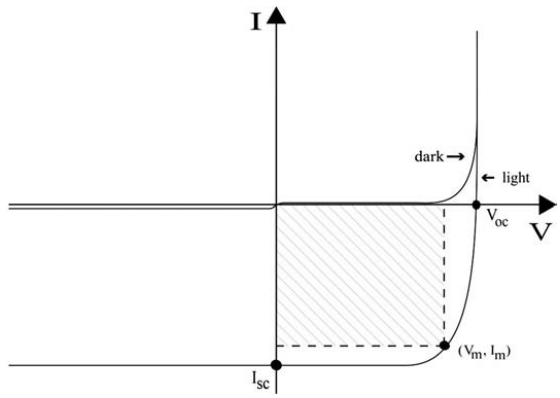

Figure 4.8 - I-V characteristics of a PV solar cell under dark and illuminated conditions [1].

There are four important parameters to consider for a solar cell device:

- Open circuit voltage ($\mathbf{V_{oc}}$): this is the voltage measured when the external circuit is in open condition, or when there is no current flow in the external circuit;
- Short circuit current ($\mathbf{I_{sc}}$): this is the current density produced when the two contacts are short circuited, or when there is zero voltage across the two contacts;
- Fill factor, or the curve factor (**FF**): this is a fraction defined to indicate the shape of the curve or the fraction of electric power that can be extracted from the solar cell. Therefore, the FF is defined as[1]

$$FF = \frac{V_M \cdot I_M}{V_{OC} \cdot I_{SC}} \tag{4.13}$$

  where V_m and I_m represent the parameters at the maximum power extraction point (V_m, I_m);
- Conversion efficiency ($\boldsymbol{\eta}$): After defining the above three parameters, the light to electric power conversion efficiency is defined as [1]

$$\eta = \frac{P_M}{P_i} \tag{4.14}$$

The standard AM 1.5 condition provides the value of $P_i = 100$ mWcm^{-2} as the solar constant to evaluate the efficiency of the device.

4.1.5 How to maximise the solar cell paramrters: V_{OC}, I_{SC} and FF

(a) Open-circuit voltage (V_{OC}) maximization: the open circuit voltage achievable from a given junction depends on the electronic properties of that interface. In order to obtain an expression for the Voc of a Schottky barrier solar cell, the diode characteristics under illumination (Eq. 4.8) can be used. By definition, V = Voc when $I_L = 0$ (the external circuit is kept open, or the current through the external circuit is zero) the V_{OC} relation is given by [1]

$$V_{OC} = n\left[\varphi_B + \frac{kT}{e} \cdot \ln\left(\frac{J_{SC}}{A^* T^2}\right)\right] \tag{4.15}$$

This indicates that the magnitude of V_{oc} depends on the value of the φ_B, present at the interface. Therefore, to obtain high values of V_{oc}, large potential barriers are desirable. It is also evident that V_{oc} depends on the value of n, the ideality factor of the diode. As reported in subsection 4.1.4, the analysis of I-V characteristic suggests that for a Schottky diode with current-transport

dominated by thermionic emission n is equal to unity. Instead, for current-transport dominated by (recombination and generation) R&G specifica acronimo di cosa (a meno che non lo riporti nella lista degli acronimi ad inizio tesi), n is equal to 2.00, indicating a helpful parameter to improve V_{oc}. In real devices, many mechanisms induce the I_{SC} reduction and then V_{oc} decreases. In addition, the temperature of the cell also affects the V_{oc}. As the temperature decreases, the V_{oc} value increases owing to the minimization of the thermal agitation of charge carriers. Thus, to increase the V_{oc} of a Schottky barrier-based solar cell, the improvement of the φ_B, the reduction of the temperature of the cell and the minimisation of the R&G process within the cell structure are desirable [1].

(b) Short-circuit current (I_{SC}) maximization: the short circuit current depends on the number of photogenerated charge carriers and their separation and collection rates in the external circuit. This requires efficient photon absorption from almost all regions of the solar spectrum by the materials used, effective carrier generations, and the high quality of the depletion region formed and hence the strength of the built-in electric field created. With the right device design, the impurity PV effect can be used to create e-h pairs using surrounding heat energy.

(c) Fill Factor (FF) maximization: to improve the shape of the I-V curve, and so the FF, the total series resistance (see circuit in fig. 4.6 (b)) should be minimised (ideally $R_s=0$). This includes resistance introduced by the electrical contacts, interfaces within the device, and materials used. The shunt resistance must be increased (ideally $R_{sh}\rightarrow\infty$). This can be achieved by minimising the R&G processes.

4.2 Plasmonics Nano-Structures (NSs) for improving photovoltaic devices

At present, the research in the photovoltaic device field has mainly focused on the large scale production of the so-called thin-film (or second generation) photovoltaic cells [8-14]. The approach proposed in literature to reduce the high costs of Si-based materials and processing is the use of thin absorber layers (1-2 μm in thickness) deposited on cheap module-sized substrates, such as glass, plastic or stainless steel. A main limitation of thin-film solar cell technologies is related to the small light absorbance of the near-band gap light, especially for indirect-band gap semiconductors such as Si. To overcome such a problem, a proposed strategy is the proper surface structuration of the thin-film solar cell so to trap the light inside the absorber layer in order to increase the absorbance. In particular, the incorporation of metallic nanoparticles (MNPs) near the solar cell absorber layer (fig. 4.9 (a)) is one of the most promising to improve the light harvesting. The incident radiation, whicht interacts with the MNPs, induces Localized Surface Plasmon Resonances (LSPR) [15-19] due to the collective oscillations of the MNPs conduction electrons. As reported by Atwater et al. [20], the resonant excitations of LSPR lead to selective photon absorption and enhancement of local electromagnetic field near the MNPs by order of magnitude. The nanoparticles then act as an effective 'antenna' for the incident sunlight that stores the incident energy in a localized surface plasmon mode (see simulation in fig. 4.9 (b)).

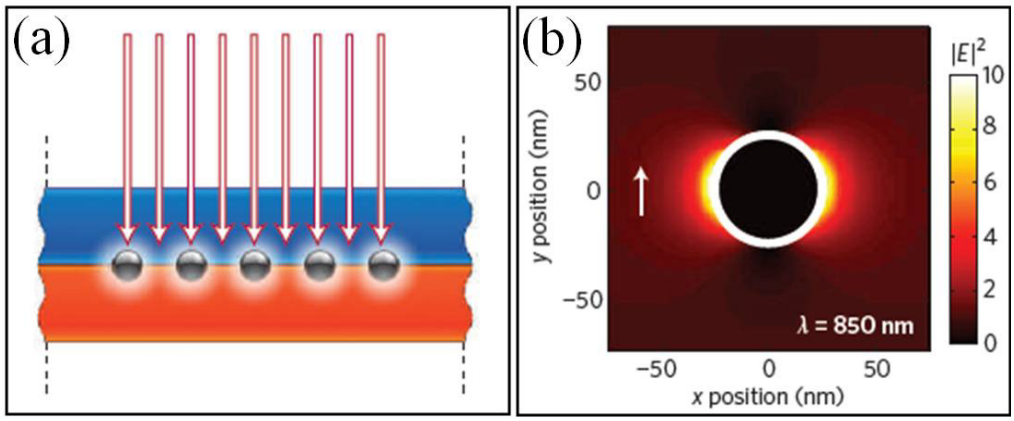

Figure 4.9 - (a) Light trapping by the excitation of localized surface plasmons in metal nanoparticles embedded in the semiconductor. (b) The excited particles' near-field causes the creation of electron–hole pairs in the semiconductor.Metal nanoparticles show an intense near-field close to the surface. Intensity enhancement around a 25-nm-diameter Au particle embedded in a medium with index n = 1.5 (plasmon resonance peak at 500 nm). Light with a wavelength λ = 850 nm is incident with a polarization indicated by the vertical arrow. The magnitude of the enhanced electric-field intensity E is indicated by the colour scale [20].

Figure 4.10 shows an alternative design of the plasmonic solar cell. The MNSs are used as sub-wavelength scattering elements to trap the sunlight into an absorbing semiconductor film by folding the light into a thin absorber layer.

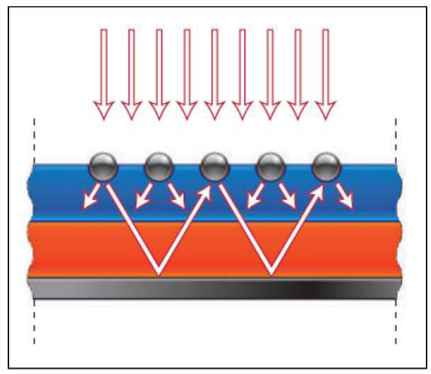

Figure 4.10 - Light trapping by scattering from metal nanoparticles at the surface of the solar cell. Light is preferentially scattered and trapped into the semiconductor thin film by multiple and high-angle scattering, causing an increase in the effective optical path length in the cell [20].

The light scattering from a small MNP embedded in a homogeneous medium is nearly symmetric in the forward and reverse directions [20-22]. When the particle is placed close to the interface between two dielectrics, the light will scatter preferably into the dielectric with the larger permittivity [20, 23]. The scattered light in the dielectric will then acquire an angular spread, which effectively increases the optical path length. Moreover, the light scattered at an angle beyond the critical value for reflection will remain trapped in the cell [13]. The fraction of radiation scattered into the absorber layer depends on the shape, size and surface density of the MNPs, and these structural parameters are key factors to determine the device efficiency [20, 24, 25]. The results of the simulations based on the first-order scattering model [20] show that particles smaller than about 10 nm, with their effective dipole moment located close to the semiconductor layer, scatter a larger fraction of the incident light into the underlying semiconductor due to the enhanced near-field coupling (fig. 4.11 (a)). In the limit of a point dipole very close to a silicon substrate, 96% of the incident light is scattered into the substrate, thus showing the efficiency of the particle scattering technique. Figure 4.11 (b) shows the path-length enhancement in the solar cell derived from fig. 4.11 (a) using a simple first-order scattering model. For 100-nm-diameter Ag hemispheres on Si, a 30-fold enhancement is found. Therefore, fig. 4.11 demonstrates the advantage of using small particles to create the forward scattering anisotropy. But very small particles suffer from significant ohmic losses, which scale with volume v, whereas scattering scales with v^2, so that using larger particles is advantageous to increase the scattering rate. For example, a 150-nm-diameter Ag particle in air has an albedo (fraction of light emitted as radiation) as large as 95% [20].

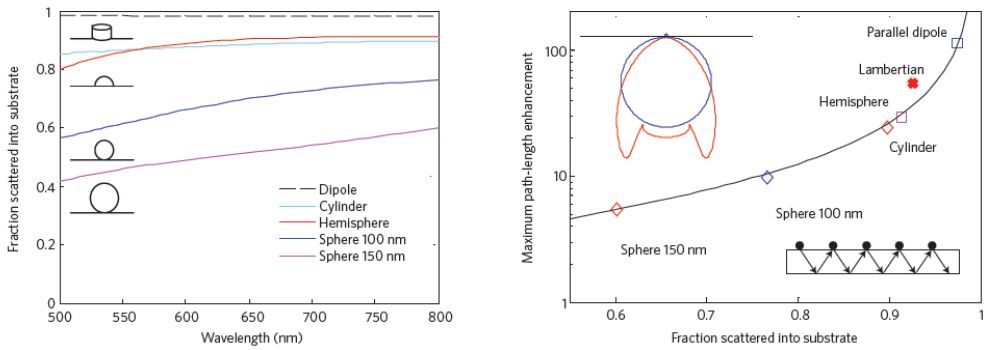

Figure 4.11- (a) Fraction of light scattered into the substrate, divided by total scattered power, for different sizes and shapes of Ag particles on Si. Also plotted is the scattered fraction for a parallel electric dipole that is 10 nm from a Si substrate. (**b**) Maximum path-length enhancement, according to a first-order geometrical model, for the same geometries as in **(a)** at a wavelength of 800 nm. Absorption within the particles is neglected for these calculations, and an ideal rear reflector is assumed. The line is a guide for the eye. Insets: (top left) angular distribution of scattered power for a parallel electric dipole that is 10 nm above a Si surface (red) and a Lambertian scatterer (blue); (lower right) geometry considered for calculating the path-length enhancement [20].

Also, the light-trapping effects are most pronounced at the peak of the plasmon resonance spectrum, which can be tuned by engineering the dielectric constant of the surrounding matrix. For example, small Ag or Au particles in air have plasmon resonances at 350 nm and 480 nm respectively; they can be redshifted in a controlled way over the entire 500–1.500 nm spectral range by embedding them in SiO_2, Si_3N_4 or Si (fig. 4.12) [26-28], which are all standard materials in solar-cell manufacturing.

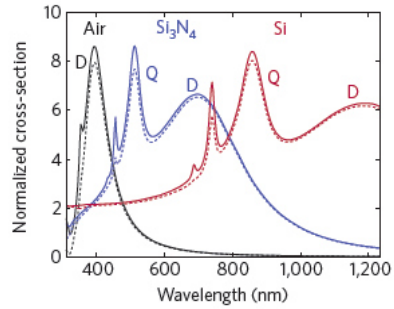

Figure 4.12 - Metal nanoparticles scatter light over a broad spectral range that can be tuned by the surrounding dielectric. The plots show the scattering cross-section spectrum for a 100-nm-diameter Ag particle embedded in three different dielectrics (air, Si3N4 and Si). Dipole (D) and quadrupole (Q) modes are indicated. The cross-section is normalized to the geometrical cross-section of the particle [20].

On the basis of the above considerations, the ability to construct optically thick but physically very thin photovoltaic absorbers might revolutionize the high-efficiency photovoltaic device design. This becomes possible by using light trapping through the resonant scattering and concentration of light in arrays of metal nanoparticles, or by coupling light into surface plasmon polaritons and photonic modes that propagate in the plane of the semiconductor layer. In this manner, it is possible to absorb the full solar spectrum by using extremely thin photovoltaic absorber layers (tens to hundreds of nanometres thick).
In the following subsection, we report some of the plasmonic solar cell designs reported in the literature.

4.3 Plasmonic solar cells: correlation between the MNSs properties and the devise performance

Taking into account the advantages to introduce the plasmonic NSs in a thin film solar cell (see Subsection 4.2), we report the correlation between the MNSs structural and optical properties and solar cell performance.
For example, S. Pillai et al. [29] propose to introduce Ag NPs in the silicon solar cell, by using the scheme of the device reported in figure 4.13. The SOI (Silicon On Insulator) cells used in their experiments are formed from a lateral p-n junction diffused into a p-type layer. The p and n metal contacts are interdigitated for maximum carrier extraction with a cell dimension of 2×2 cm. The layer thickness of the SOI devices is 1.24 μm for the silicon layer and 1.0 μm for the buried oxide layer. The samples have an approximately 30 nm top oxide that acts as a passivating layer, the thickness of which influences the coupling between the active silicon layer and the plasmons.

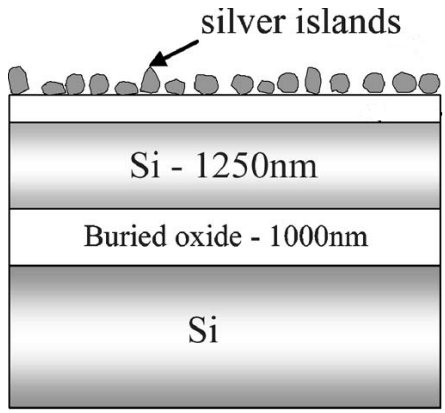

Figure 4.13 - Schematic representation of silicon device containing Ag NSs (silicon-on insulator with 1.25 μm active Si) [29].

The thickness of the oxide is so low as to provide good surface passivation without compromising the coupling to the silicon. Different mass thicknesses of silver are deposited on the samples to obtain NPs with different size. The particles, formed as a result of annealing of the starting film, tend to become larger, more elongated, and also more irregular as the mass thickness of silver is increased. This causes the bare island resonance to shift to the red, as can be seen from the transmittance plots shown in figure 4.14. A dip in the transmittance plots shows the resonance position. The resonance curves are sharper for lower mass thicknesses and tend to broaden for larger mass thicknesses. S. Pillai et al. [29] suggest that this result is due to the average over the range of shapes of the nanoparticles and the depolarization effects for larger particles.

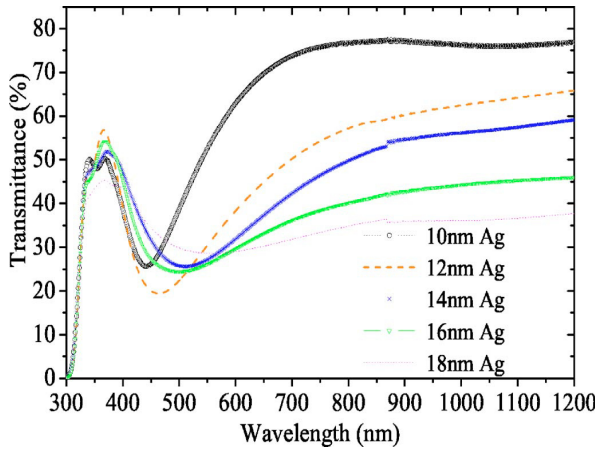

Figure 4.14 - Transmittance measurements showing redshifting of the bare island resonance of particles corresponding to increasing mass thickness of silver, which implies larger particle sizes [29]

Figure 4.15 (a) shows the photocurrent enhancement (defined as the ratio of the photocurrent response of the device measured after and before deposition of the silver islands) for the 1.25 micron SOI test cells. The interesting feature is an overall increase in current throughout the visible and near-IR close to 16-fold enhancement at around 1050 nm with particle sizes corresponding to 16 nm mass thickness of silver. These results correspond to a 33% increase of the total current of the device for particle sizes correponding to 12 nm mass thickness of silver and 16% increase for particle sizes corresponding to 16 nm silver thickness.
The absorption enhancement for the different sized particles can be seen in fig. 4.15 (b). The enhancement results from the 16 and 22 nm depositions are similar and large at long wavelengths, whereas for the 10 nm deposition the enhancement at long wavelengths is small.

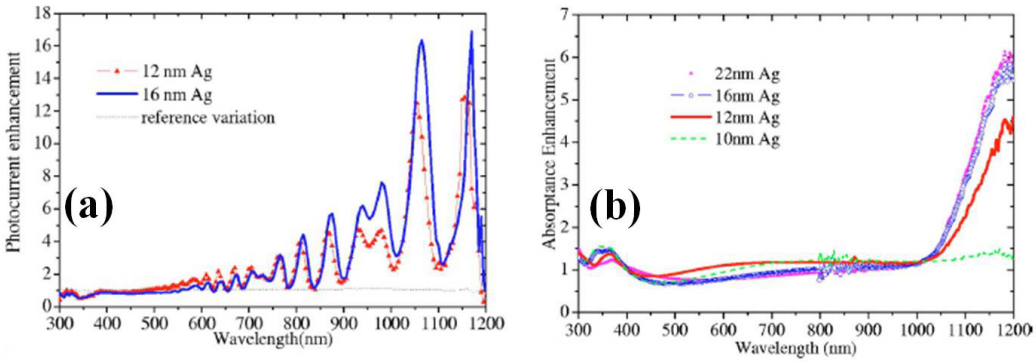

Figure 4.15- (a) Photocurrent enhancement from a 1.25 μm thick SOI test solar cell for particle sizes corresponding to 12 and 16 nm mass thickness of Ag. (b) Enhancement from a double-sided polished Si wafer characterized optically using a spectrophotometer with particle sizes formed from different mass thickness of silver by thermal evaporation followed by annealing [29)].

.

Therefore, these experimental results suggest that surface plasmons offer a promising way to improve the efficiency of thin-film solar cells, avoiding the problem of increased recombination that occurs when silicon is textured directly. By using this method, it is possible to reduce the thickness of Si below 1.5 μm with good light trapping provided by metal nanoparticles.

Figure 4.16 shows new cell designs that can benefit from the increased light confinement and scattering from metal nanostructures. First of all, plasmonic "tandem" geometries can be made, in which semiconductors with different bandgaps are stacked on top of each other, separated by a metal contact layer with a plasmonic nanostructure that couples different spectral bands in the solar spectrum into the corresponding semiconductor layer (see fig. 4.16 (a)) [30]. Coupling sunlight into SPPs could also solve the problem of light absorption in quantum-dot solar cells (see fig. 4.16 (b)). Although such cells offer potentially large benefits because of the flexibility in engineering the semiconductor bandgap by particle size, effective light absorption requires thick quantum-dot layers, through which carrier transport is problematic. In a recent example of nanoscale plasmonic solar-cell engineering, an organic photovoltaic light absorber was integrated in the gap between the arms of plasmonic antennas arranged in arrays (see fig. 4.16 (c)) [31]. Other examples of nanoscale antennas are coaxial holes fabricated in a metal film, which show localized plasmonic modes owing to Fabry–Perot resonances (see fig. 4.16 (d)) [32-34].

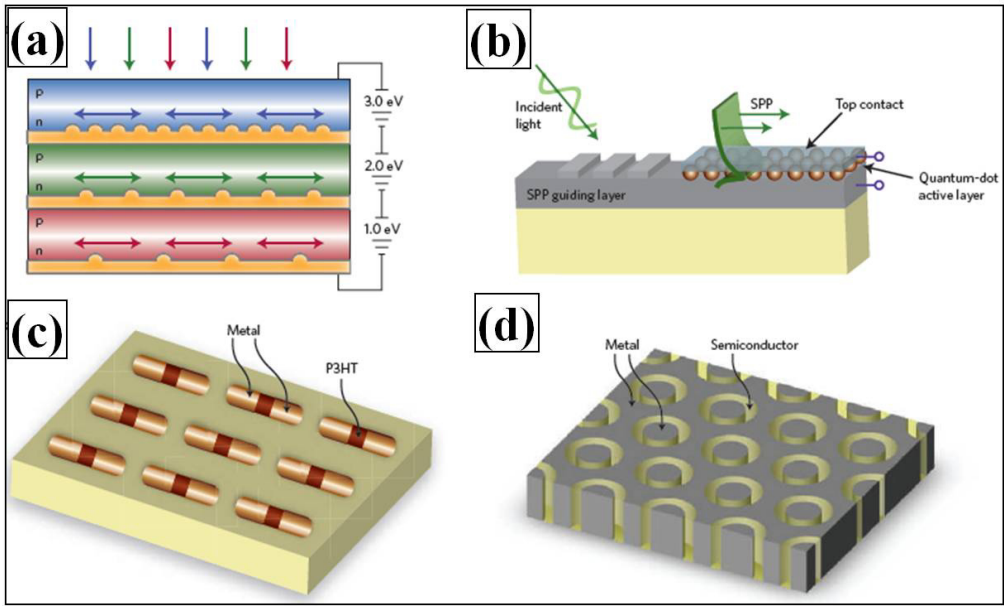

Figure 4.16 - New plasmonic solar-cell designs. (a) Plasmonic tandem solar-cell geometry. Semiconductors with different bandgaps are stacked on top of each other, separated by a metal contact layer with a plasmonic nanostructure that couples different spectral bands of the solar spectrum into the corresponding semiconductor layer. (b) Plasmonic quantum-dot solar cell designed for enhanced photoabsorption in ultrathin quantum-dot layers mediated by coupling to SPP modes propagating in the plane of the interface between Ag and the quantum-dot layer. Semiconductor quantum dots are embedded in a metal/insulator/metal SPP waveguide. (c) Optical antenna array made from an axial heterostructure of metal and poly (3-hexylthiophene) (P_3HT). (d) Array of coaxial holes in a metal film that support localized Fabry–Perot plasmon modes. The coaxial holes are filled with an inexpensive semiconductor with low minority carrier lifetime, and carriers are collected by the metal on the inner and outer sides of the coaxial structure. Field enhancements up to a factor of about 50 are possible and may serve to enhance nonlinear photovoltaic conversion effects [20].

4.4 Nano-scale structuration and optical properties of thin gold films on textured FTO (t-FTO) substrates

In this Subsection, we report about the structural and optical characterizations of a glass/t-FTO/MNPs multilayer. We obtain Au nanoparticles (NPs) on the glass/t_FTO substrate by nanosecond laser irradiation of sputter-deposited Au films. Nowadays, conductive transparent substrate, such as Fluorine-Tin-Oxide (SnO_2:F, FTO), are routinely used as transparent coating for their high electrical conductivity and high transparency at the visible and near-IR region of the electromagnetic spectrum. Besides, among bottom-up methods, used to obtain nanoscale metal structures [35-43], the application of ultrafast lasers for material nano-processing allows to obtain a wide variety of nanostructures as a result of laser induced melting and solidification dynamics [44-54]. The main advantages of laser-based approaches include: local processing down to the micrometer and sub-micrometer range; minimized thermal damage to the substrate and neighboring regions; non-contact nature and non-planar processing.

The breakup of the Au films into NPs is observed after the films laser irradiations as a consequence of the films melting and solidification processes [55-57]. The evolution of the mean size and surface density (inferred by SEM and AFM analyses) of the formed Au NPs are investigated as a function of fluence irradiation E (in the 0.50-1.0 J/cm^2 range) to find the correlation allowing the Au NPs structural characteristics tuning. In particular, data corresponding to the 0.50, 0.75, 1 J/cm^2 are presented. These values are chosen for the following reasons: a) at fluences higher than 1 J/cm^2 the ablation process of the Au films (5 and 10 nm thicknesses) became important. It is widely recognized in literature [44] that, depending on the substrate, metal film type and thickness, above a critic fluence, the temperature reached of the film can be so high to cause the film ablation as a consequence of the laser irradiation (as we observe for the 5 and 10 nm-thick Au film on the glass/FTO substrate at fluences higher than 1 J/cm^2); b) the data reported for the three selected fluence of 0.5, 0.75, and 1J/cm^2 are representative of the general trend observed in the 0-1.0 J/cm^2 energy range. We analyzed samples irradiated at several fluences in the 0-1.0 J/cm^2 but the significant data (structural and optical) are those obtained for fluences equal or higher than 0.5 J/cm^2. Indeed, fluences lower than 0.5 J/cm^2 do not determine the dewetting process of the 5 and 10 nm-thickness Au film in NPs (i. e. the temperature reached by the Au films is lower than the Au melting temperature). So, for fluence lower than 0.5 J/cm^2 the Au films are, practically, unchanged with respect to the as-deposited films. About samples prepared at fluences in between 0.5-0.75 J/cm^2 and 0.75-1 J/cm^2: increasing the fluence from 0.5 to 0.75 J/cm^2 the mean radius and surface-to-surface distance of the Au NPs experience only a slight increase. So, fluences in-between 0.5 and 0.75 J/cm^2 are little significant in analyzing the effect of the mean NPs variation on the optical properties. In this range, significant is, instead, the change of the NPs surface density. Therefore, for sake of simplicity and synthesis, we report data for only 3-fluences in the 0-1.0 J/cm^2 representative of a general trend and grouping the behavior from about 0.5 J/cm^2 to about 0.62 J/cm^2, from about 0.62 J/cm^2 to about 0.75 J/cm^2 and from about 1.0 J/cm^2. Also, we

compare the results of the structural characterizations of the glass/t-FTO/MNPs multilayer with the optical characterizations. The optical measures highlight that such a structure has interesting properties since it exhibits Au NPs structure-dependent transmission/absorption spectra. Furthermore, the electrical characterizations of the system (using the four-probe-method) suggests a sheet-resistance reduction in the glass/t_FTO/Au NPs multilayer due to the presence of the metal material on the surface. We compare, also, these results with those obtained for the same systems (glass/t_FTO/Au NPs) when standard furnace annealing processes are used to synthesize the Au NPs on the t_FTO surface. The comparison between the experimental results of the two different synthesis methodologies shows that the laser annealing processes allow a more accurate control of Au NPs structural properties, which are necessary to modulate the optical response of the glass/t_FTO/Au NPs multilayer. In contrast to the standard thermal process, the laser treatment induces the breakup of the Au film in selected areas of the sample, which allows to control the Au NPs spatial position on the textured FTO surface. Besides, the use of laser operating at 532 nm does not induce changes in the optical and structural properties of the FTO substrate, which exhibits no absorption at this wavelength. For its peculiar optical and electrical properties, the glass/t_FTO/Au NPs multilayer obtained by nanosecond laser irradiation cant be used as light-trapping-multilayer (LTM) for photovoltaic applications (fig. 4.17 shows a potential prototype) as reported in subsection 4.5.

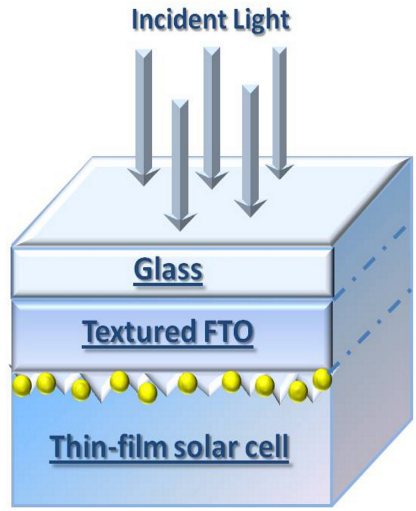

Figure 4.17 - Schematic representation of a plasmonic solar cell prototype. In the glass/t_FTO/MNPsmultilayer, the large fraction of radiation transmitted by the transparent layer interacts with the MNPs used as sub-wavelength scattering elements to couple and trap the sunlight into an absorbing semiconductor thin film by folding the light into absorber layer.

4.4.1 Experimental Details

The samples were prepared starting from the glass/t_FTO (soda-lime/SnO_2:F) substrate provided by 3SUN Industry in large slabs. From the large slab, slides of 2 cmx2 cm were cut (fig. 4.18). Au depositions were carried out on the substrate slides using a RF (60Hz) Emitech K550X Sputter coater apparatus, clamping the substrates against to the cathode located straight in front of the source (99.999% purity target). The electrodes were laid at a distance of 40 mm under Ar flow, keeping a pressure of 0.02 mbar in the chamber. After 120 s (or 240 s) time-deposition, at an emission current of 10 mA, an average thickness of d = 5nm (or 10 nm) of Au was deposited on the glass/t_FTO substrates, as indicated by Rutherford-Backscattering Spectrometry analyses. RBS analyses were performed by using 2 MeV 4He+ backscattered ions with a scattering angle of 165°.

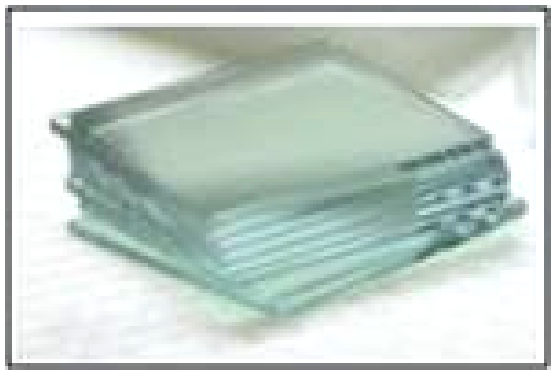

Figure 4.18 - 2 cmx 2 cm glasst/t_FTO (soda-lime/SnO_2:F) substrates obtained by large slabs provided by 3SUN Industry.

Laser irradiations were performed by pulsed (10 ns) Nd:yttrium aluminum garnet YAG laser, operating at 532 nm (Quanta-ray PRO-Series pulsed Nd:YAG laser). The spot laser has a circular shape of 4 mm in diameter. The laser intensity profile is Gaussian and it is characterized by full width at half maximum of 1 mm. 97% of the highest laser intensity is maintained within a circular area of 600 μm in diameter centered at the maximum of laser intensity. The error in the fluence E measurement is 25 mJ/cm^2.
For standard thermal treatments, the samples were annealed using a Carbolite horizontal furnace (provided by a pre-chamber) in dry N_2 (2.5 l/min), at temperatures of 400-500°C. The annealing time was 180 minutes for all processes.
In order to study the evolution of the samples morphology, SEM analyses were performed by a Zeiss FEG-SEM Supra 25 Microscope operating at 5 kV. SEM images were analyzed by Gatan

Digital Micrograph software. In particular, the SEM images were processed to determine the planar size distributions of the Au NPs. Assuming a spherical shape structure, the size distributions of the Au NPs were calculated on a statistical population of, at least, 100 NPs. AFM analyses were performed by a Veeco-Innova microscope operating in high amplitude mode, and ultra sharpened Si tips were used (MSNL-10 from Veeco Instruments, with anisotropic geometry, radius of curvature ~2 nm, tip height ~2.5 μm, front angle ~15°, back angle ~25°, side angle 22.5°). AFM images were analyzed by SPM LabAnalyses V.7.1 software.

The electrical sheet resistance and carrier mobility of the samples were measured using a four point terminal method by employing an HL5560 system (Bio-Rad, Hercules, CA, USA). The values of the sheet resistance related to all prepared samples are reported in Tab. 4.1.

Finally, optical properties were measured in the wavelength range of 330 and 1100 nm using a UV–vis Lambda 40 spectrophotometer equipped with an integrating sphere. The geometry of the integrating sphere allows the collection of the diffused light at angles above 2.1° away from the normal direction in both transmission and reflection modes.

Sample	**Sheet resistance < R_s > [ohm/sq]**
t_FTO	8.6
t_FTO_1.0 J/cm^2	8.1
t_FTO_400°C_180 min	8.6
t_FTO_500°C_180 min	22.9
t_FTO_Au5nm_as dep	7.3
t_FTO_Au10nm_as dep	7.4
t_FTO_Au5nm_400°C-3h	5.1
t_FTO_Au5nm_500°C-3h	19.7
t_FTO_Au5nm_1.0 J/cm^2	7.5
t_FTO_Au10nm_1.0 J/cm^2	7.5

Tab. 4.1-Values of the electrical sheet resistance measured using a Four-Point terminal method

4.4.2 Structural and optical characterizations of the glass/t-FTO substrate

In this Subsection, we report the results of the structural and optical characterizations of the glass/t_FTO substrate (reference sample). Several slides were cut from a main slab consisting of a FTO layer deposited on glass and chemically textured (from 3SUN industry). The representative SEM (fig. 4.18 (a)) and AFM (fig. 4.18 (b)) images highlight the typical morphology of the textured FTO surface. A mean value for the FTO roughness σ_{FTO} = 32.7±8.7 nm was estimated by averaging the values obtained from the analyses of different AFM scanned areas. Figure 4.18 (c) shows the transmittance spectra (T%) in the visible range (from 330 nm to 1100 nm) of the following samples: a reference glass/t_FTO slide (substrate); the substrate after furnace thermal process at 500°C-180 min; the substrate after laser annealing at the higher fluence (1.0 J/cm^2). These spectra suggest that the transmittance of the different pieces of the glass/t_FTO substrate does not vary significantly after the thermal treatments (furnace and laser). Indeed, the transmittance corresponding to different slides of glass/t_FTO cut from different regions of the same main slab varies within a 20% (likely modification in the t_FTO refractive index), and the transmittance values after the thermal processes range in the same interval. Furthermore, the spectra in fig. 4.18 (c) exhibit the characteristic oscillations due to the interference phenomena at glass/t_FTO interface. The shifts in the positions of the interference peaks are attributable to thickness variation of the FTO layer deposited on the main slab. The theoretical simulations, obtained using classical Fresnel formulae for thin films [58], suggest a maximum FTO thickness variation of about 30 nm, assuming the value of the FTO refractive index n_{FTO} ~2.0.

Thus, we can conclude that the variation of T% after standard or laser annealing falls within the statistical intrinsic variation of T% due to the variation in the thickness of the FTO. So, no real effect is determined by the standard or laser annealing processes on the transmittance of the starting substrates. The values of the glass/t_FTO sheet resistances and electron mobility are equal to R_s=8.6 ohm/sq (see table in fig. 4.18 (d)) and μ_s=51.2 cm²/Vs, respectively. The electrical characterization highlights an alteration of the glass/t_FTO electrical properties as a consequence of furnace thermal treatment at 500°C-180 min (R_s_500 °C=22.9 ohm/sq, μ_s_500 °C=24 cm²/Vs). Such an increase of the FTO resistivity after the 500 °C annealing is, probably, a consequence of the structural changes of the t_FTO layer at this temperature. Indeed, despite our SEM analyses did not evidence any significant surface modification of the t_FTO layer after the 500 °C annealing, it was experimentally recognized [59] that upon 500 °C the crystal lattice of SnO_2 contracts may be due to the migration of oxygen from interstitial sites of the lattice to grain boundaries. So, a mechanical stress rises which, in combination with a diffusion of alkali ions from the glass substrate into the FTO film, originate the deterioration of the film electrical properties (i.e. increase of the film resistivity). On the contrary, for the glass/t_FTO submitted to laser annealing at higher energy (1.0 J/cm^2), the value of R_s_1.0 J/cm^2=8.4 ohm/sq (see table in fig. 4.18 (d)) does not indicate any thermal damage of the substrate due to FTO local heating.

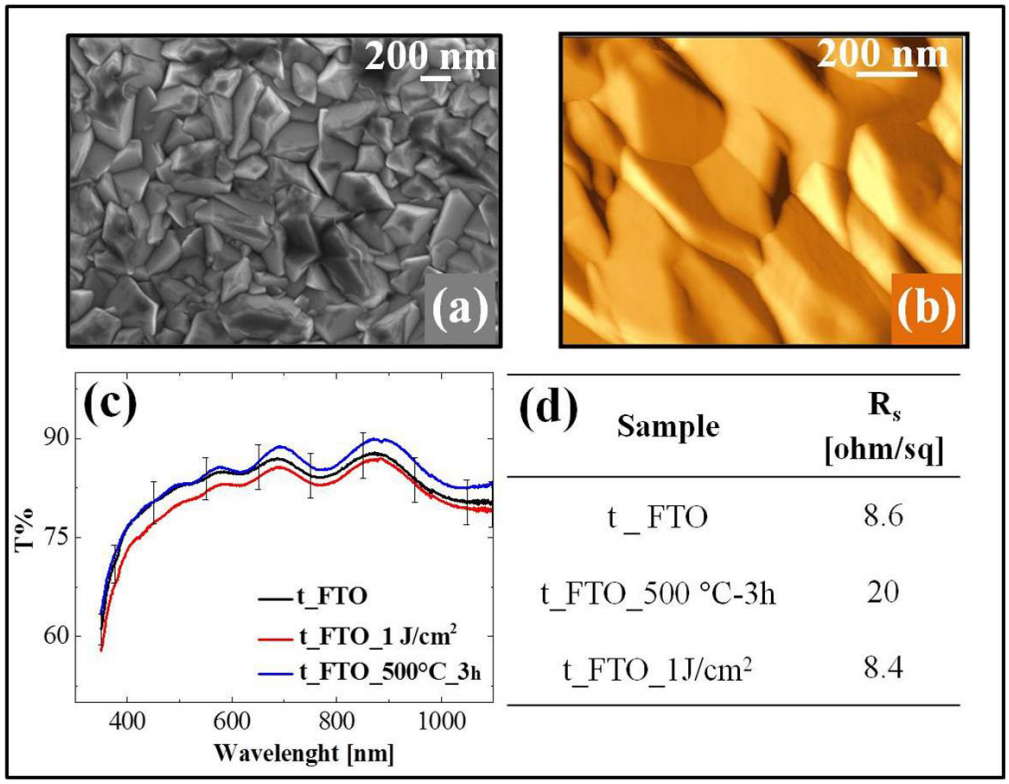

Figure 4.18 - Structural and optical characterization of glass/t_FTO substrate. (a) The representative SEM image highlights the typical morphology of the textured FTO. (b) 1 μm×1 μm AFM image of the substrate surface. (c) Transmittance spectra (T%) in the visible range related to the following samples: a reference t_FTO/glass substrate (black line); the substrate after thermal process at 500°C-180 min (blue line); the substrate after laser annealing at higher energy (red line). (d) In table are reported the values of the sheet resistance related to substrate as deposited and submitted to thermal treatments.

4.4.3 Synthesis and characterizations of the Light-Trapping-Multilayer (LTM)

In order to optimize the synthesis of metallic nanostructures, the Au-coated glass/t_FTO substrates were submitted to two different thermal treatments: standard furnace heating process at increasing T (400 °C, 500 °C for 180 min), and laser annealing at three different laser fluencies E (0.50 J/cm^2, 0.75 J/cm^2, 1.0 J/cm^2). The results of the different synthesis techniques are compared. Indeed, the aim of this work is to obtain Au NPs on the glass/t_FTO substrate so that the far-field scattering efficiencies are maximized over the wavelength range suitable for each specific type of photovoltaic device. For this purpose, it is necessary to achieve a good

compromise between the amount and directionality of the light scattered from the Au NPs. Many works in the literature [20, 60] show that the main parameter describing the correlation between LTM structural and optical parameters is the surface coverage size distribution of the MNPs. Indeed, the scattering rate increases with the particle size, but smaller NPs induce the symmetric scattering in forward and reverse directions. The integration in a thin film solar cell of a LTM (as reported in fig. 4.17), with optimized NPs coverage size distribution, may increase the light optical path length inside the absorber layer and then the solar cell efficiency.

4.4.3.a LTM synthesis by furnace thermal annealing

In this Subsection, we report the results of the standard furnace thermal processes at increasing temperature. Starting from the typical quasi-continuous percolative surface of a sputter-deposited 5 nm-thick Au film (see SEM and AFM images in fig. 4.19), it is possible to study the surface morphology evolution of the samples induced by thermal treatments (see SEM images in fig. 4.20).

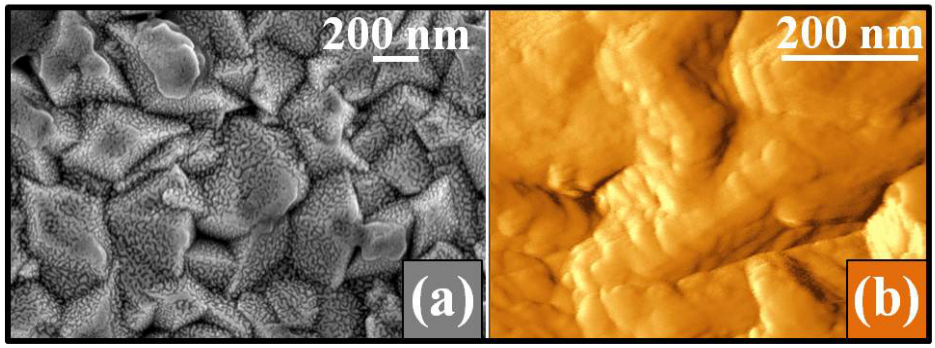

Figure 4.19 - (a) SEM image of the sputter-deposited 5 nm-thick Au film on glass/t-FTO substrate (sample as deposited). (b) 1 μm×1 μm AFM image of the sample as deposited.

In particular, figure 4.20 (a) shows the formation of an array of Au droplets due to solid-state dewetting [61]. The formation and growth of metastable holes [62] are due to the minimization of the surface energy (the driving force of dewetting process) of the thin Au film and the film-substrate interface. From the SEM images in figs. 4.20 (a) and 4.20 (b) the size distributions reported in figs. 4.14 (c) and 4.14 (d), respectively, were calculated. The generic distribution of radii, R, was fitted using the log-normal function [63]:

$$f(R) = \{(1/2\sqrt{2}\pi\sigma) \times \exp[- (\ln 2 (R/Rc) / 2\sigma^2)]\} \quad (4.16)$$

where σ is the standard deviation on R, and using R_c and σ as fit parameters.

The mean radius is obtained by ‹R›=Rc×exp(σ^2/2). For the sample thermal treated at 400°C-180 min, the mean value of the Au NPs radius is <$R_{NPs\_400°C}$>=(14.7±2.9) nm (fig.4.20 (c)).

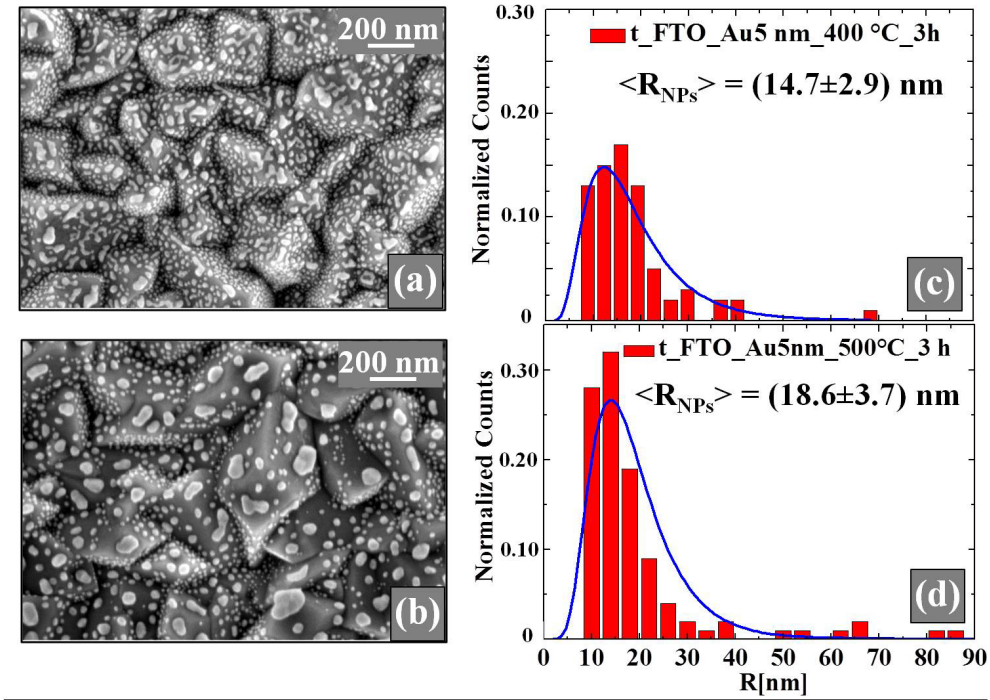

Figure 4.20 - Structural characterizations of Au coated glass/t_FTO substrates after the thermal processes at increasing T. (a)-(c) SEM image and size distribution of the sample submitted to thermal annealing at 400°C-180 min. (b)-(d) SEM image and size distribution of the sample submitted to thermal annealing at 500°C-180 min.

After the thermal process at 500°C, the Au NPs average radius is <$R_{NPs\_500°C}$>=(18.6±3.7) nm, as reported in fig. 4.20 (d). Thus, thermal annealing at higher T induces the formation of Au NPs with larger size as a consequence of the surface diffusion mechanism, which is responsible for the mass transport (proportional to the temperature) [64]. By further analyses of the SEM images, we obtained information about the evolution of the Au NPs mean surface density (<N>) and the mean surface-to-surface distance between nearest NPs (<s>). The estimated values of the surface density (by direct counting and averaging on several SEM images) are: <$N_{400°C}$> = (6.1±1.2)·10^{10} cm^{-2} and <$N_{500°C}$> = (3.2±0.6)·10^{10} cm^{-2}. Assuming that the NPs are placed in an ordered squared matrix of side L, the <s> parameter can be obtained by the following formula:

$$\langle s \rangle = [1-(2\cdot\langle R \rangle\cdot\sqrt{\langle N \rangle})]/\sqrt{\langle N \rangle} \qquad (4.17)$$

The obtained values are: $<s_{400°C}>=(13.0\pm2.6)$ nm for the sample processed at 400°C, and in $<s_{500°C}>=(25.0\pm5.0)$ nm for the sample processed at 500°C. The formation of larger Au NPs increasing T explains the reduction of <N> and the consequent increase of <s>.
The electrical characterization of the samples (see tab. 4.1) shows a strong increase of the glass/t_FTO/Au NPs sheet resistance due to thermal annealing at 500°C (R_s_500°C=19.7 ohm/sq) [59]. As reported in Subsection 4.4.3, the higher temperature process induces, reliably, structural changes of the substrate that worsen the electrical response of the multilayer. So, the standard thermal process at 500°C even if induces the formation of Au NPs with improved size, it determines the large increase of the FTO resistivity and, so, a global increase of the LTM resistivity despite the presence of the Au on surface.

4.4.3.b Synthesis and characterizations of the LTM by nanoseconds laser irradiations

In this Subsection, we report the structural and optical characterizations of Au-coated glass/t_FTO substrates submitted to laser annealing at three different fluencies, E (0.50 J/cm^2, 0.75 J/cm^2, 1.0 J/cm^2). After depositing 5 nm-thick Au film on the t-FTO surface, to obtain a uniform region of Au NPs, the laser spots were placed in a squared matrix of 5 spots×5 spots. As shown in fig. 4.22, after laser exposure the metallic films are molten and broken up into discrete-nanometer scale islands. The 3D AFM images, in fig. 4.21, show the sample surface evolution owing to the laser treatments at increasing fluence.

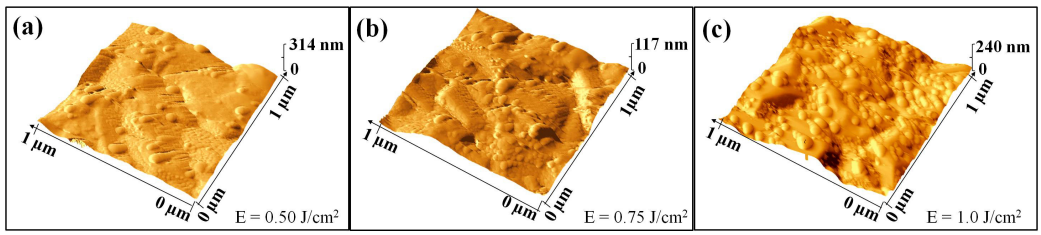

Figure 4.21 - Representative 3D AFM images (1 µm×1 µm) of the Au-coated glass/t_FTO substrates submitted to laser annealing at three different fluencies E (0.50-0.75-1.0 J/cm^2).

The SEM image in fig. 4.13 (a) shows that at the lower fluence E (0.50 J/cm^2), the break up into discrete droplets is incomplete. At fluencies higher than the threshold for breakup, the films are completely dewetted in NPs (figs. 4.13 (c), 4.13 (e)).

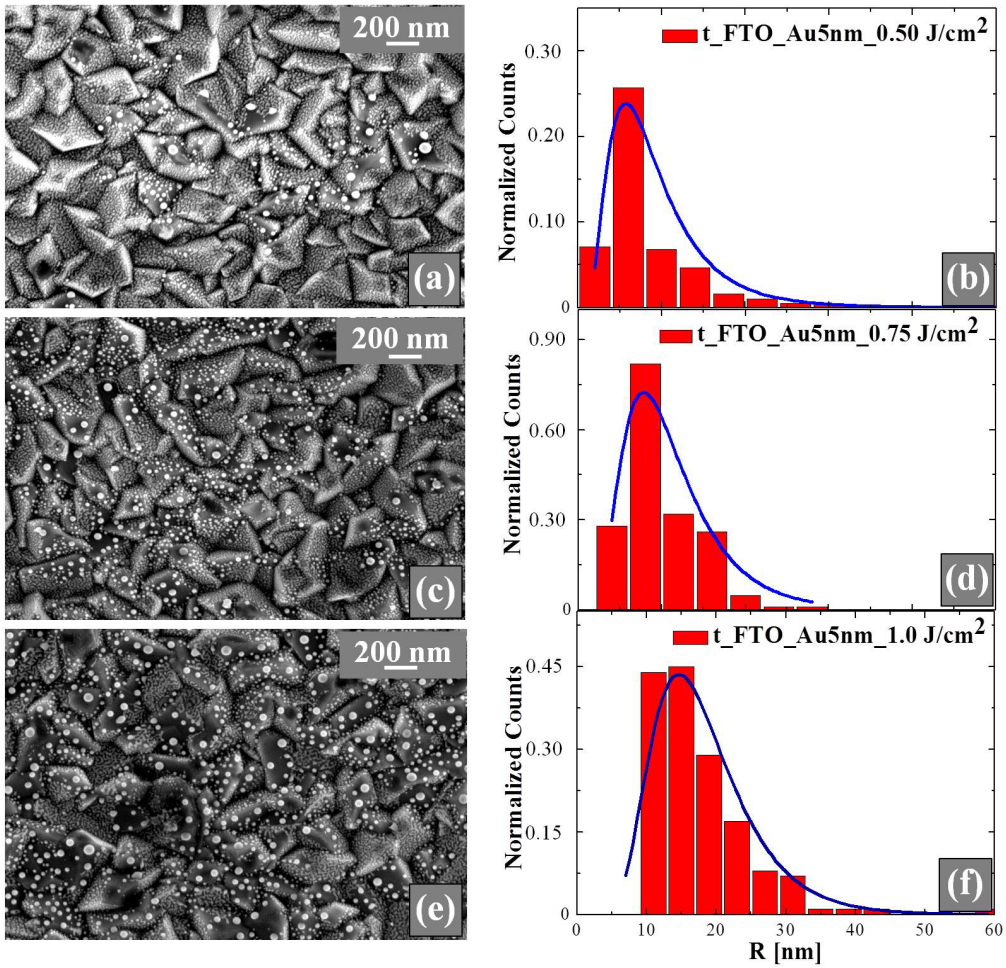

Figure 4.22 - SEM images and size distribution related to Au coated glass/t_FTO substrates submitted to laser annealing at three different fluencies: (a)-(b) FTO/glass substrates covered by 5 nm of Au and submitted to laser treatment at 0.50 J/cm^2; (c)-(d) substrate covered by 5 nm of Au and submitted to laser treatment at 0.75 J/cm^2; (e)-(f) substrate covered by 5 nm of Au and submitted to laser treatment at 1.0 J/cm^2.

The mean NPs radius is quantified as a function of laser fluence E by the analyses of the SEM images (fig. 4.22 (a)-(c)-(e)). From the inspection of the size distributions in figs. 4.22 (b), 4.22 (d) and 4.22 (f), we can observe that the mean Au NPs radius, <R>, increases from (9.3±1.8) nm to (18.2±3.6) nm when E increases from 0.50 J/cm^2 to 1.0 J/cm^2, while the sheet resistance values do not exhibit significant changes due to local heating of the samples (see tab. 4.1).

In order to obtain more information about the effects of the increasing E on the Au NPs structural parameters, we report in fig. 4.23 the <R>, <s> and <N> as a function of laser fluencies.

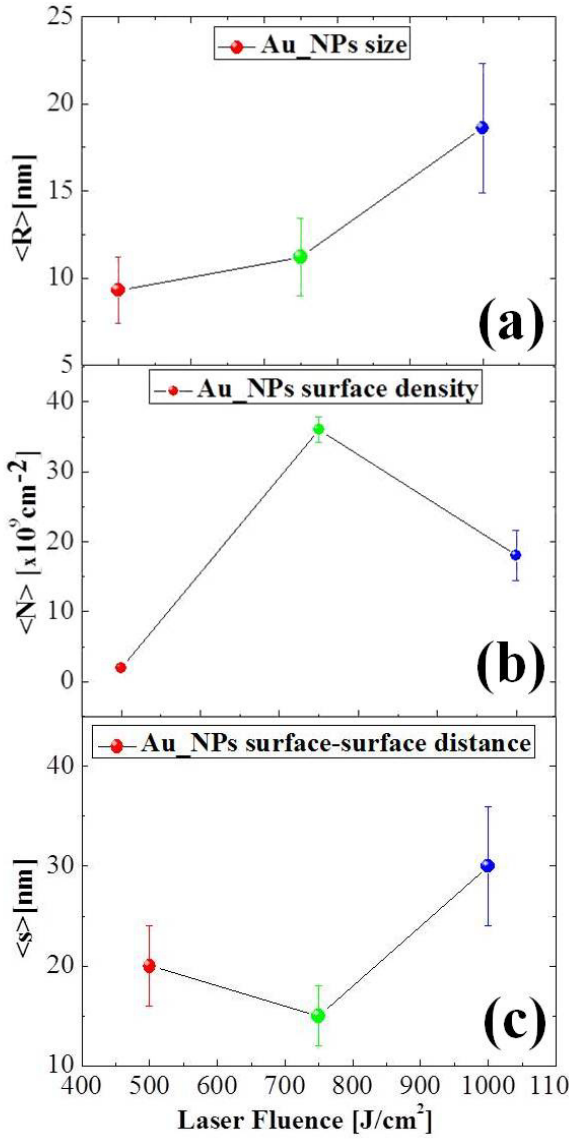

Figure 4.23 - Au NPs structural parameters as a function of laser fluencies related to the substrates covered by 5 nm-thick Au film: (a) the average size of Au NPs (<R>); (c) the surface density of Au NPs (<*N*>); (d) the average surface-surface distance between nearest NPs (<s>).

As reported above, the average size of the NPs increases when laser fluence is raised (fig. 4.23 (a)). Instead, the surface density of Au NPs (fig. 4.23 (b)) increases from $<N_{0.50}>=(2.0\pm0.4)\cdot10^{9}$ cm^{-2} to $<N_{0.75}>=(36\pm7.2)\cdot10^{9}$ cm^{-2} when E increases from 0.50 to 0.75 J/cm^2, while it decreases to $<N_{1.0}>= (18\pm3.6)\cdot10^{9}$ cm^{-2} in the energy range between 0.75 J/cm^2 and 1.0 J/cm^2. The increase of the surface density, in the laser range between 0.50 and 0.75 J/cm^2, induces the reduction of the surface-to-surface distance between nearest NPs (fig. 4.23 (c)).

To understand the correlation between the structural parameters and optical properties of the glass/t_FTO/Au NPs systems, reflectivity and transmittance measurements in the spectral range between 330 nm and 1100 nm, were performed. The absorption spectra in fig. 4.24 were calculated as

$$Abs=100-R_{tot}-T_{tot} \tag{4.18}$$

where T_{tot} is the total transmission of the glass/t_FTO/Au NPs multilayer (i.e. the sum of the collimated and diffused transmission, $T_{tot}=T_C+T_D$), and R_{tot} is total reflection ($R_{tot} = R_C+ R_D$).

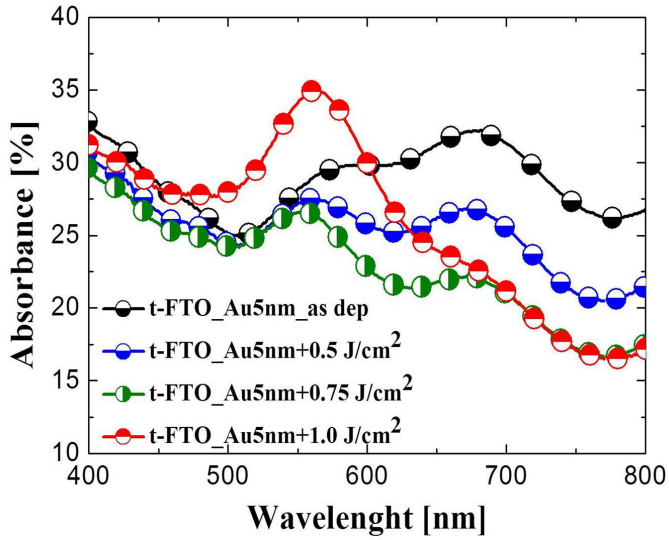

Figure 4.24 - Comparison between absorption spectra of sample as deposited (black line) and the samples covered by 5nm-thick Au film submitted to laser treatment at: 0.50 J/cm^2 (blue curve); at 0.75 J/cm^2 (green curve) and at 1 J/cm^2 (red curve). The spectrum of the samples treated at higher laser fluente (0.75-1.0 J/cm^2) highlight the plasmonic peak at about 560 nm owing to the resonant couplingbetween incident light and Au NPs.

Since the amount of radiation absorbed or scattered by Au NPs depends on their density and size, the gradual breaking of the Au film due to increasing laser energies justifies the different trends of the absorption spectra (see fig. 4.24). The spectra, for each laser fluence, show the plasmonic peak at about 560 nm owing to the resonant coupling between incident light and

Au NPs. Indeed, after laser anneling at fluencies between 0.5-1.0 J/cm^2, the formation of Au NPs on the t-FTO surface justifies the presence of the plasmonic peak (at about 560 nm) due to the resonant coupling between the incident light and Au NPs. Assuming Au NPs with the same shape, the values of the Au NPs radius, which vary between 5 and 50 nm, do not induce significant shifts in the plasmonic peak [65]. As reported in the SEM images of figs. 4.22 (a) - 4.22 (e), the increased laser fluence induces the increase of the surface area covered by Au NPs (F_{Au_NPs}), with respect to the area covered by non-dewetted Au film ($F_{Au\ \_film}$). The increase of F_{Au_NPs} and the decrease of F_{Au_film}, with increasing the laser fluence, is responsible for the increase of the scattering cross section ($\sigma_{scat}t > \sigma_{abs}$). This point will be further clarified in the following fig. 4.28, by reporting quantitative evaluations on the scattering and absorption cross sections. For this reason, in fig. 4.24 we observe the reduction of the average absorption values when the laser fluence is raised up to 1.0 J/cm^2. As shown in fig. 4.24, the higher intensity of the plasmonic peak is obtained as a consequence of laser annealing at 1.0 J/cm^2. For this sample, the larger fraction of scattered radiation by Au NPs explains the decreasing trend of the absorption values for wavelengths above 680 nm.
Therefore, as suggested from the structural and optical characterizations of the 5 nm-thick Au film submitted to laser annealing at increasing laser fluencies, the heating stage at 1.0 J/cm^2 induces the complete break-up of the Au film into discrete nano-droplets, which exhibit an optimized resonant coupling with the incident light in the visible spectral range.
In order to modulate the optical response of Au NPs, a 10 nm-thick Au film was deposited on the glass/t_FTO substrate (see SEM image in fig. 4.25), and the laser treatment at 1.0 J/cm^2 was performed.

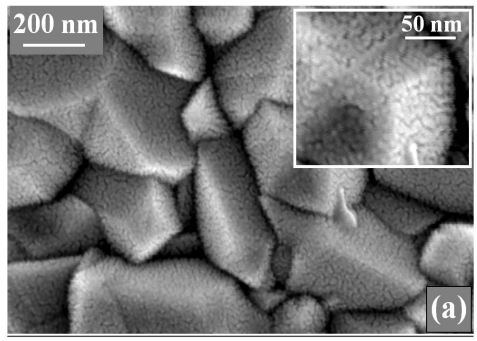

Figure 4.25 - SEM image of the sputter-deposited 10 nm-thick Au film on glass/t-FTO substrate (sample as deposited). The inset is high-resolution SEM image of the sample surface.

The representative SEM image (fig. 4.26 (a)) of the sample surface after the heating treatment was analyzed to determine the NPs structural parameters. The average radius of NPs is $\langle R \rangle$ = (24.0±4.8) nm (fig. 4.26 (b)); their surface density is $\langle N_{\_1.0} \rangle$=(9.3±1.9).10^9 cm^{-2}; the surface-surface distance between nearest nanoparticles is $\langle s_{\_1.0} \rangle$=(52.0±10.4) nm.

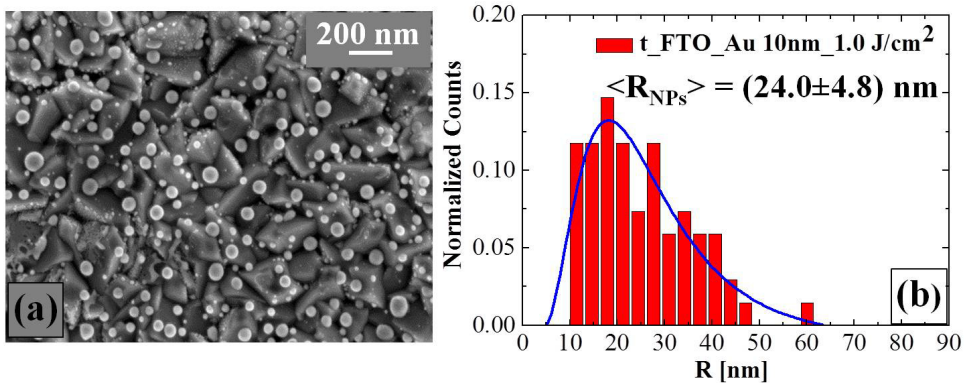

Figure 4.26 - SEMimage and size distribution related to deposited 10 nm-thick Au film on glass/t-FTO substrate submitted to laser annealing at higher laser fluence (1 J/cm^2).

After the structural characterizations of the metallic nanostructures with higher planar size, we are interested to study the Au NPs structure-dependent absorption spectra. Therefore, the measurements of the total transmission (T_{tot}), as well as the total reflection (R_{tot}), were performed (see spectra in fig. 4.27 (a)). Then, the light absorption spectrum of the LTM multilayer with larger Au NPs was calculated using relation 4.18. Figure 4.27 (b) shows the comparison between the absorption spectra related to the substrates covered by 5 nm or 10 nm Au films and submitted to laser treatment at 1 J/cm^2.

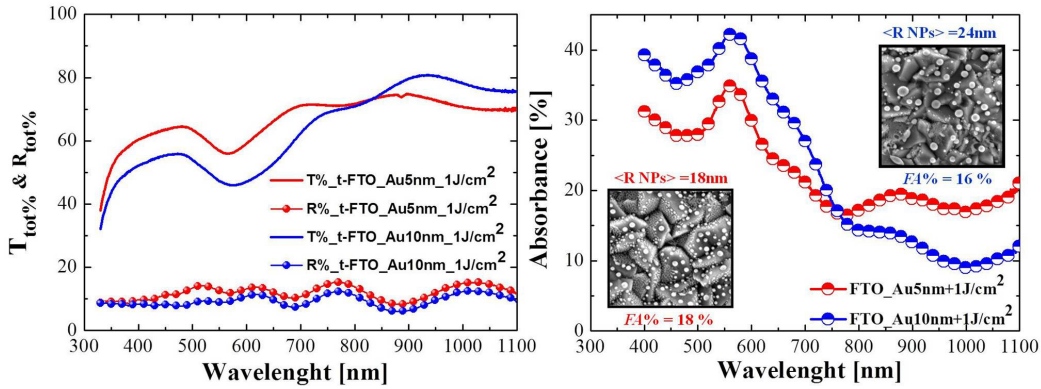

Figure 4.27 - (a) Total reflectivity ($R_{tot}=R_C+R_{D)}$ and total transmission ($T_{tot}=T_C+T_{D)}$ spectra in the spectral range between 330 nm and 1100 nm. (b) Comparison between the absorbance values related to the substrates covered by 5 nm (red curve) or 10 nm of Au (blue curve) and submitted to laser treatment at higher energy. The values of the filled area (FA%) and the unlike Au NPs sizes justify the differences in the absorption spectra.

In order to obtain information about the different trends of the absorption curves, SEM images (figs. 4.22 (e) and 4.26 (a) were analyzed to determine the mean values of the surface area covered by Au NPs. These values were calculated by

$$FA\% = \left(< N > \cdot \frac{A}{S} \right) \cdot 100 \tag{4.19}$$

where <N> is the average number of counted nano-structures, A is the average area covered by a single structure and S is the scanned area. The resulting fraction of covered areas by the NPs are FA%_Au5nm = 18% and FA%_Au10nm = 16%. Thus, the higher absorption, obtained in our data for larger Au NPs (fig. 4.21 (b)), cannot be justified assuming that the absorbed component is strictly related to the fraction of covered area, indeed in this case the light absorptions should be the same for the two samples. Instead, the sample with larger Au NPs exhibits a higher absorption in the analyzed spectral range (fig. 4.27 (b)) that may be attributed to the increased size of Au nanoparticles.

To understand the difference in the fraction of diffused radiation with respect to the absorbed radiation when the NPs size is increased, we run a simulation of the ratio between the scattering cross section (σ_{scatt}) and absorption cross section (σ_{abs}) of Au NPs surrounded by a dielectric and isotropic medium such as the FTO (see fig. 4.28). The Mie plot public domain software [66, 67] simulates the σ_{scatt} and σ_{abs} in agreement with the Mie theory of the scattering and absorption of electromagnetic radiation by homogeneous sphere of any diameter and any composition in a homogeneous medium. The simulation assumes isolated Au spherical shaped NPs of radius R, inside the homogeneous and isotropic medium with refractive index (n_{FTO}~2.0); the refractive index of bulk Au was used in the simulation since for NPs larger than 10 nm the physical constants of the metal Au may be applied as a first approximation [58, 68, 69].

In fig. 4.28, the values of $\sigma_{scatt}/\sigma_{abs}$ are lower than 1 for both samples in the range from 200 nm to about 600 nm. This result highlights that the absorption efficiency (scaling with R^3) dominates over scattering efficiency (scaling with R^6). For wavelength values above 600 nm, the ratio becomes higher than 1 for the sample with bigger NPs (<R>=24 nm), and it is larger than the ratio derived for the sample with smaller NPs (<R>=18 nm). The highest value of the ratio is obtained for a wavelength of about 700 nm for both samples. Moreover, the insets in fig. 4.28 show that, by varying the NPs size, the scattering intensity remains symmetric in forward and reverse directions. Therefore, in the range between 600 nm and 1100 nm, the fraction of the radiation diffused in forward and reverse directions by Au NPs, with a radius of about 24 nm, is greater than the absorbed component. This means that the surface coverage size distribution of MNPs is the key parameter to correlate the LTM structural and optical properties (as reported in Subsection 4.4.3).

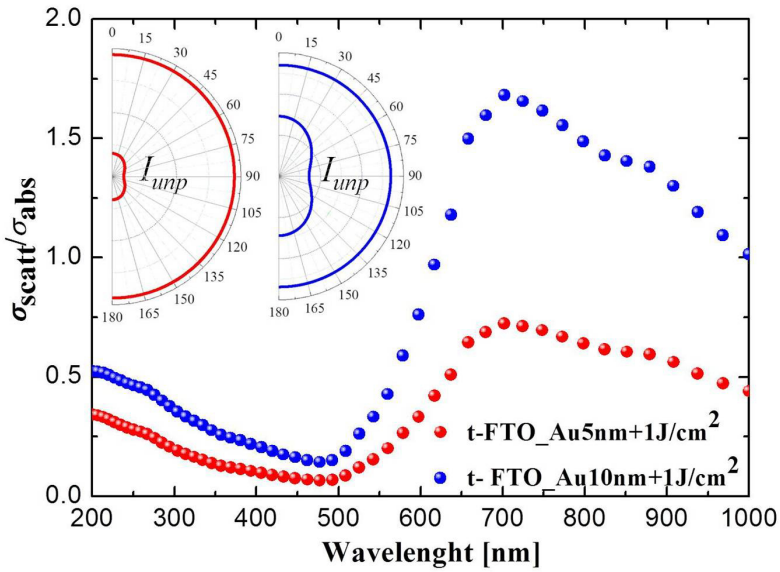

Figure 4.28 - Simulated trends in the visible spectral range of the ratio between the scattering cross section (σ_{scatt}) and absorption cross section (σabs) related to substrates covered by Au NPs with different size. The efficiency of absorption dominates over the scattering efficiency in the range from 200 nm to about 600 nm for both samples. At λ=600 nm, the ratio becomes higher than 1for the sample with bigger NPs (blue curve) and is much larger than the ratio derived for the sample with smaller NPs (red curve). The insets show that, by varying the NPs size, the scattering remains symmetric in forward and reverse directions by raising Au NPs size from 18 nm to 24 nm.

.

4.5 Applications: thin film solar cell containing Au nano-particles at the textured FTO/p-i-n interface (t_FTO/Au NPs solar cells)

4.5.1 Fabrication of t_FTO/Au NPs solar cells

As reported in Subsection 4.4, the structural and optical characterizations of the samples covered by gold films (5/10 nm Au thickness) and submitted to laser annealing at high laser fluence (see schematic picture in fig. 4.29 (a)), exhibit the formation of gold nanoparticles (Au NPs) on the t-FTO surface (see schematic picture in fig. 4.29 (b)). The NPs size were modulated by tuning the starting thickness of the sputtered deposited Au film to achieve a good compromise between the amount and directionality of the light scattered by Au NPs.

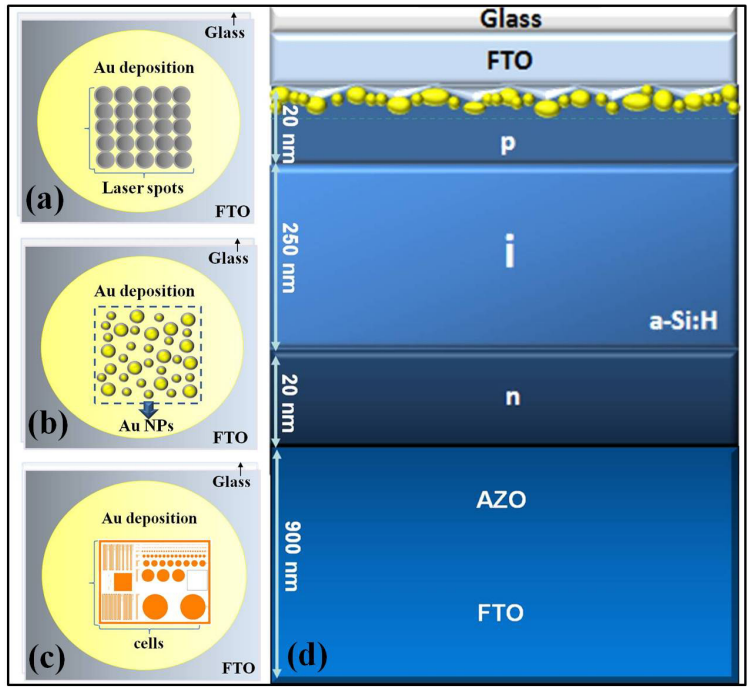

Figure 4.29 - Schematic pictures of Au-coated glass/t-FTO substrates (plan-view from the top): (a) submitted to laser annealing (each circle represents a laser spot); (b) after the laser annealing (each circle represents a gold nanoparticle); (c) after the photolithography process (the lines and the circles represet cells with different shape and sizes). (c) Structure of the thin-film solar cell with glass/t-FTO/Au NSs multilayer (cross-section).

In order to integrate the light-trapping multilayer in photovoltaic devices, the preparation and characterization of Au NPs with different size (<R>= 8/24 nm) were reproduced on the glass/t-FTO slides with size suitable for industrial lithography processes (6" substrates). Indeed,

photolithography and etching process are used to define cells with different shape and size on the sample surfaces (fig. 4.29 (c)).

As reported in fig. 4.29 (d), the active layer of the cell is the p-i-n structure (see subsection 4.1.1) formed by: 20 nm p-type Si (p-region), 250 nm hydrogenated amorphous Si (a-Si:H, intrinsic region), 20 nm n-type Si (n-region). This active layer is grown on the glass/t_FTO/Au NSs multilayer (top of the device, from which the radiation arrives). The device is completed by the second electrode (back of the device) formed by a FTO/AZO (Al doped zinc oxide) multilayer. To obtain information about the performances of the solar devices with or without the Au NPs at the interface, the current-voltage (I-V) characteristics (measured using as electrodes the two FTO layers) under standard illumination conditions (AM 1.5G spectrum, 1000 MW/m^2 incident optical power, 25 °C sample temperature) were taken by Keithley 236 source-measure unit and Solar-Simulator by Oriel, with a 2"×2" collimated beam with 1600 W xenon, ozone free arc lamp, and by illuminating the cells from the glass side under normal light incidence. Figure 4.30 shows the I-V curves related to the t-FTO reference thin solar cell and the t-FTO/Au NPs solar cells under light condition (fig. 4.30 (a)) and under dark condition (fig. 4.30 (b)).

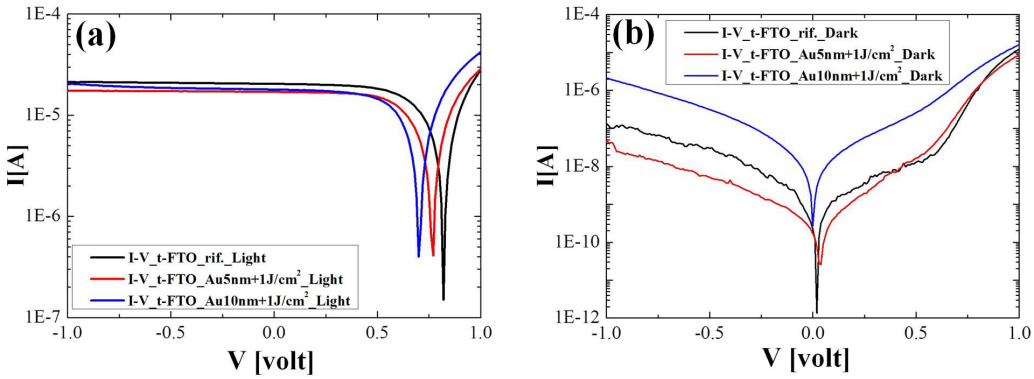

Figure 4.30 - The current-voltage (I-V) characteristics related to the reference solar cell (black line) and the solar cells with Au NPs at FTO/p-i-n interface (red line Au 5nm, blue line Au 10nm): (a) under light condition; (b) under dark condition.

We derive the solar cells parameters by quantitative analyses of the I-V characteristics reported in fig. 4.24 (a). As reported in subsection 4.1.4, the first step of the analysis is generating the forward biased I-V curve between the two points (V_1 = 0, I_1 = Isc), and (V_2 = Voc, I_2 = 0) in order to extract the short-circuit current (I_{SC}) and open-voltage V_{OC} values (see I-V characteristics in fig. 4.31). Figure 4.31 also reports the values of maximum cell current (I_m) and voltage (V_m) at the maximum power point, $P_m = I_m \cdot V_m$, for each I-V characteristic analysed.

The experimental data highlight that the incorporation of size-selected Au NSs, at the t_FTO/p-i-n interface, induces the modulation of the device electrical parameters, such as V_{OC}

and I_{SC}. In particular, the comparison between the current-voltage (I-V) characteristics shows that the V_{OC} values decrease by increasing the size of Au NP, while I_{SC} increases by improving the NPs size. The value of I_{SC} related to the cell with larger Au NPs is lower than the one obtained for the reference t_FTO thin film solar cell. This result suggests a light trapping reduction, which decreases by increasing the size of NPs introduced at the t_FTO/p-i-n interface.

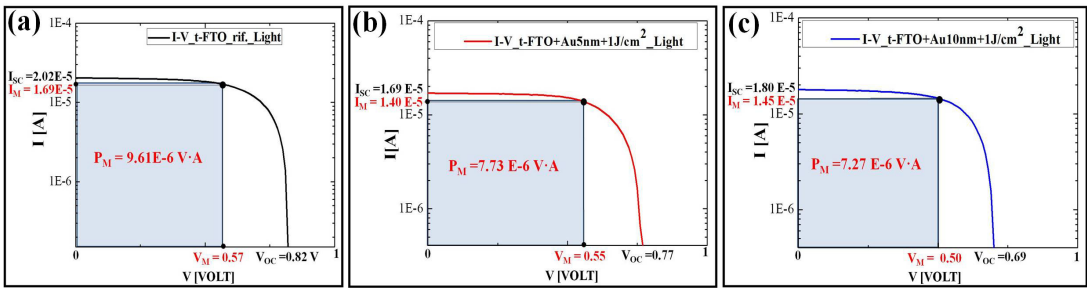

Figure 4.31 - I-V characteristics related to: (a) t_FTO thin film solar cell; (b) t_FTO/Au NPs thin film cell containing Au NPS with smaller size (<R> = 18 nm); (c) t_FTO/Au NPs thin film cell containing Au NPS with larger size (<R> = 24 nm). The pictures report the values of I_{SC}, V_OC, I_M, V_M and P_M.

The changes on V_{OC} and I_{SC} affect the solar cells parameters. Indeed, the values in table 4.2 indicate that the incorporation of Au NSs at the FTO/p-i-n interface worsens the parameters, such as the fill-factor (FF) and yield factor (η), calculated using Eqs. 4.13- 4.14 (see Subsection 4.1.4).

Solar Cell	V_{OC} [V]	I_{SC} [10^{-5}A]	V_M [V]	I_M [10^{-5}A]	P_M [10^{-6}A]	FF	η
t-FTO _ rif.	0.82	2.02	0.57	1.69	9.61	0.58	7.6%
t-FTO_Au5nm+1J/cm^2	0.77	1.69	0.55	1.40	7.73	0.59	6.1%
t-FTO_Au10nm+1J/cm^2	0.69	1.80	0.50	1.45	7.27	0.58	5.8%

Tab. 4.2 – Values of the device parameters related to t_FTO and t_FTO/Au NPs solar cells.

To understand how the Au NPs incorporation affects the electrical properties of devices, we report in the following subsesction the electrical characterization of thin film solar cells containing a glass/t_FTO/Au NPs multilayer.

4.5.2 Electrical properties modulation of the t-FTO/Au NPs solar cells

In this Subsection, we show the comparison between the electrical properties of the reference solar cell (glass/t_FTO/p-i-n) and the same device with Au NPs at the t_FTO/p-i-n interface. To study the effects of the incorporation of Au NPs on the device properties (under dark conditions), the values of the Schottky barrier height (φ_B) of the contact at the FTO/p interface (in the p-i-n structure) were calculated according with the thermionic emission theory (see subsection 4.1.4) by using the following relation:

$$\varphi_B = \frac{KT}{q} \ln\left(\frac{AA^*T^2}{I_S}\right) \tag{4.20}$$

where I_s is the saturation current, A is the contact area, A*is the Richardson constant for the p-type Si (32 A· cm^{-2}·K^{-2}), T is the absolute temperature, K is the Boltzmann constant and q is the electron charge [70]. The φ_B values are in excess of ~ 0.40 eV and suggest that the interfaces have rectifying electrical properties (see Subsection 4.1.2). Figure 4.32 (a) shows the trend of φ_B as a function of the Au NPs radius. Besides, the barrier height decreases from $\varphi_{B\_t\text{-}FTO}$=(0.80±0.06) to $\varphi_{B\_FTO+NSs}$=(0.70±0.05) eV when <R> rises to (24.0±4.8) nm. The reduction of φ_B induces the improvement of the spatial charges collection across the solar device. Indeed, the analysis of the I-V characteristics, under dark conditions, indicates that the saturation current increases from $I_{s\_t\text{-}FTO} = 6.30\cdot10^{-11}$ A to $I_{s\_FTO+NSs} = 6.25\cdot10^{-9}$ A when the barrier height is reduced to $\varphi_{B\_FTO+NSs}$ = 0.70 eV (as reported in Subsection 4.1.3, the saturation current, I_s, can be extracted in a plot ln [I(V)] versus forward bias). Thus, by varying <R>, φ_B can be tailored, so effecting the I-V characteristics of the devices.

Instead, under light conditions, the I-V characteristics (fig. 4.32 (b)) highlight a reduction of V_{OC} for the solar cells with Au NSs at the t_FTO/p-i-n interface, with respect to the reference device (see fig. 4.31). To understand the variations on the device electrical parameters, we analize the gass/t_FTO/Au NPs multilayer optical properties, reported in Subsection 4.4.3.b. The comparison between the absorption spectra related to two substrates, covered by Au NPs with different size, shows that the multilayer with larger Au NPs exhibits a higher absorption (fig. 4.27 (b)). This absorption improvement is attributed to the increased Au NSs size, since the Filled Area (FA) covered by Au NPs is the same for both multilayers (FA_NSs ~ 17%). Besides, the simulations in fig. 4.28 shows that for wavelength values above 600 nm, the ratio $\sigma_{scatt}/\sigma_{abs}$ becomes higher than 1 for the sample with bigger NPs (<R> = 24 nm), and it is larger than the ratio derived for the sample with smaller NPs (<R>=18 nm). Therefore, the improvement of the radiation scattered by larger NPs into the solar cell absorber layer justifies the increase of the I_{SC} values (see fig. 4.32 (b)).

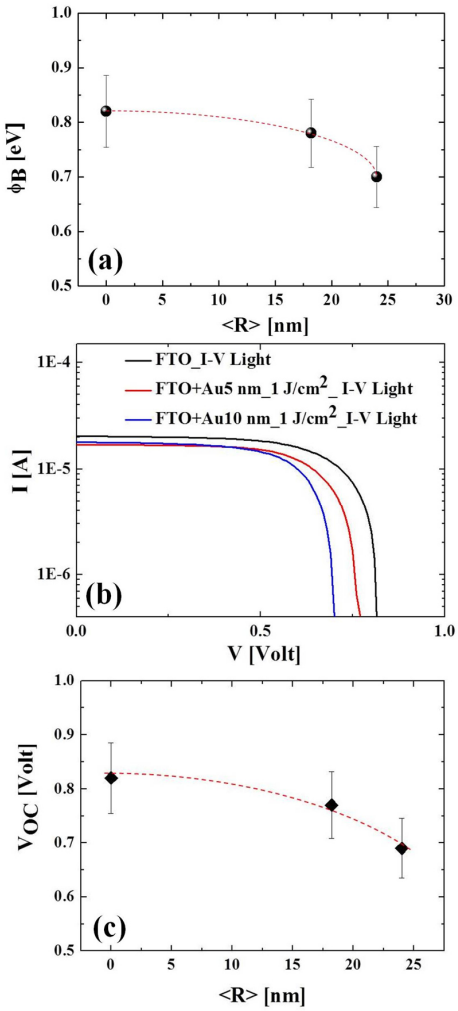

Figure 4.32 - (a) Trend of the Schottky barrier heights (φB) as a function of the Au NSs size. (b) Comparison between I-V characteristics (under light conditions) related to the reference cell (black curve) and the cells containing Au NSs with different size at the t-FTO/p-i-n interface (red and blue curves). (c) Trend of the open-circuit voltage (V_{OC}) as a function of the Au NSs size.

As reported above, the analysis of the I-V characteristics under dark conditions, indicates an improvement on I_s of about one order of magnitude (I_{s_Au5nm} = $2.64 \cdot 10^{-10}$ A and I_{s_Au10nm} = $6.25 \cdot 10^{-9}$ A) when the Au NPs size is increased. The open circuit voltage, V_{OC}, depends on I_s and I_{SC}, according to the relation [1]:

$$V_{OC} = \left(\frac{K_B T}{q}\right) \cdot \left[\ln\left(\frac{I_{SC}}{I_s}\right) + 1\right] \tag{4.21}$$

where T is the absolute temperature, k_B is the Boltzmann constant, q is the electron charge and I_{SC} and I_s are the short-circuit and saturation current.
The relation 4.21 indicates that the open-circuit voltage increases logarithmically by decreasing the saturation current, I_s. Thus, the enhancement of the saturation current (determined by mechanisms such as the recombination or diffusion currents) induces a V_{OC} reduction that increases with the improvement of the NSs size.
Therefore, as reported in Subsection 4.1, the decrease in V_{OC} indicates a current-trasport dominated by R&G (recombination and generation) processes. This result suggest that, in solar devices with larger Au NSs at the t_FTO/p-i-n interface, the depletion regions and the interfaces are full of R&G centers, with respect to the reference device. Taking into account the presence of Au NPs at the FTO/p-i-n interface, R&G centers may be metal-induced gap-states or defect-realeted states at the MS interface, in agreement with the Fermi level pinning proposals (see Subsection 4.1.3).
We conclude that the incorporporation of MNPs at the t_FTO/p-i-n interface induces the reduction of the Schottky barrier height and the likely presence of impurity states at the interface, which are responsible of the V_{OC} reduction. This conclusion is supported by the ideality factor values obtained for the solar cells with Au NPs at the interface. Indeed, the n values, calculated by the analysis of I-V characteristics under dark conditions (see Subsection 4.1.4) are higher than 2 (n>>2: non-ideality Schottky diode) for the devices containing Au NPs with respect to the reference device. Besides, the n value increases with the NPs size, and highlights a reduction of the gradient related to the log-linear curve at the high forward-bias region. Such reduction may be due to large values of R_s (series resistance, see schematic diagram in fig. 4.6) or tunneling processes through the device, which tend to increase the low forward bias current, thus decreasing the gradient of the log-linear I-V curve and increasing n. Therefore, according to the concepts reported in subsection 4.1.4, the changes on I_{SC} and V_{OC} (owing to the presence of the Au NPs at the t-FTO/p-i-n interface) worsen the solar cell parameters, such as the Fill Factor (FF) and yield factor (η).

4.6 Conclusions

In this Chapter, we have shown that the thermal treatments of thin Au films, deposited on a glass/t_FTO substrate, can induce the growth of Au NPs whose structural characteristics can be modulated by varying the parameters of the heating stages. For standard thermal processes, the temperature and time of the heating process are key parameters to induce the gold film break up and NPs growth. The structural characterizations of the thermal treated samples have shown that a temperature well below the gold melting point (1064 °C) induces the formation of arrays

of Au nanodroplets due to the solid-state dewetting process. In particular, the heat treatment at high temperature (500 °C-180 min) allows a whole break up of the Au film into nanoparticles, but induces structural changes of the substrate, so that the electrical response of the glass/FTO/Au NPs multilayer is worsened. This result implies that the standard thermal process at T above 400°C does not allow to obtain a glass/t_FTO/MNPs multilayer with electrical properties suitable for photovoltaic applications.

After the Au NPs synthesis by standard annealing, we have submitted the samples as deposited to laser irradiation at increasing fluence (0.50-1.0 J/cm^2) in order to optimize the synthesis process of Au NPs and preserve the structural and electrical properties of the t_FTO/glass substrates. The electrical measurements have suggested that the laser operating at 532 nm does not produce any thermal damage due to local heating of the FTO layer. The structural analyses of the Au coated-substrates have indicated that the metallic films are molten and broken up into discrete-nanometer scale islands after laser exposure. At lower energy, the break up into discrete droplets is incomplete. At fluencies higher than the threshold for breakup (1.0 J/cm^2), the films are fully dewetted in Au NPs. The comparison between the absorption spectra, related to the substrates covered by 5 nm or 10 nm of Au and submitted to laser treatment at higher energy, have indicated an improvement of the absorbed radiation from the sample with larger Au NPs. The simulated trends of the ratio between scattering cross section and absorption cross section in the visible spectral range have suggested that the efficiency of absorption dominates over scattering efficiency in the spectral range between 200 and 600 nm for both samples. For wavelength values above 600 nm, the ratio becomes higher than 1 for the sample with bigger NPs (<R> = 24 nm), and is much larger than the ratio derived for the sample with smaller NPs (<R> =18 nm). These results suggest that the glass/t_FTO/Au NPs with larger gold nanoparticles exhibit a reduction of the parasitic absorption and an improvement of the scattering cross section in the spectral range between 600 nm and 1100 nm. By varying the NPs radius from about 18 nm to 24 nm, the simulation have shown that the scattering remains symmetric in forward and reverse direction. Thus, the experimental results have indicated that the surface coverage size distribution of MNPs is the key parameter to correlate the structural and optical properties of the glass/FTO/Au NPs multilayer.

For its peculiar optical and electrical properties, we have intruduced the glass/t_FTO/Au NPs multilayer (obtained by nanosecond laser irradiation) with optimized MNPs coverage size distribution, as Light-Trapping-Multilayer (LTM), into thin film solar cells. In order to obtain information about the effects of the introduction of Au NPs at the t_FTO/p-i-n interface of solar devices, the I-V characteristics have been taken into account. The analysis of I-V characteristics under dark conditions have indicated a decrease of the Schottky barrier φ_B by increasing the Au NPs size. This phenomenon have induced an improvement on saturation current of about one order of magnitude ($I_{S\_Au5nm}=2.64\cdot10^{-10}$ A, and $I_{S\_Au10nm}=6.25\cdot10^{-9}$ A). The enhancement of the saturation current and the reduction of SB height (determined by mechanisms such as the recombination or diffusion currents) have induced a V_{OC} reduction that increases with the improvement of the NPs size. The V_{OC} reduction have suggested a higher amount of recombination phenomena in the solar devices with larger Au NPs at the t_FTO/p-i-n interface,

with respect to the reference device. The improvement of the recombination process may be due to the presence of metal-induced gap states or defect-realeted states, in agreement with the Fermi-level (FL) pinning by electronic states at the MS interface. These processes reduce light trapping and then the I_{SC} values. Indeed, the analyses of I-V characteristics under light conditions have highlighted an improvement of I_{SC} due to the increase of the radiation scattered by larger NSs. Despite this increase, the value of I_{SC} is lower than one related to the reference device (t_FTO thin solar cell). Thus, the changes of I_{SC} and V_{OC} have worsened the solar cell parameters, such as the Fill Factor (FF) and yield factor (η).

References

[1] Dharmadasa IM (1988) "*Advances in thin film solar cells"* - Taylor & Francis Group, LLC (2012)

[2] Rhoderick EH and Williams RH "*Metal-SemiconductorContacts"* 2nd edn, Oxford Science Publications

[3] W. Monch, "*Electronic Properties of Semiconductor Interfaces"*-vol.43, Springer Series in Surface Science (2004)

[4] Tung RT, Physical Review B, Surface plasmon enhanced silicon solar cells. Vol. 45, N°. 23 (1992)

[5] Ruffino F, Crupi I, Irrera A, and Grimaldi MG, Pd/Au/SiC Nanostructured Diodes for Nanoelectronics: Room Temperature Electrical Properties. IEEE Transaction on Nanotechnology, Vol. 9, N°. 4 (2010)

[8] Green MA, Recent developments in photovoltaics. Sol Energy 76:3–8 (2004)

[9] Green MA, Basore PA, Chang N, Clugston D, Egan R, Evans R, Hogg D, Jarnason S, Keevers M, Lasswell P, O'Sullivan J, Schubert U, Turner A, Wenham SR, Young T, Crystalline silicon on glass (CSG) thin-film solar cell modules. Sol Energy 77:857–863 (2004)

[10] Aberle AG, Progress with polycrystalline silicon thin-film solar cells on glass at UNSW. J Cryst Growth 287:386–390 (2006)

[11] Mishra YK, Kabiraj D, Sulania I, Pivin JC, Avasthi DK, Synthesis and characterization of gold nanorings. J Nanosci Nanotech 7:1878–1881(2007)

[12] Mishra YK, Adelung R, Kumar G, Elbahri M, Mohapatra S, Singhal R, Tripathi A, Avasthi DK, Formation of selforganized silver nanocup-type structures and their plasmonic absorption. Plasmonics 8:811–815 (2013)

[13] Avasthi DK, Mishra YK, Kabiraj D, Lalla NP, Pivin JC, Synthesis of metal–polymer nanocomposite for optical applications. Nanotechnology 18:125604 (2007)

[14] Mishra YK, Mohapatra S, Chakravadhanula VSK, Lalla NP, Zaporojtchenko V, Avasthi DK, Faupel F, Synthesis and characterization of Ag-polymer nanocomposites. J Nanosci Nanotech 10:2833–2837 (2010)

[15] Hutter E, Fendler JH, Exploitation of localized surface plasmon resonance. Adv Mater 16:1685–1706 (2004)

[16] Haes AJ, Zou S, Schatz GC, Van Duyne RP, A nanoscale optical biosensor: the long range distance dependence of the localized surface plasmon resonance of noble metal nanoparticles. J Phys Chem B 108:109–116 (2004)

[17] Kityk IV, Plucinski KJ, Ebothe´ J, Ali Umar A, Oyama M, Control of the plasmon absorption of gold nanoparticles with a two-color excitation. J Appl Phys 98:084304(2005)

[18] Eustis S, El-Sayed MA, Why gold nanoparticles are more precious than pretty gold: Noble metal surface plasmon resonance and its enhancement of the radiative and nonradiative properties of nanocrystals of different shapes. Chem Soc Rev 35:209–217(2006)

[19] Szunerits S, Praig VG, Manesse M, Boukherroub R, Gold island films on indium tin oxide for localized surface Plasmon sensing. Nanotechnology 19:195712(2008)

[20] Atwater HA, Polman A, Plasmonics for improved photovoltaic devices. Nat Mater 9:205–213 (2010)
[21] Bohren CF, Huffman DR, Absorption and scattering of light by small particles. Wiley-InterScience, New York (1998)
[22] Kreibig U, Vollmer M, Optical properties of metal clusters Springer, Berlin (1995)
[23] Mertz J, Radiative absorption, fluorescence, and scattering of a classical dipole near a lossless interface: a unified description. J Opt Soc Am B 17:1906–1913(2000)
[24] Catchpole KR, Polman A, Design principles for particle plasmon enhanced solar cells. Appl Phys Lett 93:191113(2008)
[25] Catchpole KR, Polman A, Plasmonic solar cells. Opt Express 16:21793–21800 (2008)
[26] Xu, G., Tazawa, M., Jin, P., Nakao, S. & Yoshimura, K. Wavelength, tuning of surface plasmon resonance using dielectric layers on silver island films. Appl. Phys. Lett. 82, 3811–3813 (2003)
[27] Mertens, H., Verhoeven J., Polman A. & Tichelaar F. D., Infrared surface plasmons in two-dimensional silver nanopartice arrays in silicon. Appl. Phys. Lett. 85**,** 1317–1319 (2004)
[28] Beck FJ, Polman A & Catchpole K R, Tunable light trapping for solar cells using localized surface plasmons. J. Appl. Phys. 105**,** 114310 (2009)
[29] Pillai S, Catchpole KR, Trupke T, and Green MA, Jorn. of Appl. Phys. 101, 093105 (2007)
[30] Fahr S, Rockstuhl C & Lederer F, Metallic nanoparticles as intermediate reflectors in tandem solar cells. Appl. Phys. Lett. 95, 121105 (2009)
[31] O'Carroll D, Hofmann CE & Atwater HA, Conjugated polymer/metal nanowire heterostructure plasmonic antennas. *Adv. Mater.* doi:10.1002/ adma.200902024 (2009)
[32] Labeke DV, Gerard D, Guizal B, Baida F I & Li L, An angleindependent frequency selective surface in the optical range. *Opt. Express* 14**,** 11945–11951(2006)
[33] De Waele R, Burgos SP, Polman A & Atwater HA, Plasmon dispersion in coaxial waveguides from single-cavity optical transmission measurements.*Nano Lett.* 9, 2832–2837 (2009)
[34] Kroekenstoel EJA, Verhagen E, Walters R J, Kuipers L & Polman A, Enhanced spontaneous emission rate in annular plasmonic nanocavities. *Appl. Phys. Lett.* **95,** 263106 (2009)
[35] Rizza G, Cheverry H, Gacoin T, Lamasson A, Henry S, Ion beam irradiation of embedded nanoparticles: toward an in situ control of size and spatial distribution. J Appl Phys 101:014321(2007)
[36] Ramjauny Y, Rizza G, Perruchas S, Gacoin T, Botha R, Controlling the size distribution of embedded Au nanoparticles using ion irradiation. J Appl Phys 107:104303 (2010)
[37] Chen Y, Palmer RE,Wilcoxon JP, Sintering of passivated gold nanoparticles under the electron beam. Langmuir 22:2851–2855(2006)
[37] Ruffino F, Grimaldi MG, Giannazzo F, Roccaforte F, Raineri V, Bongiorno C, Spinella C, Kinetic mechanisms of the in situ electron beam-induced self-organization of gold nanoclusters in SiO2. J Phys D Appl Phys 42:075304(2009)

[38] Wenzel T, Bosbach J, Goldmann A, Stietz F, Tra¨ger F, Shaping nanoparticles and their optical spectra with photons. Appl Phys B 69:513–517 (1999)
[39] Hubenthal F (2009) Nanoparticles and their tailoring with laser light. Eur J Phys 3:S49
[40] Forte K, Serbin J, Koch J, Egbert A, Fallnich C, Ostendorf A, Chichkov BN, Towards nanostructuring with femtosecond laser pulse. Appl Phys A 77:229–235 (2003)
[41] Korte F, Koch J, Chichkov BN, Formation of microbumps and nanojets on gold targets by femtosecond laser pulse. Appl Phys A 79:879–881 (2004)
[42] Henley SJ, Poa CHP, Adikaari ADT, Giusca CE, Carrey JD, Silva SRP, Excimer Laser nanostructuring of nickel thin films for the catalytic growth of carbon nanotubes. Appl Phys Lett 84:4035–4037 (2004)
[43] Koch J, Korte F, Bauer T, Fallnich C, Ostendorf A, Chichkov BN, Nanotexturing of gold films by femtosecond laser-induced melt dynamics. Appl Phys A 81:325–328 (2005)
[44] Henley SJ, Carrey JD, Silva SRP, Pulsed-laser-induced nanoscale island formation in thin metal-on-oxide films. Phys Rev B 72:195408 (2005)
[45] Henley SJ, Carrey JD, Silva SRP, Laser-nanostructured Ag films as substrates for surface-enhanced Raman spectroscopy. Appl Phys Lett 88:081904 (2006)
[46] Favazza C, Trice J, Krishna H, Kalayanaraman R, Sureshkumar R, Laser-induced short- and long-range orderings of Co nanoparticles on SiO2. Appl Phys Lett 88:153118 (2006)
[47] Longstreth-Spoor L, Trice J, Zhang C, Kalyanaraman R, Nanostructure and microstructure of laser-interference-induced dynamic patterning of Co on Si. J Phys D Appl Phys 39:5149–5159 (2006)
[48] Trice J, Thomas D, Favazza C, Sureshkumar R, Kalyanaraman R, Pulsed-laser-induced dewetting in nanoscopic metal films: theory and experiments. Phys Rev B 75:235439 (2007)
[49] Favazza C, Kalayanaraman R, Sureshkumar R, Dynamics of ultra-thin metal films on amorphous substrates under fast thermal processing. J Appl Phys 102:104308 (2007)
[50] Favazza C, Trice J, Kalayanaraman R, Sureshkumar R, Self-organized metal nanostructures through laser-interference driven thermocapillary convection. Appl Phys Lett 91:043105 (2007)
[51] Kuznetsov AI, Koch J, Chichkov BN, Nanostructuring of thin gold films by femtosecond lasers. Appl Phys A 94:221–230 37 (2009). Moening JP, Thanawala SS, Georgiev DG, Formation of high-aspect-ratio protrusions on gold films by localized pulsed laser irradiation. Appl Phys A 95:635–638 (2009)
[52] Sivakumar M, Venkatakrishnan K, Tan B, Characterization of MHz pulse repetition rate femtosecond laser-irradiated gold-coated silicon surfaces. Nanoscale Res Lett 6:78 (2011)
[53] Bauerle D, Laser processing and chemistry, 3rd edn. Springer, Berlin (2000)
[54] Meshcheryakov YP, Bulgakova NM, Thermoelastic modeling of microbump and nanojet formation on nanosize gold films under femtosecond laser irradiation. Appl Phys A 82:363–368 (2006)
[55] Poate JM, Mayer JW, Laser annealing of semiconductors. Academic, New York (1982)
[56] De Gennes PG, Brochard-Wyart F, Quere D, Capillarity and wetting phenomenon. Springer, New York (2003)

[57] Ruffino F., Carria E., Kimiagar S., Crupi I., Simone F., Grimaldi M.G., Formation and evolution of nanoscale metal structures on ITO surface by nanosecond laser irradiations of thin Au and Ag films. Sci Adv Mater 4:708–718 (2012)
[58] Johnson P.B., Christy R.W., Optical constants of the noble metals. Phys Rev B 6:4370–4379 (1972)
[59] Boltz J., Sputtered tin oxide and titanium oxide thin films as alternative transparent conductive oxides. Ph. D. Dissertation (2011)
[60] Morawiec S., Mendez M.J., Mirabella S., Simone F., Priolo F., Crupi I., Self-assembled silver nanoparticles for plasmonenhanced solar cell back reflectors: correlation between structural and optical properties. Nanotechnology 24:265601 (2013)
[61] Thompson C.V., Solid-state dewetting of thin films. Annu Rev Mater Res 42:399–434 (2012)
[62] Srolovitz D.J., Goldiner M.G., The thermodynamics and kinetics of film agglomeration. J Miner Met Mater Soc 47:31–36 (1995)
[63] Granqvist C.G., Buhrman R.A., Ultrafine metal particles. J Appl Phys 47:2200–2219 (1976)
[64] Presland A., Price G.L., Trimm D.L., Kinetics of hillock and island formation during annealing of thin silver films. Prog Surf Sci 20:10816–10826 (1972)
[65] Hu M., Chen J., Li Z.Y., Au L., Hartland G.V., Li X., Marquez M., Xia Y., Gold nanostructures: engineering their plasmonic properties for biomedical applications. Chem Soc Rev 35:1084–1094 (2006)
[66] Bohren C.F., Huffman D.R., Absorption and scattering of light by small particles. Wiley, New York (1983)
[67] Van de Hulst HC, Light scattering by small particles. Dover, New York (1981)
[68] Takami K., Kurita H., Koda S., Laser-induced size reduction of noble metal particles. J Phys Chem B 103:1226–1232 (1999)
[69] Kreibig U., Vollmer M., Optical properties of metal clusters. In: Toennies JP (ed) Springer series in Materials Science. Springer, New York (1995)
[70] Rhoderick E. H., and Williams R. H., *Metal–Semiconductor Contacts*, Oxford, U.K.: Clarendon, (1988).

Summary and Conclusion

This work has presented the results of the synthesis processes and structural, optical and electrical characterizations of metal-based complex morphology and composition nano-composite materials (such as Au Dendrites, SiO_2 Nanowires-Au Nanoparticles pea-podded composites, glass/textured_FTO/Au NPs multilayer). The aim is to assess the state of the art and, then, show the innovative contributions that can be proposed in this research field. Opportune methodologies, based on self-organization, have been developed for the production of such materials. Several microscopic techniques have been used to analyze the structural properties of the synthesized materials (i.e. RBS, SEM, AFM, TEM, EDX, EELS), and macroscopic measurements have been used to probe their electrical and optical properties. To understand the growth dynamic and the evolution of these complex systems, the correlation between structural and optical parameters has been established, and phenomenological growth models have been drafted.

The entire work has been focused on the research of innovative, versatile and low-cost synthesis techniques, suitable to provide a good control on the size, surface density and geometry of the complex nanostructures. Such optimization of the structural parameters is necessary to modulate the metallic nanostructures optical and electrical properties for each specific application. Therefore, the aim of this study is the fabrication of functional nano-scale-size materials, whose properties can be tailored, in a wide range, simply by controlling the structural characteristics. Optimized optical and electrical properties are required to improve the performance of new photovoltaic devices, biosensors, nano-scale optical devices, sensors and SERS active-substrates.

An overwiev of the basic concepts on the correlation between structural and optical parameters of plasmonic nanostructures, and the possible solutions offered by nanotechnology science in a large range of applications (catalysis, electronics, photonics, sensing), have been reported in the Chapter 1. Significantly, most of these applications require the use of metals in a finely divided state, preferably in the form of nanomaterials with precisely controlled properties. In order to understand what techniques are employed to obtain a controlled synthesis of complex shape nanostructures, some experimental and theoretical works on the more common synthesis techniques and characterization of metallic nano-scale materials have been presented. The aim has been to assess the state of the art, and then show the innovative contributions that can be proposed in this research field. These concepts are fundamental to understand the objectives of the experimental works presented in later chapters.

As concerns the innovative synthesis methods, in Chapter 2 an alternative procedure based on physical processes has been suggested to obtain aggregates of Au nanodendrites (reminiscent of fractal morphologies). Unlike the chemical methods proposed in the literature, a physical growth process (based on sputtering deposition of Au film and subsequently thermal treatment at high temperature) has been employed to obtain an μm-scale aggregate of Au dendritic nanostructures on different substrates with semiconductor matrix (c_Si, poly_Si, SOS). Since

the transfer of the Au ds from the solution to the substrate has been eliminated, we have obtained a greater control over the spatial arrangement of these complex nanostructures. Indeed, the uniform distribution of the Au dendrites, facilitates the structural and optical characterization of these materials. Besides, the kinetic processes that occur at the Au-Si interface in a far-from-equilibrium condition, and the parameters that affect the Au Ds dynamic growth and evolution (temperature, substrate and ramp rate during the thermal treatment) have been explained. Corcerning the optical properties of Au Ds, the SERS measurements (performed by using MB or thiophenol as probe molecules) have shown that the dendritic nanostructures can be used as SERS-active substrate to obtain amplification factors of electromagnetic field due to the resonant coupling between the Raman signal and plasmonic oscillations related to the sharp tips of the dendritic structures.

Another complex shape, based on metal nanoparticle-dielectric matrix composite systems, has been proposed in the Chapter 3. Many experimental works in the literature report the synthesis methods and the properties of this complex systems, but do not clearly explain how such a pea-pod structure is obtained. Up to now, the more detailed and reliable explanation models are based on a simple diffusion mechanism or thermodynamic instability process, which produces individual nano-beads, but in regular succession in the SiO_2 nanowires. For this reason, the purpose of this work has been to provide a systematic and quantitative analysis of the correlation between structural parameters of the SiO_2 NWs and the Au NPs included in the oxide matrix, during the growth process. From the experimental correlations of structural parameters, some information on the mechanisms governing the formation of the SiO_2 NWs-Au NPs pea-podded structures has been inferred. In particular, the different size and non-regular spacing between neighboring NPs have pointed out the likely co-existence of both diffusion and thermodynamic instability phenomena in the determination of the formation processes. On the basis of the experimental data, a phenomenological model for the formation and time evolution of the SiO_2 NWs/Au NPs pea-podded structures has been proposed. Then, a wide range of applications have been presented.

In Chapter 4, instead, the introduction of Au nanostructures with appropriate size and surface density has been suggested to improve the conversion efficiency of thin film solar cells. The aim has been to obtain Au NPs on the glass/t_FTO substrate, in order to maximize the far-field scattering efficiencies over the wavelength range suitable for each specific type of photovoltaic device. For this purpose, it is necessary to achieve a good compromise between the amount and directionality of the light scattered from the Au NPs. Part of the literature shows that the main parameter describing the correlation between LTM structural and optical parameters is the surface coverage size distribution of the MNPs. Therefore, we have proposed a simple stragegy, based on sputtering deposition of Au films and laser annealing at different fluencies, to obtain Au NPs on the glass/t_FTO surface, and modulate the NPs structural parameters such as size, surface density and surface-surface distance between neighboring NPs. Unlike standard thermal processes, the laser treatment has induced the fusion and, then, the breaking of the metal films into discrete-nanometer scale islands, but has not worsened the electrical properties of the substrates. After the optimization of the synthesis processes, the results of the optical

measurements have shown the possibility to use the Au NPs as sub-wavelength scattering elements to trap the sunlight into an absorbing semiconductor film by folding the light into a solar cell thin absorber layer. The electrical response of the solar cells, containing Au NPs with different size at t_FTO/p-layer interface (in the p-i-n structure), has been compared with that of the reference solar cell (glass/t_FTO/p-i-n structure), and the characteristic parameters of the devices have been obtained by analyses of the I-V characteristics. The study of the changes related to the electrical parameters has allowed to analyze the effects on the PV devices electrical response due to the introduction of the MNPs at the t_FTO/p-i-n interface.

The works proposed in this thesis represent a step ahead for the understanding of the phenomena involved in the nanoscale structuration of metallic materials with complex shape and composition, which are required in the design of plasmonic devices with improved performances.

List of publications

The present dissertation is based on the following publications:

1. Electrical properties modulation of thin film solar cell using gold nanostructures at t-FTO/p-i-n interface - **A. Gentile**, G. Cacciato, F. Ruffino, R. Reitano, G. Scapellato, M. Zimbone, S. Lombardo, A. Battaglia, C. Gerardi, M. Foti, M. G. Grimaldi - FUNCTIONAL MATERIAL LETTERS, Vol. 8, No.8 1550017 (2015);

2. Nanoscale structuration and optical properties of thin gold films on textured FTO - **A. Gentile**, G. Cacciato, F. Ruffino, R. Reitano, G. Scapellato, M. Zimbone, S. Lombardo, A. Battaglia, C. Gerardi, M. Foti, M. G. Grimaldi - JOURNAL OF MATERIAL SCIENCE 49, 8498–8507 (2014);

3. Structural and optical properties of solid-state synthesized Au dendritic structures - **A. Gentile**, F. Ruffino, L. Romano, S. Boninelli, R. Reitano, G. Piccitto, M. G. Grimaldi - APPLIED SURFACE SCIENCE 296, 177–184 (2014);

4. SiO_2 nanowires-Au nanoparticles peapodded composites: synthesis and structural analyses - **A. Gentile**, F. Ruffino, S. Boninelli, M. G. Grimaldi
(SUBMITTED FOR PUBLICATION)

Other publications:

5. Matrix role in Ge nanoclusters embedded in Si_3N_4 or SiO_2 - S. Mirabella, S. Cosentino, **A. Gentile**, G. Nicotra, N. Piluso, L. V. Mercaldo, F. Simone, C. Spinella, and A. Terrasi - APPLIES PHYSICS LETTERS 101, 011911 (2012).

Contributions to international conferences:

1. IEEE-Nanotechnology Materials and Device Conference 13/15 Ottobre 2014 Aci Castello (Italy)

• **Nano-scale structuration and optical properties of thin gold films on textured FTO** (**ORAL PRESENTATION -** Symposium: nanostructures for future generation solar cell);

• **SiO_2 nanowires-Au nanoparticles peapodded composites: synthesis and structural analyses**
(POSTER PRESENTATION - Symposium: advanced characterization of nanomaterials and nanostructures).

2. European Materals Research Society (EMRS) SPRING MEETING 26/31 Maggio 2014-Lille (France)

• **Synthesis and characterization of hybrid metal based nanosystems**
(POSTER PRESENTATION - Symposium Q: Hybrid materials engineering in biology, chemistry and physics);

• **Laser based synthesis of metallic nanoparticles towards efficient plasmonic solar cells**
(POSTER PRESENTATION - Symposium Y: Advanced materials and characterization techniques for solar cells II).

3. European Materials Research Society (EMRS) SPRING MEETING 26/31 2013-Strasburgo (France)

• **Compex morphology of Au nanostructures for improving plasmonic effects** (**ORAL PRESENTATION -** Symposium N: Atomic-scale engeneering of mutifunctional nano-sized materials and film).

Participations to international schools:

1. Course of International School of Solide State Physics on "Materials for Renewable Energy", Erice – 13/18 Luglio 2014 (Italy)

Nano-scale structuration and optical properties of thin gold films on textured FTO (POSTER PRESENTATION);

2. Course of International School of Solide State Physics on "Materials for Renewable Energy", Erice – 18/28 Luglio 2012 (Italy)

Compex morphology of Au nanostructures for improving plasmonic effects (POSTER PRESENTATION).

Acknowledgments

There are a lot of people who I wish to acknowledge for their help, guidance, collaboration, suggestions, support, incitements and friendship. All of them, in a way or another one, contributed to my human, scientific and cultural formation and to the development of this thesis.

First of all, I would like to thank Professor Maria Grazia Grimaldi (University of Catania), the tutor of the present work. By her experience, support, encouragement and supervision, she guided me during these my Ph. D. course.

Besides, I am deeply grateful to Dr. Francesco Ruffino, the supervisor of this thesis, who introduced me in this research field and supported me his with friendship, kindness, competence and patience. His contribution to this work has been fundamental, and his human and scientific teaching will remain always for me irreplaceable.

Then, I wish to tank Professor Francesco Priolo (University of Catania and MATIS CNR-INFM) and Dr. Vittorio Privitera (CNR IMM), which gave me the opportunity to work at MATIS CNR-INFM, Dr. Corrado Spinella (CNR IMM), who gave me the opportunity to work at IMM-CNR.

Special thanks go to Dr. Giovanni Piccitto (University of Catania) for his several teachings about plasmonic nanostructures, Professor Riccardo Reitano (University of Catania) and Professor Francesca Simone (University of Catania) for the optical measurements reported in this work.

In addition, I want to express sincere thanks to all the other people who I had the opportunity to meet during my Ph. D. course, and that accompanied me during this period: Professor Antonio Terrasi (University of Catania), Dr. Lucia Romano (University of Catania), Dr. Isodiana Crupi (MATIS CNR-IMM), Dr. Salvo Mirabella (MATIS CNR-IMM), Dr. Giuliana Impellizzeri (MATIS CNR-IMM), Dr. Elena Bruno (University of Catania), Dr. Simona Boninelli (CNR-IMM), Dr. Massimo Zimbone (MATIS CNR IMM), Dr. Maria Miritello (CNR IMM MATIS) Dr. Giorgia Scapellato (CNR IMM MATIS) and Giuseppe Cacciato (MATIS CNR IMM).

I also thank Dr. Anna Battaglia (3SUN S.r.l.), Dr. Andrea Canino (3SUN S.r.l), Dr. Salvo Lombardo (CNR-IMM), Dr. Marina Foti (STMicroeletronics), Dr. Cosimo Gerardi (STMicroeletronics), Dr. Pietro Gucciardi (CNR IPCF-Messina) and Dr. Christiano D'Andrea (CNR IPCF-Messina) for the opportunity to work at their laboratories and for all their suggestions.

A special thanks to the lab technicians (Giuseppe Pantè, Salvo Tatì and Carmelo Percolla) and my colleagues (Paolo Sberna, Stefano Boscarino, Salvo Cosentino, Saro Raciti, Simone Maenza, Lina Scuderi etc.) for the essential help.

Finally, I want to dedicate a space to my dear ones. Deep acknowledgments to my parents, which, throughout all my life, gave me encouragements, moral and practical supports.

At the end, the deeper, grateful, sincere thanks go to Reito: he has always believed in my abilities and gave me help and support. His presence has been and will be essential.